

# Magnetism, structure and vibrational dynamics of nanoscaled heterostructures: interfaces, ultrathin films and multilayers

Vom Fachbereich Physik – Technologie der  
Gerhard-Mercator-Universität Duisburg  
zur Erlangung des akademischen Grades eines  
Doktors der Naturwissenschaften (Dr. rer. nat.)  
genehmigte Dissertation

von  
**Beatriz Roldán Cuenya**  
aus  
Oviedo

Referent: Prof. Dr. W. Keune  
Korreferent: Priv. Doz. Dr. Günter Dumpich

Tag der mündlichen Prüfung: 24.09.2001



---

# Contents

<b>1</b>	<b>General Introduction</b>	<b>1</b>
<b>2</b>	<b>Experimental techniques</b>	<b>5</b>
2.1	Sample preparation . . . . .	5
2.1.1	Molecular beam epitaxy (MBE) . . . . .	5
2.2	Magnetic characterization techniques . . . . .	6
2.2.1	$^{57}\text{Fe}$ and $^{119}\text{Sn}$ Mössbauer spectroscopy . . . . .	6
2.2.2	Magneto-optic Kerr effect (MOKE) . . . . .	13
2.3	Structural characterization techniques . . . . .	14
2.3.1	Auger Electron Spectroscopy (AES) . . . . .	14
2.3.2	Low-Energy Electron Diffraction (LEED) . . . . .	14
2.3.3	Reflection High-Energy Electron Diffraction (RHEED) . . . . .	15
2.3.4	X-Ray Diffraction (XRD) . . . . .	17
2.3.5	$^{119}\text{Sn}$ Nuclear Resonant Inelastic X-Ray Scattering (NRIXS) . . . . .	17
<b>I</b>	<b>Structure and magnetism</b>	<b>23</b>
<b>3</b>	<b>Growth and magnetic properties of epitaxial submonolayer Fe on stepped Pd(110)</b>	<b>25</b>
3.1	Introduction . . . . .	25
3.2	Experimental . . . . .	26
3.2.1	UHV system configuration . . . . .	26
3.2.2	Sample preparation . . . . .	28
3.3	Results and Discussion . . . . .	29
3.3.1	Structural characterization: RHEED . . . . .	29
3.3.2	Magnetic characterization: MOKE . . . . .	33
3.3.3	$^{57}\text{Fe}$ CEMS . . . . .	43
3.4	Conclusions . . . . .	45
<b>4</b>	<b>Observation of the fcc-to-bcc Bain transformation in epitaxial Fe ultra-thin films on <math>\text{Cu}_3\text{Au}(001)</math></b>	<b>47</b>
4.1	Introduction . . . . .	47
4.2	Experimental . . . . .	51
4.3	Results and Discussion . . . . .	52
4.3.1	RHEED: in-plane atomic spacing . . . . .	52
4.3.2	$^{57}\text{Fe}$ CEMS . . . . .	59
4.4	Atomic volume and epitaxial lines . . . . .	63
4.5	Conclusions . . . . .	67

<b>5</b>	<b>Epitaxial growth of Fe on GaAs(001) and GaAs(001)-HEMT</b>	<b>69</b>
5.1	Introduction . . . . .	69
5.2	Experimental procedure . . . . .	70
5.3	Results and discussion . . . . .	73
5.3.1	RHEED . . . . .	73
5.3.1.1	Fe/GaAs(001) . . . . .	73
5.3.1.2	Fe/GaAs(001)-HEMT . . . . .	75
5.3.2	$^{57}\text{Fe}$ CEMS . . . . .	78
5.3.2.1	Fe/GaAs(001) . . . . .	78
5.3.2.2	Fe/GaAs(001)-HEMT . . . . .	80
5.3.2.3	$^{57}\text{Fe}$ (3 ML)/GaAs(001) . . . . .	82
5.4	Conclusions . . . . .	86
<b>II</b>	<b>Structure and vibrational dynamics</b>	<b>87</b>
<b>6</b>	<b>Epitaxial growth and interfacial structure of Sn on Si(111)(7x7)</b>	<b>89</b>
6.1	Introduction . . . . .	89
6.2	Experimental . . . . .	90
6.3	Results . . . . .	90
6.3.1	RHEED . . . . .	90
6.3.2	LEED . . . . .	96
6.3.3	Auger Electron Spectroscopy (AES) . . . . .	100
6.3.4	Scanning Electron Microscopy (SEM) . . . . .	100
6.3.5	$^{119}\text{Sn}$ CEMS . . . . .	100
6.4	Discussion . . . . .	106
6.5	Conclusions . . . . .	107
<b>7</b>	<b>Structure and vibrational dynamics of interfacial Sn layers in Sn/Si multilayers</b>	<b>109</b>
7.1	Introduction . . . . .	109
7.2	Experimental . . . . .	110
7.2.1	Sample preparation . . . . .	110
7.2.2	$^{119}\text{Sn}$ CEMS . . . . .	111
7.2.3	$^{119}\text{Sn}$ Inelastic Nuclear Resonant Scattering (NRIXS) . . . . .	111
7.2.4	Raman spectroscopy . . . . .	112
7.3	Results . . . . .	112
7.3.1	X-ray reflectometry and diffractometry . . . . .	112
7.3.2	$^{119}\text{Sn}$ CEMS . . . . .	114
7.3.3	Raman spectroscopy . . . . .	120
7.3.4	Nuclear resonant inelastic X-ray scattering (NRIXS) . . . . .	121
7.4	Discussion . . . . .	129

---

7.4.1	Structure . . . . .	129
7.4.2	Vibrational dynamics . . . . .	130
7.5	Concluding remarks . . . . .	135
	<b>Summary</b>	<b>147</b>
	<b>Acknowledgments</b>	<b>149</b>
	<b>Curriculum Vitae</b>	<b>151</b>
	<b>List of publications</b>	<b>153</b>



---

# 1 General Introduction

In the last decade it has been shown that thin film growth techniques, such as molecular beam epitaxy (MBE) under ultrahigh vacuum (UHV) conditions, can be used to create new metastable magnetic and non-magnetic phases which do not exist in the equilibrium phase diagram at room temperature. Famous examples of these materials include bcc-Co, bcc-Ni, fcc-Fe and  $\alpha$ -Sn. Despite of a long history of investigations, the physical properties of ultrathin metastable phases and their dependence on the atomic volume, details of the crystal structure, and film thickness are still a topical subject. A very sensitive dependence of the properties and the final film structure on the film growth conditions, including type of substrate, substrate temperature and growth rate, has been demonstrated in the literature.

Magnetic nanoscaled heterostructures have a number of applications as recording media, magnetoresistive sensors, read heads and magnetic random access memory. Thin films with an orientation of the magnetization perpendicular to the film plane may be useful as magnetic recording media. Such systems promise a substantial increase in the density of information that can be saved in smaller domains or bit sizes, a necessary condition to fulfill the actual demand of more storage capacity.

The first part (part I) of this thesis contains an investigation of the relation between magnetism and atomic nearest neighbor distance in nanoscaled heterostructures such as epitaxial ultrathin Fe films on Cu<sub>3</sub>Au(001), nearly one-dimensional (1D) Fe stripes on Pd(110), and nanoclustered Fe films on GaAs(001) and Fe/GaAs(001) interfaces. The existence of magneto-volume instabilities (low-moment/high moment transition) in metastable fcc-like Fe thin films can produce dramatic changes in the Fe atomic magnetic moment as well as in the magnetic structure or exchange coupling. Additionally, reduced dimensions and the presence of interfaces can alter magnetic properties of these systems such as magnetic anisotropy or domain formation. Knowledge of the magnetic state of the Fe/GaAs interface is essential for the understanding of injection of spin-polarized electrons from the ferromagnetic metal into the semiconductor. This belongs to the rapidly developing field of "spin electronics".

Epitaxial self assembly of magnetic nanowires with single atomic height and a width from 100 Å down to single atomic chains has recently started to attract attention because of its potential in making regular magnetic arrays at length scales beyond the lithographic limit. One approach is to decorate step edges of a vicinal surface by depositing metal atoms, as will be shown in [chapter 3](#) for Fe/Pd(110). The aim of this work was to gain insight in the general and system-specific properties of a quasi-1D system and in how it would approach 1D from 2D. Finite size scaling of the shift exponent for the Curie temperature, and on an exponential decay of the saturation and remanent magnetization with increasing temperature below 0.7 monolayers (ML) is reported, which is in contrast to the behavior of a 2D system. An early onset of ferromagnetism at 0.3 ML Fe, and out-of-plane magnetization below coverages of 0.6-0.7 ML Fe have been observed, making this system interesting for the applications mentioned above. In addition, in-situ <sup>57</sup>Fe

Mössbauer and reflection high energy electron diffraction (RHEED) measurements will show that the metastable fcc-like-Fe phase (fct) can be stabilized at RT on Pd(110) for ultrathin films with in-plane magnetization.

Chapter 4 will report on the pseudomorphic growth of ultrathin fcc-like-Fe on  $\text{Cu}_3\text{Au}(001)$ , and on the correlation observed between the fcc-to-bcc transformation and the reorientation of the magnetization from perpendicular to in-plane. The experimental observation of a continuous fcc-to-bcc Bain transformation with increasing Fe coverage is described, contrary to the usual discontinuous martensitic transition of Fe. The atomic volume of tetragonal states that are produced by epitaxial strain was found to follow closely fct (face-centered tetragonal) or bct (body-centered tetragonal) epitaxial lines, according to strain energy calculations in the literature, with a critical value of the in-plane lattice spacing,  $a$ , for crossover from the fct to the bct epitaxial line.

It is expected that the storage and transport of electronic spin (spintronics) may revolutionize the electronic device industry, with spin-based transistors, opto-electronic devices and memory. Although efficient room temperature electrical spin injection in metals has been commercially employed in today's magnetic read heads through giant magnetoresistance, electrical spin injection from ferromagnetic metal electrodes into semiconductors has not been convincingly demonstrated, and is a challenging task. One of the most investigated epitaxial metal/semiconductor systems is Fe/GaAs(001). The successful growth of very smooth epitaxial Fe layers is of high relevance for their posterior lithographic patterning and integration in semiconductor nanostructured devices. The aim of the present work on Fe/GaAs(001) and Fe/GaAs(001)-HEMT (HEMT=high electron mobility transport), as described in chapter 5, is the optimization of growth parameters such as surface termination of the substrate or deposition temperature to avoid the formation of "magnetic dead layers" at the Fe/GaAs interface that prevents the injection of highly spin-polarized electrons into the semiconductor, since a high spin polarization and large ferromagnetically ordered moments, even in the first metallic monolayer at the interface, is a necessary condition.

In part II of this thesis the structural and vibrational dynamics of another metastable thin film phase, namely  $\alpha$ -Sn, is investigated. The structural stability of  $\alpha$ -Sn on semiconducting substrates was studied, concentrating in the interfacial structure of epitaxial Sn grown on Si(111)-(7x7). The structure of Sn in Sn/Si multilayers was discovered, in particular by  $^{119}\text{Sn}$  Mössbauer spectroscopy and phonon density of states measurements.

It is well known that bulk Sn is an element that can undergo a phase transformation at 13.2°C upon cooling from its metallic body centered tetragonal phase ( $\beta$ -Sn) to a semiconducting phase,  $\alpha$ -Sn, with diamond structure. Epitaxial growth of Sn on appropriate substrates (InSb(001) or CdTe(001)) allows the room temperature stabilization of the low temperature  $\alpha$ -Sn phase. Sn/Si(111) is an example of an abrupt metal/semiconductor interface, uncomplicated by interdiffusion or chemical reaction, that can be used to understand the details of the origin of the Schottky barrier. For the Pb/Si(111) system, the existence of a correlation between the electronic and geometric structure at the interface has already been reported in the literature, where different Si(111) surface reconstructions led to differences in the height of the Schottky barriers measured in Pb/Si contacts.



Up to now, the structure of Sn at the buried Sn/Si interface is still an open question. It is not known whether interfacial  $\alpha$ -like-Sn remains stabilized after the deposition of thicker Sn layers that undergo the transition to  $\beta$ -Sn. The purpose of chapter 6 is to clarify this question.

Chapter 7 reports on studies of the structure and lattice dynamics of interfacial Sn in Sn/Si multilayers, where the Sn layers are embedded between amorphous Si layers. Phonons in superlattices are of general interest, because phenomena like Brillouin zone folding, interface modes and confined phonon modes that do not exist in bulk materials may be observed. In the present work the phonon or vibrational density of states of this system was measured, from which thermodynamical quantities, such as the vibrational entropy, can be derived.

A large number of experimental techniques have been employed for the study of structural and magnetic properties of the systems presented. These are separately introduced briefly in chapter 2.



## 2 Experimental techniques

### 2.1 Sample preparation

#### 2.1.1 Molecular beam epitaxy (MBE)

Molecular beam epitaxy allows the growth of high-purity epitaxial layers with fairly abrupt interfaces and good control of thickness, doping and composition. In MBE, the materials are thermally evaporated from Knudsen-cells or electron-guns, and condense on a substrate forming a thin film. To obtain high-purity layers, it is critical that the material sources are extremely pure and the whole process must be done in an ultra-high vacuum (UHV) environment. The growth rates are typically on the order of 0.01 to 0.1 Å/s and the beams can be shuttered allowing nearly atomically abrupt transitions from one material to another.

Most of the samples studied in this thesis (except the ones in chapter 3, and those of chapter 7) were grown in Duisburg, in a home-built MBE chamber [1] that consists of two main vacuum chambers: a UHV-growth chamber, and a load-lock. The load lock is used to transfer samples in and out of the vacuum environment while maintaining the UHV integrity of the other chamber. A scheme of the growth chamber is illustrated in Fig.2.1 (obtained from Ref. [1]).

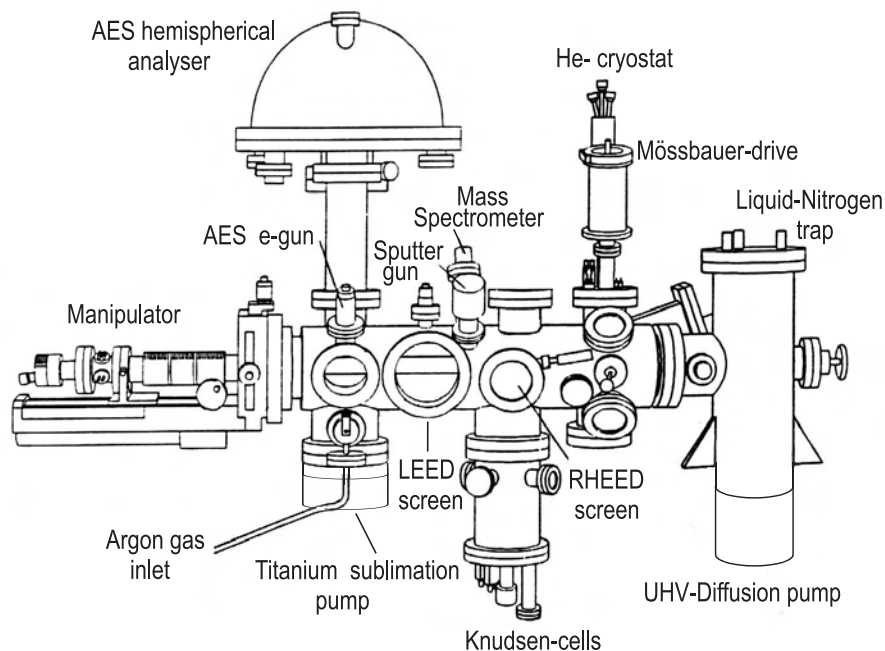


**Figure 2.1:** Front view of the UHV-chamber.

The pressure in the main chamber was measured with an ion gauge. A mass spectrometer was utilized to monitor the residual gases, and check for leaks. A UHV pressure on the order of  $1 \times 10^{-10}$  mbar was maintained by means of UHV-diffusion pump (with nitrogen-trap) and a titanium sublimation pump. The vacuum in the load-lock chamber was generated by a turbo-molecular pump.

An  $\text{Ar}^+$  sputter-gun was available for the in-situ cleaning of the substrates. The sample temperature is controlled up to  $900^\circ \text{C}$  by means of a thermocouple fixed at the sample-holder. To reach the higher temperatures required in the preparation of the  $\text{Si}(7 \times 7)$  surface reconstruction ( $\sim 1000^\circ \text{C}$ ), an additional resistively heated shield was placed very close to the sample to avoid heat radiation losses. The design of the sample-holder also makes it possible to cool the sample to  $-140^\circ \text{C}$ .

The MBE growth chamber is equipped with four Knudsen-cells and one e-gun evaporator for high vapor deposition pressure materials such as Si. Thickness control was achieved by means of calibrated quartz monitors. A shutter was positioned in front of the sample to shutter the flux reaching the sample.

The growth chamber was also equipped with LEED, RHEED, AES and conversion electron Mössbauer spectroscopy (CEMS) for the in-situ structural and magnetic characterization of the samples. Real-time monitoring of the growth kinetics and calibration of growth rates (RHEED intensity oscillations) were achieved by means of RHEED. For in-situ Mössbauer spectroscopy (CEMS) a liquid He cooled cold-finger permitted measurements at variable temperature down to 20 K.

A different MBE-UHV chamber was used for the preparation of the amorphous Sn/Si multilayers of chapter 7. In this case, no in-situ surface or magnetic characterizations were possible. The third MBE-UHV system used in the Fe/Pd study as described in chapter 3, is located at Argonne National Laboratory in Argonne, IL, USA.

## 2.2 Magnetic characterization techniques

### 2.2.1 $^{57}\text{Fe}$ and $^{119}\text{Sn}$ Mössbauer spectroscopy

The Mössbauer effect provides information about the local magnetic and electronic environment of Mössbauer nuclei (i.e.  $^{57}\text{Fe}$  or  $^{119}\text{Sn}$ ) in a sample. Since this technique does not require the application of an external field, it is possible to observe very weak magnetic interactions, without the perturbing effect of the external field [2–4].

#### *Principles of the method*

Mössbauer spectroscopy is essentially the observation of fine structure in the transition between nuclear energy levels, i.e. of  $^{57}\text{Fe}$  or  $^{119}\text{Sn}$  nuclei, by means of nuclear resonance absorption or fluorescence of gamma radiation.

In nuclear transitions, the conservation of momentum requires the emitting nucleus to have a significant recoil energy,  $E_R$ .

The conservation of momentum requires that the recoil momentum must be equal and opposite to the ( $\gamma$ -ray) photon momentum,  $\mathbf{P}_R = -\hbar \mathbf{k}$ ; then, the recoil energy is:

$$E_R = \frac{\hbar^2 k^2}{2m} \quad (2.1)$$

From eq. (2.1), it can be seen that an emitter with high mass ( $m$ ) has a small recoil energy. In our case, the emitter is not a free atom, but part of a large crystal, so the atom cannot simply recoil. It must interact with phonons. The recoil momentum of the Mössbauer nucleus is taken by the phonons; however, some of the emission processes will proceed elastically, that is, without the emission of a phonon. Then the recoil momentum is taken up by the entire crystal. If the mass in eq. (2.1) is that of the crystal, the recoil energy becomes infinitely small, as desired. Although in this process the recoil momentum is finite, it is called recoilless emission (or recoilless absorption for the inverse process).

In the Debye model the fraction of  $\gamma$ -rays emitted or absorbed without recoil energy is given by the Lamb-Mössbauer factor [3] in the low temperature approximation:

$$f = \exp \left( -\frac{\hbar^2 k^2}{2m} \frac{3}{2k_B \theta_D} \left[ 1 + \frac{2}{3} \left( \frac{\pi T}{\theta_D} \right)^2 \right] \right) \quad (2.2)$$

where  $\theta_D$  is the Debye temperature of the solid. Resonance fluorescence can take place, if a significant fraction of the  $\gamma$ -rays are both emitted and absorbed recoillessly. This results in extremely sharp spectral lines: the transition takes its natural linewidth (given by Heisenberg's uncertainty principles) and natural lineshape. This leads to a very high resolving power ( $\sim 10^{-13}$  in the case of  $^{57}\text{Fe}$ ).

The  $^{57}\text{Fe}$  and  $^{119}\text{Sn}$  Mössbauer nuclear level scheme are shown in Fig.2.2(a) and (b), respectively. In a Mössbauer experiment, the radioactive source, e.g. an unstable  $^{57}\text{Co}$  nucleus, decays via electron capture to a highly excited  $I=5/2$  state of  $^{57}\text{Fe}$ , which quickly decays to the  $I=3/2$  first excited state, or directly to the  $I=1/2$  ground state. The transition with a half-life time of 97.7 ns from the 14.4 keV first excited state to the ground state is the Mössbauer transition. Of these events, 90 % result in internal conversion of core-electrons, and only 10 % in photon emission.

The 14.4 keV  $\gamma$ -rays created by the de-excitation of this  $^{57}\text{Fe}$  nuclear state in the source can be resonantly absorbed by an absorber (sample) containing also  $^{57}\text{Fe}$  atoms. The  $^{57}\text{Fe}$  atoms of the absorber are now excited to their 14.4 keV level. The experimental detection of this resonant absorption process can be carried out in the standard transmission geometry (Fig. 2.3 bottom), by measuring the intensity reduction of the  $\gamma$ -rays due to the absorption, or in a scattering geometry (Fig. 2.3 top) by registering the conversion electrons. This last technique (CEMS) is useful from the fact that it counts 90 % of the events, rather than 10 % as in the transmission configuration.

CEMS is based on the fact that the excited  $^{57}\text{Fe}$  nucleus in the absorber can decay via re-emission of a 14.4 keV  $\gamma$  quantum or, alternatively, via the transfer of its energy to its own electron shells, preferentially to the K-shell being closest to the nucleus. A

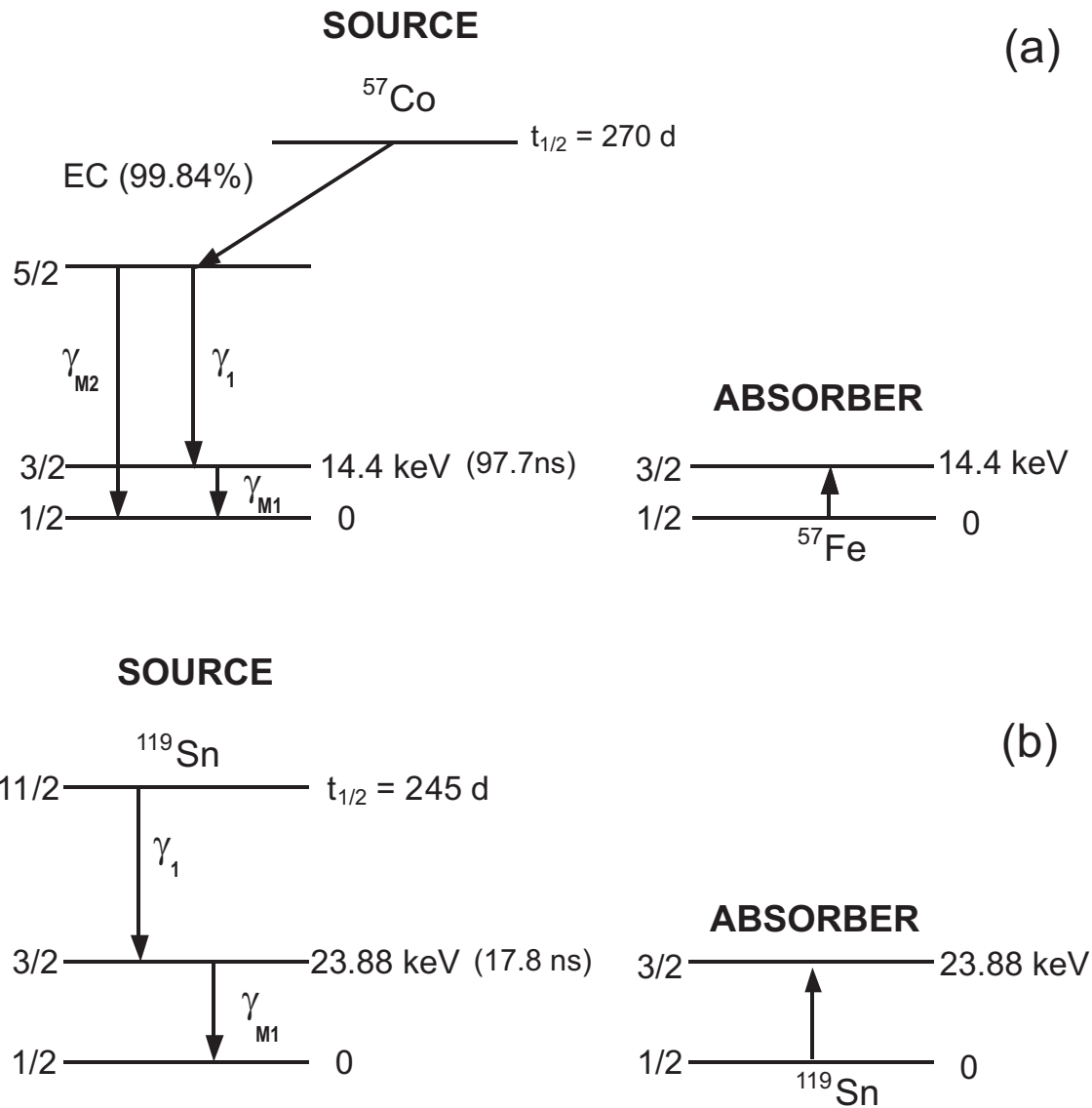


**Figure 2.2:** Nuclear level scheme of (a)  $^{57}\text{Fe}$ , and (b)  $^{119}\text{Sn}$ .  $\gamma_{M1}$  denotes the 14.4 keV or 23.88 keV Mössbauer transition of  $^{57}\text{Fe}$  and  $^{119}\text{Sn}$ , respectively. EC=electron capture

K-conversion electron is ejected from the  $^{57}\text{Fe}$  atom with a kinetic energy of  $E_{kin} = E_{\gamma} - E_{K-binding} = 14.4 - 7.1 \text{ keV}$ . Of course, L- and M-conversion electrons can originate similarly, but with less probability.

Due to the scattering processes within the absorber and the relatively small kinetic energy of 7.3 keV, the conversion electrons can leave the absorber only if they have been created within a subsurface region of at most 100 nm. This is the characteristic range of  $^{57}\text{Fe}$  CEMS investigations. Because the electrons lose energy travelling through

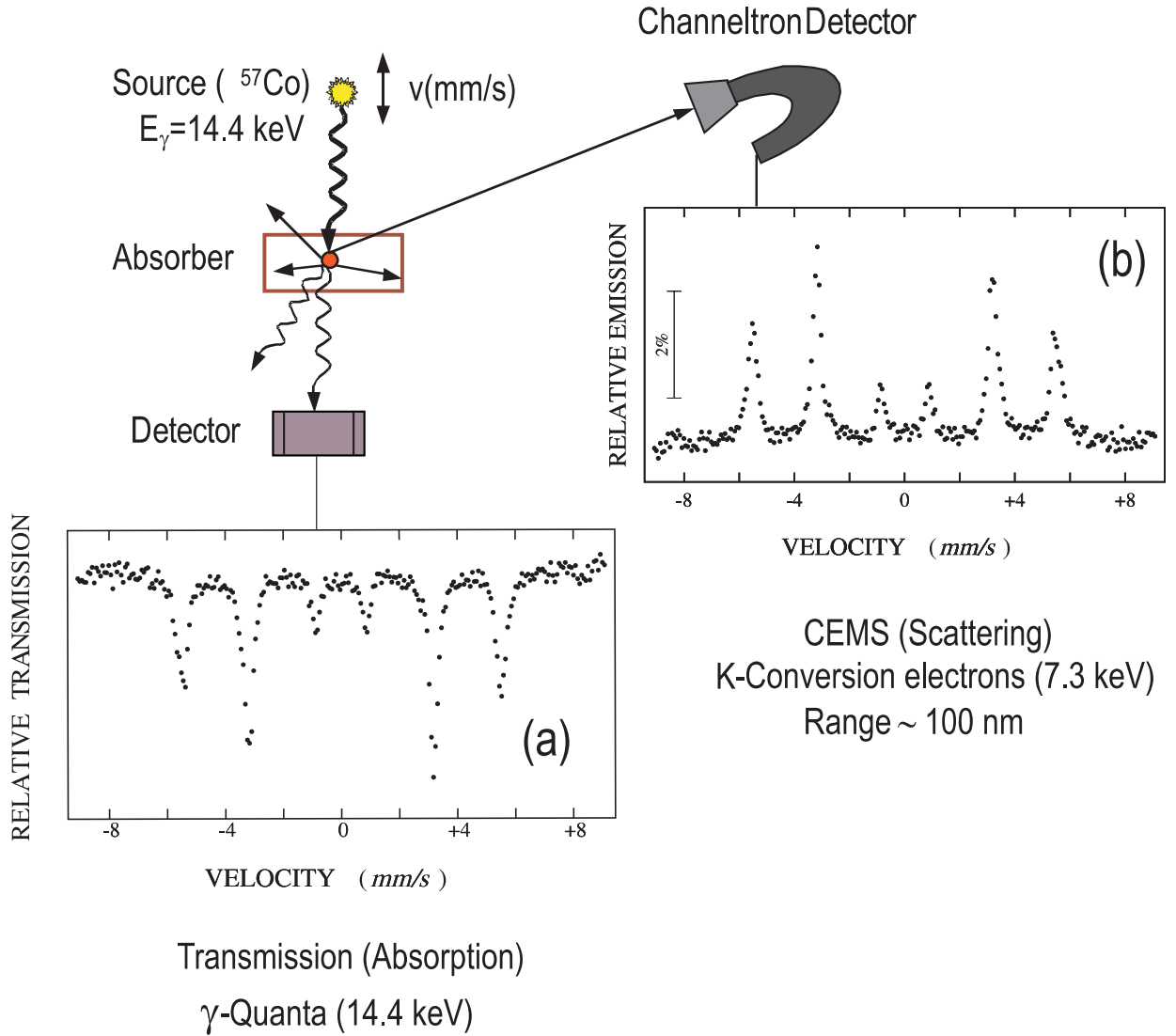


**Figure 2.3:** Setup of Mössbauer experiments in transmission geometry (a) or scattering geometry (CEMS) (b). The spectra represent the magnetically split sextet of  $\alpha$ -Fe at room temperature.

the absorber, their exit energy provides information on the depth of their origin and by means of an electron energy analyzer one can perform depth selective CEMS (DCEMS).

Most of the spectra shown in this dissertation were measured in the CEMS configuration and not under transmission geometry. The samples are in the thickness range where CEMS is still sensitive. The detection limit in CEMS amounts to  $\sim 10^{14}$  atoms/cm<sup>2</sup> for <sup>57</sup>Fe, and  $\sim 10^{15}$  atoms/cm<sup>2</sup> for <sup>119</sup>Sn [2], much less than measurable by the transmission technique.

Mössbauer spectroscopy can be used to measure small shifts in the nuclear energy levels, caused by the interaction of the nucleus with the local electron or spin density. The relevant terms are the electric monopole term (isomer shift,  $\delta$ ), the electric quadrupole

term (quadrupole splitting,  $2\epsilon$ ) and the magnetic dipole term (magnetic hyperfine splitting,  $B_{hf}$ ). The first two terms provide chemical and structural information. The third term provides the splitting of the ground state and first excited state of the  $^{57}\text{Fe}$  nucleus caused by the Zeeman effect resulting from the hyperfine magnetic field at the Mössbauer nucleus.  $B_{hf}$  originates mainly from the core polarization of the 1s, 2s, and 3s shells due to the (unfilled) 3d shell of Fe. Furthermore, polarized conduction electrons provide an additional (smaller) contribution to  $B_{hf}$ .

In a Mössbauer spectrum the *isomer shift*  $\delta$  is the velocity of the center of gravity of the spectrum with respect to zero-velocity. Since  $\delta$  is proportional to the s-electron density at the nucleus, this parameter can be used to gain information about the valence state of the Mössbauer atom or of charge transfer, and is also useful to detect lattice expansions/compressions, as these also change the electronic density. In our case,  $\delta$  will be utilized to distinguish the  $\alpha$ -Sn phase with diamond structure from the  $\beta$ -Sn phase with body centered tetragonal structure.

The *quadrupole splitting*  $2\epsilon$  is proportional to the electric field gradient acting on the quadrupole moment of the Mössbauer nucleus. Its applications are the investigation of local symmetry around the Mössbauer atom and the configuration of its valence electrons.

The magnetic *hyperfine field* can be derived from the magnetic (Zeeman) splitting of the Mössbauer spectrum. In magnetically ordered materials, the measured effective magnetic field,  $B_{hf}$  acting on the Mössbauer nucleus is composed of:

$$B_{hf} = B_{int} + B_{dem} + B_L + B_{dip} + B_{ext} \quad (2.3)$$

Here,  $B_{int}$  denotes the intrinsic hyperfine field,  $B_{dem}$  the demagnetization field,  $B_L$  the Lorentz field,  $B_{dip}$  the dipolar field within the Lorentz sphere, and  $B_{ext}$  the external field. If  $B_{ext}$  defines the positive direction,  $B_{int}$  and  $B_{dem}$  are known to be negative, and  $B_L$  is positive.

$B_{int}$  has contributions of the dominant core polarization field being proportional to the local Fe atomic moment, the polarization of conduction electrons, dipolar fields of the spin and angular momentum of the incomplete magnetic shell (3d), and other transferred hyperfine fields from the magnetic neighboring atoms. The temperature dependence of  $B_{int}$  provides information on the spin-wave spectrum. The temperature dependence of the hyperfine field, when extrapolated to  $T \approx 0$ , provides the hyperfine field at saturation (electronic ground state value), which is useful to estimate the Fe atomic moment,  $\mu_{Fe}$ .

The Lorentz field  $B_L = \mu_0 M_S / 3$  and the dipolar field  $B_{dip}$  are small ( $\lesssim 0.73$  T) and will be neglected ( $M_S$ =saturation magnetization). The demagnetizing field is approximately given by  $B_{dem} \approx \mu_0 M_S \cos\theta$  ( $\theta$ =angle between magnetization or spin direction and the film normal direction).  $B_{dem} = 0$  T for an in-plane magnetized film, and  $B_{dem} = 2.19$  T for perpendicular magnetized bcc Fe film [5]. This means that in the case of a perpendicularly magnetized film,  $B_{hf}$  is larger by  $\sim 2$ T than the intrinsic hyperfine field,  $B_{int}$ .

The intensity ratio of the six resonance lines of a magnetically split Mössbauer spectrum amounts to 3:R:1:1:R:3, where R is given by:



$$R = \frac{4\sin^2\theta}{(1 + \cos^2\theta)} \quad (2.4)$$

$\theta$  is the angle between the direction of the incoming  $\gamma$ -rays (perpendicular to the film surface) and the direction of  $B_{hf}$ , averaged over the sample. The ratio  $R$  can vary between 0 and 4. Since the direction of  $B_{hf}$  is determined by the direction of the magnetization of the sample, the magnetization direction (e.g. out-of-plane or in-plane) can be obtained from the measured intensity ratio  $R$ . If  $R=0$ , the film is magnetized completely perpendicular to its surface. The magnetization will be completely in-plane oriented for  $R=4$ . If the sample is unmagnetized, with randomly orientated magnetic domains,  $R$  is equal to 2. The total intensity (total spectral area) of the Mössbauer spectrum is related to the Lamb-Mössbauer factors (or  $f$ -factors) of the source ( $f_S$ ) and of the absorber ( $f_A$ ).

A summary of the effect of the different hyperfine interactions is plotted in Fig.2.4.

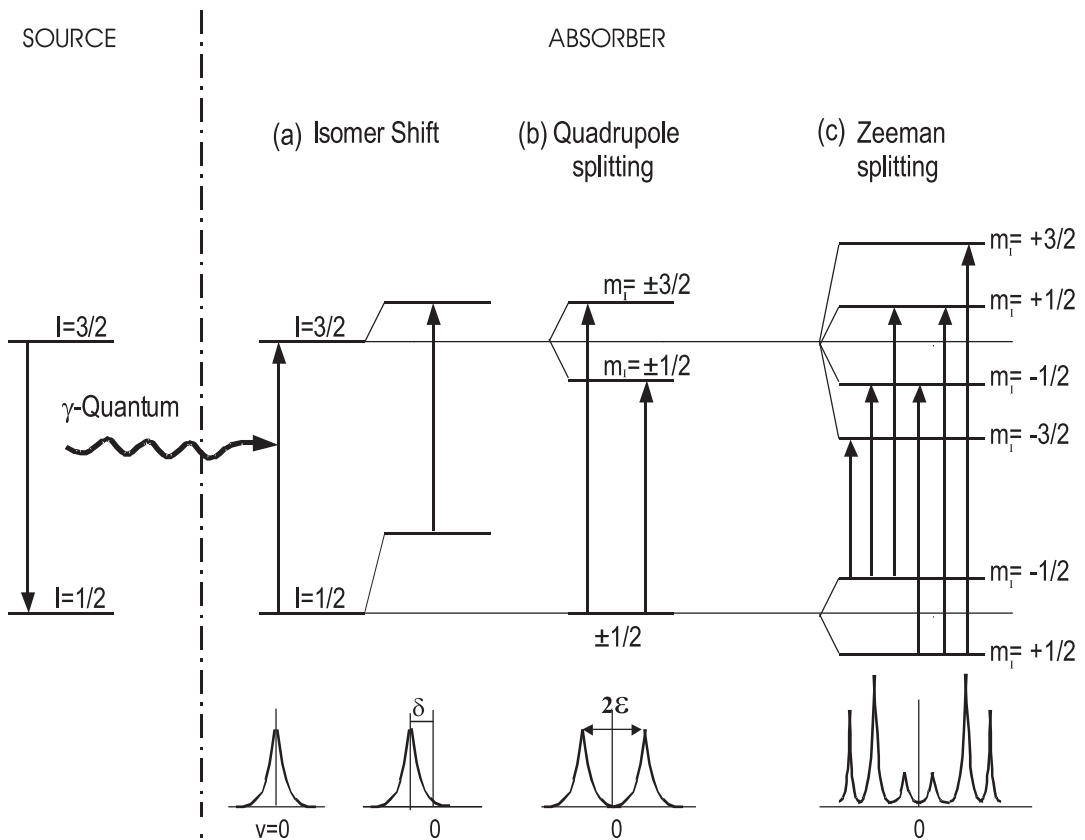


**Figure 2.4:** Hyperfine splitting scheme for the  $^{57}\text{Fe}$  Mössbauer transition induced by (a) Coulomb interaction (isomer shift), (b) quadrupole interaction and (c) magnetic dipole (Zeeman) interaction between the nucleus and the electrons. The corresponding CEMS spectra are shown schematically. Also shown are the six allowed  $\gamma$ -ray transitions, each of which corresponds to an absorption line in the CEMS spectrum (c) (bottom).

The monopole term does not depend on  $m_I$ , and causes a uniform shift of each level, but different for the nuclear ground and excited state. The quadrupole term splits the states with different  $|m|$ , but not with  $|m|=1/2$ . The magnetic dipole term removes any remaining degeneracies by splitting the levels according to the Zeeman effect:

$$\Delta E = g_I \mu_n m_I B \quad (2.5)$$

where  $g_I$  is the nuclear g-factor,  $\mu_n$  is the nuclear magneton,  $B$  is the magnetic field, and  $m_I = -I, -I+1, \dots, +I$  is the magnetic quantum number. The magnetic-dipole interaction imposes the selection rule of  $\Delta m_I = 0, \pm 1$  on the transitions, resulting in six possible transitions. The spacing between the lines of the sextet gives the hyperfine field.

### Setup and components

The experimental arrangement for CEMS is schematically shown in figure 2.5. The

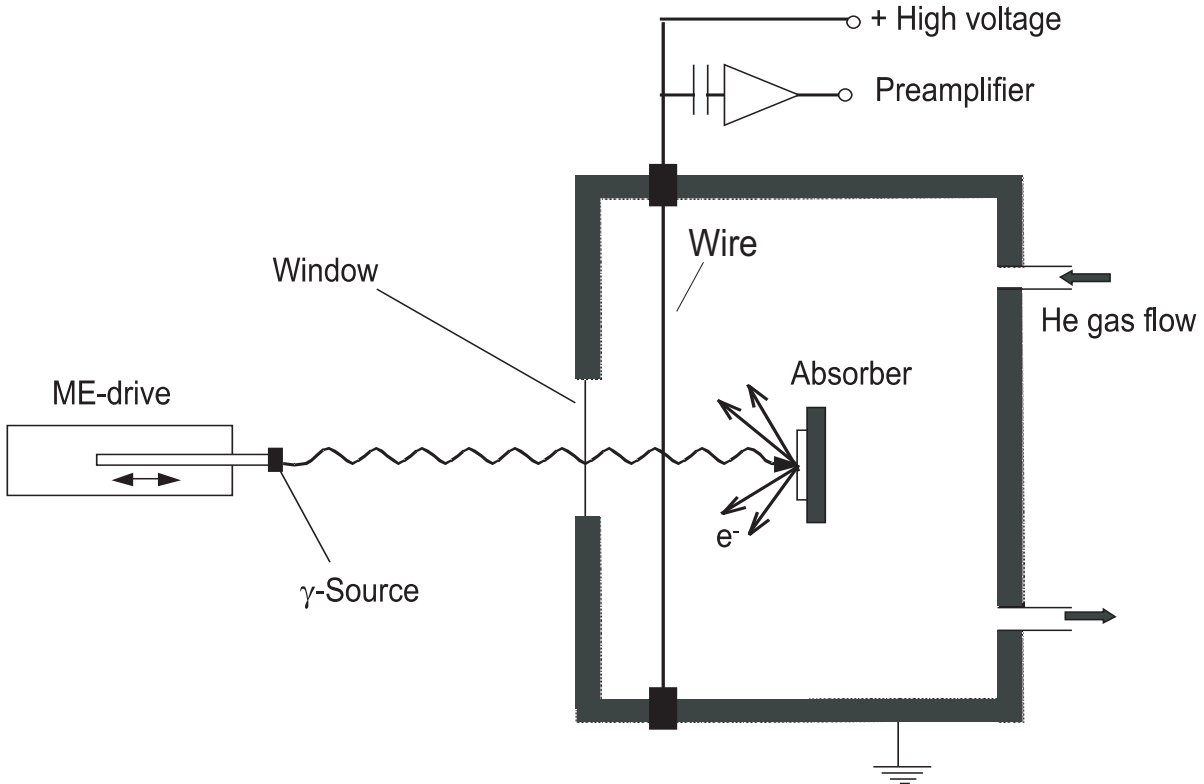


**Figure 2.5:** Gas-flow proportional counter used for CEMS (schematically)

$^{57}\text{Co}$  source is a thin metal foil (usually Rh) into which radioactive  $^{57}\text{Co}$  atoms have been diffused. Activities of up to 100mCi were used. Rh metal is cubic and diamagnetic, and thus the electric quadrupole and Zeeman interactions for the paramagnetic  $^{57}\text{Co}/^{57}\text{Fe}$  impurities in Rh are zero. Moreover, the magnetic relaxation time for this impurities in Rh

is much shorter than the Mössbauer transition time. All of these phenomena result in an unsplit (single line) Mössbauer source. The energy of the source radiation is Doppler modulated by moving the source back and forth with a linear ramped velocity. In this way, the  $\gamma$ -ray energy can be scanned through the various nuclear levels in the absorber (sample), and when the resonance condition is fulfilled, the transition probability increases. The measured spectrum is a convolution of the single-line emission spectrum of the source and the sample absorption spectrum. In the thin source/thin absorber approximation these spectra have Lorentzian line shape.

CEMS measurements were performed by detecting all conversion/Auger electrons coming from the sample surface without any energy discrimination. Depth selective measurements were achieved by using a thin  $^{57}\text{Fe}$  (or  $^{119}\text{Sn}$ ) probe layer (of 2-3 ML) artificially inserted at a certain depth position in an Fe (Sn) film that otherwise consists of the non-Mössbauer isotope  $^{56}\text{Fe}$  ( $^{120}\text{Sn}$ ) or of natural Fe (2.1 %  $^{57}\text{Fe}$  abundance), or natural Sn (8.6 %  $^{119}\text{Sn}$  abundance).

For the CEMS ex-situ measurements, a gas-flow proportional counter was used as a detector due to the large solid angle of  $2\pi$  covered. He-4%  $\text{CH}_4$  gas flows continuously through a small proportional counter containing the absorber. The conversion and Auger electrons leaving the absorber surface are absorbed in the gas volume with high probability. (See figure 2.5).

In order to perform in-situ CEMS measurements in UHV on clean surfaces a channeltron was used for electron detection. Unfortunately, channeltrons possess a very poor detection efficiency for 7.3 keV electrons. To improve the detection efficiency, the entrance cone of the channeltron has been covered with MgO, where secondary electrons of very low energy (5-20 eV) are produced by the incoming primary conversion and Auger electrons. Additionally, a positive potential of about 100 V between absorber and channeltron collects the secondary electrons at the opening of the channeltron.

More information about the Mössbauer effect and its application in the study of magnetic ultrathin films and multilayers can be found in Ref. [2-4].

### 2.2.2 Magneto-optic Kerr effect (MOKE)

When a beam of polarized (laser) light reflects on a magnetized surface, a change in the polarization of the incident light happens. This change, known as magneto-optic Kerr effect (MOKE), can be a rotation of the polarization axis, or a change from linear to elliptical polarization, and is proportional to the magnetization of the material. Since the effect is highly sensitive, and can detect a sub-monolayer amount of magnetic material on a non-magnetic substrate, it is sometimes called SMOKE or Surface MOKE [6]. However, the light is known to penetrate about 20 nm into the surface for most metals, which means that MOKE is not particularly surface sensitive.

Due to the small dimension of the incident laser beam spot (0.1 mm), MOKE is a suitable technique for measuring magnetization at different points of a wedge sample.

Changing the geometry of the experimental setup, in-plane (longitudinal Kerr) and out-of-plane (polar Kerr) magnetic moments can be measured.

The in-situ Kerr measurements shown in this thesis were performed at the Argonne National Laboratory (Illinois, USA) in collaboration with Dr. Dongqi Li. A detailed description of the experimental setup used is given in section 3.2.1 and figure 3.2.

## 2.3 Structural characterization techniques

### 2.3.1 Auger Electron Spectroscopy (AES)

A hemispherical Auger electron analyzer (HAC 5000 designed by VGW) permitted the non-destructive determination of the chemical composition of the surface in UHV conditions. This technique is especially useful when combined with sputter cleaning.

Electrons of energy 2-20 keV are incident upon a conducting sample and cause core electrons (K shell) from atoms contained in the sample to be ejected. This results in a free electron and an atom with a core hole. The ionized atom then relaxes via electrons with a lower binding energy (L shell) dropping into the core hole. The energy released can be converted into a characteristic X-ray or emitted as a secondary Auger electron; a fraction of this energy is required to overcome the binding energy of this second electron, the remainder is retained by this emitted Auger electron as kinetic energy. After the emission, the atom is left in a doubly ionized state. The energy of the Auger electron is characteristic of the element that emitted it, and can be used to identify the element.

Since the escape depth of Auger electrons with energies up to 2 keV is small, only electrons from the first few atomic layers will escape from the material, ensuring the surface sensitivity.

AES cannot detect hydrogen or helium, but is sensitive to all other elements, especially to the low atomic number elements. Examples and details of AES can be found in Refs. [7, 9].

### 2.3.2 Low-Energy Electron Diffraction (LEED)

LEED is a widely used technique for the study of solid crystal surfaces and thin films under UHV conditions. Usually it provides qualitative information on size, symmetry, periodicity, and rotational alignment of the adsorbate unit cell with respect to the substrate unit cell. Quantitative LEED, which is a more sophisticated version of LEED, involves spot intensity measurements as a function of the primary electron energy (I/V curves), and theoretical description according to the dynamical scattering; this method provides accurate lattice parameters in the surface region.

Diffraction images are taken with a 3-mesh commercial rear view LEED optics (VG, RVL03). A low-energy electron beam ( $V_E=10$  eV-1 keV) produced by an electron gun hits the sample perpendicular to its surface, as plotted in figure 2.6.

Considering that the electron energies used are low, it is essential that there are no electric or magnetic fields in the vicinity of the sample. In order to ensure this, the

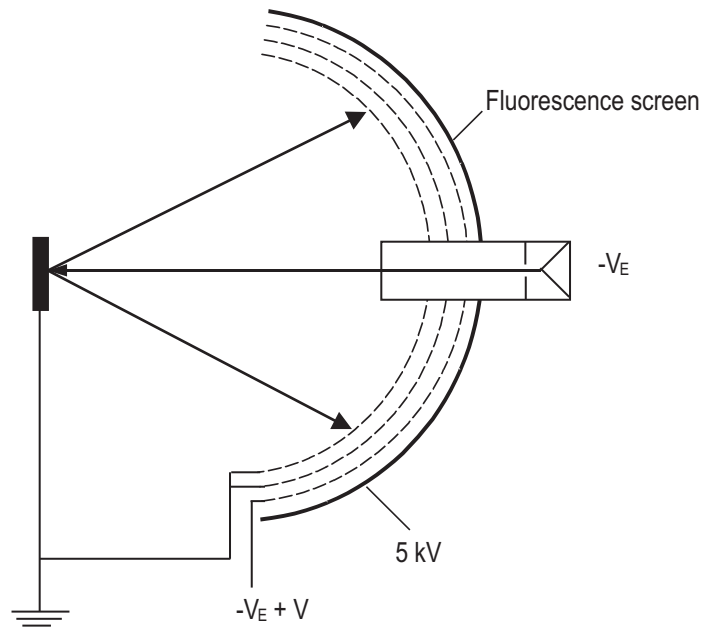


**Figure 2.6:** LEED optics schematic.

sample and the two grids closest to the sample are grounded. The third mesh is held at a retarding potential close to that of the source filament ( $-V_E + V$ ). This rejects most of the inelastically scattered electrons. Finally, the quasi-elastically scattered electrons are accelerated by a potential of +5 kV towards the fluorescence screen where the LEED pattern is visible.

Since the energy of the incident electrons is not high enough to penetrate deeply into the material, the LEED pattern corresponds exclusively to the diffraction pattern from crystallographically ordered atoms in the topmost surface layers.

The diffraction spots will move as the energy of the incident electrons changes. By monitoring the intensity change of the specular (0,0) LEED spot as a function of the primary electron energy, e.g. with a CCD camera connected to a computer, the lattice parameter at the surface in the surface normal direction can be estimated in the kinematic approximation.

A more detailed description of LEED and its applications to surface characterization can be found in Refs. [8, 10, 11].

### 2.3.3 Reflection High-Energy Electron Diffraction (RHEED)

A collimated electron beam with high energy (5-15 keV) is directed to the sample surface at grazing angle ( $\sim 0.5 - 2^\circ$ ). The electrons are diffracted by the crystal structure of the sample and then impinge on a phosphor screen mounted opposite to the electron gun. Fig. 2.7 shows the basic components for a RHEED experiment.

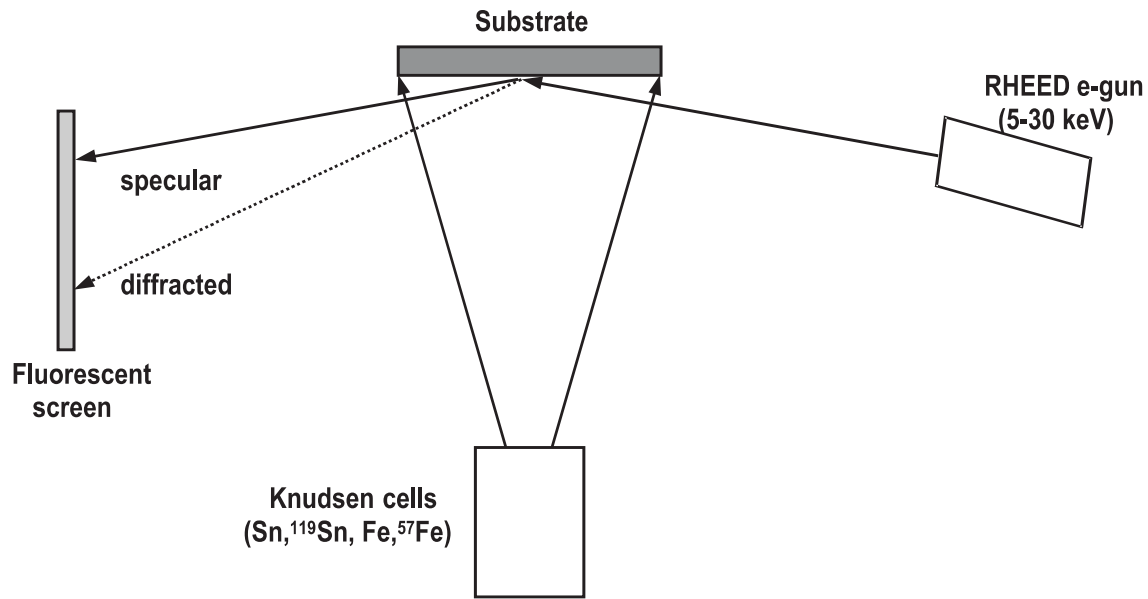


**Figure 2.7:** Experimental arrangement for RHEED. All components are in UHV.

The grazing incidence angle ensures surface specificity, and the component of the electron momentum perpendicular to the surface is small despite of the high energy of the incident electrons.

The RHEED pattern for a perfect surface consists of spots lying on an arc (Laue zone), arising from the intersection of the reciprocal lattice rods with the Ewald sphere. The spots become streaked to some extent along the film normal direction due to broadening of the rods that is caused by energy and angular spread of the incident electron beam, surface defects, or inelastic phonon scattering and refraction at the surface. (See reference [8] for more detailed information about RHEED.)

Since the angular spacing of the diffracted RHEED beams depend only on the real space lattice periodicity perpendicular to the incident electron beam, it is possible to calculate the in-plane atomic distance as well as the in-plane symmetry from the measurement of the distance in reciprocal space between contiguous streaks.

In a LEED pattern, the surface symmetry is immediately apparent, as the pattern directly corresponds to the Ewald sphere for the incident energy. Since the RHEED pattern is a projection of the reciprocal lattice, the sample must be rotated about its surface normal (azimuthal angle) and the pattern must be examined from at least two azimuthal angles to establish the surface symmetry. The intensity variation along a RHEED streak contains equivalent information to a I/V LEED curve, but extracting quantitative information is difficult and requires multiple scattering theory and modelling.

An EIKO Engineering (MB-1000) RHEED system was used for the studies presented in this thesis. The arrangement of RHEED components lets the front of the sample free for instruments such as evaporators. This permits structural changes during film deposition to be monitored. In the case of Frank-Van-der-Merwe (layer-by-layer) growth, intensity

oscillations of monolayer periodicity can be observed, if the surface step density varies during deposition. The RHEED images were recorded by a CCD camera connected to a PC for the posterior data analysis.

### 2.3.4 X-Ray Diffraction (XRD)

The X-ray diffraction intensity was measured in the  $\theta$ - $2\theta$  configuration with a Philips PW1730 X-ray powder diffraction system equipped with a Cu-anode X-ray tube, and a graphite monochromator.

If Bragg's equation is satisfied, constructive interference will occur, and a peak in the diffraction intensity versus angle  $\theta$  will appear. Information about crystal orientation, lattice constants, layer thicknesses and roughness can be obtained by analyzing the interference peaks in the  $\theta$ - $2\theta$  scan. For the characterization of thin films and multilayers, X-ray reflectivity measurements under grazing incidence were performed.

### 2.3.5 $^{119}\text{Sn}$ Nuclear Resonant Inelastic X-Ray Scattering (NRIXS)

#### *Principles of the method*

Nuclear Resonant Inelastic X-ray scattering (NRIXS) is a new technique to study lattice dynamics that provides direct access to the phonon or vibrational density of states (VDOS) [12–14]. This technique does not necessarily require single crystal samples and can also be applied to disordered and amorphous materials, allowing investigations of lattice dynamics during a phase or structural transformation.

By definition, NRIXS is only sensitive to the vibrations of atoms with Mössbauer nuclei, which imposes a certain limitation on the accessible materials. On the other hand, it gives *site selectivity*, and provides a partial density of states for the selected isotopes.

An important property of the nuclear resonance is the energy width of the excited state or natural line width ( $\Gamma$ ). Because of the very small value of  $\Gamma$  (25.70 neV for  $^{119}\text{Sn}$ ), only X-ray sources with high spectral intensity (synchrotron radiation) have a reasonable chance of exciting the nucleus. The  $^{119}\text{Sn}$  nucleus decays then with a natural life time of 25.10 ns. Even though the level width is small, the nuclear resonant cross section is large, being  $\sigma=1.4$  Mb [13].

The energy scales involved in these processes are:

$$\text{transition energy (keV)} \leftrightarrow \text{phonon energy (meV)} \leftrightarrow \text{nuclear level width (neV)}$$

The energies are different by six orders of magnitude. Figure 2.8 illustrates this situation. In Fig.2.8(a), the nucleus is held fixed, i.e., we neglect recoil from photon absorption, and only X-ray photons with width  $\Gamma$  around the transition energy can excite the resonance. This behavior is qualitatively described by the excitation probability density  $S(E)$ , and the cross section for a particular scattering channel is proportional to  $S(E)$ . The value  $S(E)dE$  gives the probability that the nucleus can be excited by an X-ray in the energy range  $[E, E+dE]$ . If the nucleus is allowed to oscillate with a particular frequency

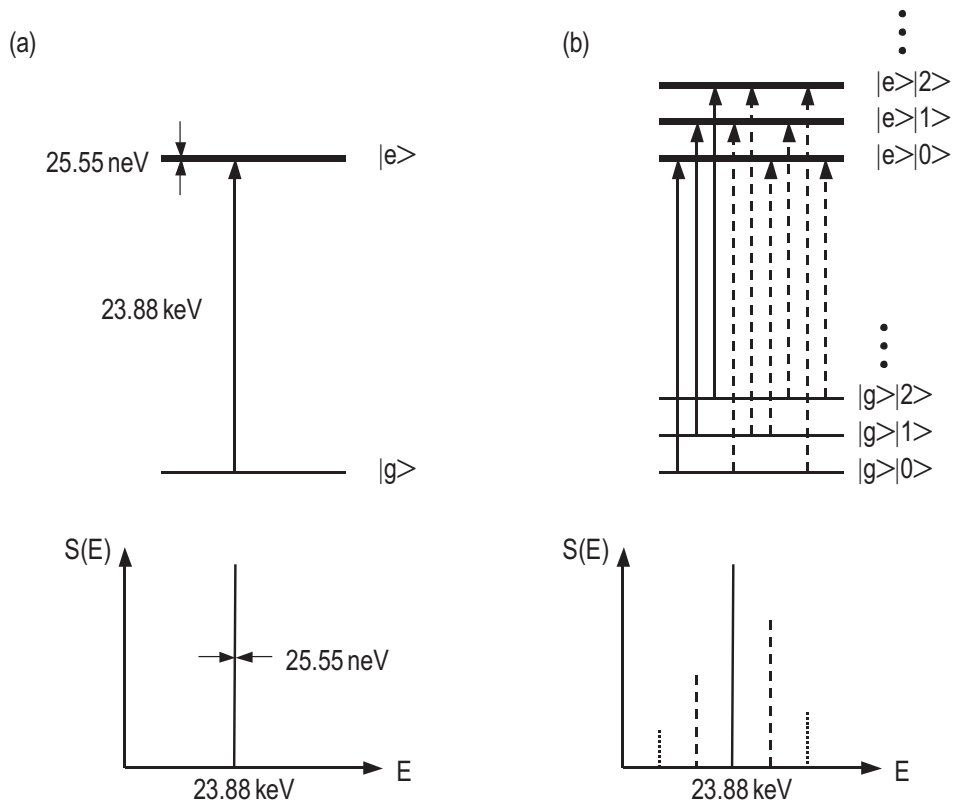


**Figure 2.8:** Energy levels scheme of a  $^{119}\text{Sn}$  nucleus at rest (a), and of a nucleus embedded in an Einstein solid (b). In addition to the elastic peak at the nuclear transition energy of  $23.88 \text{ keV}$ , the dashed lines in the excitation probability density  $S(E)$  (b) indicate transitions that include creation or annihilation of one phonon with the Einstein energy. The dotted lines describe two-phonon creation/annihilation.  $|g\rangle$ ,  $|e\rangle$  = nuclear ground and excited state, respectively.  $|0\rangle$ ,  $|1\rangle$ ,  $|2\rangle$ ... = vibrational states of the Einstein solid.

(Einstein model of a solid) the picture changes (Fig.2.8(b)), and new energy levels from combinations of nuclear states and phonon states appear.

$|g\rangle|1\rangle$  displays, for example, a quantum state with the nucleus in the ground state and one phonon present. The weak coupling between nucleus, phonon, and X-ray photon and the different energy scales involved make such state a good approximation of the exact eigenstates of the coupled system. In a real material, phonons with many different energies exist, and the side bands in  $S(E)$  become smeared out. However, the classification into one-phonon, two-phonon, etc... events remain valid. If the incident X-ray energy is too small to excite the nucleus resonance directly, phonons have to be annihilated. This process will always be less likely than the creation of phonons with the same energy. The ratio is given by the Boltzmann factor:



$$S(E) = \exp\left(\frac{E}{k_B T}\right) S(-E) \quad (2.6)$$

with temperature  $T$  and Boltzmann's constant  $k_B$ .

At zero temperature phonon annihilation becomes impossible, and  $S(E)$  has only one side band at positive energies. Measuring the probability of exciting a nucleus we can derive  $S(E)$  which contains all the phonon energies. After the excitation, the nucleus will decay into the ground state either by emission of an X-ray photon of 23.88 keV (for  $^{119}\text{Sn}$ ) or by transferring the excitation energy to the electron shell. In the last case, a conversion electron is expelled (most likely from the L-shell of  $^{119}\text{Sn}$ ) and the hole is rapidly filled by other electrons under the emission of fluorescence X-rays. These decay products are emitted with some delay relative to the time of excitation, and the average time is given by the natural life time.

Figure 2.9 displays schematically the scattered intensity of a material in case of a nuclear resonance after excitation with a synchrotron radiation pulse. Scattering of X-rays from electronic charge is prompt ( $<10^{-12}\text{s}$ ), almost immediately after the pulse arrives. The response of the resonant nuclei is delayed ( $\sim 10^{-7}\text{s}$ ). If the energy of the incident X-ray is close to the nuclear transition energy, nuclei are excited, and delayed emission of X-rays can be observed.

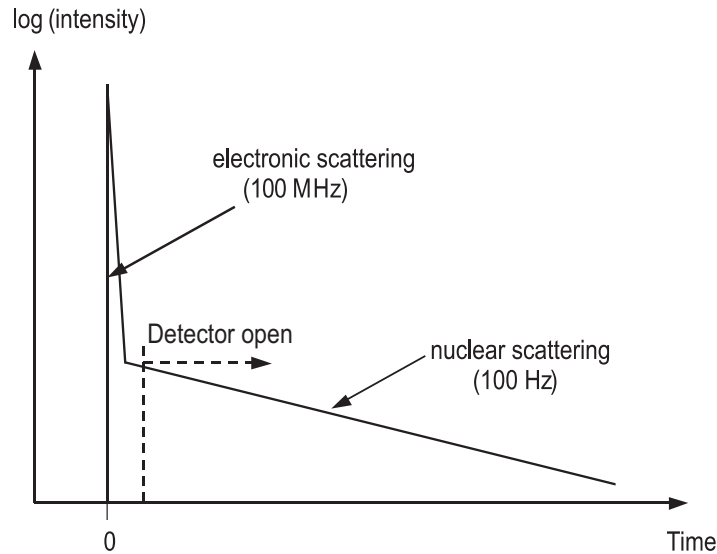


**Figure 2.9:** Scattered intensity versus time after nuclear excitation in an NRIXS experiment (schematically). At time zero, a synchrotron radiation pulse excites a material containing a nuclear resonant isotope. The scattering from electrons is prompt, i.e., almost immediately after the pulse arrived. The response of the resonant nuclei is delayed. Time discrimination permits to distinguish nuclear and electronic scattering.

The quantitative analysis gives the probability for the excitation of the nuclear resonance when the energy is tuned away by an amount needed for creation or anni-

hilation of phonons. The arrival of a very short ( $<100$  ps) synchrotron radiation flash triggers the emission process of an inelastically scattered photon and of a conversion electron and subsequent fluorescence radiation. The discrimination of the delayed events, which then signal the creation or annihilation of phonons from all other non-nuclear scattering contributions, that are prompt in time, is achieved by conventional electronic timing methods. If only the delayed photons are counted, one can expect to measure a function that is proportional to  $S(E)$ .  $S(E)$  is obtained from the measured data after normalization, and the partial phonon or vibrational density of states (VDOS) can be extracted by a mathematical procedure mentioned in 7.3.4.

### Setup and components

NRIXS experiments require synchrotron radiation of high brightness and high spectral density, being feasible mainly at third-generation synchrotrons like the European Synchrotron Radiation Facility (ESRF) in Grenoble, the Advanced Photon Source (APS) in Argonne (USA), and SPRING8 in Japan. A typical experimental setup of a nuclear resonance beamline is shown in figure 2.10.

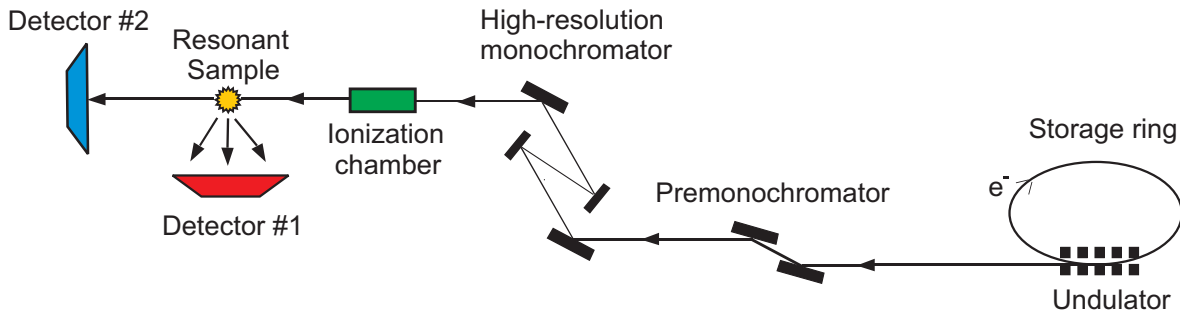


**Figure 2.10:** Experimental set-up for measurements of inelastic nuclear resonant scattering (schematic).

The X-ray source are electrons that are orbiting in the storage ring and periodically (once per turn) pass through an undulator. The X-rays are monochromatized in two steps (premonochromator and high-resolution monochromator) to an energy bandwidth that is much narrower than the phonon spectrum of our samples. The monochromatic X-rays excite nuclear resonances in the sample, and the re-emitted X-radiation is observed with the detector. An electronic timing circuit measures the elapsed time between excitation and re-emission and removes prompt effects. A control unit permits us to remotely interact with the devices that are inside the radiation area and thus are not directly accessible during the measurement.

The first component of the experimental setup is an undulator, which creates a broad energy band of X-rays ("white beam") that ranges from about 6 keV up to several 100 keV. A water-cooled diamond double-crystal monochromator is used as premonochromator (or high-heat monochromator) to filter an energy band of about 1 eV from the white

beam. This bandwidth is not narrow enough to perform phonon spectroscopy (phonon energies are typically less than 0.1 eV), but the total power in the X-ray beam is reduced from 1000 W to 0.1 W. The reduction in power is important because the subsequent high resolution monochromator is very sensitive to temperature gradients. Two diamond crystals in non-dispersive arrangement (like a channel-cut) operate at their (111) Bragg reflections to perform the task of filtering and power reduction.

Because of the channel-cut crystals in this experimental setup the monochromatized beam is parallel to the incident beam with a vertical offset. The premonochromator is adjusted to transmit around the  $^{119}\text{Sn}$  nuclear resonance energy of 23.88 keV. Also the undulator is tuned to produce an intense peak at this energy. As opposed to the premonochromator, the high-resolution monochromator requires a separate set of crystals for each nuclear transition (e.g.  $^{57}\text{Fe}$ ,  $^{119}\text{Sn}$ ,  $^{151}\text{Eu}$ ,...). Because a gain in energy resolution is often achieved at the expense of loss in throughput, the actual choice of the high-resolution monochromator should be adjusted to the particular experiment.

After the high-resolution monochromator the beam passes through an ionization chamber, which monitors the flux of incident radiation, irradiates the samples and excites the resonant nuclei. Scattered radiation is counted by two avalanche photodiode (APD) detectors. The first detector is located close to the sample and counts the quanta scattered in a large solid angle. The second detector, located far away from the sample, counts the quanta scattered by the nuclei in the forward direction.

The two detectors monitor different processes of nuclear scattering. Being scattered inelastically, the quantum acquires a certain phase shift, and is no longer coherent with the incident radiation. If the phase shift is random for various nuclei, the scattering is spatially incoherent, and the scattered quanta may be associated with some particular nucleus. The products of the de-excitation are emitted as a spherical wave (neglecting polarization effects). The intensity of incoherent nuclear scattering, which may proceed both inelastically and elastically, is monitored by the first detector. This detector should cover a large solid angle to collect a sufficient flux, therefore it is placed close to the sample. At ambient conditions, the sensitive area of the detector can be located about 1mm from the sample, covering about a quarter of the complete sphere.

The second detector monitors nuclear forward scattering, as it is located far away from the sample in order to avoid a contribution of incoherent scattering. The paths of the waves scattered by various nuclei in the forward direction are indistinguishable, therefore all waves have the same phase and the scattering is spatially a result of collective scattering by the nucleus ensemble. This is an elastic process, and any local energy transfer will destroy the coherence. Coherent scattering will appear only when the energy of the incident radiation coincides with the energy of a nuclear transition. The data provide the instrumental function of the high-resolution monochromator, because the width of the nuclear transition in this scale is negligible. The peak gives a precise indication of the energy position of nuclear resonance. Incoherent scattering, in addition to the central elastic peak, has a certain probability outside the nuclear resonance, the latter corresponding to inelastic nuclear scattering accompanied by the creation or annihilation of phonons.

Precise monitoring of the instrumental function in parallel with the measurements is

extremely important for the subsequent data analysis, because a Fourier image of the instrumental function is required for the deconvolution procedure used in the calculation of the vibrational density of states.

**Part I**

**Structure and magnetism**



# 3 Growth and magnetic properties of epitaxial submonolayer Fe on stepped Pd(110)

## 3.1 Introduction

The field of two-dimensional magnetism has advanced both in fundamental science and industrial applications thanks to discoveries of new magnetic phenomena that occur at small length scales [15]. Lower dimensional systems, such as quasi-1D magnetic wires, however, remain less investigated due to difficulties in fabrication at the length scale  $< 10$  nm.

It is theoretically known that an isolated 1D Ising chain should not support long range order at equilibrium above 0 K. It is not clear how a real experimental system would approach 1D from 2D, and how it should behave when it weakly interacts with another system such as a substrate, or away from equilibrium. Recently, epitaxial self-assembly of nanowires with single atomic height and width from  $\sim 100$  Å down to single atomic chains has started to attract attention because of its potential in making regular arrays at a length scale beyond the lithographic limit. One approach is to decorate step edges of a vicinal surface by depositing metal atoms [16–18]. Some promising magnetic characterizations have been reported for Fe/W(110) [19, 20] and Fe/Cu(111) [21], though the wires are less than perfect.

The pioneering work by Elmers et al. [19] demonstrates that smooth Fe stripes grown at 660 K on W(110) have an in-plane easy axis in-plane across the stripes, and they seem to be perfectly ferromagnetic from widths of 44 Å down to 4 atomic rows or  $\sim 8$  Å. The temperature dependence of the magnetization shows a 2D-like behavior with no relaxation, and a finite width scaling of the stripes was found in agreement with the 2D Ising model. The work by Shen et al. [21], on the other hand, reports strong temperature dependence in remanent magnetization ( $M_R$ ) for Fe stripes consisting of connected islands at the step edges on Cu(111). Here,  $M_R$  is always significantly smaller than the saturation magnetization ( $M_S$ ), with the system easily saturated under small fields. However, what are the general properties of a quasi-1D system, and what are the system-specific ones are still open questions.

There are some Monte Carlo calculations for isolated stripes which show that they should be metastable, but the time constants can be extremely large compared to experimental time scales [22]. The key for a better understanding is to discover and investigate new quasi-1D magnetic systems.

The choice of Pd(110) as a substrate surface was motivated for several reasons. First of all, the formation of smooth metallic nanowires requires not only that adatoms diffuse across terraces to stick at step edges, but also that diffusion along the step edges is fast enough in order to form smooth, straight chains. It is well known, that initial metal growth on Pd(110) surfaces is highly anisotropic and tends to form nanoscale wires even on flat surfaces [23]. This would ensure that, on a stepped surface with edges along the fast diffusing direction ( $[1\bar{1}0]$  in Pd(110)), the growth front of the wires would be straight as

long as step decoration occurs. Secondly, Pd is also known to be nearly magnetic and can have an induced magnetic moment through proximity when placed next to ferromagnetic atoms [24]. This helps the Fe wires to remain ferromagnetic.

To the best of my knowledge, there has been no magnetic study of submonolayer Fe on Pd(110). Work on growth and magnetic properties of Fe/Pd(001) demonstrated a normal ferromagnetic onset at the island percolation limit [25]. The magnetic easy axis in the Fe/Pd(001) system is perpendicular to the sample surface for low temperature growth and in-plane for room temperature growth [26].

An earlier onset of ferromagnetism (at  $\sim 0.3$  ML coverage) has been observed for the Fe/Pd(110) system during these experiments. It will be shown in this chapter that step decoration, and, therefore, Fe stripe formation occurs in Fe/Pd(110). The system exhibits typical ferromagnetic hysteresis loops with full remanence even down to  $\sim 0.3$  ML. The shift exponent for the Curie temperature can be described by finite size scaling. Below 0.7 ML, both  $M_R$  and  $M_S$  decay exponentially with increasing temperature, in contrast to that of 2D magnetic systems. The coercivity in the same coverage range exhibits weak temperature dependence, while the coercivity of the samples around or above 0.7 ML is very sensitive to temperature. Superparamagnetism will be ruled out as explanation for the anomalous temperature behavior observed.

## 3.2 Experimental

### 3.2.1 UHV system configuration

The experiments were carried out in a UHV chamber (Fig. 3.1) equipped with RHEED, LEED, AES and MOKE.

The vacuum system(Phi 5100) used for the fabrication of the Fe/Pd(110) films, the Spherical Capacitor Energy Analyzer SCA (Phi 10-360), 5 keV sputter gun (Phi 04-303), and 10 keV RHEED gun (Phi 06-190) are from Perkin Elmers Physical Electronics Division. The Reverse-View retractable 10 keV LEED optics is made by Omicron.

The sample manipulator (from Kurt J. Lesker) is a Vacuum Generators HPLT model, with 500 mm Z,  $\pm 25$  mm X-Y travel with differential pumping on the continuous primary rotation, and  $\pm 90^\circ$  rotation in the azimuthal direction.

The ultrahigh vacuum was generated by a TNB-X ion pump system (300 l/s), with a titanium sublimation pump. A 170 l/s Balzers turbomolecular pump was used for initial pump down and differential pumping of the 5 keV sputter gun. This combination is capable of a base pressure of  $1.0 \times 10^{-10}$  mbar and a growth pressure during deposition ranging from  $2-4 \times 10^{-10}$  mbar.

The vacuum was monitored with an ionization gauge and a quadrupole mass spectrometer used as residual gas analyzer (RGA). Residual gas analysis indicated that the vacuum consisted mainly of water vapor,  $H_2$ ,  $N_2$  and Ar.  $N_2$  and  $H_2O$  may come from the walls of the vacuum chamber and sample transfer-line.  $O_2$ ,  $H_2$  and other reactive gases were present at levels generally less than  $7 \times 10^{-11}$  mbar partial pressure. Argon residual gas comes from the sputtering process.



The system was also equipped with a loadlock subsystem which allowed the insertion of samples without breaking the vacuum in the growth chamber. A 60 l/s turbomolecular pump is used for pumping the loadlock chamber. A loadlock is a necessity in an UHV system, since exposing the chamber to atmosphere requires a bakeout period of up to one week to remove the gas that adsorbs on the chamber walls.

The growth subsystem consisted of three electron-beam evaporators, a resistive sample heating capable of 900°C, a continuous-flow Oxford cryostat able to reach temperatures < 20 K, and a quartz crystal microbalance for thickness monitoring.

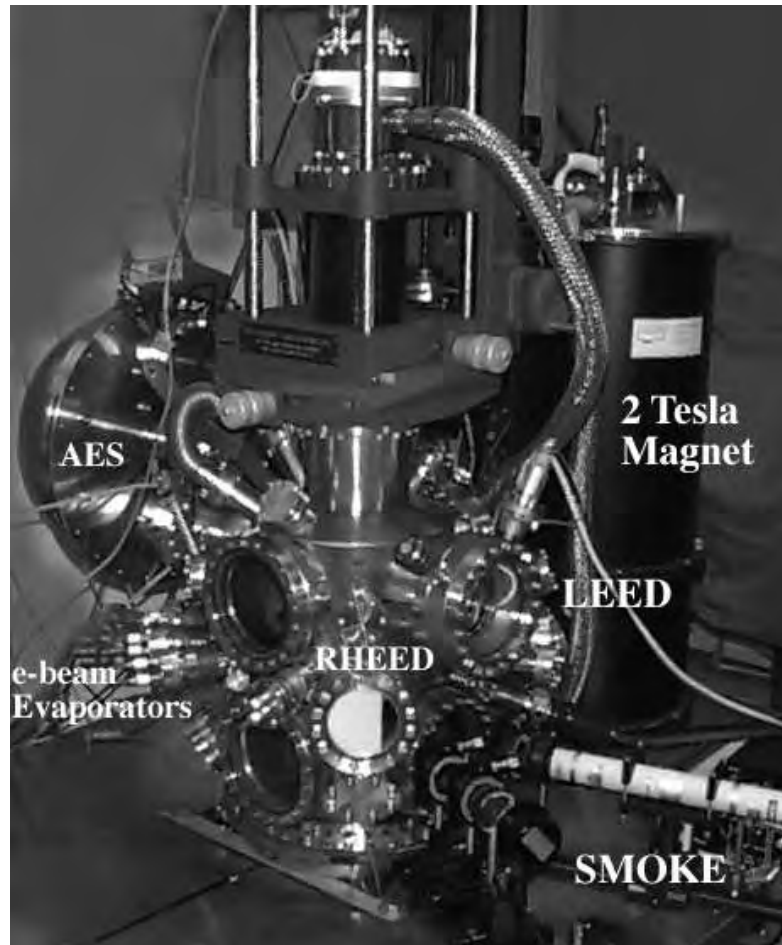


**Figure 3.1:** Ultrahigh Vacuum Chamber designed for Molecular Beam Epitaxy growth at the Argonne National Laboratory, USA.

The in-situ RHEED subsystem consisted of a 10 keV electron gun and phosphor screen arranged for grazing incidence scattering during growth. This gun is capable of generating a collimated beam with  $\sim 1$  mm diameter at an angle of incidence of 1-2°. The gun is also equipped with X-Y deflection plates to allow the beam to be moved over the surface of the sample. The sample stage can be rotated during growth and during the observation of the RHEED patterns, allowing the determination of in-plane symmetry.

The system was equipped with a 5 keV Argon-sputter gun and an O<sub>2</sub> line for the in-situ cleaning of the samples. AES measurements were performed by means of a hemispherical energy analyzer (25 meV resolution, 280 mm mean diameter and a single channel detector) to check possible surface contamination.

A UHV compatible superconducting two Tesla magnet (from Oxford Instruments) with a maximum field of 2T was used for the MOKE measurements. The optical set-up for MOKE consisted of a He-Ne intensity stabilized laser (Spectra 117A), a chopper, two polarizers, a quarter wave plate, a lens, and a Si photodiode detector (Ealing) connected to a LOCK-IN amplifier as shown in Fig. 3.2. A simple rotation of the sample inside the magnet allows the measure of the Kerr signal in both, polar and longitudinal configurations. The measurements were carried out with an angle of  $90^\circ \pm 0.5^\circ$  between the polarizers. The He-Ne laser beam focused to 0.2 mm was used to scan along the wedge samples to obtain Kerr-ellipticity hysteresis loops for different Fe thicknesses. The height of the loops in remanence ( $M_R$ ) is proportional to the remanent magnetization.

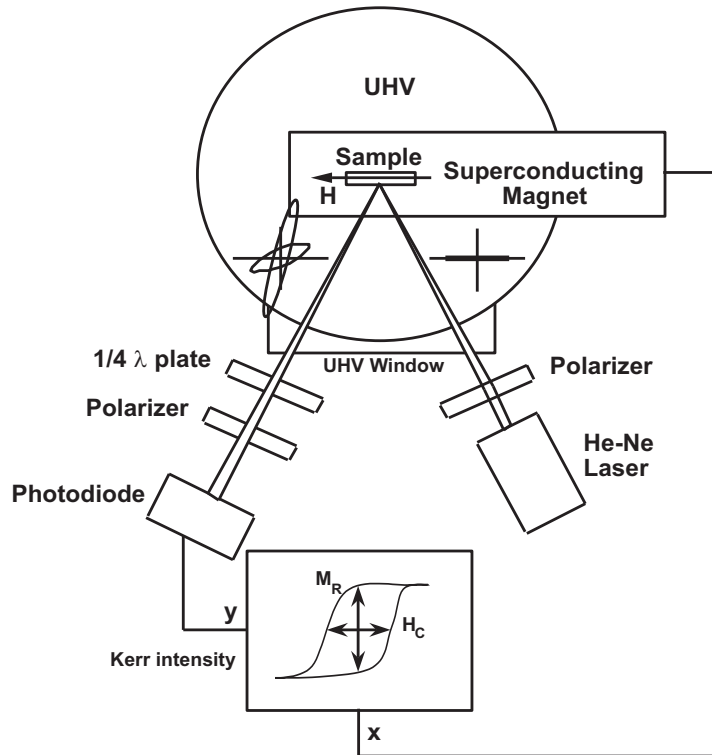


Figure 3.2: Experimental set-up for the MOKE measurements.

### 3.2.2 Sample preparation

The stepped Pd(110) substrate, with an average terrace width of  $\sim 20 \text{ \AA}$  and vicinal angle  $< 5^\circ$ , was cleaned in UHV by cycles of Ar<sup>+</sup> sputtering at 700 K and annealing at

950 K. The crystal was also occasionally annealed in oxygen at  $1 \times 10^{-7}$  Torr and 620 K for several minutes to eliminate residual C and S impurities. The cleaned substrate and the subsequent deposited Fe films are free of any measurable contamination within the AES sensitivity.

Fe was evaporated with a typical rate of 0.2-0.3 Å/min via electron-beam bombardment from a W crucible filled with pure Fe. The pressure during deposition was  $2-4 \times 10^{-10}$  mbar. Fe wedges of 0-6 ML thickness were grown with a slope of  $\sim 0.2-0.4$  ML/mm by moving the substrate behind a mask during deposition at 343 K.

The crystallographic order of the crystal and the films were confirmed with RHEED and LEED, recorded using a charge-coupled diode (CCD) camera. The images were analyzed digitally to quantify both the changes in atomic spacing along the wedges and the average terrace size of the substrate. A model of the stepped substrate surface is displayed in Fig. 3.3(a). Fig.3.3(b)(left) shows a LEED image of the substrate. The spots are elongated along the [001] direction, perpendicular to the step edges. While double spots, typical of an ordered stepped surface with wide terraces, are not observed, the asymmetric diffuse shape of the spots suggests that the average terrace size is small and is about 5-6 atomic rows, or  $\sim 20$  Å.

### 3.3 Results and Discussion

#### 3.3.1 Structural characterization: RHEED

RHEED measurements were carried out during growth with the electron beam along the [001] direction of the Pd(110) surface. For the clean surface (Fig.3.4(a)) and the Fe films of less than  $\sim 1.5$  ML (Fig.3.4(b)), sharp streaks are observed, indicating smooth, well-ordered surfaces. The first Fe layer grows pseudomorphically with the same lateral lattice parameter as the Pd substrate.

Above  $\sim 1.6$  ML (Fig.3.4(c)), the streaks begin to break up into spots, indicating the initiation of 3D growth (Fig.3.4(d),(e)). Clear RHEED patterns with similar characteristics, though with increasingly spotty and diffuse reflections, are observed up to 11 ML, where the experiment was terminated.

The measured distance among the streaks/spots is inversely proportional to the in-plane atomic spacing. This allows the precise determination of the in-plane atomic distance (perpendicular to the scattering plane) relative to that of the Pd(110) substrate. The result is plotted in Fig.3.5.

After the deposition of the first 0.5 ML Fe, the in-plane atomic spacing decreased by  $\sim 0.6$  %. Between 0.5 and 1.3 ML, a plateau-like behavior is observed, with only  $\sim 0.4$  % decrease between 0.5 and 1 ML, followed by  $\sim 0.7$  % decrease between 1-1.3 ML. Thus, the films grow pseudomorphic in this thickness range, with a maximum compression of  $\sim 1.7$  %. Above 1.3 ML Fe the in-plane atomic distance is reduced more rapidly, which is evidence of structural relaxation of the Fe films. This is consistent with 3D growth that starts above 1.5 ML as shown in Fig.3.4. The in-plane atomic spacing approaches saturation at  $\sim 3$  ML with a total *compression* of  $\sim 7$  %.

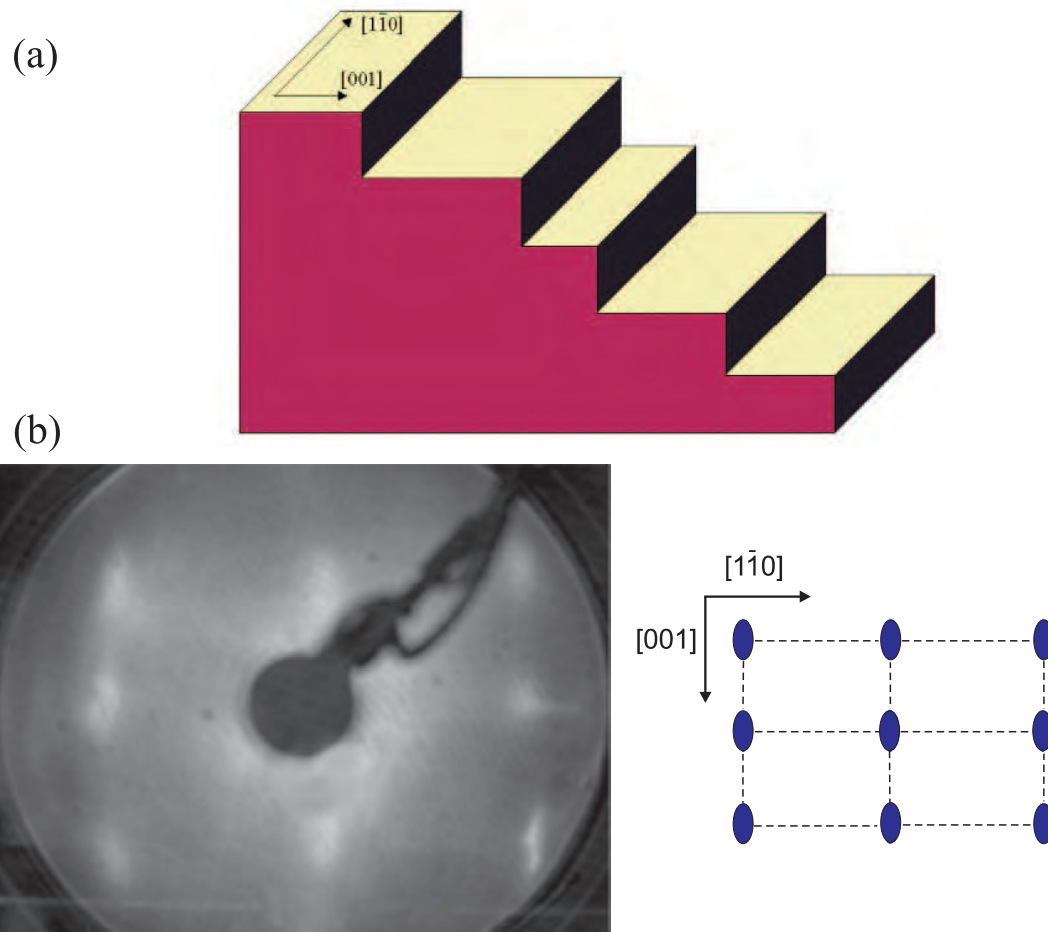


**Figure 3.3:** (a) Model of the stepped substrate surface, (b) LEED pattern of the Pd(110) substrate at  $E=75.7$  eV (left). The high symmetry directions are marked on the schematics (right). The elongated spots along  $[001]$  are caused by a relatively broad terrace width distribution as discussed in the text.

If one assumes that the epitaxy is for bcc Fe(110) to match the fcc Pd(110) (Fig.3.6(a), and (b)), then unrelaxed pseudomorphic bcc Fe should experience an in-plane compression of  $\sim 4.2\%$ , according to Fig. 3.6. Therefore with increasing Fe thickness a relaxation towards the *larger* bulk-Fe atomic spacing should occur, which disagrees with our experimental data. (We measured a  $\sim 7\%$  compression of the in-plane atomic distance).

Another possibility is that the initial growth creates fcc-like Fe (Fig.3.6(c)). The lattice constant of metastable bulk fcc-Fe at room temperature extrapolated from high temperature is  $3.59 \text{ \AA}$ , i.e.,  $\sim 8.3\%$  smaller than that of Pd ( $3.89 \text{ \AA}$ ). Thus, an expanded fcc-like phase in the initial growth stage would be consistent with the observed lattice compression with increasing Fe thickness (Fig. 3.5), though it would involve a much larger lattice mismatch with respect to the Pd(110) surface than for bcc Fe. Fcc-like Fe is consistent with the fact that the initial growth is clearly pseudomorphic.

A study of Fe growth on Pd(001) suggests that above 10 ML the epitaxial Fe films

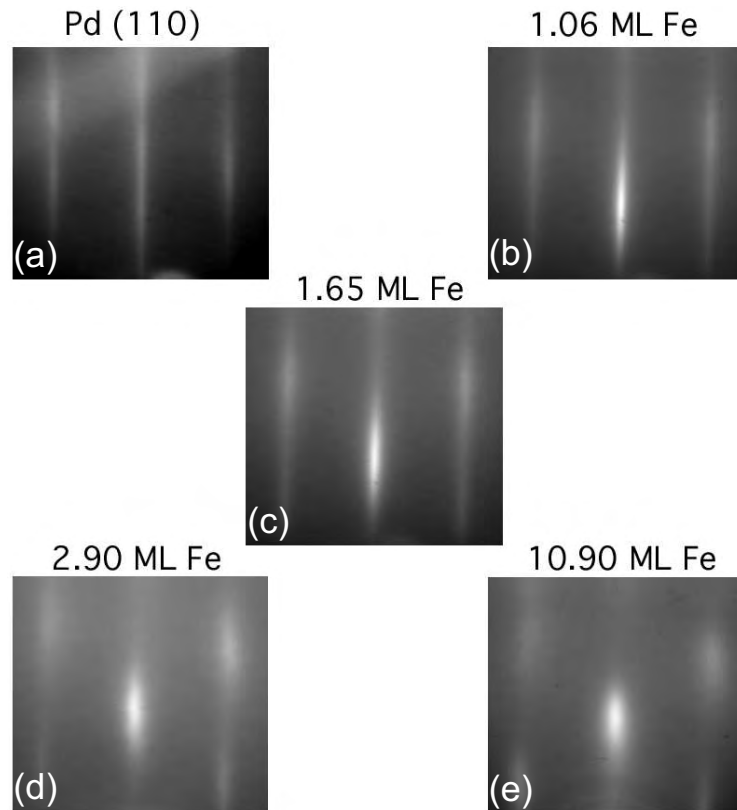


**Figure 3.4:** RHEED images of (a) the clean Pd(110) substrate, covered by (b) 1.06 ML, (c) 1.65 ML, (d) 2.90 ML and (e) 10.90 ML Fe, grown at 343 K. Note that the streaks start to become spotty in (c), indicating beginning of 3D growth. The incidence plane of the electron beam is parallel to the Pd [001] direction ([001] azimuth). (Electron energy 10 keV).

are body-centered tetragonal; but the researchers could not fit their LEED I/V results at lower coverage [27]. The present RHEED results provide evidence for the fcc-like Fe structure on Pd(110) in the initial growth stage. In section 3.3.3 the in-situ Mössbauer (CEMS) results on 3 ML Fe/Pd(110) are shown that are consistent with the RHEED result.

Fig.3.7 shows a typical set of RHEED intensity oscillations taken at (i) the position of the (1,0) streak and (ii) in the center and (iii) at the tail of the (0,0) streak, as marked in Fig.3.7(right). Both (i) and (ii) show the normal oscillation with 1-ML period in the first 1-2 ML. Similar oscillations are also observed for the (2,0) streak (not shown). They indicate smooth, layer-by-layer growth of Fe on Pd(110). But case (iii), taken at the smallest glancing exit angle ( $1-2^\circ$ ), exhibits an oscillation with a 0.5-ML period up to 1.5 ML. Such a behavior can only be observed for the (0,0) streak at the extremely glancing exit angle and closest to the direct beam (diffuse scattered part). It is well known that the phase and intensity of RHEED oscillations should vary at different angles or at different

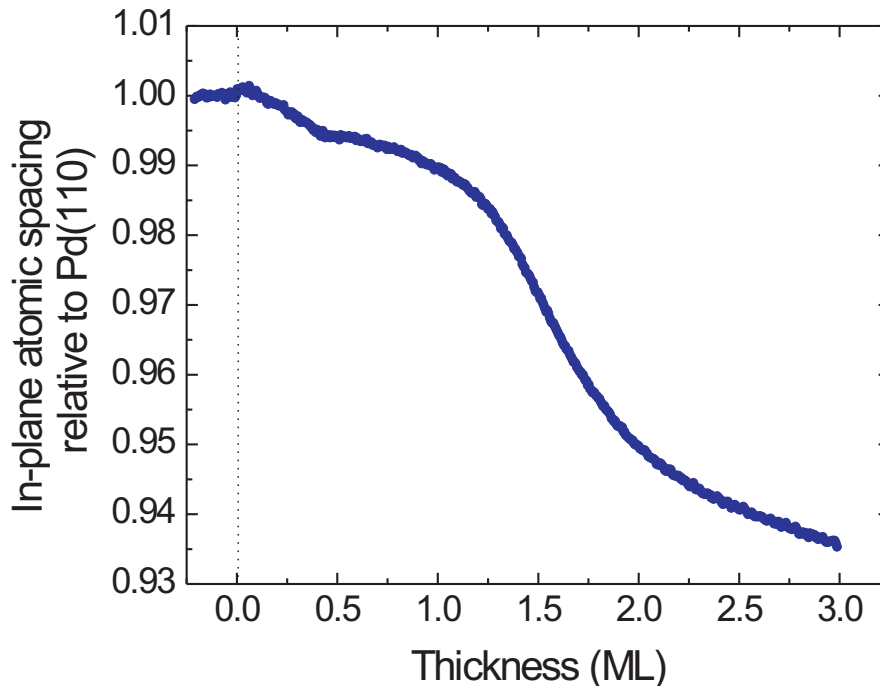


**Figure 3.5:** Relative in-plane atomic spacing along the Pd[110] direction as a function of Fe film thickness derived from RHEED images. Significant lattice relaxation is observed after 1.3 ML of Fe.

streaks. A change in periodicity is not so common and difficult to explain by an ordinary layer-by-layer growth mode. Such a change in periodicity is interpreted as the result of Fe step decoration.

A peak at 0.5 ML was first observed with thermal energy atomic scattering (TEAS) by Gambardela et al. on a stepped surface [17, 18], and was confirmed by scanning tunneling microscopy (STM). Suppose the starting substrate surface is stepped with a relatively broad distribution of terrace widths as illustrated in Fig.3.8.

If the adatoms are confined to their landing terrace and diffuse to the step edges to form monolayer-high stripes, then, at each given Fe coverage, more atomic rows will appear on wider terraces than on the narrow ones. At around 0.5 ML, all the terraces will be half-filled, giving a much narrower distribution of terrace widths as indicated in Fig.3.8. The narrowing of the distribution sharpens the diffraction streaks and yields the RHEED intensity peak at 0.5 ML coverage.

When intensity oscillations of atom or electron beams are monitored with glancing incidence angles and glancing exit angles, the lateral structure is probed. A peak at 0.5 ML therefore appears in the oscillation due to the change in lateral morphology. The fact that a half-ML oscillation is observed in Fig. 3.7 suggests that step decoration occurs for this

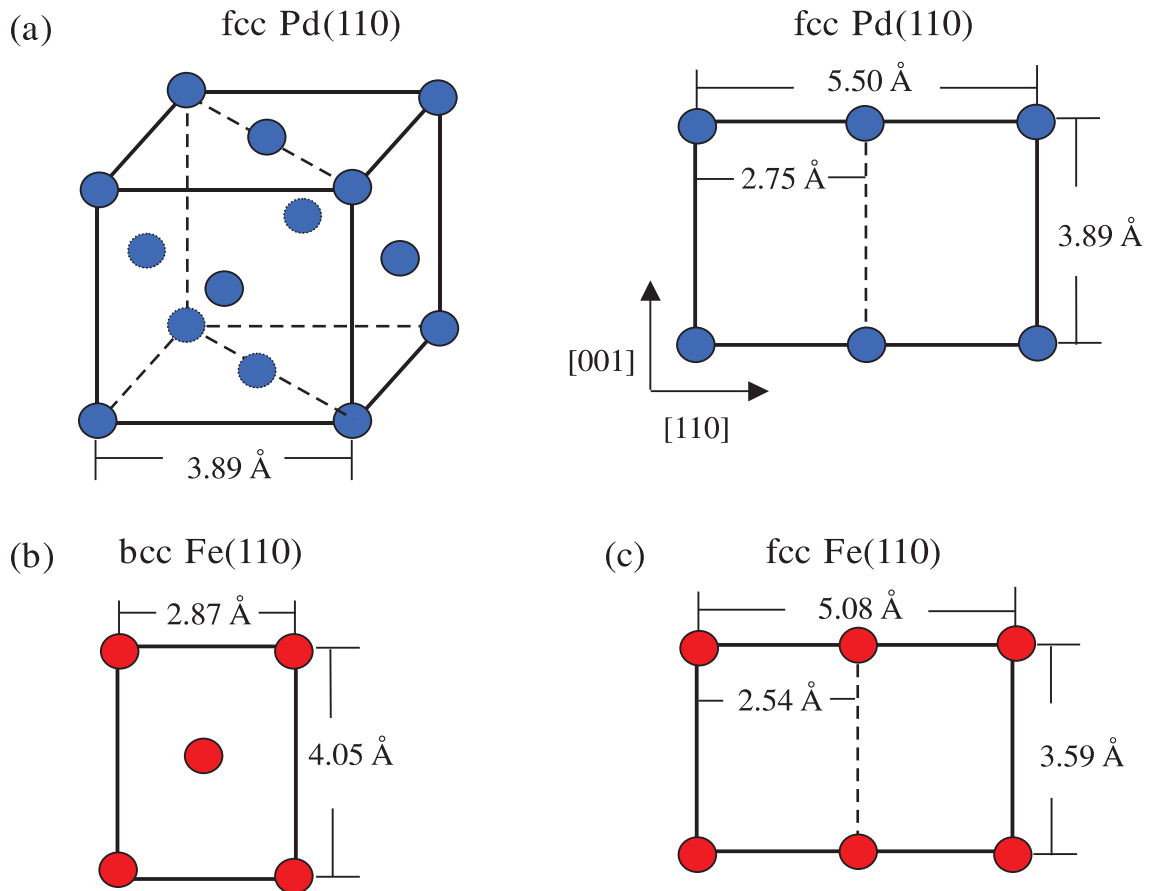


**Figure 3.6:** Schematics of (a) fcc-Pd(110), (b) bcc-Fe(110) and (c) fcc-Fe(110) surface structures. The lattice parameters  $a$  are  $3.89 \text{ \AA}$ ,  $2.87 \text{ \AA}$  and  $3.59 \text{ \AA}$  for Pd, bcc Fe and fcc Fe, respectively, at room temperature.

system. The width and spacing of Fe stripes, however, is likely to have a relatively broad distribution due to irregularities in the substrate. The hypothesis of a "step-decoration" growth for Fe on Pd(110) should be confirmed with STM in the future.

### 3.3.2 Magnetic characterization: MOKE

In-situ polar and longitudinal magneto-optic Kerr effect (MOKE) measurements were carried out at  $\sim 40 \text{ K}$  for several Fe thicknesses. The result of polar measurements (applied field perpendicular to the sample surface) is shown in Fig.3.9(right) demonstrating that submonolayer Fe films remain ferromagnetic down to  $0.3 \text{ ML}$ . All loops exhibit full remanence at zero magnetic fields. No time dependence is observed in our experimental time scale. The linear background slope observed in all the loops is an artifact from the window or due to paramagnetic impurities in the substrate.

The system is ferromagnetic down to submonolayer Fe coverage. Fig.3.10 displays the remanent magnetization measured with polar and longitudinal MOKE at  $42 \text{ K}$ . In both

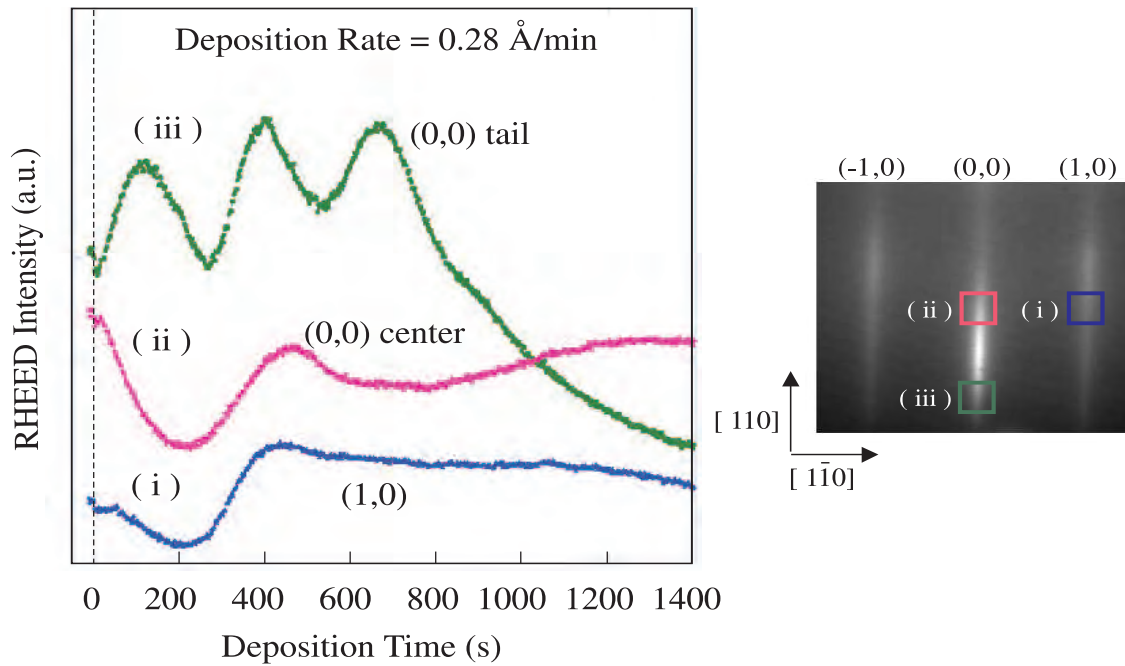


**Figure 3.7:** RHEED intensity oscillations (left) observed at (i) the (1,0) streak; (ii) the center of the (0,0) streak; (iii) the low angle tail of the (0,0) streak, as indicated on the right.

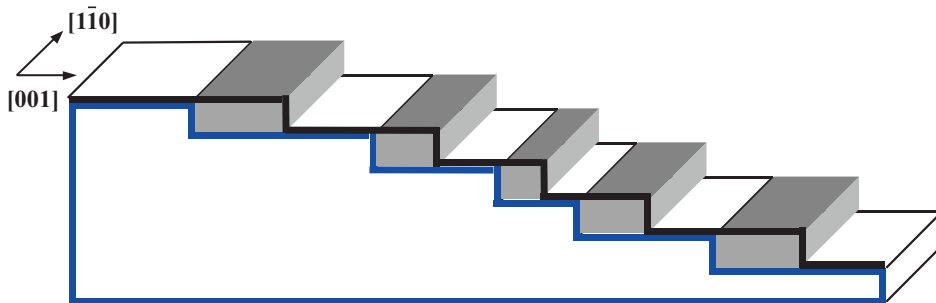


**Figure 3.8:** Schematics of the proposed growth mode for Fe on stepped Pd(110) with step decoration. Note that after deposition of 0.5 ML Fe, the terrace widths become significantly more uniform.

sets of measurements, remanent and saturation magnetization remain virtually the same. Polar Kerr signals (Fig.3.9(right)) are observed for as low as  $\sim 0.3$  ML and persist up to  $\sim 1.2$  ML. The polar  $M_R$  first increases as a function of coverage and reaches a maximum at  $\sim 0.6$ - $0.7$  ML. Then it decreases, while the coercivity field,  $H_C$ , increases. This decrease in  $M_R$  is accompanied by the emergence of the longitudinal Kerr signal (Fig.3.9 (left)). This indicates that the easy axis is perpendicular to the surface up to  $0.6$ - $0.7$  ML, where inter-stripe interactions emerge or the individual stripes start to connect, affecting the magnetic anisotropy.

Normally, for submonolayer films consisting of small islands, ferromagnetic order starts



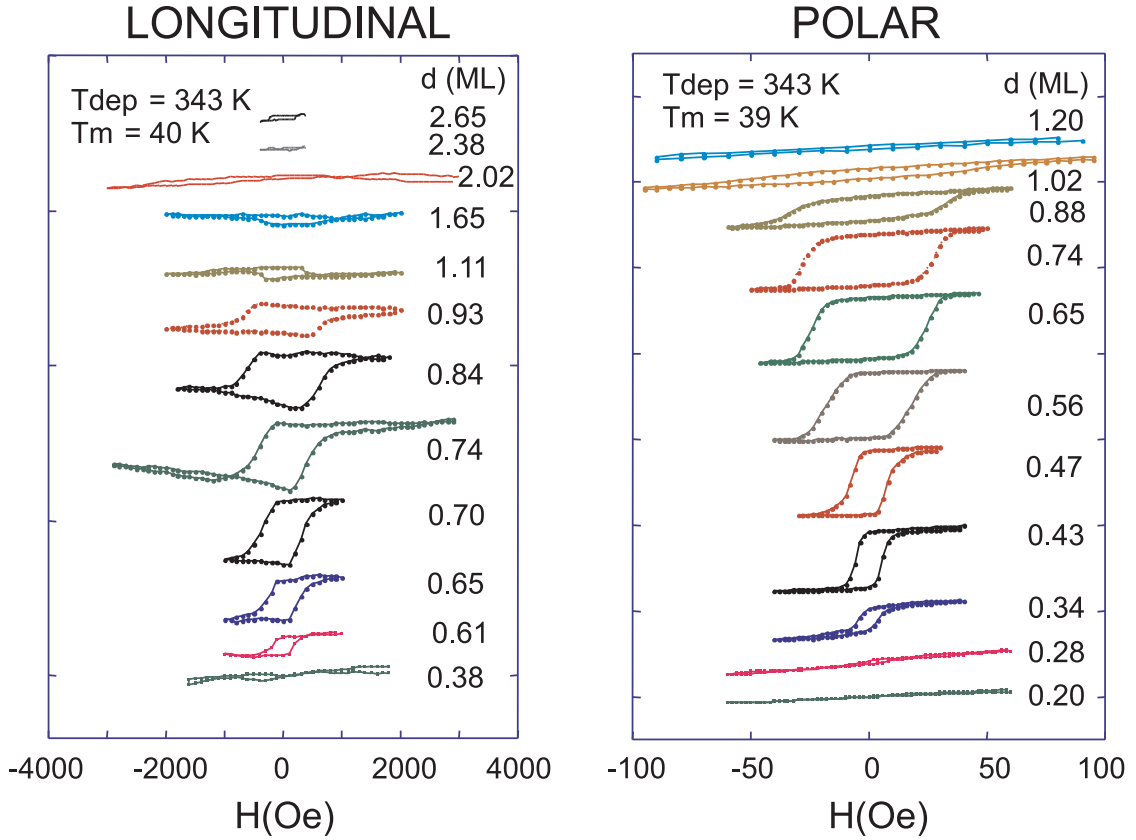


**Figure 3.9:** MOKE loops as a function of Fe thickness for the polar (right) and longitudinal (left) configurations.

to appear at an island percolation coverage of  $\sim 0.6$  ML. One possibility for a lower ferromagnetic onset in this system ( $\sim 0.3$  ML) is that the nearby Pd atoms could be polarized to make the magnetic islands larger and, therefore, coalesce earlier. Such an onset for Fe/Pd(001), however, was observed between 0.5-1 ML at low temperature, which corresponds to its island percolation observed with STM [25]. This demonstrates that Pd polarization does not contribute to an earlier onset, which is possibly because the magnetic proximity is of very short range and may only polarize the nearest Pd atoms directly below the Fe atoms. Comparing Fe on Pd(110) and Pd(001), it is suggested that the low ferromagnetic onset for Fe/Pd(110) is related to the chain-like growth as discussed earlier.

Longitudinal Kerr signals, taken with the magnetic field along the step edges, are observed for thicknesses  $\geq 0.5$  ML (Fig.3.9(left)). Fig.3.10 shows that above  $\sim 1.5$ -2 ML, the longitudinal Kerr signal increases about linearly with film thickness as expected. This region coincides with the start of 3D-growth and lattice relaxation. Between 0.5-1.2 ML, an anomalous peak exists, where the longitudinal Kerr signals are surprisingly large and even larger than those of the thicker films. In that region, there is a coexistence of both, polar and longitudinal signals, and an increase in coercivity. This complicated behavior

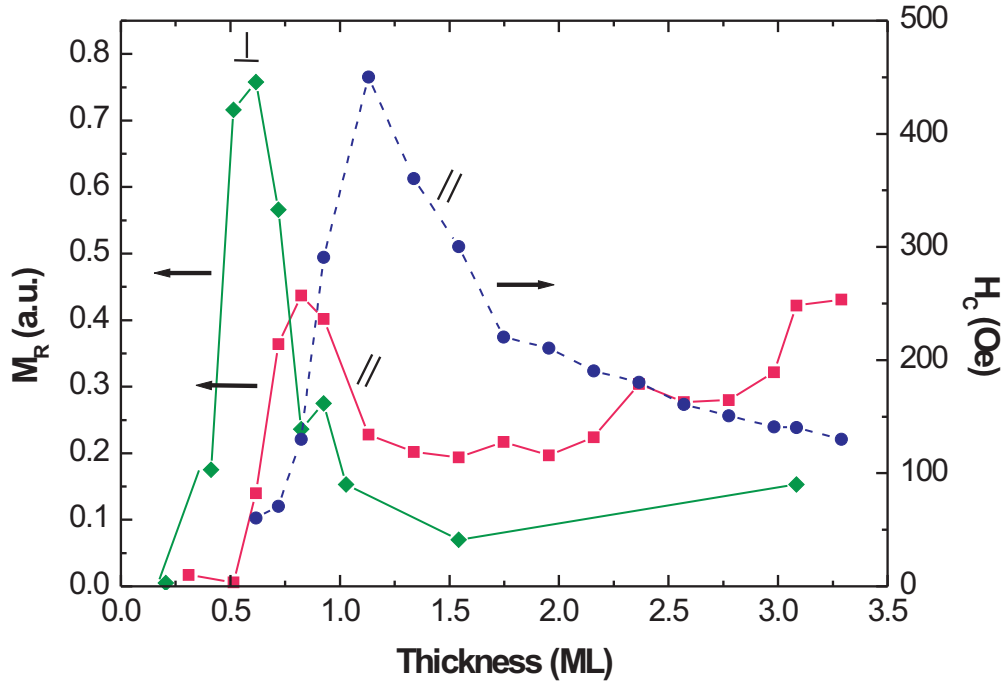


**Figure 3.10:** Thickness dependence of the polar ( $\perp$ ) and longitudinal ( $//$ ) remanent magnetization, along with the coercivity in the longitudinal signals ( $//$ ) measured with MOKE at 42 K.

of the system could be due to the presence of mixed magnetic phases, combined with a canting angle of the magnetization in the critical thickness region where the transition between out-of-plane to in-plane magnetization occurs.

The results indicate that the magnetic easy axis is perpendicular to the surface at very low coverage of 0.3-0.6 ML, while it is clearly in-plane above 1.5 ML. The initial perpendicular anisotropy may be induced by the step edges and/or the terraces.

A tight-binding calculation [28] predicts that the easy axis of a freestanding 1D Co chain is in-line to the chain, while it switches to perpendicular to the surface for Co/Pd(110). No calculation, however, is available for Fe/Pd(110). In Fe/Pd(001) experiments, the easy axis is in-plane for 300 K growth, and out-of-plane for 100 K growth [26]. Fe stripes on Cu(111) exhibit perpendicular anisotropy as does one monolayer Fe deposited on Cu(111) [20]. For comparison, an in-plane easy axis perpendicular to the stripes was observed during the growth of Fe stripes on W(110) [19].

At  $\sim 0.9$ -1.5 ML, the coercivity field of the in-plane magnetization significantly increases, being also an indication of mixed magnetic phases at a phase transition boundary [47].

The strong thickness dependence of the magnetic properties in the quasi-one-

dimensional Fe stripes was shown above. Temperature dependent measurements of the magnetization, performed for several selected thicknesses, will show the existence of a correlation between the magnetic and the structural properties of the samples, and will contribute to the understanding of how the 2D  $\rightarrow$  1D transition takes place.

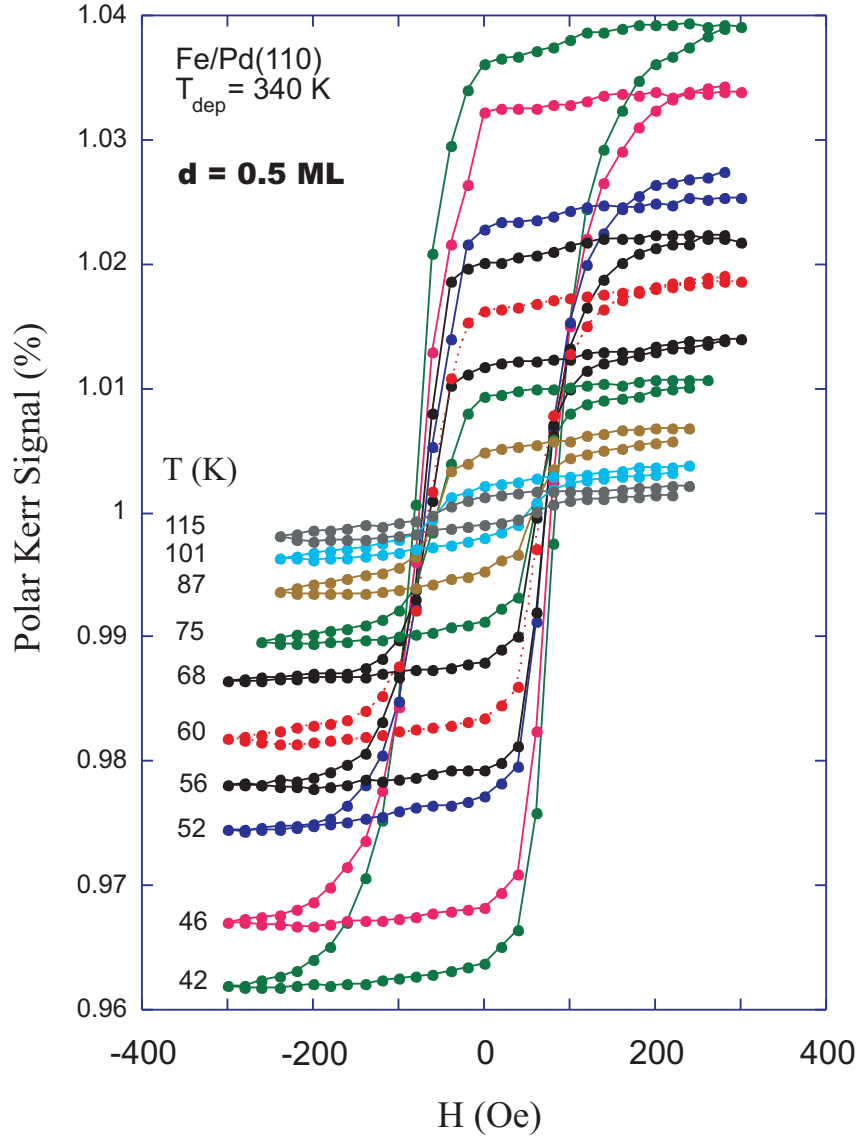


**Figure 3.11:** Temperature dependence of polar Kerr magnetization loops for 0.5 ML Fe on Pd(110).

Remanent magnetization versus temperature measurements were carried out for different sample thicknesses in the polar Kerr geometry. Fig.3.11 shows the results obtained for a 0.5 ML thick Fe sample. Ferromagnetic behavior was observed from 42 K up to 115 K. Both, coercivity and saturation magnetization monotonically decrease with increasing temperature, however the change in the coercivity is not very large. Again,  $M_R$  remains

virtually the same as  $M_S$  within the error bar, although the loops of 0.5 ML are sheared instead of square. This is different from the case of Fe stripes on Cu(111), where  $M_R$  is always significantly less than  $M_S$ , especially at higher temperatures.

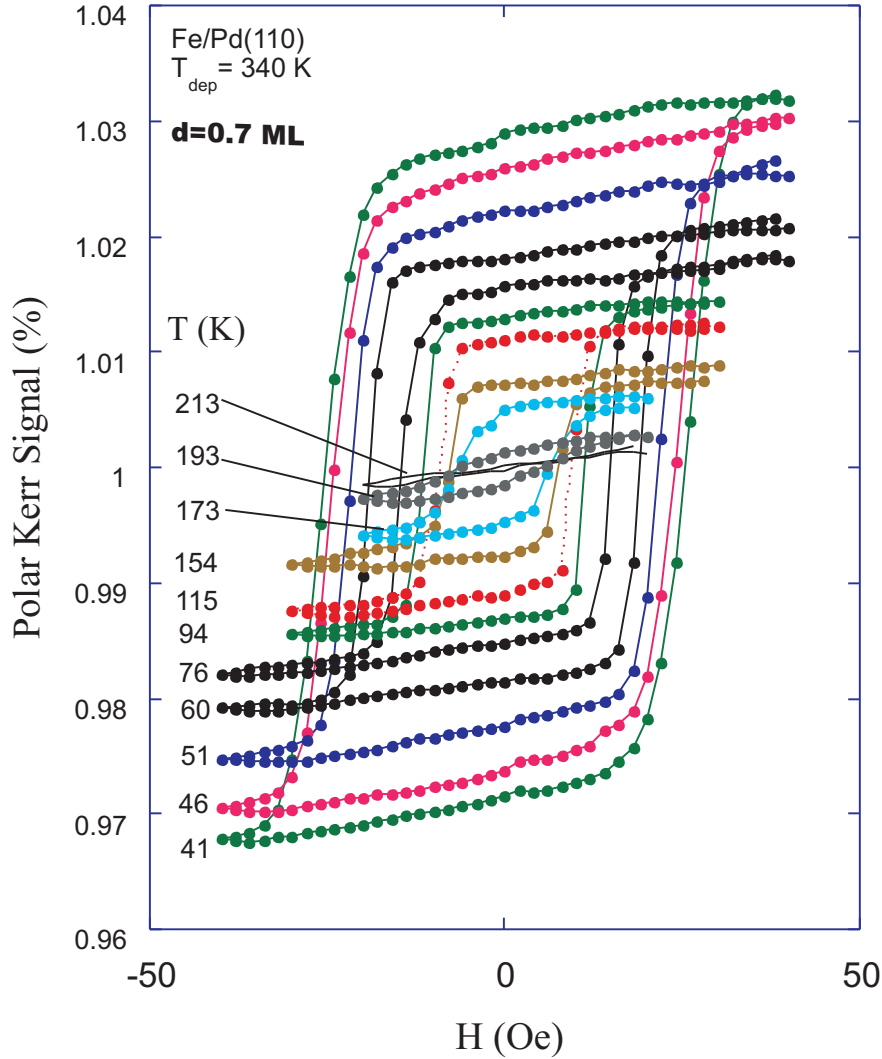


**Figure 3.12:** Temperature dependence of polar Kerr magnetization loops for 0.7 ML Fe on Pd(110).

At 0.7 ML, both  $M_R$  and  $H_c$  decrease as temperature increases (Fig.3.12). Ferromagnetism is observed up to 213 K. At 0.5 ML, however, while  $M_R$  decays drastically,  $H_c$  only decreases gradually (see inset in Fig.3.13), and does not approach zero as one expects at the Curie temperature  $T_C$ , or blocking temperature  $T_B$  in superparamagnetism. All the samples with coverages  $< 0.5$  ML showed the same characteristic behavior. Ordinarily,  $H_c$  should be strongly temperature dependent and approach zero at high temperature [30]. However, the nucleation process or step pinning could significantly alter the magnetic switching process, and hence the coercivity in stripe systems. It is an interesting issue

for future research to understand this behavior and see if it is related to the quasi-1D geometry.

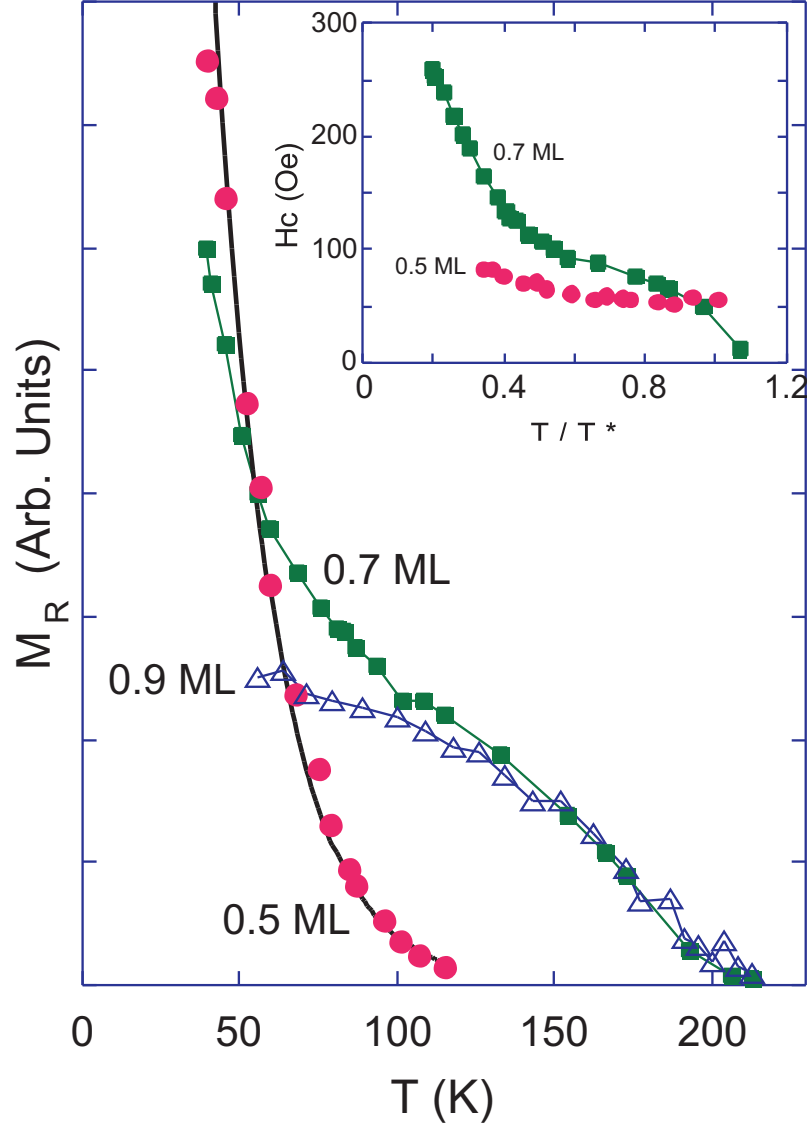


**Figure 3.13:** Remanent magnetization versus temperature obtained from polar Kerr measurements on 0.9 ML (open triangles), 0.7 ML (full squares), and 0.5 ML (full circles) Fe/Pd(110). The solid line for 0.5 ML is a fit of the data as discussed in the text, while the other lines are a guide for the eye.

The temperature dependence of  $M_R$  at different thicknesses is shown in Fig.3.13.  $M_R$  was derived from the original data sets shown in figures 3.11 and 3.12. First of all, it is observed that the transition temperature increases with increasing Fe coverage, and starts to saturate for 0.7-1 ML at around 215 K.

The temperature dependence of  $M_R$  obtained for the 0.9 ML sample behaves like the order parameter in a second-order phase transition. It initially decreases gradually

with increasing temperature and then drops rapidly as the temperature approaches  $T_C$ . This behavior reproduces quite well the behavior of a two-dimensional system in the critical transition limit. The 0.5 ML sample, however, presents a surprisingly different temperature dependence, with an exponential decrease of  $M_R$  with increasing  $T$ . This anomalous behavior could be an indication of a reduction of the dimensionality of the system, corresponding to the quasi-1D stripes suggested by the RHEED intensity oscillations. The most representative case is the intermediate 0.7 ML sample, where a crossover between the two qualitatively different kinds of behavior is evident as the curvatures of the temperature dependent curve are clearly different below and above  $\sim 100$  K. This is consistent with the fact that the 0.7-ML sample is at the boundary of a magnetic phase transition, related with the beginning of the percolation of the nearly-1D chains into 2D islands and with the change in the magnetic anisotropy mentioned above.

No inflexion point, a common way to define  $T_C$ , exists in a wide temperature range of 40-100 K (Fig. 3.13). All the curves are reversible during warming up and cooling down. If the transition temperature  $T_C$  is defined as the inflexion point of this decaying M-T curve, then it should be at, or lower than the lowest measured temperature of  $\sim 40$  K for all films of  $d \leq 0.7$  ML. Yet the curves appear ferromagnetic with non-vanishing  $H_c$  in a wide temperature range of 40-100K. Such a temperature dependence is different from the Fe stripes on W(110) [19], where a normal 2D Ising behavior was observed. It is also different from the case of Fe stripes on Cu(111), where  $M_R$  decays but  $M_S$  still follows a 2D Ising model.

An exponential-like decay in both  $M_R$  and  $M_S$  found for the 0.5 ML sample has never been observed before for a ferromagnetic system, quasi-1D or not, though superparamagnetic systems indeed show a similar behavior in  $M_R$ . In those systems, blocks of spins in fine grains behave as giant magnetic moments that can easily rotate in direction. This results in a temperature activated process for  $M_R$  decaying rapidly before the temperature reaches the blocking temperature ( $T_B$ ) and remaining zero above  $T_B$ . Even at 0K,  $M_R$  should remain to be  $M_R/2$  after turning off the external field [31].  $M_S$  on the other hand, shows 2D or 3D Ising behavior [31]. These properties are clearly different from the present case, where  $M_R$  and  $M_S$  are always about the same. In addition, the measured coercivity  $H_c(T)$  and magnetization  $M(H,T)$  also do not follow the well established temperature and field dependence for superparamagnetism [31]. As an additional test to exclude superparamagnetic behavior in this system, polar Kerr loops on a  $\sim 0.8$  ML sample deposited at 340 K and measured at  $\sim 117$  K and 53 K were recorded (Fig.3.14). The square shape of the loops, and its saturation in a "plateau" even for very high applied fields (up to 6000 Oe), are other arguments against the existence of superparamagnetism. Therefore superparamagnetism is ruled out as the origin of the peculiar temperature dependence we observe.

Although the transition temperature  $T_C$  becomes ill defined at low coverage, an extrapolated value for  $T_C$  ( $T_C^*$ ) is used to describe the effective transition temperature ( $T_C^*$ ) at different thicknesses. At each temperature,  $M_R$  is measured across the wedge and then extrapolated to zero to determine a critical coverage (Fig.3.15). ( $T_C^*$ ) is then defined as the measurement temperature at that critical coverage. Fig. 3.15 shows some of the raw

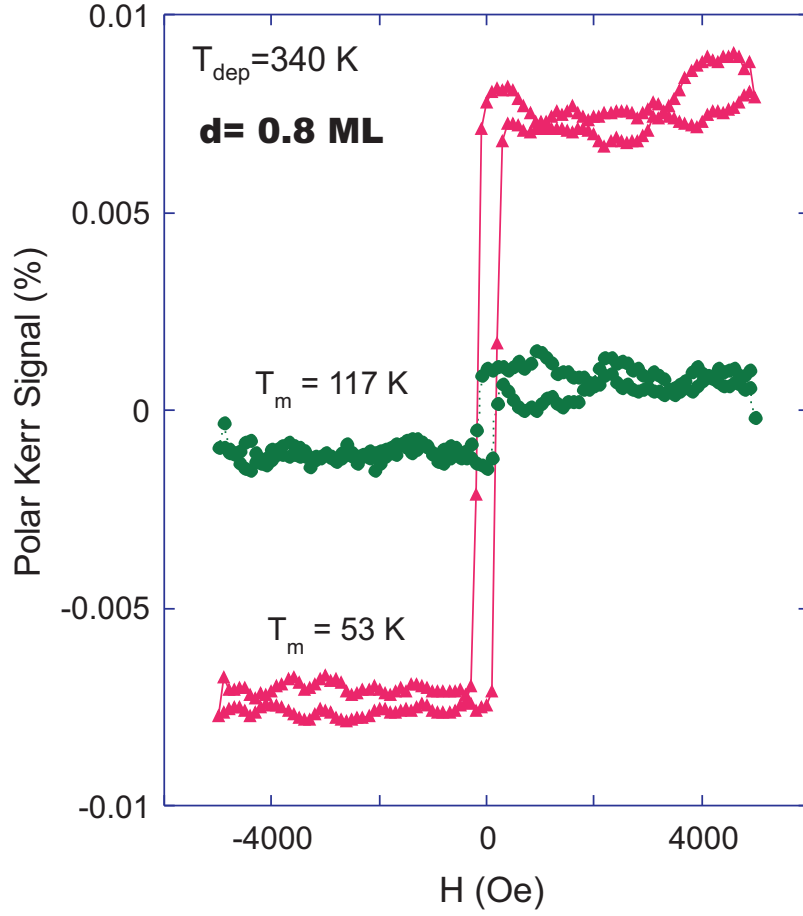


**Figure 3.14:** Polar Kerr loops of 0.8 ML Fe/Pd(110) deposited at 340K and measured at 53 K (solid triangles) and 117 K (solid circles)

data employed for the determination of  $T_C^*$ .  $d$  is equal to the Fe coverage (or thickness). For each measurement temperature, a linear extrapolation of the slope (left side) of the  $M_R$  versus coverage curves was performed. The  $d$  value obtained from the cut of the extrapolation line and the  $M_R=0$  axis (solid line in Fig.3.15) will be the critical coverage for which our measurement temperature is a transition temperature.

$T_C^*$  is plotted in Fig.3.16 versus coverage.  $T_C^*$  increases as a function of coverage or stripe width, and saturates near  $\sim 0.7$ -1 ML at 210 K. Only the data from  $d < 0.7$  ML are plotted and included in the finite-size scaling fit, since the magnetic behavior changes beyond that point. Using  $T_C^*$  to approximate  $T_C$ , their thickness dependence can be described by the finite size scaling expression:

$$T_C(d) = T_{C0}[1 - (d/d_0)^{-\lambda}] \quad (3.1)$$

where  $\lambda$  is the shift exponent [32]. The value of  $d_0$  obtained from the fit is  $0.32 \pm 0.09$  ML, below which the film is no longer ferromagnetic. Considering the average terrace

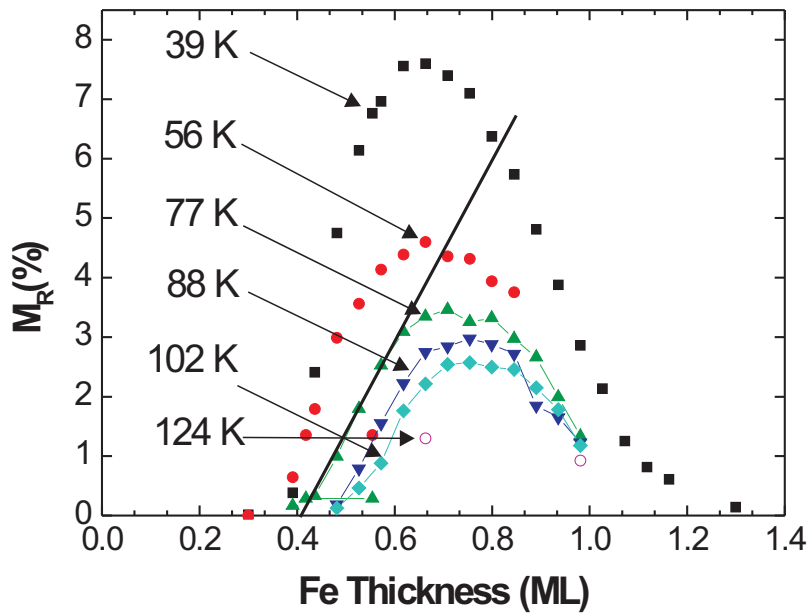


**Figure 3.15:** Remanent magnetization versus coverage measured along a Fe wedge at different fixed temperatures: 39 K (solid squares), 56 K (solid circles), 77 K (solid triangles), 88 K (solid down triangles), 102 K (solid diamonds) and 124 K (open circles). The full line is an example of the extrapolated critical coverage obtained for the transition temperature of 77K.

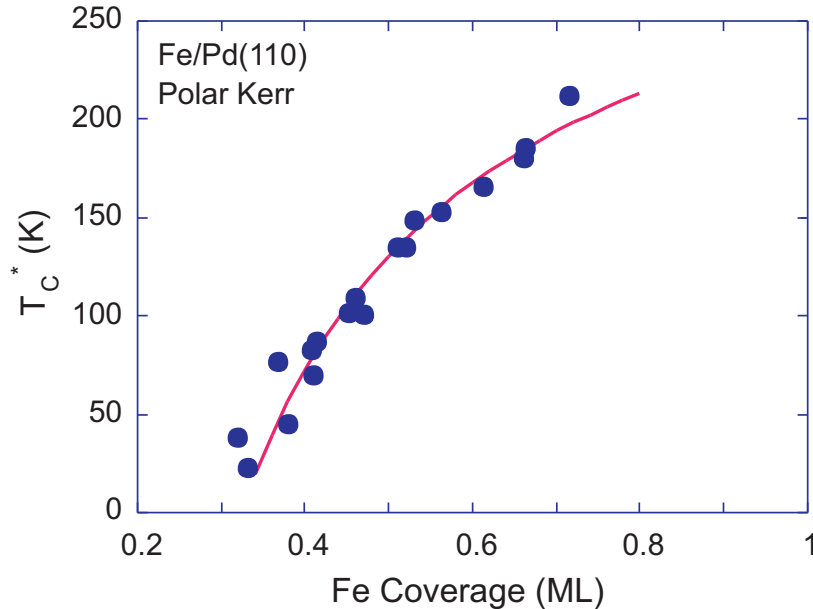


**Figure 3.16:** Extrapolated transition temperature  $T_C^*$  versus Fe coverage. The solid line is a fit with finite size scaling as discussed in the text.



width of  $\sim 20 \text{ \AA}$ , this corresponds to a stripe width of  $\sim 6 \text{ \AA}$  for a 1 ML high Fe stripe, because the stripe width ( $w$ ) is related to the terrace width ( $W$ ) and the Fe coverage parameter  $d_0$  by:  $w=W\cdot\theta_0$  ( $\theta_0=d_0/1 \text{ ML}$  is the coverage parameter).

The shift exponent  $\lambda$  is determined as  $1.2 \pm 0.3$ , in agreement with the 2D Ising model, which predicts  $\lambda=1$  as 2D stripes change their width [32]. The observation of finite-size scaling suggests that the stripes are effectively isolated.

A similar behavior for  $T_C(d)$  was earlier observed by Elmers et al. in submonolayer Fe/W(110) for stripes widths  $\geq 44 \text{ \AA}$  [19]. The differences in the width range of the stripes may explain the differences in the temperature dependence of  $M_R$  between Ref. [19] and the present work. The narrower Fe-stripe arrays on stepped W(110) exhibited inter-stripe dipolar couplings, which tend to align the moments in-plane [20]. For Fe/Pd(110), since the easy axis is perpendicular to the surface, a dipolar interaction would cause antiferromagnetic alignment among the stripes. No sign of such a coupling is observed in view of the full remanence, which may result from the strong perpendicular anisotropy.

In addition to the shift exponent discussed above, the phase transition of a finite system also expects a rounding  $\Delta T$  of the transition temperature:

$$\delta = \frac{\Delta T}{T_{C0}} \propto \frac{1}{d^\theta} \quad (3.2)$$

where  $\Delta T$  is due to the fact that the correlation length cannot diverge in a finite system [32]. The exponent  $\theta$  for a finite-size 2D Ising system is  $\theta=1$ , indicating a significant broadening in the transition region as  $d$  decreases. This may be related to our unusual  $M(T)$  behavior (Fig. 3.13), though a definitive determination requires measurements at even lower temperature to observe the whole curve. A distribution of stripe-widths and therefore  $T_C$  values should also cause a broadening of the transition region [33], but the present experimental  $M(T)$  curves could not be described by a Gaussian distribution of  $T_C$  values, each with a 2D dependence.

### 3.3.3 $^{57}\text{Fe}$ CEMS

A Mössbauer (CEM) spectrum of 3 ML Fe on Pd(110) at 25 K (i.e. near magnetic saturation) is shown in Fig. 3.17. The measurement time was 2 weeks, using a 40mCi  $^{57}\text{Co}$  source. This spectrum exhibits a Zeeman sextet with a large value of the hyperfine magnetic field,  $B_{hf}$  or, equivalently, with large Fe atomic moments. The film is magnetically ordered at 25 K. Because of the rather large width of the outer lines and its asymmetry, the spectrum has been least-squares fit with a distribution of hyperfine magnetic fields, including a weak electric quadrupole interaction. The Mössbauer spectral parameters obtained from the fitting are given in Table 3.1, together with experimental results for thin fct-Fe layers (3ML) deposited on  $\text{Cu}_3\text{Au}(001)$  (see chapter 4.3.2) or for  $\text{Fe}(15 \text{ \AA})/\text{Pd}$  multilayers [34].

The spectrum of 3 ML Fe (Fig. 3.17) and its spectral parameters (Table 3.1) are distinctly different from those of bulk bcc-Fe, and rather close to those of fct-Fe in Fe/Pd multilayers or fct-Fe/ $\text{Cu}_3\text{Au}(001)$ . The fit provided a hyperfine field distribution with a

peak at 39.2 T, which is very large compared to the value of 34 T measured at 25 K for bcc-Fe. The observed relatively large (negative) quadrupole interaction ( $2\epsilon$ ) of -0.09 mm/s, reflects the non-cubic structure (lattice distortion) of the 3 ML Fe film (for bulk Fe with ideal bcc structure  $2\epsilon$  is zero).

The average angle between the incident  $\gamma$ -ray direction (perpendicular to the sample surface) and the direction of  $B_{hf}$ , i.e. the spin direction, can be obtained from the line intensity ratio in Fig. 3.17. From the least-squares fit we obtained the ratio  $I_{2,5}/I_{3,4}=R=3.5 \pm 0.2$ , which yields  $\theta=75^\circ \pm 4^\circ$  from eq. (2.4), section 2.2.1. This indicates a preferred in-plane spin orientation, analogous to the case of 6 ML Fe (15 Å) in the Fe/Pd multilayers [34], where  $\theta \sim 79^\circ$ .

The change in sign of  $2\epsilon$  in going from Fe(3 ML)/Pd(110) to Fe(4 ML)/Cu<sub>3</sub>Au(001) is explained by the different Fe spin orientations in both systems: nearly in-plane on Pd(110), and preferentially perpendicular orientation on Cu<sub>3</sub>Au(001).

The strong 15 % enhancement (relative to bulk bcc Fe at 25 K) of the measured most-probable (peak-) hyperfine field in Fe(3ML)/Pd(110) can not be explained by the additional contribution of the demagnetizing field,  $|B_{dem}| \simeq \mu_o M_S \cos \theta$ , for the case of nearly in-plane spin orientation (see eq.(2.3) section 2.2.1). In our case  $B_{ext}=0$  and  $|B_{dem}| \simeq 0.5$  T (taking  $\theta=75^\circ$  and assuming that fct and bcc Fe have about the same saturation magnetization  $\mu_o M_S$  of about 2T), and this is very small. Therefore, the measured hyperfine field ( $|B_{hf}|$ ) is nearly equal to the intrinsic hyperfine field ( $|B_{int}|=|B_{hf}|-|B_{dem}|=38.5$  T), which is approximately proportional to the local Fe moment  $\mu_{Fe}$ . 3 ML fcc-like Fe on Pd(110) apparently are in high-moment ferromagnetic state with a value of  $\mu_{Fe} \approx 2.6 \mu_B$ , as estimated from our peak- $B_{hf}$  value. This value is in fairly good agreement with the enhanced moment,  $\mu_{Fe}=2.7 \pm 0.1 \mu_B$ , deduced by Mühlbauer et al. [35] from magnetization measurements on polycrystalline Fe/Pd multilayers.

The average center line shift at 25 K ( $\delta$ , relative to bulk bcc-Fe at RT) given in Table 3.1 includes the chemical shift (isomer shift) and the (thermal) second-order Doppler shift.

Sample	$T_m$ (K)	$\delta$ (mm/s)	$2\epsilon$ (mm/s)	$\theta$ ( $^\circ$ )	$B_{hf}$ (T)
<sup>57</sup> Fe(3 ML)/Pd(110)	25 K	$0.217 \pm 0.002$	$-0.09 \pm 0.03$	$75^\circ$	$34.5 \pm 0.4$ (peak) 39.2
<sup>57</sup> Fe(4 ML)/Cu <sub>3</sub> Au(001)	25 K	$0.26 \pm 0.08$	$0.07 \pm 0.02$	$25^\circ$	$36.2 \pm 0.5$
[Fe(15 Å/Pd(40 Å)) <sub>30</sub> /Sapphire [34]	4.2 K	$0.180 \pm 0.002$	$-0.01 \pm 0.01$	$79^\circ$	$35.5 \pm 0.3$ (peak) 36.8

**Table 3.1:** Mössbauer parameters (isomer shift  $\delta$  (including the second-order Doppler shift), quadrupole splitting  $2\epsilon$ , average angle between  $\gamma$ -ray direction and Fe spin direction  $\theta$ , and average hyperfine field  $B_{hf}$ ) obtained from a least-squares fit of the spectrum displayed in Fig. 3.17. Also the most-probable hyperfine field (peak) is given. Mössbauer parameters from Fig. 4.9(a) (chapter 4) and from Fig.8 in Ref. [34] are shown for comparison. The isomer shift values are referred to bulk bcc-Fe at 300K.  $T_m$  is the measurement temperature.

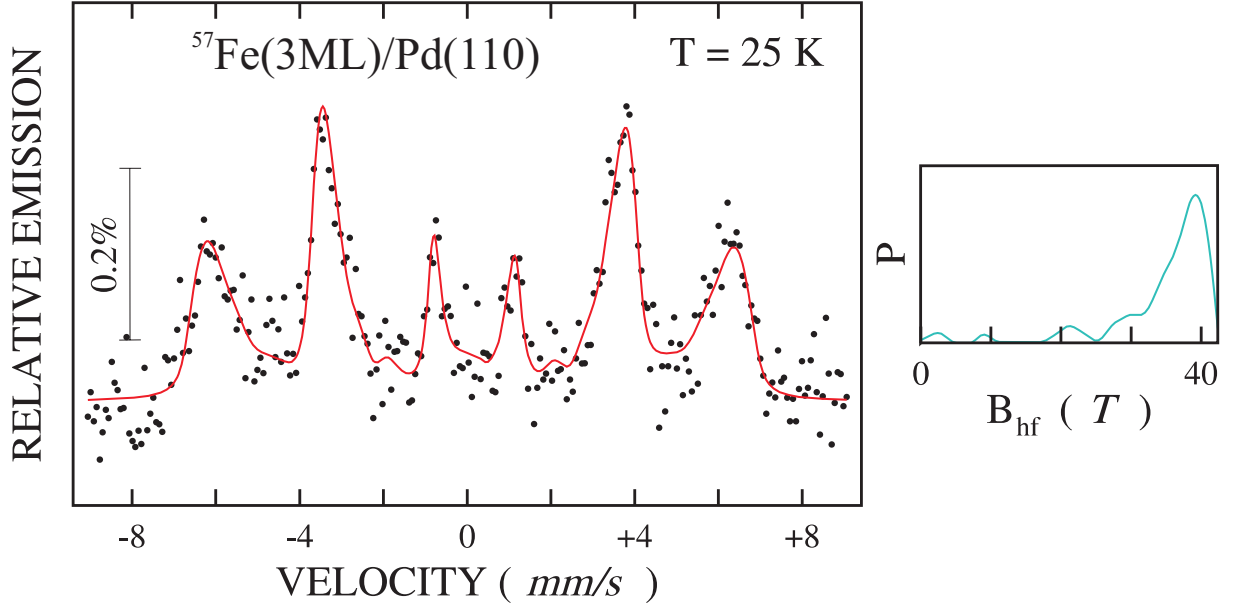


**Figure 3.17:** Mössbauer spectrum (CEMS) of  $^{57}\text{Fe}(3 \text{ ML})/\text{Pd}(110)$  measured in-situ in UHV at 25 K. Right hand side: distribution of hyperfine magnetic fields,  $P(B_{\text{hf}})$ .

### 3.4 Conclusions

The growth and magnetic properties of epitaxial submonolayer Fe on a vicinal stepped Pd(110) surface has been investigated by means of RHEED and MOKE. RHEED intensity oscillations suggest that step decoration occurs in the first deposited 1.5 ML, when the films are pseudomorphic. The Fe atoms decorate the steps to form monolayer-height stripes at a growth temperature of 340 K, up to a coverage of  $\sim 0.7$  ML, when the stripes start to connect. These stripes are ferromagnetic starting at  $\sim 0.3$  ML coverage, or at a stripe width of  $\sim 6 \text{ \AA}$ , and have magnetic easy axis along the surface normal. The onset of ferromagnetism is earlier than the normal percolation limit. The stripes initially have a magnetic easy axis perpendicular to the surface, but above  $\sim 0.7$  ML the easy axis starts to reorient towards the film plane.

Both, remanent magnetization and saturation magnetization show an exponential decay with increasing temperature in a large temperature range of 40-100 K. Superparamagnetism can be ruled out as the origin of this anomalous temperature behavior. The finite size rounding of the Curie temperature of quasi 1D stripes may be the origin of this unusual result.

The effective Curie temperature as a function of coverage exhibits finite size scaling with a shift exponent  $\lambda$  of  $1.2 \pm 0.3$ , consistent with the two-dimensional Ising model. The coercivity shows intriguing behavior at  $\sim 0.5$  ML Fe coverage, suggesting that the nucleation of reversed domains in the stripes or step pinning may profoundly influence the magnetization switching process.

The RHEED determination of the in-plane atomic distance versus Fe film thickness provides evidence for stabilization of the metastable fcc-like Fe structure on Pd(110). This interpretation is supported by  $^{57}\text{Fe}$  CEMS measurements which indicate a  $\sim 15\%$  enhanced saturation hyperfine field. A large, though less enhanced hyperfine field is also observed in distorted fcc-like (fct) Fe films on other substrates, like  $\text{Cu}_3\text{Au}(001)$  (see chapter 4). These results suggest that fcc-like Fe films on Pd(110) are in a ferromagnetic high-moment state with a considerably enhanced Fe magnetic moment.

# 4 Observation of the fcc-to-bcc Bain transformation in epitaxial Fe ultrathin films on $\text{Cu}_3\text{Au}(001)$

## 4.1 Introduction

Face-centered cubic (fcc or  $\gamma$ -) iron is a fascinating system because of its intriguing magnetic properties and its delicate interplay between magnetism and structure [36–38]. Interest for this system is stimulated by the extreme atomic-volume dependence of the ground-state magnetic properties (magneto-volume instabilities or low-moment/ high-moment transition) predicted theoretically for bulk fcc-Fe [36–38], and observed experimentally for epitaxial fcc-like Fe thin films [39]. The prediction that both the magnetic exchange coupling and the Fe magnetic moment in fcc Fe depend strongly on interatomic distances initiated a vast number of investigations on epitaxial fcc or fcc-like Fe thin films on Cu(001) and other related substrates [39–41]. Such epitaxial growth allows the low-temperature stabilization of the high-temperature fcc Fe phase in the form of a metastable thin film.

The basis for epitaxial growth of fcc Fe films on fcc Cu(001) is the similarity of lattice parameters of Cu ( $a = 3.615 \text{ \AA}$  at 295 K) and  $\gamma$ -Fe ( $3.588 \text{ \AA}$  at 293 K, extrapolated from equilibrium (bulk)  $\gamma$ -Fe data above  $910^\circ\text{C}$  [42], or  $3.5757 \text{ \AA}$  at 80 K, measured on coherent  $\gamma$ -Fe precipitates in a Cu matrix [43]). It is generally accepted now that room-temperature (RT) grown fcc-type Fe films on Cu(001) in the 2-4 monolayer (ML) thickness range are ferromagnetic (FM) with a high Fe-spin magnetic moment (high spin state) of  $2.8 \mu_B$  [44] and a large saturation hyperfine field ( $B_{hf}$ ) of  $\sim 31\text{-}34 \text{ T}$  [40] (incidentally similar to that of bcc Fe), and has the fct structure with an expanded atomic volume, including some "buckling" of Fe atoms [45]. For thicker (RT-grown) Fe films on Cu(001) in the  $\sim 5\text{-}10 \text{ ML}$  range the ideal fcc structure with a smaller atomic volume is paramagnetic at RT and very likely antiferromagnetic (AFM) at low T with a low hyperfine field,  $B_{hf}$ , of  $\sim 1\text{-}2 \text{ T}$  [40], while FM is restricted to the film-vacuum surface region [40, 46, 47] with an average Fe spin moment of  $0.8 \mu_B$  [44]. Until recently it was assumed that the epitaxial growth of fcc-type Fe on Cu(001) is pseudomorphous [48], which would result in a strained fcc-Fe lattice due to the misfit of  $\sim 0.7 \%$  with respect to the Cu lattice. However, a recent RHEED study proves that epitaxial fcc-type Fe films on Cu(001) are non-pseudomorphous and grow strain free [49].

The structural and magnetic properties of ultrathin epitaxial Fe films grown at room temperature (RT) or low temperature (LT) on  $\text{Cu}_3\text{Au}(001)$  have been studied in the past decade by several groups [50–58]. Pseudomorphic growth at RT of fcc-Fe/ $\text{Cu}_3\text{Au}(001)$  below 7 ML Fe coverage was reported by Lu et al. [51], Rochow et al. [53], and Baudelet et al. [55], based on low energy electron diffraction (LEED) results. Considering the relatively large lattice misfit (4.2 %) of bulk fcc ( $\gamma$ -)Fe ( $a_o = 3.59 \text{ \AA}$  at 293 K) and  $\text{Cu}_3\text{Au}$  ( $a_o = 3.75 \text{ \AA}$ ), a tetragonal distortion (fct structure) in the Fe films was not excluded

in ref. [55]. Upon increasing the Fe coverage, Lin et al. [50, 56] reported an fcc-to-bcc transformation at a critical thickness of 3.5 monolayers (ML) for RT growth, correlated with a magnetization reorientation transition from perpendicular to in-plane direction, (observed earlier in Ref. [55]), and the coexistence of fcc-like and bcc-like phases from 3.5 ML up to  $\sim 6$  ML Fe. By contrast, Schirmer et al. [58] conclude from quantitative LEED results that 3.3-4.8 ML thick films are strained bcc Fe(001) rather than the previously proposed fcc structure.

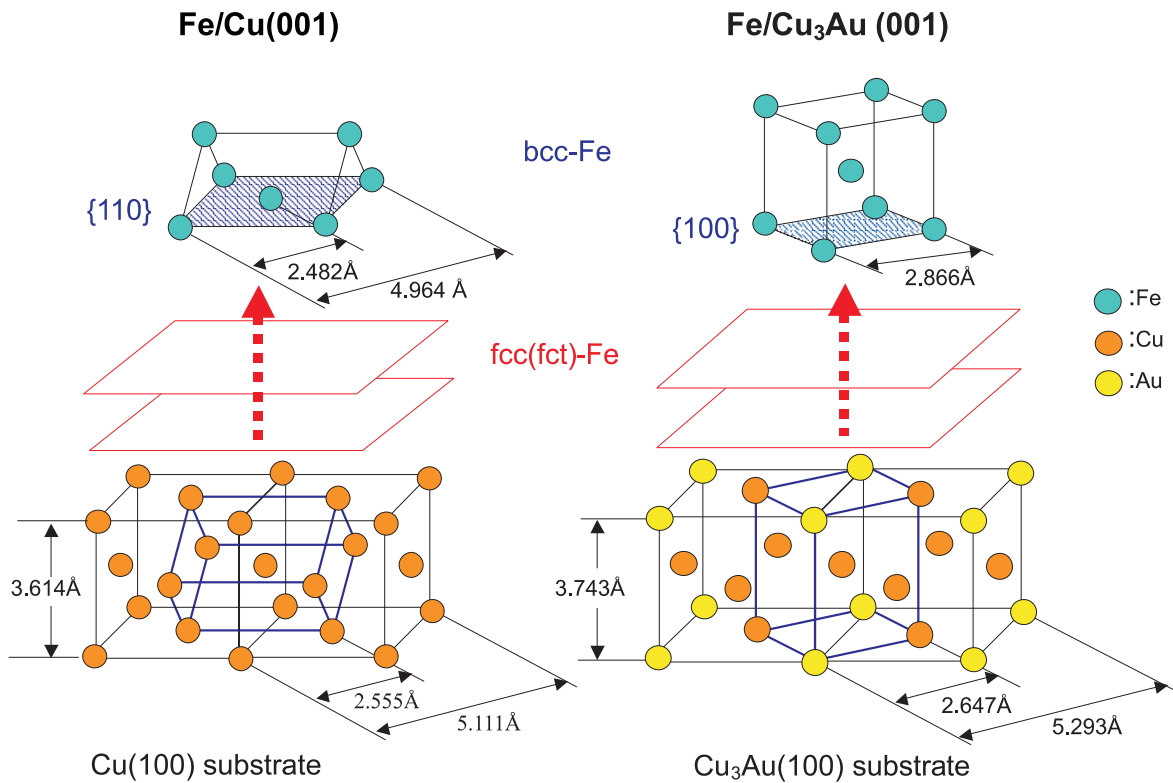


**Figure 4.1:** Schematic of the epitaxial growth of Fe on Cu(001) (left) and Cu<sub>3</sub>Au(001) (right).

Fig. 4.1 shows a schematic comparison of the growth of Fe on Cu(001) and Cu<sub>3</sub>Au(001) based on the minimization of the lattice mismatch between substrate and Fe layers. In both cases, the first layers near the Fe/substrate interface were found to be fct or fcc-Fe, stabilized by heteroepitaxy on the fcc substrates. With increasing thickness, bct or bcc-Fe becomes the most stable Fe phase at RT. In Fig. 4.1(right) the most favorable surface orientation for the growth of bcc-Fe on Cu<sub>3</sub>Au(001) is the {100}, where an expansion of the in-plane unit mesh of  $\sim 8.3\%$  with respect to the substrate is expected. On the other hand, bcc-Fe(110) grows on Cu(001) with a  $\sim 3\%$  contraction of the in-plane lattice parameter. In this chapter it will be shown, that there are other important differences between the Fe/Cu(001) and Fe/Cu<sub>3</sub>Au(001) systems. This study will concentrate on the fcc to bcc phase transformation of Fe/Cu<sub>3</sub>Au(001).

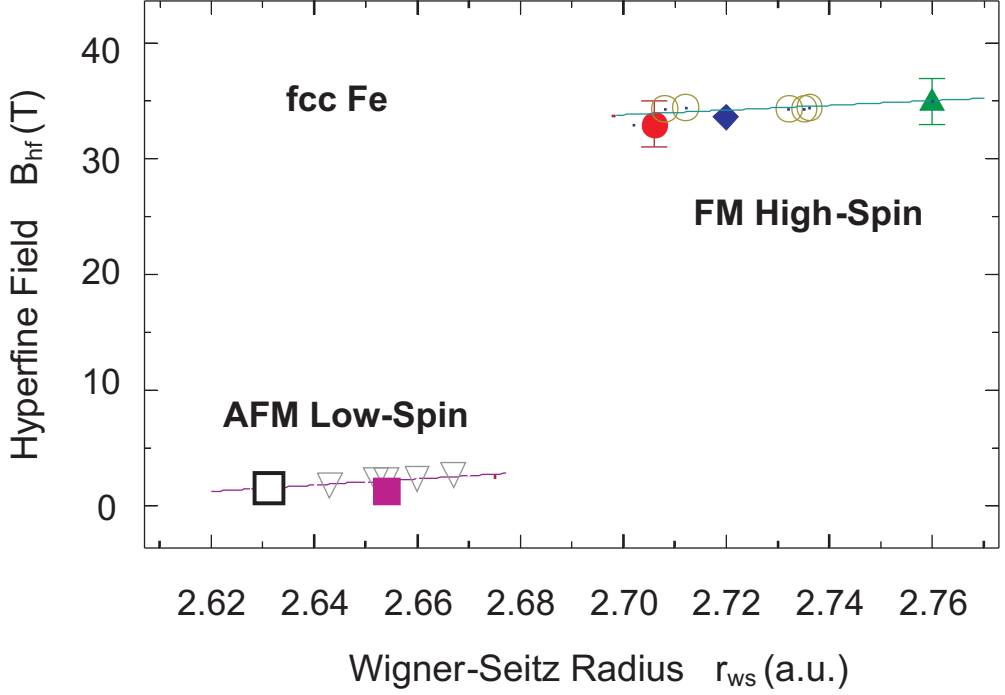


**Figure 4.2:** Hyperfine field near magnetic saturation as a function of the Wigner-Seitz radius,  $r_{ws}$ . Full square: 300-K grown 5-10 ML fcc-Fe/Cu(001) at 35 K. Full circle: 300-K grown and 100-K grown fct-Fe/Cu(001) and 100-K grown 7 ML fct-Fe/Cu(001) at 40-55 K. Full triangle: 300-K grown 5 ML fcc-Fe/Cu<sub>3</sub>Au(001) at 30 K. Open circles: 275-K grown [fcc-Fe/Cu<sub>100-x</sub>Au<sub>x</sub>(001)] multilayers at 15 K. Open triangles: fcc Fe precipitates in Cu<sub>100-x</sub>Al<sub>x</sub> matrix at 4.2 K. Open square: fcc Fe precipitates in Cu<sub>86</sub>Al<sub>14</sub> matrix under high pressure (58 kbar) at 4.2 K. Full diamond: 475-K grown [hcp-Fe/Ru(0001)] multilayer at 4.2 K. (Atomic volume =  $4\pi r_{ws}^3/3$ ; 1 a.u. = 0.529 Å) (figure taken from ref. [39])

The magnetic hf field,  $B_{hf}$ , measured, at low T (near saturation) is roughly proportional to the local Fe atomic moment. Therefore, a measurement of  $B_{hf}$  provides information about possible high or low Fe magnetic moments in Fe films. Fig. 4.2 exhibits a plot of the saturation hf field versus the Wigner-Seitz radius  $r_{ws}$  [59] (in atomic units) for different fcc-like Fe systems [39]. (Note that  $r_{ws}=2.67$  a.u. for Cu at 300 K).  $B_{hf}$  was measured by  $^{57}\text{Fe}$  Mössbauer spectroscopy. Fig. 4.2 demonstrates unambiguously that there is a transition from a low-moment fcc-Fe state to a high-moment fcc-like Fe state. The transition seems to occur around  $r_{ws} \sim 2.69$  a.u., which is in good agreement with theoretical predictions for bulk fcc Fe [36–38].

A word of caution is justified in view of the  $r_{ws}$  values associated with the data points in Fig. 4.2. The only experimentally determined  $r_{ws}$  values are those of 5-10 ML thick low-moment fcc-Fe/Cu(001) ( $r_{ws} = 2.653$  a.u., full square) and 2-4 ML thick high-moment fct-Fe/Cu(001) ( $r_{ws} = 2.705$  a.u., full circle), reported in Refs. [45, 48, 60] on the basis of quantitative LEED results, as well as the value of  $r_{ws} = 2.643$  a.u. (open triangle) reported for AFM low-moment  $\gamma$ -Fe precipitates in a Cu matrix [43]. The other  $r_{ws}$  data in Fig. 4.2 are nominal values that were obtained under the following assumptions: (i) the lattice

parameter of AFM low-moment fcc-Fe precipitates in a  $\text{Cu}_{1-x}\text{Al}_x$  matrix (open triangles) is expanded with increasing  $x$  in proportion to the lattice parameter increase of the matrix [61, 62]; (ii) the FM high-moment fct-Fe films in  $\text{Fe}/\text{Cu}_{1-x}\text{Au}_x(001)$  multilayers (open circles [63]) and on ordered  $\text{Cu}_3\text{Au}(001)$  (full triangle [62]) expand their atomic volume proportional to that of the substrate. As compared to Cu, atomically ordered  $\text{Cu}_3\text{Au}$  has an expanded lattice parameter of 3.75 Å. Whether assumption (ii) is justified will be studied later.

Many of the unique physical and magnetic properties of bulk iron-based alloys are related to the martensitic transformation (MT), i.e. the fcc-bcc phase transformation of iron. This is a first-order *discontinuous* non-diffusive transition that involves a sudden lattice deformation via a correlated motion of groups of atoms, and large lattice strain. The MT has been investigated in bulk iron-base materials for decades [37, 64–66].

More recently, the MT in pure ultrathin epitaxial Fe films on single-crystal  $\text{Cu}(001)$  substrates has become the subject of considerable interest: scanning tunneling microscopy (STM) [67–70] and other techniques [40, 71, 72] including computer simulations [73] revealed a discontinuous transformation from the metastable fcc to the stable bcc phase at a critical film thickness of usually  $\sim 10$  monolayers (ML) Fe upon increasing the thickness. In theoretical work, the energetics of the fcc-bcc MT may be described by a *continuous* transition known as the Bain transformation from fcc to bcc structures [74]. Already in 1924 Bain [74] suggested that an fcc phase can transform spontaneously into a bcc phase by a contraction of the interlayer spacing along the  $c$ -axis and biaxial expansion of the in-plane lattice along  $\langle 110 \rangle$  directions in the fcc(001) plane (see Fig. 4.3).

According to Fig. 4.3, the lattice parameter,  $a_0$ , of the fcc lattice defines the in-plane atomic distance  $a=a_0/\sqrt{2}$  and the lattice parameter  $c=a_0$ , being twice the interlayer distance along the  $c$  axis. The path of tetragonal states with  $\sqrt{2} \geq c/a \geq 1$  between the fcc and bcc phases is called the Bain path. It has been used to calculate the ground-state energetics of the MT [37, 65, 75, 76]. However, one has to keep in mind that this *continuous* Bain path is a convenient theoretical tool only, to the best of my knowledge it has never been observed experimentally.

Searching for a Bain-transformation, pseudomorphic metal films grown on (001) surfaces of fcc substrates are attractive systems [77]. A sharp strain-driven fcc-bcc phase transition of pseudomorphic Cu films on  $\text{Pd}(001)$  with increasing film thickness shows features of a Bain transition [77]. Based on a low energy electron diffraction (LEED) and scanning tunneling microscopy (STM) study, recently M.-T. Lin et al. [50] suggested that the observed structural transformation from fcc(001) to bcc(001) of pseudomorphic Fe films on  $\text{Cu}_3\text{Au}(001)$  is driven by lattice mismatch induced strain through a Bain path; however, a continuous fcc-to-bcc lattice deformation was not reported by these authors [50], and only the initial (fcc(001)-oriented) and final (bcc(001)-oriented) Fe phases of the presumed Bain transition were observed [50].

This work reports on the experimental observation of the continuous fcc-to-bcc Bain transformation in ultrathin epitaxial Fe films on  $\text{Cu}_3\text{Au}(001)$  with increasing Fe coverage, contrary to the usual discontinuous MT of Fe. The out-of-plane interlayer distance ( $c=a_0$ , Fig. 4.3) and the in-plane atomic distance ( $a=a_0/\sqrt{2}$ , Fig. 4.3) of the growing Fe film



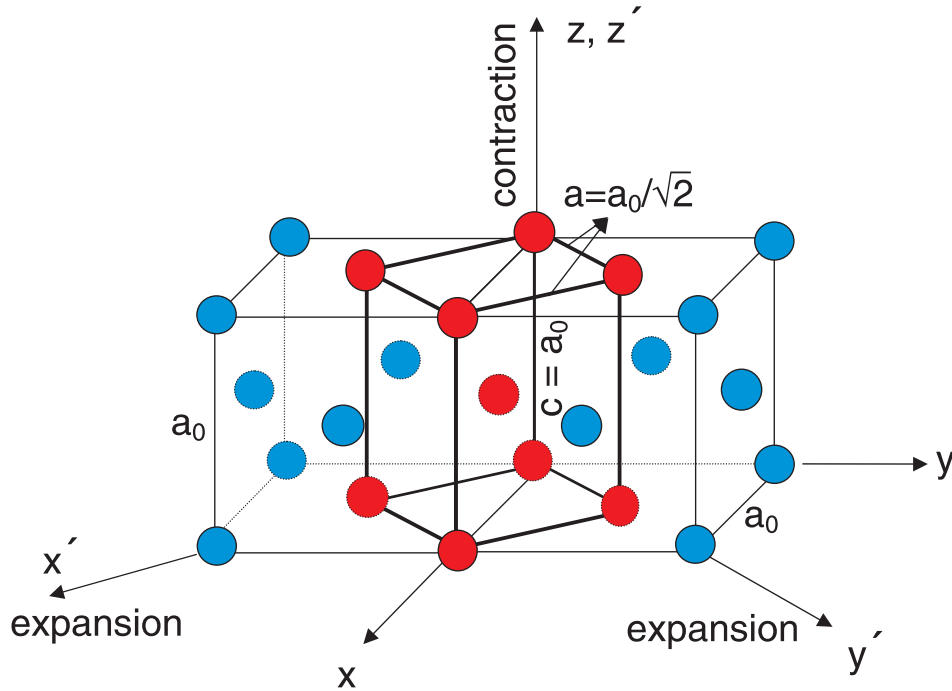


**Figure 4.3:** Lattice distortion during the fcc-bcc transition according to Bain [74].  $a_0$  is the lattice parameter of the fcc unit cell.

were precisely determined by combining X-ray photoelectron diffraction (XPD) [78] and reflection high-energy electron diffraction (RHEED) results. The XPD investigation was performed in the group of Prof. R. Courths (Duisburg).

Lattice parameters  $c$  and  $a$  both were observed to behave monotonically as a function of film thickness from the fct to the bcc region. The atomic volume of tetragonal states that are produced by epitaxial strain was found to follow closely fct (face-centered tetragonal) or bct (body-centered tetragonal) "epitaxial lines" according to strain-energy calculations [79], with a critical value of  $a$  for crossover from the fct to the bct epitaxial line. The fct and bct states were found to be distinguishable by  $^{57}\text{Fe}$  conversion electron Mössbauer spectroscopy (CEMS), and a Fe spin reorientation transition was directly observed by CEMS.

## 4.2 Experimental

The samples were prepared by molecular beam epitaxy (MBE) in an ultrahigh vacuum (UHV) system with a base pressure of  $6 \times 10^{-11}$  mbar. In order to obtain a clean  $\text{Cu}_3\text{Au}(001)$  surface the single crystal surface was mechanically polished first, followed by  $\text{Ar}^+$  sputter cleaning in the UHV system (1 kV,  $5 \times 10^{-5}$  mbar Ar pressure) at  $200^\circ\text{C}$  for 2-3 h, until no impurities could be detected by Auger electron spectroscopy (AES). Subsequent  $\text{Ar}^+$  sputter smoothing of the surface (0.5 kV, and  $5.5 \times 10^{-5}$  mbar Ar pres-

sure) was achieved at 200°C for 40 min. The atomically ordered Cu<sub>3</sub>Au(001) surface was obtained after subsequent sequential annealing at 447°C for 1 h, at 417°C for 1 h, and at 327°C for 15 h, i.e. below the chemical order-disorder transition temperature of 390°C for Cu<sub>3</sub>Au [34]. Several cycles of sputter smoothing and annealing were performed until sharp half-integer streaks of the ordered c(2x2) superstructure appeared in the RHEED pattern (Figs. 4.4(a),(e) and Fig. 4.5), in addition to the fundamental streaks, revealing the well ordered atomically flat Cu<sub>3</sub>Au(001) surface. RHEED was used to select the azimuthal orientation of the Cu<sub>3</sub>Au(001) surface with an accuracy of  $\pm 1^\circ$ . The iron films were deposited from shielded water-cooled Knudsen cells with alumina crucibles. Natural Fe (99.9985 at. % purity) or <sup>57</sup>Fe metal (95.5 % isotopic enrichment) were used as starting materials. The evaporation sources were outgassed and stabilized carefully prior to sample deposition. The film thickness and deposition rate (1.8 Å/min) were measured by quartz-crystal microbalances that were calibrated previously by RHEED intensity oscillations observed during fcc-Fe deposition onto a clean Cu(001) substrate. The film thicknesses are estimated to be accurate within  $\pm 10\%$ . During deposition, the substrate temperature, though nominally RT, increased continuously up to  $\sim 40^\circ\text{C}$  for the thickest films, as measured by the thermocouple of the sample holder.

RHEED patterns were recorded during growth by a CCD camera connected to a computerized data storage and processing system. I/V-curves of the specular (0,0) LEED spot were measured by the same CCD camera/computer data storage system. <sup>57</sup>Fe CEMS spectra were measured in-situ in UHV, with the sample transferred to the UHV cold-finger of a liquid He-cooled flow cryostat. Electrons emitted from the sample surface after the nuclear resonant absorption were detected by a channeltron [80]. A <sup>57</sup>Co-in-Rh Mössbauer source of  $\sim 100$  mCi activity was used. The incoming 14.4 keV  $\gamma$ -ray entered the UHV chamber through a Be window in normal incidence to the film plane.

## 4.3 Results and Discussion

### 4.3.1 RHEED: in-plane atomic spacing

Typical RHEED patterns at various Fe coverages are shown in Fig. 4.4 for the  $[100]_{fcc}$  azimuthal direction (Fig. 4.4(a)-(d)) and  $[110]_{fcc}$  azimuthal direction (Fig. 4.4(e)-(h)) of Cu<sub>3</sub>Au(001). (These directions are also labelled  $[100]_{CA}$  and  $[110]_{CA}$ , respectively).

The half-integer (2x2) superstructure streaks of the ordered flat Cu<sub>3</sub>Au(001) surface (Fig. 4.4(a)) were found to persist for small coverage ( $< \sim 1$  ML), but disappear at larger Fe thicknesses, where only fundamental streaks are observed, as can be seen for 2 and 6 ML in Fig. 4.4(b), (f) and Fig. 4.4(c), (g), respectively. Fig. 4.4 demonstrates that the Fe films up to 6 ML thickness grow epitaxially, presumably with fcc-like structure, and a rather flat surface. Compared with the pattern of the clean substrate, the streaks of the Fe films are broadened, indicating some structural disorder or atomic-scale surface roughness. At 13-14 ML coverage the RHEED pattern changes to a dot-type pattern that is typically observed in 3-dimensional (3D) film growth; this pattern indicates 3D growth of epitaxial (presumably bcc-like) Fe.

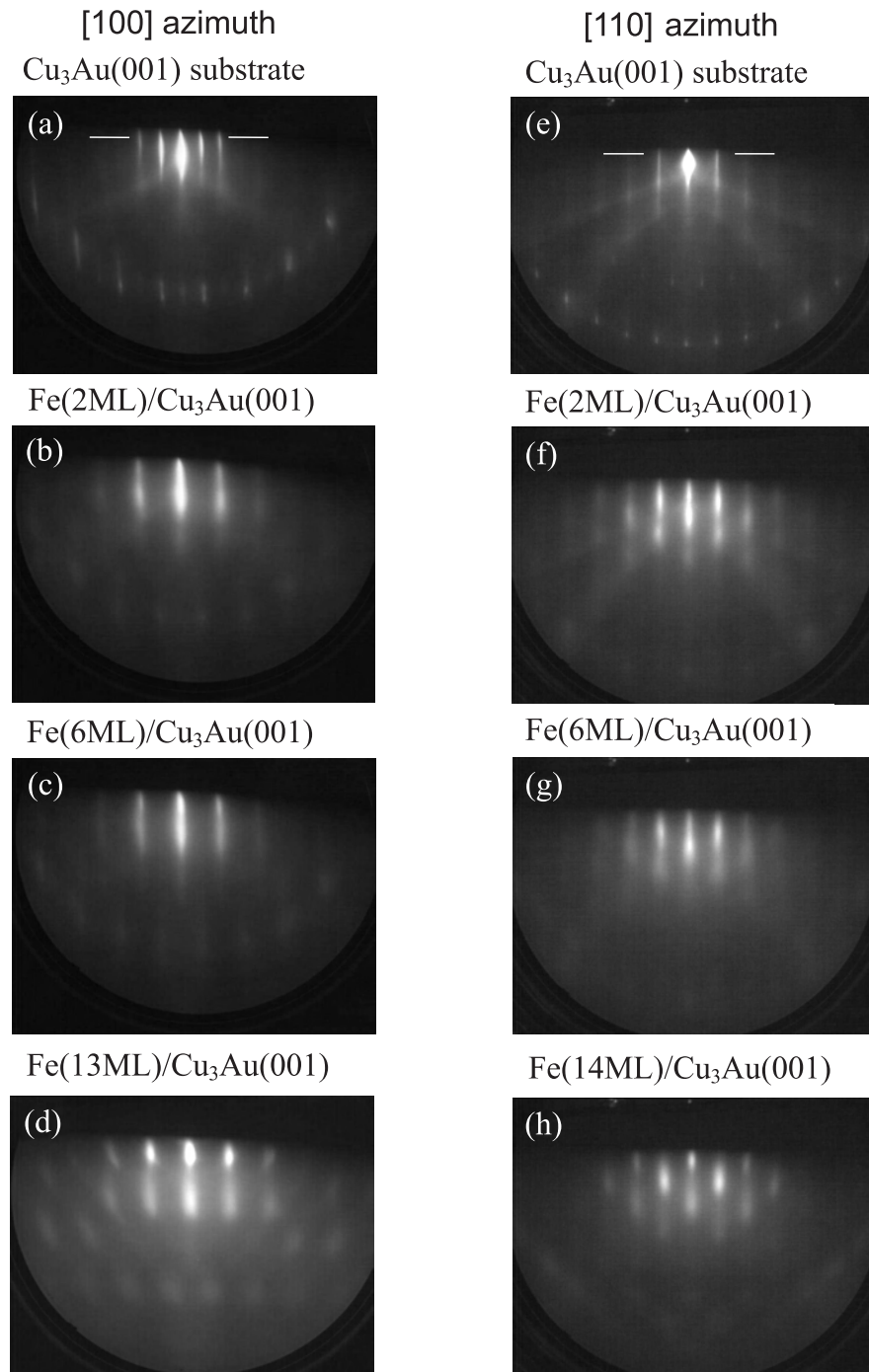


**Figure 4.4:** RHEED patterns along the  $[100]_{fcc}$  azimuth (left) and  $[110]_{fcc}$  azimuth (right) of  $\text{Cu}_3\text{Au}(001)$ : clean atomically ordered  $(2 \times 2)$   $\text{Cu}_3\text{Au}(001)$  surface (a) and (e), covered by 2 ML Fe (b) and (f), 6 ML Fe (c) and (g), and 13 ML Fe (d) and 14 ML Fe (h). (Beam voltage: 12 kV, angle of incidence  $\sim 3^\circ$ ).

The separation of the RHEED streaks in reciprocal space is a measure of the in-plane atomic spacing in real space [81] in a direction perpendicular to the scattering plane. The in-plane atomic spacing of the growing Fe film relative to that of the substrate was determined from the measured distance in reciprocal space between (-1,-1) and (1,1) streaks observed along the  $[100]_{fcc}$  azimuth of  $\text{Cu}_3\text{Au}(001)$ , and between (-1,0) and (1,0) reflections observed along  $[110]_{fcc}$  of  $\text{Cu}_3\text{Au}(001)$ . RHEED intensity profiles were measured along the horizontal direction marked by the white lines in Fig. 4.4(a),(e), for various Fe coverages.

Typical intensity profiles for the  $[100]_{fcc}$  azimuth are shown in Fig.4.5. The (2x2) superstructure peaks of the substrate are observed up to  $\sim 1$  ML coverage, indicating Fe island growth in this thickness regime, in agreement with STM results of [50]. By least-squares fitting the measured intensity profiles with Lorentzian lines (as described in Fig. 4.5) the peak positions of the RHEED reflections (and consequently the in-plane atomic spacing) can be obtained with high precision [49, 81]. The separation of the fundamental peaks of Fe (seen as outer shoulders in the (-1,-1) and (1,1) peaks for small coverages) clearly decreases continuously with increasing Fe film thickness (Fig. 4.5), implying a continuous increase of the atomic distance perpendicular to the scattering plane.

The apparent in-plane atomic distance  $\mathbf{a}$  (relative to that of the substrate) of the planar Fe unit cell as a function of Fe coverage, as deduced from the apparent separation of the fundamental peak positions in reciprocal space, is shown in Fig. 4.6 for the  $[100]_{fcc}$  azimuth (open circles) and for the  $[110]_{fcc}$  azimuth (open squares). It is unexpected that these apparent relative  $\mathbf{a}$  values do not coincide for both azimuthal directions in the coverage regime between  $\sim 1$ -13 ML, but show very different behavior. This demonstrates that the concept of a perfect Fe lattice in complete registry with the underlying substrate lattice (i.e. pseudomorphic growth) must be abandoned. Instead, it is assumed that the Fe films show some degree of atomic disorder and grow in crystallographic domains that are not exactly in registry with the fcc substrate.

In order to deduce the true in-plane atomic spacing of the Fe films, the structural model sketched in Fig. 4.7(a) is proposed, which is based on three assumptions: (i) the planar unit mesh remains a square, (ii) the Fe films grow in the form of crystallographic "twist" domains, and (iii) a certain intrinsic atomic disorder exists in the Fe lattice that leads to a specific lateral broadening of the reciprocal lattice rods. The model is outlined in more details as follows:

Fig. 4.7(a) shows a schematic view of the Fe reciprocal lattice along the surface normal direction (view onto the surface plane). The original square reciprocal lattice of ordered Fe, that is in registry with the underlying  $\text{Cu}_3\text{Au}(001)$ -substrate lattice, is indicated by small black dots (projection of reciprocal lattice rods) forming the full-drawn square. The original separation of the (-1,0) and (1,0) reflections, as observed from the  $[110]_{fcc}$  azimuthal direction, is indicated by heavily dotted horizontal arrows (labelled "original"). Similarly, the original separation of the (-1,-1) and (1,1) reflections, as observed from the  $[100]_{fcc}$  azimuth, is indicated by heavily dotted diagonal arrows (also labelled "original"). Two "twisted" square reciprocal lattices which arise by simple symmetrical rotation of the original reciprocal lattice by a positive and negative "twist angle", respectively, are indi-

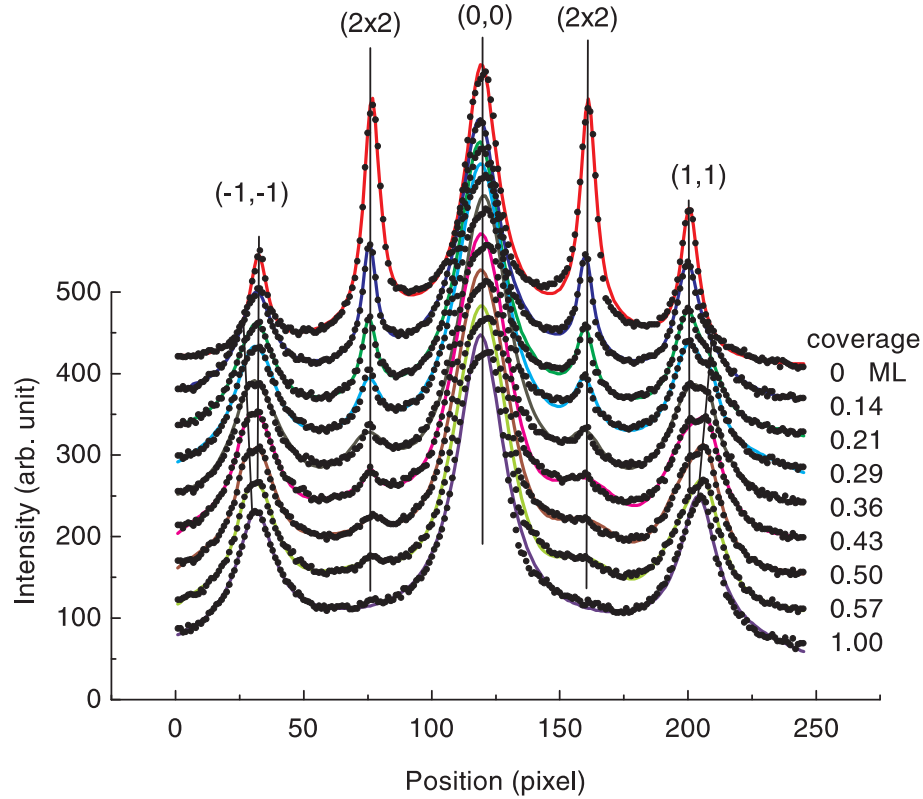


**Figure 4.5:** Typical RHEED intensity profiles along the horizontal direction marked by a white line in Fig. 4.4(a), as a function of Fe film thickness in the low coverage regime. The (2x2) superstructure peaks and the fundamental (1,1) and (-1,-1) peaks of clean  $\text{Cu}_3\text{Au}$  (top) disappear near  $\sim 1.0$  ML Fe (vertical lines). The separation of the (1,1) and (-1,-1) peaks of Fe (evidenced as shoulders for small coverages) is clearly larger than that of  $\text{Cu}_3\text{Au}$  in this coverage regime, but decreases with increasing coverage (tilted straight lines). Data points were least-squares fit with Lorentzian lines and a (weak) smooth background intensity. The fit curves are indicated by solid lines.

cated by the two lightly dotted squares. The reciprocal lattice rods of the twisted lattices are assumed to be laterally elongated in the rotational direction, as shown schematically by the ellipsoidal streaks in Fig. 4.7. Such a special streak shape might be caused by some type of crystallographic disorder, possibly induced by twist and/or tilt boundaries due to a large density of screw dislocations [82]. In STM observations on Fe/ $\text{Cu}_3\text{Au}$ (001) by Lin et al. [50] a network-like surface topography with a lateral period of 3-5 atoms was possibly connected with screw dislocations. The presence of atomic disorder is also evident from the relatively large linewidths observed in the Mössbauer spectra (see section 4.3.2 below). Courths et al. [78] showed that the behavior of the Fe3p forward scattering intensity as a function of Fe film thickness is compatible with our atomic disorder/twisted domain model.

The intersections of these reciprocal lattice rods of elongated cross-section (Fig. 4.7(a)) with the Ewald sphere then result in a slightly larger separation (as compared with that

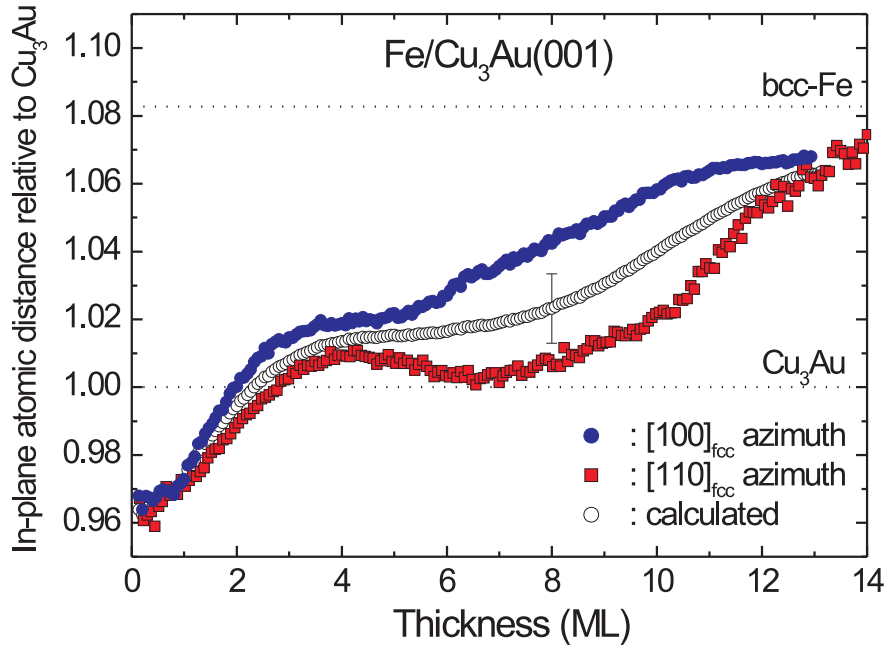


**Figure 4.6:** Fe thickness dependence of the in-plane atomic nearest-neighbor distance,  $a$ , relative to that of  $\text{Cu}_3\text{Au}$ , as obtained from the RHEED streak separation along  $[100]_{fcc}$  (closed circles) and  $[110]_{fcc}$  (closed squares) azimuthal directions. Open circles: calculated values as described in the text and Fig. 4.7.

of the original reciprocal lattice) between the  $(-1,0)$  and  $(1,0)$  reflections (indicated by the horizontal black arrows marked "twist"), when observed along the  $[110]_{fcc}$  azimuth.

The reverse is the case for the  $[100]_{fcc}$  azimuthal direction: here, the apparent separation between the  $(-1,-1)$  and  $(1,1)$  reflections (indicated by the diagonal black arrows marked "twist") is slightly smaller than the corresponding separation in the original reciprocal lattice. Since the spot separation in reciprocal space is inversely proportional to the periodicity in the real lattice, then the model proposed explains the different behavior (Fig. 4.6) of the apparent in-plane atomic separations measured along the  $[110]_{fcc}$  and  $[100]_{fcc}$  azimuthal directions: the apparent in-plane atomic distance determined along the  $[100]_{fcc}$  azimuth is larger than that measured along the  $[110]_{fcc}$  azimuth. This difference appears in that Fe thickness region where the assumed twisted crystallographic domains are present.

The "true" in-plane lattice parameter within a twisted domain of the Fe film has been calculated from the measured data in Fig. 4.6 along the  $[100]_{fcc}$  and  $[110]_{fcc}$  azimuths by applying the described model and assuming the "best" twist angle that yields self-consistency. The Fe thickness dependence of the calculated true in-plane atomic spacing,  $\mathbf{a}$ , and of the corresponding twist angle are shown in Fig. 4.6 (open circles) and Fig. 4.7(b), respectively. Fig. 4.7(b) shows that the twist angle first increases with increasing Fe coverage from near  $0^\circ$  up to about  $10 \pm 3^\circ$  at 8-10 ML Fe, and then decreases to zero again. The deduced in-plane atomic distance,  $\mathbf{a}$ , of Fe (Fig. 4.6, closed circles) exhibits monotonic

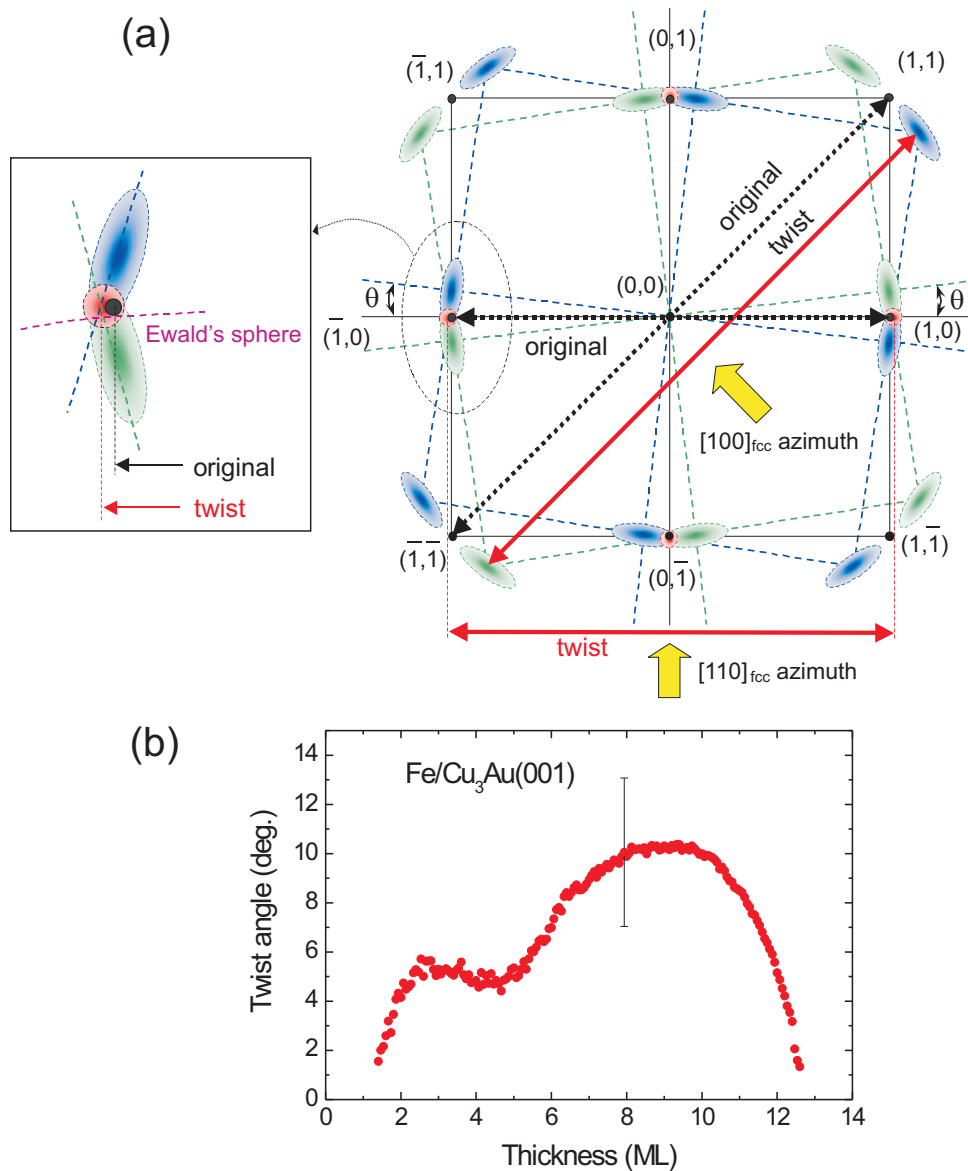


**Figure 4.7:** (a) View along the surface normal direction (onto the surface plane) of the reciprocal lattice of the Fe film (schematic drawing). The original (square) reciprocal lattice is indicated by small black dots (reciprocal lattice rods) forming the full drawn square. Two twisted square reciprocal lattices which are rotated symmetrically relative to the original reciprocal lattice by a positive or negative twist angle, respectively, are indicated by the two dashed squares. The lattice rods of the twisted reciprocal lattices are assumed to be laterally elongated, as indicated schematically by ellipsoidal streaks. When viewed along  $[110]_{fcc}$  or  $[100]_{fcc}$  azimuthal directions, the intersections of these elongated rods with the Ewald sphere (see inset) then lead to slightly different separations of reflections (as indicated by the horizontal and diagonal black arrows labelled "twist") when compared with the corresponding separations in the original reciprocal lattice. (b) Twist angle versus Fe film thickness resulting from the model in (a) and from the measured data in Fig. 4.6, leading to the calculated in-plane atomic distance in Fig. 4.6.

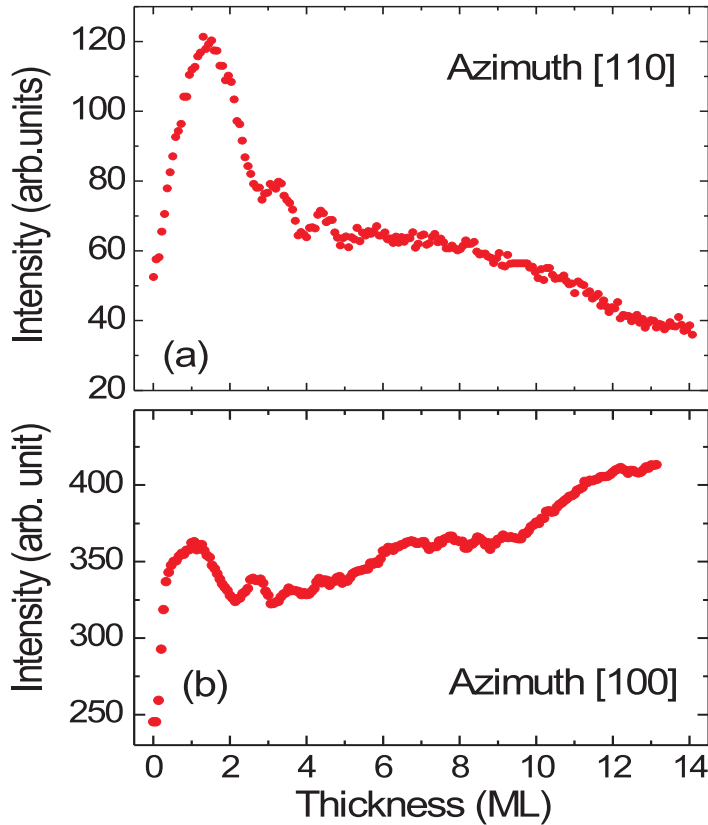


**Figure 4.8:** Specular RHEED intensity oscillations observed during Fe deposition along the (a) [110] and (b) [100] azimuthal directions.

behavior as a function of Fe coverage. Below  $\sim 2$  ML Fe, **a** values are observed to be smaller than that of the  $\text{Cu}_3\text{Au}(001)$  substrate ( $a_0/\sqrt{2} = 2.652 \text{ \AA}$  for  $\text{Cu}_3\text{Au}$ ), possibly due to a surface contraction during island growth, similar to the fcc-Co/Cu(001) and fcc-Fe/Cu(001) systems [49, 81]. Between  $\sim 3.5$ -6.5 ML Fe, the in-plane atomic distance exhibits a plateau-like behavior near  $2.685 \pm 0.006 \text{ \AA}$ , which is slightly larger than that of the substrate ( $2.652 \text{ \AA}$ ), but is considerably smaller than the in-plane atomic distance (lattice parameter) of bcc-Fe(001) ( $a_o = 2.866 \text{ \AA}$ ). This is a hint to Fe growth with distorted fcc structure in this coverage regime. For 13.5 ML Fe an in-plane atomic distance of  $2.819 \pm 0.013 \text{ \AA}$  was determined, which is closer to the lattice parameter of bcc Fe ( $a_o = 2.866 \text{ \AA}$ ), indicating a transition to distorted bcc Fe.

Also measured was the specular RHEED intensity along  $[100]_{fcc}$  and  $[110]_{fcc}$  azimuths during deposition as a function of Fe thickness. The result (Fig. 4.8) is similar to the specular MEED-intensity behavior in Ref. [50], that is characterized by several regions of growth: region A (for island growth between 0-2.5 ML), region B (for layer-by-layer-like growth with large average roughness between 2.5-5.5 ML, including three RHEED oscillations with 1 ML period), and region C (for film morphology with large roughness above 6 ML, characterized by a continuous RHEED intensity change).



### 4.3.2 $^{57}\text{Fe}$ CEMS

Mössbauer spectroscopy provides (via the hyperfine interaction) local (atomistic) information about the magnitude of the Fe atomic moment, the atomic environment and its symmetry around the Fe atom, and about the s-electron density at the  $^{57}\text{Fe}$  nucleus in the sample [83]. It gives also information upon the presence of different magnetic and/or crystallographic phases in the sample. In-situ Mössbauer (CEMS) spectra of 4, 8 and 15 ML Fe on  $\text{Cu}_3\text{Au}(001)$  at 25 K (i.e. near magnetic saturation) are shown in Figs. 4.9(a), (b) and (c), respectively.

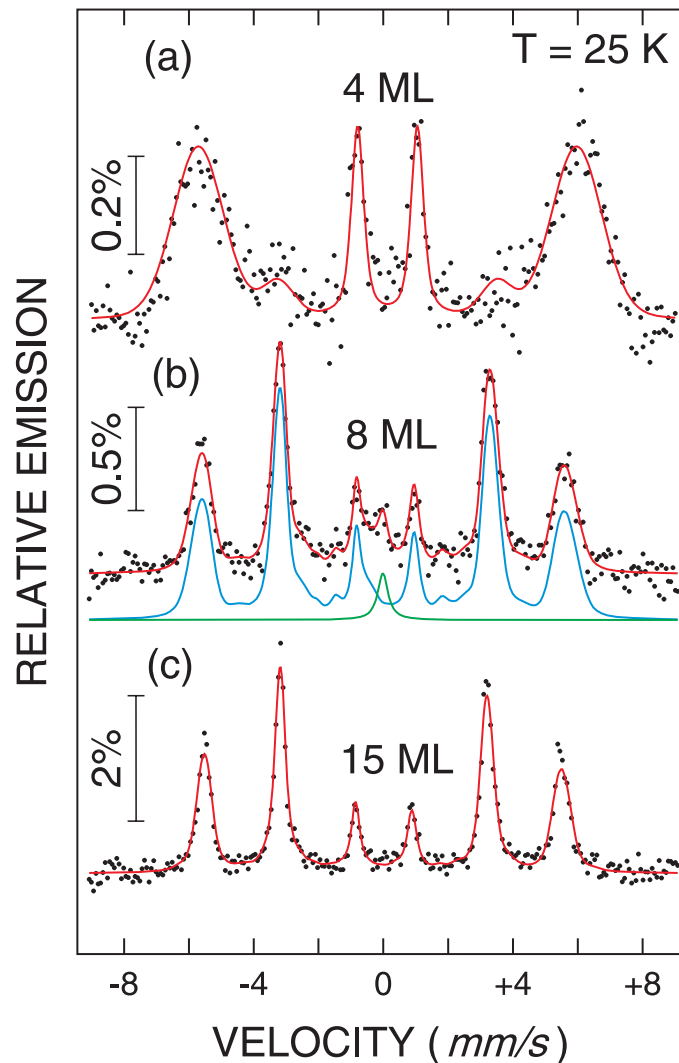


**Figure 4.9:** In-situ Mössbauer spectra (CEMS) of  $\text{Fe}/\text{Cu}_3\text{Au}(001)$  in UHV at 25 K for Fe coverages of 4.0 ML (fcc-Fe) (a), 8.0 ML (bcc-Fe) (b) and 15 ML (bcc Fe) (c). The drawn lines are least-squares fits to the data points.

All spectra exhibit Zeeman sextets with large values of the hyperfine magnetic fields

or, equivalently, with large Fe atomic moments. All films are magnetically ordered at 25 K. Because of the rather large width of the outer lines, the spectra have been least-squares fitted with a distribution of hyperfine fields including a small electric quadrupole interaction. The Mössbauer spectral parameters obtained from the fitting are give in Table 4.1.

	4 ML	8 ML	15 ML
$B_{hf}$ (T)	$36.2 \pm 0.5$	$32.4 \pm 0.4$	$33.1 \pm 0.3$
$\Gamma$ (mm/s)	$1.8 \pm 0.1$	$0.9 \pm 0.1$	$0.6 \pm 0.1$
$\theta$	$25.2^\circ$	$90^\circ$	$90^\circ$
$2\varepsilon$	$+0.07 \pm 0.02$	$-0.06 \pm 0.01$	$-0.022 \pm 0.007$
$\delta$ (mm/s)	$+0.26 \pm 0.08$	$+0.099 \pm 0.002$	$-0.60 \pm 0.09$

**Table 4.1:** Mössbauer spectral parameters at 25 K of 4, 8 and 15 ML Fe on  $\text{Cu}_3\text{Au}(001)$ .  $B_{hf}$  = average hyperfine magnetic field,  $\Gamma$  = apparent width of outer lines (FWHM),  $\theta$  = average angle between  $\gamma$ -ray direction and Fe spin direction,  $2\varepsilon$  = average electric quadrupole interaction,  $\delta$  = average center line shift relative to bulk bcc-Fe at 300 K.

The Mössbauer spectrum of the 15 ML film (Fig. 4.9(c)) and its parameters (Table 4.1) are rather close to bulk bcc Fe (for comparison:  $B_{hf} \simeq 34$  T for bulk bcc Fe at 25 K). This agrees with the RHEED results and XPD results from Courths et al. [78], summarized in Fig. 4.11(a), which show that the lattice parameters  $a$  and  $c$  of 15 ML Fe are those of bcc Fe. Nevertheless, the somewhat larger apparent linewidth ( $\Gamma \sim 0.6$  mm/s) and the small quadrupole interaction ( $2\varepsilon \sim -0.02$  mm/s) are an indication of some residual strain and/or defects in the 15 ML film. (For comparison, measured values for bulk bcc Fe are  $\Gamma \sim 0.3$  mm/s and  $2\varepsilon = 0$  mm/s).

By contrast, the spectrum of 4 ML Fe (Fig. 4.9(a)) and its spectral parameters (Table 4.1) are distinctly different from those of the 15 ML bcc-Fe film (Fig. 4.9(c)) or from bulk bcc Fe. This agrees with the different crystallographic structures of both films. According to Fig. 4.11(a) the 4 ML film has the fct structure (compressed fcc), while the 15 ML film is bcc. Thus, the spectrum in Fig. 4.9(a) is typical for fct Fe. It is characterized by an apparent hyperfine field of  $\sim 36$  T, a very large apparent linewidth (1.8 mm/s), and a relatively large (positive) quadrupole interaction of  $+0.07$  mm/s. A similar line broadening for fct 3 ML-Fe/Cu(001) [40] was ascribed to some kind of structural disorder in the films. This agrees with the present RHEED results and XPD results from Courths et al. [78], which are interpreted in terms of a certain degree of structural atomic disorder and/or defects. Moreover, the (non-cubic) fct structure of 4 ML Fe is reflected in a measured (positive) quadrupole interaction  $2\varepsilon$ , similar to the case of fct 3 ML-Fe/Cu(001) [40, 84].

The 8 ML Fe film has a thickness in the transition region from fct to bcc structure, Fig. 4.11. According to the  $a$  and  $c$  values in Fig. 4.11(a), this film has the bct structure (expanded bcc), resulting in the (negative) quadrupole interaction of  $-0.06$  mm/s (Table 4.1). Its apparent linewidth of 0.9 mm/s is midway between that of 4 ML and 15 ML Fe. The important feature in Fig. 4.9 is that the 8 ML spectrum (Fig. 4.9(b)) is clearly not a superposition of the spectra of fct Fe (Fig. 4.9(a)) and bcc Fe (Fig. 4.9(c)). The spectrum

of 8 ML Fe and its Mössbauer parameters rather appear as part of a continuous evolution from bcc Fe (Fig. 4.9(c)) to fct Fe (Fig. 4.9(a)). Therefore, the coexistence of fct (or fcc) and bct (or bcc) phases in the transition region, i.e. a two-phase structure [50, 56], does not exist in these films.

A striking difference in the spectra of Fig. 4.9 is the drastic reduction of the relative line intensities of lines number 2 and 5 [the ( $\Delta m=0$ )-nuclear transitions] for 4 ML Fe (Fig. 4.9(a)) as compared to those of 8 and 15 ML Fe (Fig. 4.9(b), (c)). This effect is caused by the different spin orientations (given by the angle  $\theta$  between the incident  $\gamma$ -ray direction or film-normal direction and the direction of  $B_{hf}$ , i.e. the spin direction (see chapter 2.2.1)). For the 4 ML film we obtain  $\theta = 25^\circ$  (Table 4.1), indicating a strong (but not complete) perpendicular spin orientation (or perpendicular magnetic anisotropy [36, 55–58]). This result is the direct (atomistic) observation of preferential perpendicular spin orientation in Fe/Cu<sub>3</sub>Au(001). The other two samples (8 and 15 ML Fe) exhibit in-plane spin orientation with  $\theta = 90^\circ$  (Table 4.1). The change in sign of  $2\varepsilon$  is explained by the spin reorientation from nearly perpendicular (at 4 ML) to in-plane orientation (at 8 and 15 ML) [40, 84].

The 6.4 % enhancement relative to that of bulk bcc Fe at 25 K of the measured hyperfine field,  $B_{hf}$ , in 4 ML Fe can be explained by the additional contribution of the perpendicular demagnetizing field,  $B_{dem} \simeq \mu_o M_S \cos \vartheta$ , for the case of nearly perpendicular spin orientation [85]. The intrinsic hyperfine field,  $B_{int}$ , (which is approximately proportional to the local Fe moment) and  $B_{dem}$  both are antiparallel to the perpendicular magnetization direction. (For in-plane magnetization,  $B_{dem} = 0$  and  $B_{hf} \approx B_{int}$ , as for 8 and 15 ML Fe). According to eq. (2.3) one can calculate for 4 ML Fe  $B_{int} \approx B_{hf} - B_{dem} \simeq 34.4$  T, taking  $\theta = 25.2^\circ$  and assuming that fct and bcc Fe have about the same saturation magnetization  $\mu_o M_S$  of about 2T. As compared to bulk bcc-Fe ( $B_{int}=34.0$  T) the enhancement of the intrinsic hyperfine field is negligible, contrary to the case of fcc-like Fe on Pd(110) (see chapter 3).

Since within error bars the value of  $B_{int}=34.4$  T is equal to that of bulk bcc Fe and is close to that of 8 and 15 ML Fe (Table 4.1), one may conclude that the atomic moment of the FM fct high-spin phase is about equal to that of bulk bcc Fe. However there is a small enhancement of about  $2.0 \pm 0.9$  T in the intrinsic hyperfine field,  $B_{int}$ , of 4 ML (fct) as compared to  $B_{hf}$  of 8 ML (bct) Fe (see table 4.1) which cannot be attributed to the demagnetizing field, but might be related to a small moment enhancement in 4 ML Fe as compared with 8 ML Fe.

The average center line shift  $\delta$  at 25 K given in Table 4.1 includes the chemical shift (isomer shift) and the second-order (thermal) Doppler shift. Assuming thickness-independent Debye temperatures, the changes in  $\delta$  values with film thickness at 25 K then are variations of the isomer shift. Obviously the isomer shift becomes continuously more positive with decreasing Fe thickness, i.e. in going from the bcc (at 15 ML) to the fct (at 4 ML) structure. This means that the s-electron density at the <sup>57</sup>Fe nucleus is continuously reduced in going from the bcc (via the bct) to the fct structure, as expected for a simultaneous increase of the atomic volume, e.g. in the Fe/Cu(001) system [40, 84].

In the case of 8 ML Fe, an additional weak single line (in Fig. 4.9(b)) with a center line shift at 25 K of  $+ 0.091 \pm 0.042$  mm/s (relative to bulk bcc Fe at RT) and  $\Gamma =$

$0.38 \pm 0.14$  mm/s had to be taken into account, contributing 3.8 % to the total intensity (spectral area). This single line might be caused by a small fraction of low-moment Fe or, more likely, by a small fraction of rapidly relaxing (superparamagnetic-like) bct Fe islands in the film. It should be mentioned that the RT Mössbauer spectrum of the 4 ML film was rather smeared out and exhibited extremely broad lines, typical for thermally fluctuating Fe moments with relaxation times of the order of the Mössbauer life time of  $\sim 10^{-7}$  s. A single line has been observed earlier in the Fe/Cu<sub>3</sub>Au(001) system [52].

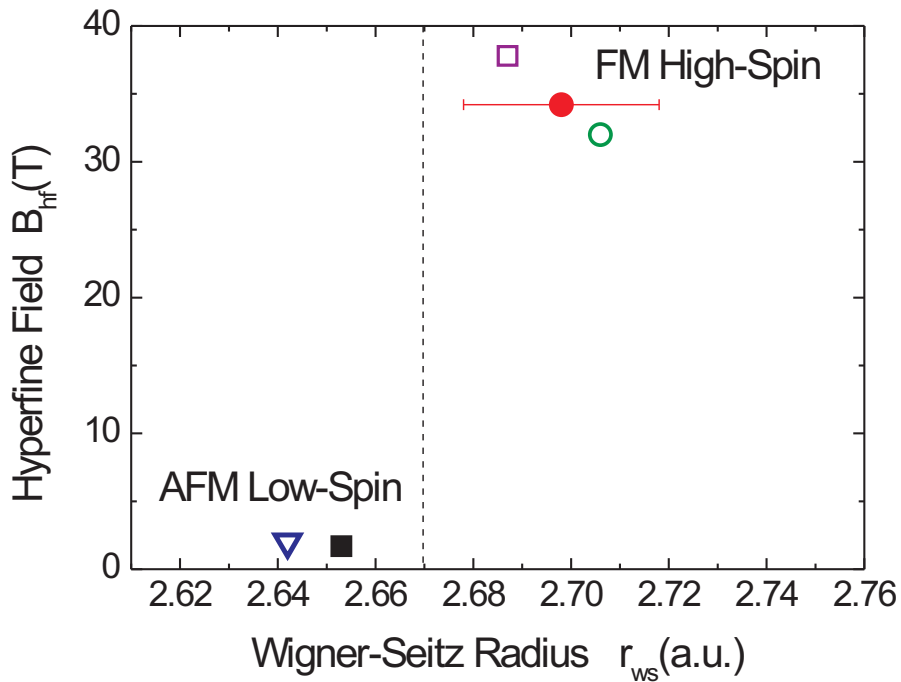


**Figure 4.10:** Hyperfine field near magnetic saturation as a function of the measured Wigner-Seitz radius,  $r_{ws}$ , for fcc-like Fe systems. Open triangle: AFM Fe precipitates in Cu matrix at 4.2 K [39]. Full square: 300-K grown AFM 5-10 ML fcc-Fe/Cu(001) at 35 K [39]. Open circle: 300-K grown FM fct-Fe/Cu(001) at 40 - 55 K [39]. Full circle: 313-K grown FM 4.0 ML fct-Fe/Cu<sub>3</sub>Au(001) at 25 K (present work). Open square: 300-K grown FM [fct-Fe(15 Å)/Pd(40 Å)]<sub>30</sub> multilayer at  $\sim 5$  K [34]. (The temperatures stated are the measurement temperature for the hyperfine field. For full square and open circle:  $r_{ws}$  was calculated by using the out-of-plane lattice parameter from LEED [48,60] and the in-plane lattice spacing from RHEED [49]. The dashed line represents the Wigner-Seitz radius predicted by theory for the AFM low-spin to FM high-spin transition [38].

Fig. 4.10 exhibits the correlation of the hyperfine field,  $B_{hf}$ , measured at low temperature (near the magnetic saturation) and the measured Wigner-Seitz radius,  $r_{ws}$ , for fcc-like Fe systems including the case of Fe/Cu<sub>3</sub>Au(001) investigated in the present work. The  $r_{ws}$  values have been calculated as a function of the atomic volume [59], i.e., as a

function of the lattice parameters  $c$  and  $a$ , as determined by XPD [78] and RHEED (present work). Comparison with Fig. 4.2 shows that a plot of  $B_{hf}$  versus the nominal  $r_{ws}$  values of the substrate as displayed in Fig. 4.2 is by no means justified for fcc-like Fe films, because in reality the films are tetragonally distorted in a way that depends on the specific substrate used (Cu, Cu<sub>3</sub>Au, or Pd), and because the in-plane atomic distance differs from that of the substrate. The highest  $r_{ws}$  value is achieved in ferromagnetic expanded fcc (fct-) Fe films on Cu(001) [39] (open circle), followed (in descending order) by the compressed fct-Fe film (4 ML) on Cu<sub>3</sub>Au(001) (closed circle), and by the compressed fct-Fe films in Fe/Pd multilayers (open square) [34]. This group of data points exhibits hyperfine fields between 32-38 T, indicating the high-spin state. It is important to note that the Wigner-Seitz radius obtained for 4 ML Fe/Cu<sub>3</sub>Au(001) is closer than that of fct-Fe/Cu(001) than to that of bulk bcc Fe ( $r_{ws} \simeq 2.667$  a.u.). The bcc structure for this film can definitively be excluded, since the Mössbauer spectrum shown in Fig. 4.9(a) has a shape and spectral parameters that are incompatible with bulk bcc Fe.

The data points for AFM low-spin Fe in Fig. 4.10 are located at lower  $r_{ws}$  values than those of FM high-spin Fe. Fig. 4.10 shows that the AFM low-spin to FM high-spin transition in fcc-like Fe occurs near  $r_{ws} \sim 2.67$  a.u., in agreement with theoretical predictions of Herper et al. [38].

## 4.4 Atomic volume and epitaxial lines

The combination of the present RHEED data and XPD results from Courths et al [78], i.e. the film-thickness dependence of the in-plane atomic distance,  $a$ , and of the perpendicular lattice parameter,  $c$ , is shown in Fig. 4.11(a). With increasing Fe coverage the  $c$  parameter is continuously and about linearly compressed, while simultaneously the  $a$  parameter is continuously expanded. This means the observation of a continuous Bain transformation from fcc to bcc structure in our films. One should emphasize that there is a thickness region between  $\sim 3.5$ - $6.5$  ML Fe, where the in-plane distance,  $a$ , shows plateau-like behavior and remains nearly constant at  $\sim 2.68$  Å, which is close to the in-plane atomic distance (2.652 Å) of the Cu<sub>3</sub>Au(001) substrate. In this region the in-plane lattice parameter of the growing film appears to be clamped by epitaxial interaction with the substrate surface. Epitaxy produces large strains in the overlayer, in this case tensile in-plane strain and compressive out-of-plane strain, leading to tetragonal states with different atomic volumes. Marcus and Jona [79] have calculated "epitaxial lines" for tetragonal structural strained fcc and bcc Fe under the assumption that the Poisson ratios and elastic moduli of fcc and bcc Fe films remain constant during the deformation, and that they can be described by bulk elastic constants. The epitaxial line that relates the Fe atomic volume,  $V=ca^2/2$ , of a tetragonal state to its in-plane atomic spacing,  $a$ , is obtained by integration of eq.(6) in Ref. [79] as:

$$V = V_o(a/a_o)^{2-\gamma} \quad (4.1)$$

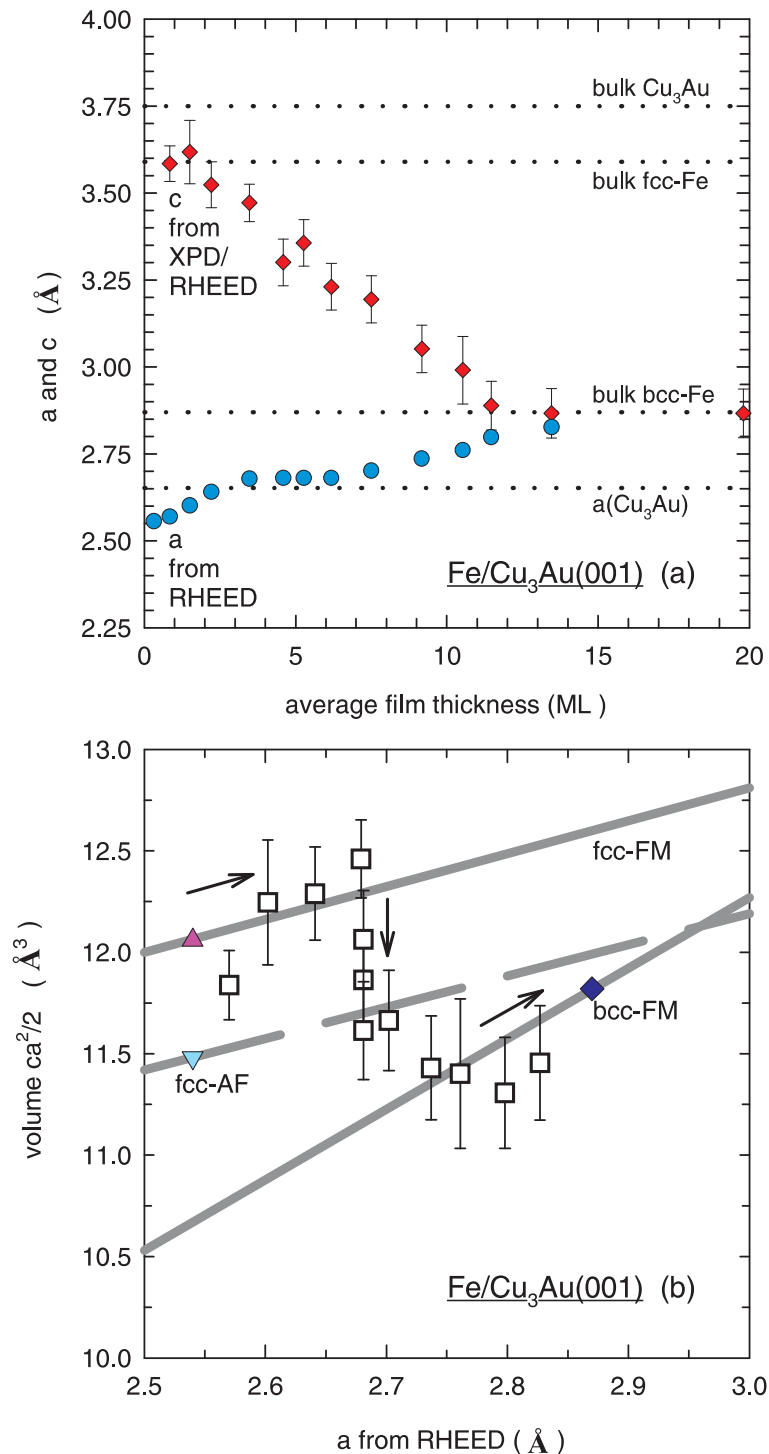


**Figure 4.11:** (a) In-plane lattice spacing  $a$  from RHEED and perpendicular lattice parameter  $c$  from combining XPD (see Ref. [78]) and RHEED (Fig. 4.6) data, as function of Fe film thickness.  $c$  is only given for those film thicknesses where XPD measurements have been performed. For the definition of  $c$  and  $a$ , see Fig. 4.3 and Fig. 4.7. (b) Fe atomic volume  $V$  versus in-plane atomic distance  $a$  (open squares). Also given are volumes  $V_o$  of ferromagnetic high-moment high-volume fct-Fe/Cu(001) ( $12.06 \text{ \AA}^3$ ) and of antiferromagnetic low-moment low-volume fcc-Fe/Cu(001) ( $11.48 \text{ \AA}^3$ ) according to Ref. [45, 49], and  $V_o$  for bulk bcc-Fe ( $11.8 \text{ \AA}^3$ ). Full straight lines: Theory according to Ref. [79]. The step-like change of  $V$  at  $a = 2.68 \text{ \AA}$  is caused by the change in  $c$  at nearly constant  $a$  in the film thickness range between about 3.5 - 6.5 ML Fe (see Fig. 4.6, open circles).

where  $\gamma = 2\nu/(1-\nu)$  and the Poisson ratio  $\nu = c_{12}/(c_{11}+c_{12})$ , with elastic constants  $c_{11}$  and  $c_{12}$ .  $V_o$  is the atomic volume of the unstrained, equilibrium film structure (fcc or bcc). In Fig. 4.11(b) the epitaxial line for the different states of iron are shown. For the calculation a value  $\gamma_{fcc} = 1.64$  and  $\gamma_{bcc} = 1.16$  was used [58], and  $V_o = 11.8 \text{ \AA}^3$  was taken for bcc Fe. Fe(fcc) appears in two different equilibrium states which are epitaxially stabilized in the Fe/Cu(001) system: a ferromagnetic (FM) high-volume state with  $V_o = 12.06 \text{ \AA}^3$ , and an antiferromagnetic (AF) low-volume state with  $V_o = 11.48 \text{ \AA}^3$  (both values according to Ref. [45] and corrected for in-plane spacing in Ref. [49]). The experimental  $V$  values, obtained from the data in Fig. 4.11(a), are also shown in Fig. 4.11(b) (open squares). For small Fe thicknesses ( $t \lesssim 3.5 \text{ ML}$ ) and  $\mathbf{a} \lesssim 2.68 \text{ \AA}$ , the experimental data are closest to the epitaxial line of FM high-volume fcc Fe (fcc-FM), and, consequently, the structure of these films is fct. For the thickest films in the region  $9 \text{ ML} \lesssim t \lesssim 13.5 \text{ ML}$  and  $\mathbf{a} \gtrsim 2.74 \text{ \AA}$  the experimental values are closest to the epitaxial line of bcc Fe (bcc-Fe); therefore, their structure is bct, in agreement with results by Schirmer et al. [58]. For the medium thickness region  $3.5 \text{ ML} \lesssim t \lesssim 7.5 \text{ ML}$ , which contains the plateau in the  $\mathbf{a}$  values at  $2.68 \text{ \AA}$  (Fig. 4.11(a)), a step-like drop from fct states to bct states is observed by increasing the film thickness. This crossover between tetragonal states seems to resemble a first-order phase transition.

Indeed, Krasko and Olson [37] have calculated the ground-state enthalpy curve along the Bain deformation path of iron and predicted a first order phase transition between ferromagnetic (FM) bcc-like states and fcc-like states (the latter being non-magnetic, however, and not FM like in the present case), accompanied by a volume discontinuity at a critical ratio  $c/a=1.23$ . According to Fig.8 in Ref. [78] (bottom panel) this critical ratio corresponds to a film thickness of 6 ML Fe with an in-plane atomic distance of  $2.68 \text{ \AA}$ , which is the  $\mathbf{a}$  value observed in the volume discontinuity of Fig. 4.11(b). However, the latter is probably not related to a first order transition, since the  $c$ -parameter behaves continuously in that region (Fig. 4.11(a)), with the  $\mathbf{a}$  values remaining about constant. Moreover, a fct and bct two-phase mixture was not observed, such as in a nucleation and growth process of a first-order (martensitic) transition. Therefore, the results (Fig. 4.11(a)) demonstrate that a continuous Bain transformation takes place in Fe/Cu<sub>3</sub>Au(001), contrary to the Fe/Cu(001) system, where a martensitic transition was observed [67–70]. According to Fig. 4.11(b) and to the Mössbauer results (chapter 4.3.2) this transition takes place from ferromagnetic high-moment high-volume fct Fe to ferromagnetic bcc Fe, whereby the atomic volume decreases. By contrast, the usual martensitic transformation involves a transition from a non-magnetic fcc to a ferromagnetic bct (or bcc) state, whereby the atomic volume increases [64, 66]. It is the magneto-volume effect in fct Fe that causes this different behavior.

Fig. 4.12 displays the present experimental Fe-atomic volume values (full squares) plotted as function of the lattice parameters ratio  $c/a$ , together with ab-initio calculations of the total energy of iron as a function of  $c/a$  and volume within the generalized gradient approximation (GGA) taken from Friak et al. [86]. All volumes are normalized to the FM bcc-Fe equilibrium state ( $V_{exp}=11.72 \text{ \AA}^3$ ) as employed by Friak et al. in Ref. [86] (Fig.3(a)). In this picture, only states with minimum energy are plotted.

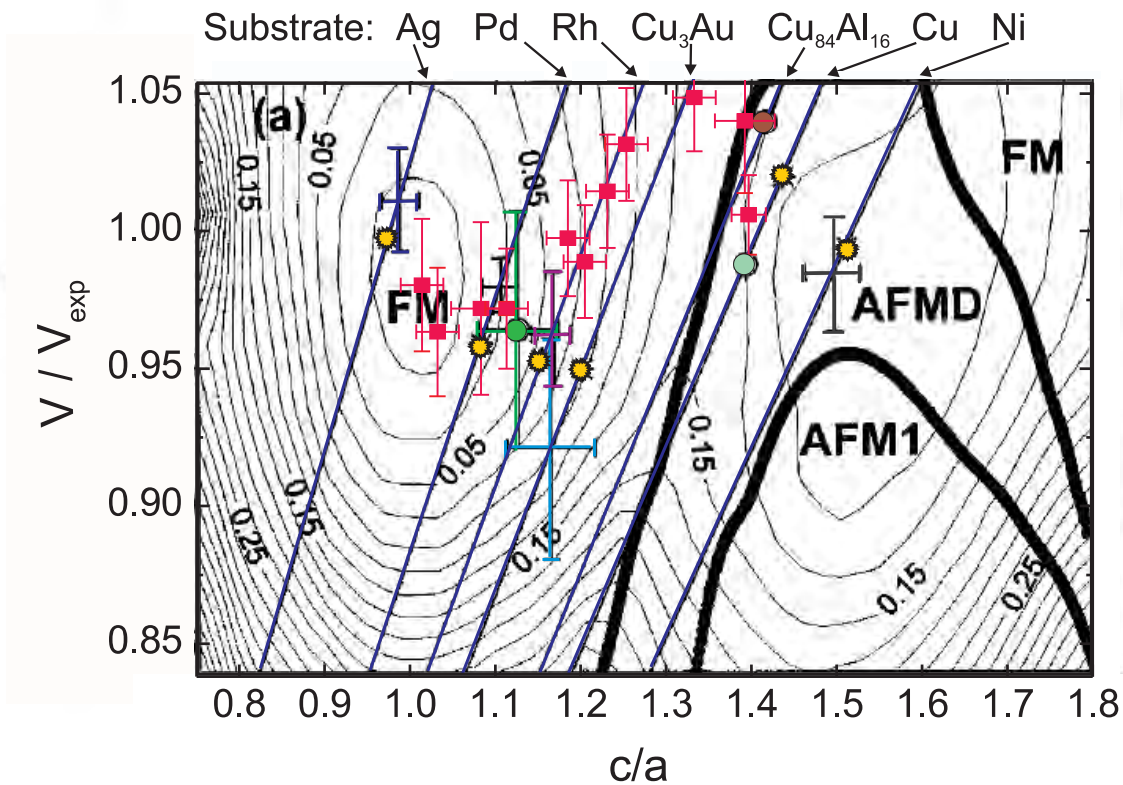


**Figure 4.12:** Relative Fe atomic volume  $V$ , (full squares) versus the lattice parameter ratio  $c/a$ , experimentally obtained combining present RHEED results and XPD results (Courths et al. [78]). Also plotted are results from ab-initio calculations of the total energy of iron as a function of  $c/a$  (along the Bain-path) and of the atomic volume within the GGA (generalized gradient) approximation performed by Friak et al. [86]. The experimental atomic volume of FM bcc Fe ( $V_{exp}=11.72 \text{ \AA}^3$ ) was used for normalization. Only states with minimum energy are shown. Thick black lines show the FM/AFMD and AFMD/AFM1 phase boundaries. The dark blue straight lines correspond to constant lateral lattice parameters of various (001) substrates. The crosses composed by the vertical and horizontal error bars centered at the straight lines, represent structures of Fe films on the corresponding substrates found experimentally. The green circle, shifted from the straight line, stands for Fe/Cu<sub>3</sub>Au [58]. The other two circles show experimental structures where no error bars were given. Yellow asterisks represent the theoretical results found by Friak et al. [86].

Thick black lines show the FM/AFMD (ferrromagnetic/double-layer antiferromagnetic) and AFMD/AFM1 (double-layer antiferromagnetic/single-layer antiferromagnetic) phase boundaries. The included straight lines correspond to constant lateral lattice parameters of various (001) substrates, assuming that the pseudomorphic Fe overlayers adopt the lateral lattice dimensions of the substrate in the (001) plane and relax only the interlayer distance (characterized by  $c/a$ ). The large crosses composed of the vertical and horizontal error bars centered at those straight lines and the full circles represent experimental data of Fe films on the corresponding substrates reported in the literature. Yellow asterisks



represent theoretical results by Friak et al. [86].

The theoretical calculations for the Fe/Cu<sub>3</sub>Au(001) case are within error bars in accordance with the experimental Fe-atomic volume obtained by Feldmann et al. [57] (light blue cross) that lies on the straight line for the Cu<sub>3</sub>Au substrate. However, the atomic volume determined by Schirmer et al. (green circle) [58] is shifted from the Cu<sub>3</sub>Au line, but can be found in the FM area of the plot. Almost all experimental volumes of the present thesis (full squares) can be also found in the ferromagnetic region predicted in the calculations [86], although the two volumes corresponding to  $1.39 \leq c/a \leq 1.40$  are close to the calculated FM/AFMD phase boundary. One can notice that most of the present experimental values (full squares) do not follow the calculated straight line behavior for the Cu<sub>3</sub>Au substrate.

## 4.5 Conclusions

The structure of epitaxial Fe films on Cu<sub>3</sub>Au(001) was precisely determined by the present RHEED measurements and XPD results by Courths et al. [78]. With increasing film thickness a nearly linear continuous compression of the perpendicular lattice parameter,  $c$ , and a simultaneous continuous expansion of the in-plane atomic distance,  $\mathbf{a}$ , was observed. Films with thicknesses between  $\sim 1$ -12 ML do not grow pseudomorphous, but appear to form twisted crystallographic domains including some kind of atomic disorder. Apparently, the strain energy induced by the compressed perpendicular interlayer spacing is lowered by rotating the planar Fe unit mesh array from the surface mesh of the substrate. Films thinner than  $\sim 2$  ML are fct and show reduced in-plane spacings as compared to the substrate surface due to island growth and lattice relaxation. Up to  $\sim 3.5$  ML the film structure is fct. There is an intermediate region between  $\sim 3.5$  ML - 6.5 ML, where the in-plane atomic spacing of  $\sim 2.68$  Å remains nearly independent of thickness, while the perpendicular spacing  $c$  changes continuously. Above 6.5 ML thickness the films have bct structure, and  $\mathbf{a}$  as well as  $c$  approach bulk bcc-Fe values at  $\sim 13.5$  ML. The observed continuous compression of  $c$  and the simultaneous continuous expansion of  $\mathbf{a}$  implies that a continuous fcc-bcc Bain transformation takes place in the Fe/Cu<sub>3</sub>Au(001) system with increasing film thickness, contrary to the Fe/Cu(001) system, where a discontinuous martensitic transformation is known to exist. One can speculate that Au atoms observed to be present at the Fe film surface in the case of Fe/Cu<sub>3</sub>Au(001) [78] act as surfactants and prevent the martensitic transformation. The atomic volume of the tetragonal states was found to be close to fct or bct epitaxial lines [79]. A crossover from ferromagnetic high-moment high-volume fct to bct Fe was found to occur in the intermediate thickness range between  $\sim 3.5$  ML - 6.5 ML where the in-plane atomic distance  $\mathbf{a}$  is nearly constant. Conversion electron Mössbauer spectroscopy (CEMS) was used to prove that a fct-plus-bct two-phase structure does not exist. Fct-Fe films are in a high moment FM state. The Mössbauer results also prove that the structural changes observed by RHEED and XPD (which are surface sensitive techniques) do not occur only in the surface region, but seize the film as a whole.

Correlated with the Bain transformation is a spin-reorientation from preferentially perpendicular (for fct structure) to in-plane (for bct structure) spin direction at 25 K.

## 5 Epitaxial growth of Fe on GaAs(001) and GaAs(001)-HEMT

### 5.1 Introduction

Fe on GaAs is one of the most investigated epitaxial ferromagnetic metal/semiconductor systems due to the increasing interest in integrating magnetic thin films with semiconductor heterostructures for the realization of spin-sensitive devices [87]. The storage and transport of electronic spin, "spintronics", may revolutionize the electronic device industry, with spin based transistors, opto-electronic devices and memory. Although efficient room temperature electrical spin injection in metals has been commercially employed into today's magnetic read heads through giant magnetoresistance, electrical spin injection from ferromagnetic metal electrodes into semiconductors has not been convincingly demonstrated and is a challenging task.

GaAs is an ideal substrate for the epitaxial growth of Fe in the stable bcc phase, since the bulk lattice parameter of Fe is approximately half of that of the zinc-blende-type GaAs ( $2a_{Fe}/a_{GaAs}=1.012$ ). The achievement of single-crystal epitaxy is important, since for many applications one needs to exploit the magnetic anisotropy of the material and, therefore, amorphous, polycrystalline, or even oriented polycrystalline films are not acceptable.

Epitaxial growth of Fe on GaAs(001) and GaAs(110) substrates by molecular beam epitaxy (MBE) has been widely reported in the literature [88–101], together with detailed investigations on the magnetic properties, e.g., the evolution of the ferromagnetic order, the relationship between uniaxial and cubic magnetic anisotropy as a function of layer thickness, as well as magnetic reversal processes [92–94]. These properties have been related to the interfacial compound formation and the atomic scale nucleation processes for various Ga- and As- terminated GaAs(100) substrate surface reconstructions [95–97].

Recently, Schönherr et al. [99] studied the growth of Fe on the (100),(311)A, and (331)A GaAs surfaces and its dependence on the growth temperature and termination of the GaAs surface, in an attempt to obtain macroscopically smooth Fe layers. They found by atomic force microscopy (AFM) that very smooth Fe layers, free from macroscopic defects, were formed on GaAs(100) with As-rich surface reconstructions at a growth temperature of 50°C, and that less As-rich surfaces produced macroscopic defects, whose density increased with more Ga-rich surfaces. At higher and lower growth temperatures, the Fe layer roughened and consisted of  $\mu\text{m}$ -sized islands for 175°C growth. They observed a similar island morphology on GaAs(311)A and GaAs(331)A substrates at 50°C, while smooth layers were obtained at 0°C. Again As-rich surfaces favored the formation of smooth Fe layers.

The successful growth of very smooth epitaxial Fe layers is of high relevance for their posterior lithographic patterning and integration in semiconductor nanostructured devices. The use of As-rich GaAs reconstructions has been shown to reduce the density of defects in the Fe layers [99], nevertheless, it is also well known, that non-ferromagnetic Fe-As

compounds will form at the As-rich Fe/GaAs interface, producing interfacial "magnetic dead layers" [100], or  $\text{Fe}_3\text{Ga}_{2-x}\text{As}_x$  interlayers with only about half of the magnetization of bulk bcc-Fe [91, 100] due to interdiffusion of As into the Fe overlayer. From such an interface, the injection of highly spin-polarized electrons into the semiconductor will become unlikely, since a high spin polarization and large ferromagnetically ordered moments even in the first metallic monolayers at the interface are a necessary condition. By an appropriate pretreatment, the GaAs(001) surface should be sufficiently depleted of As to avoid the formation of Fe/As compounds [100]. Also the growth of the Fe layers should be done at sufficiently low temperature to minimize intermixing.

The aim of the present work is to prevent the formation of these interfacial non-magnetic layers at the Fe/GaAs(001)(4x6) and Fe/GaAs(001)-HEMT structure (HEMT=high electron mobility transport) by means of an appropriate selection of the growth parameters.

## 5.2 Experimental procedure

An UHV system (base pressure  $\leq 6 \times 10^{-11}$  mbar) equipped with LEED, RHEED and in-situ conversion electron Mössbauer spectroscopy (CEMS) was used for the MBE growth of Fe films on GaAs(001) and GaAs(001)-HEMT substrates. The subsequent ex-situ magnetic characterization of the Fe/GaAs interfaces was done by CEMS. The HEMT substrates used were prepared and provided the group of Prof. A. Wieck and Dr. D. Reuter (Ruhr-Universität Bochum), and were designed to allow the formation of a 2D electron gas that should facilitate the spin-dependent transport. The layered structure of the GaAs(001)-HEMT substrates is schematically displayed in Fig. 5.1.

All substrates were cleaned just before being loaded into the chamber with 2-propanol. Auger electron spectra of the GaAs(001) and GaAs(001)-HEMT surfaces prior to the in-situ cleaning showed considerable C and O contamination. The substrates were cleaned by sputtering with Argon ion bombardment (0.5 keV) at a current density of  $1 \mu\text{A}/\text{cm}^2$  ( $P=5.5 \times 10^{-5}$  mbar) at a temperature of  $450^\circ\text{C}$  for 15 minutes followed by final annealing at  $500^\circ\text{C}$  for about 12 hours. After this treatment, no surface impurities were detected by AES, and spectra typical of a Ga-enriched GaAs surface were observed. LEED (Fig. 5.2(a)) and RHEED (Fig. 5.3(a),(b)) images of the clean substrate revealed a flat surface, with a pseudo-(4x6) reconstruction, characteristic of a Ga-terminated GaAs(001) surface [98]. Recent studies performed in our laboratory by M. Doi demonstrate that sputtering (0.5 keV) of the GaAs substrates at a temperature of  $600^\circ\text{C}$  during 30 minutes leads to sharper (4x6) reconstructions for the GaAs(001) surfaces (Fig. 5.2(b) and Fig.5.3).

It must be emphasized, however, that the high-temperature annealing at  $600^\circ\text{C}$ , although optimal for achieving flat and well ordered GaAs(001) surfaces, destroys the 2D electron gas in the HEMT structure, while the lower temperature annealing at  $500^\circ\text{C}$  retains the property of the 2D electron gas. This was demonstrated via Shubnikov-DeHaas measurements on these samples by the group of Prof. A. Wieck and Dr. D. Reuter (Ruhr Universität Bochum).

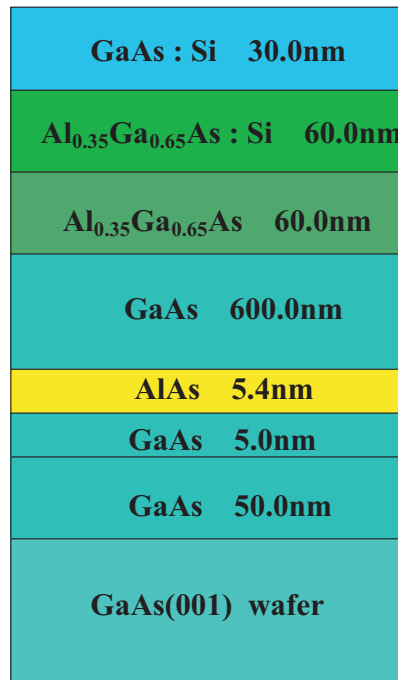


**Figure 5.1:** Schematics of the layered structure of the GaAs(001)-HEMT substrates.

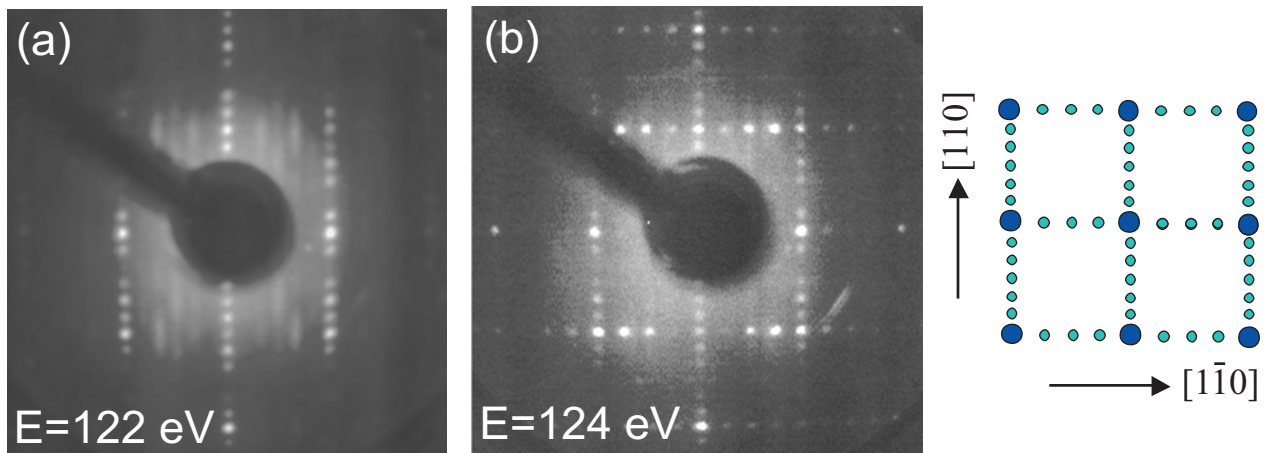


**Figure 5.2:** LEED patterns of the clean GaAs(001) surface after annealing at 500°C (a), and 600°C (b), measured with 122 eV and 124 eV, respectively. Right-hand side: schematics of the (4x6) Ga-rich GaAs(001) LEED pattern.

The (4x6) surface reconstruction observed by conventional diffraction techniques (LEED and RHEED) was found by STM [102] to originate either from a superposition of two domains (2x6)+(4x2) or by a periodic arrangement of Ga clusters on top of the 4x2 phase. Thus, the structure observed by RHEED/LEED is a "pseudo (4x6)" structure.

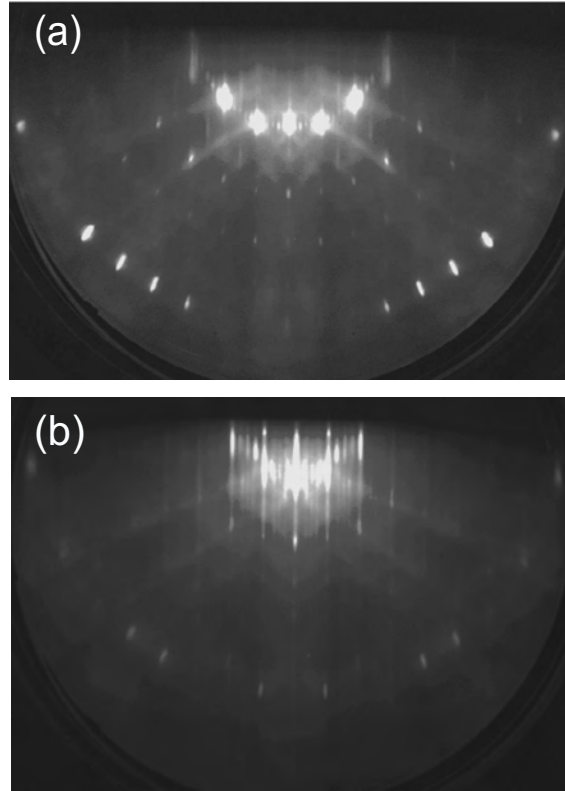


**Figure 5.3:** RHEED patterns of the clean GaAs(001) surface along (a) the  $[1\bar{1}0]$  and (b) the  $[110]$  azimuthal directions, measured at 10 keV after annealing at  $600^\circ\text{C}$ .

Fig. 5.4 shows schematically the proposed model for the Ga-rich  $(4\times 6)$  reconstruction by Xue et al. [102].

Films of 70 to 77 Å of either natural Fe or 95 % enriched  $^{57}\text{Fe}$  were deposited on clean GaAs(001) or GaAs(001)-HEMT substrates held nominally at RT with a deposition pressure of  $1.5\times 10^{-9}$  mbar at a rate of 0.03 Å/s. However, during deposition the substrate temperature increased to  $40\text{--}50^\circ\text{C}$ , as measured by a thermo-couple at the sample-holder. The evaporation rate and film thickness were monitored with a calibrated quartz-crystal microbalance and were calculated from the bulk density of bcc Fe. All samples were covered by a 40 Å thick Sn layer for protection. Two  $^{57}\text{Fe}$ -probe-layer samples, Sn(40 Å)/Fe(70 Å)/ $^{57}\text{Fe}$ (7.2 Å)/GaAs(001), and Sn(40 Å)/ $^{57}\text{Fe}$ (6.7 Å)/Fe(70 Å)/GaAs(001) were prepared in order to investigate the effects at the interfaces of Fe/GaAs and Sn/Fe (samples B and C, respectively). In addition, two  $^{57}\text{Fe}$ -probe-layer samples, Sn(40 Å)/Fe(70 Å)/ $^{57}\text{Fe}$ (7.2 Å)/GaAs(001)-HEMT, were investigated (samples D and E). Finally, an uncoated  $^{57}\text{Fe}$ (4.3 Å)/GaAs(001) sample (sample F) was grown to study the magnetic behavior as a function of temperature of ultrathin Fe film in-situ in UHV. The composition of the samples studied is described in Table 5.1.

Surface structure and magnetic properties of the epitaxially grown Fe films have been studied by LEED and RHEED and in-situ and ex-situ  $^{57}\text{Fe}$  Mössbauer spectroscopy

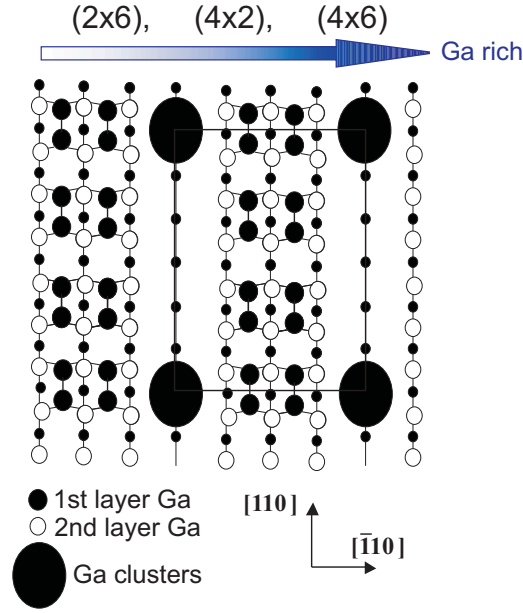


**Figure 5.4:** Proposed structure model for the (4x6) phase [102].

Sample	Composition	Substrate annealing temperature	Measured growth temperature
A	Sn(40 Å)/ <sup>57</sup> Fe(70 Å)/GaAs(001)	500 °C	40 °C
B	Sn(40 Å)/Fe(70 Å)/ <sup>57</sup> Fe(7.2 Å)/GaAs(001)	500 °C	40 °C
C	Sn(40 Å)/ <sup>57</sup> Fe(6.7 Å)/Fe(70 Å)/GaAs(001)	500 °C	40 °C
D	Sn(40 Å)/Fe(70 Å)/ <sup>57</sup> Fe(7.2 Å)/GaAs(001)-HEMT	500 °C	50 °C
E	Sn(40 Å)/Fe(70 Å)/ <sup>57</sup> Fe(7.2 Å)/GaAs(001)-HEMT	600 °C	50 °C
F	<sup>57</sup> Fe(4.3 Å)/GaAs(001)	600 °C	50 °C

**Table 5.1:** Sample description and growth conditions.

(CEMS). Continuous RHEED observation during growth was achieved with a CCD camera connected to a computer for data storage and image processing. This method allows the real-time monitoring of film growth and in-plane atomic spacing.

## 5.3 Results and discussion

### 5.3.1 RHEED

#### 5.3.1.1 Fe/GaAs(001)

Figs. 5.5(a) and (b) show typical RHEED patterns of the clean GaAs(001)(4x6) surface along the [110] and [1 $\bar{1}$ 0] azimuthal directions, respectively, after sputtering and annealing at 500°C (lower annealing temperature). After deposition of 5.5 monolayers (ML) of Fe (Fig. 5.5(c)), the surface reconstruction disappears, and a (1x1) pattern is observed up

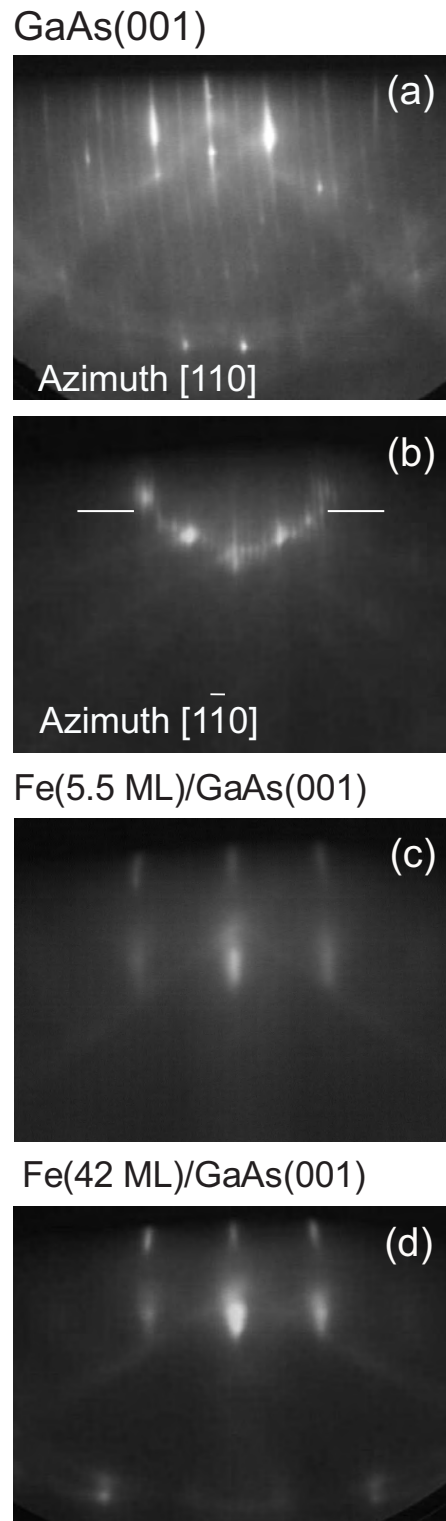


**Figure 5.5:** RHEED patterns of clean GaAs(001) substrate after annealing at 500°C with (4x6) reconstruction along (a)  $[110]$  azimuth and (b) along  $[\bar{1}\bar{1}0]$  azimuth; covered by (c) 5.5 ML Fe and (d) 42 ML Fe ( $[\bar{1}\bar{1}0]$  azimuth). (Beam energy 9 keV, 35  $\mu$ A).



to a coverage of 42 ML (Fig. 5.5(d)). The Fe films grow epitaxially with (001) orientation on GaAs(001), since the fundamental RHEED streaks in Fig. 5.5 (sample A) do not disappear with increasing thickness. The spotty patterns observed above 5.5 ML coverage (Fig. 5.5(c),(d)) indicate 3D-growth, as sketched in Fig. 5.6(a)(right-hand side).

The evolution of the RHEED intensity during growth (Fig. 5.6(a)(left)) was measured in the center of the (0,0) streak/spot. The intensity first slightly decreases after opening the shutter, and then (due to surface roughening) increases strongly up to  $\sim 5$  ML Fe coverage. Weak RHEED intensity oscillations with 1 ML Fe periodicity can be observed above 5 ML coverage up to a total thickness of 50 ML (see magnified region in the insert of Fig. 5.6(a)(left)). The appearance of RHEED oscillations suggests that a gradual smoothing of the Fe surface follows the 3D island formation. Coalescence occurs between 3-4 ML, and after 5 ML no significant change in the RHEED pattern was observed. Fig. 5.6(a)(right) shows the schematic of the growth mode proposed. These results (for growth at 40-50°C) are in agreement with previous reports by Brockmann et al. [101] on room-temperature grown Fe/GaAs(001) samples. They found by STM that the roughness amplitude of 1-2 ML remained unchanged with increasing Fe thickness, indicating a quasi-layer-by-layer growth mode which leaves the surface structure of the Fe films unchanged. For growth at 150°C, however, Bland's group found pyramid-like structures and a step density which increased approximately linearly with film thickness [94].

The intensity profiles obtained for different thicknesses from the horizontal scan (see Fig.5.5(b)) were least-squares fitted with three Lorentzian lines (one for each intensity peak of the fundamental reflections  $(\bar{1},0)$ ,  $(0,0)$  and  $(1,0)$ ) and a parabolic background. A typical example is shown in the insert of Fig.5.6(b). The distance ( $k_{Fe//}$ ) between the  $(\bar{1},0)$  and  $(1,0)$  RHEED streaks in reciprocal space is a measure of the Fe in-plane atomic distance ( $d_{Fe//}$ ) in real space (perpendicular to the scattering plane) relative to that of the GaAs(001) substrate ( $d_{sub//}$ ):  $d_{Fe//}/d_{sub//} = k_{sub//}/k_{Fe//}$ . The least-squares fitting method allows the precise determination of the peak distance  $k_{Fe//}$ . After an initial irregular behavior, the measured in-plane relative atomic distance of the Fe film shows monotonic behavior as function of coverage (Fig. 5.6(b)). Above  $\sim 5$  ML, the in-plane atomic distance of Fe remains  $\sim 1.35$  % larger than that of GaAs. This is in very good agreement with the lattice mismatch between bulk bcc-Fe and bulk GaAs ( $2a_{Fe}/a_{GaAs} \simeq 1.0138$ ), and agrees with results by Zölfl et al. [100], who obtained a misfit of  $\sim 1.5$  %. Therefore, bcc-Fe(001) films grown on GaAs(001) at 40-50°C are not significantly in-plane strained.

### 5.3.1.2 Fe/GaAs(001)-HEMT

Since the last layer of the GaAs-HEMT substrate is a 30 nm thick GaAs(001) film (doped with Si), it is not expected to find remarkable differences between the epitaxial growth of Fe on GaAs-HEMT(001) (Fig. 5.7) or on GaAs(001) (Fig. 5.5). Nevertheless, the RHEED streaks of the clean GaAs(001)-HEMT surface obtained after annealing up to 500°C (Fig.5.7(a)) were not as sharp as those of the corresponding clean GaAs(001) surface

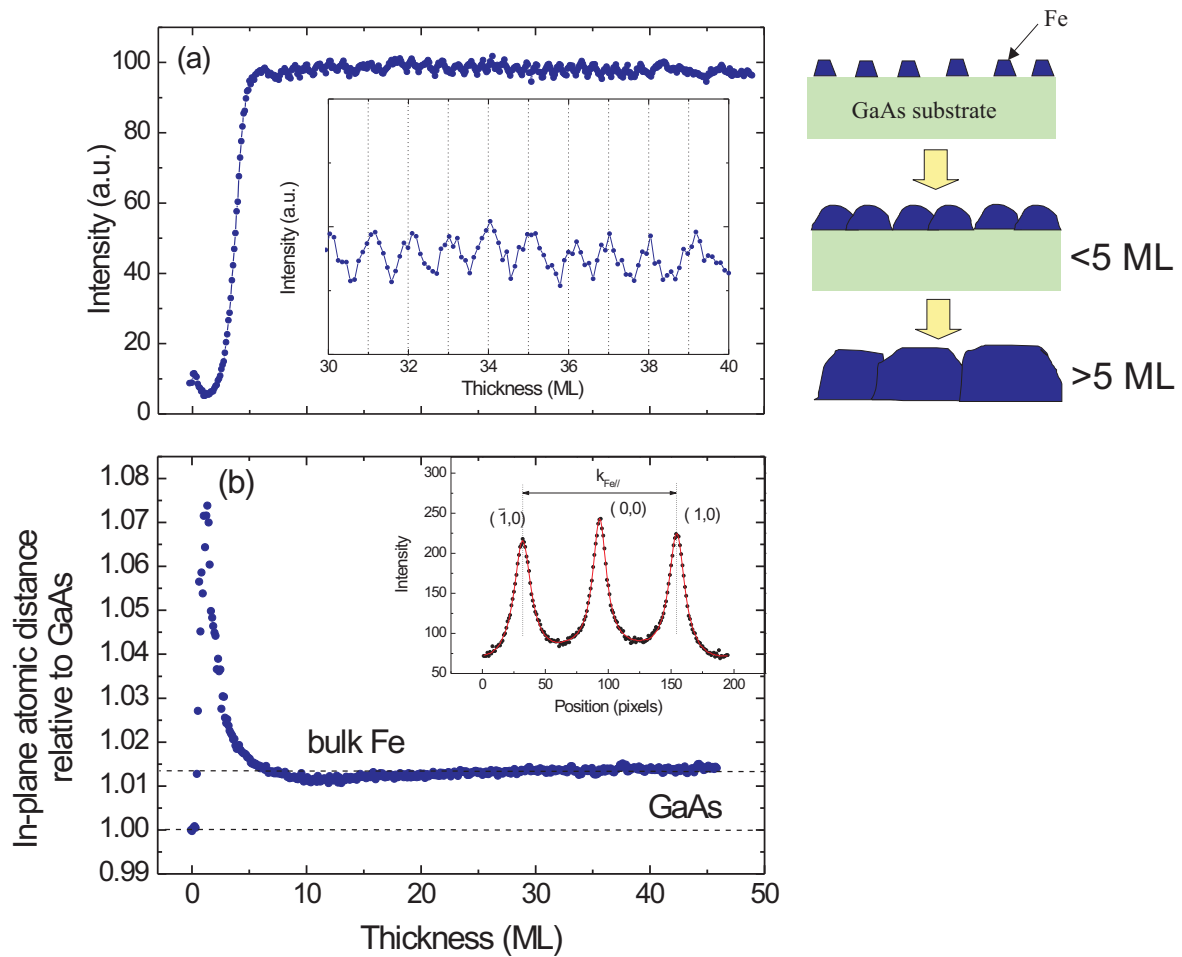


**Figure 5.6:** (a)(left) Specular RHEED intensity versus Fe thickness (the insert shows a magnified section); (right) schematics of the growth morphology. (b) Thickness dependence of the relative Fe in-plane atomic distance (relative to that of GaAs(001)) measured along the [110] azimuthal direction. Insert: intensity profile obtained for 30 ML Fe thickness from the horizontal scan indicated in Fig. 5.5(a) and least-squares fitted with three Lorentzian lines and a parabolic background.

(Fig.5.5(a)), and the HEMT surface did not show a clear surface reconstruction (Fig. 5.7(a)).

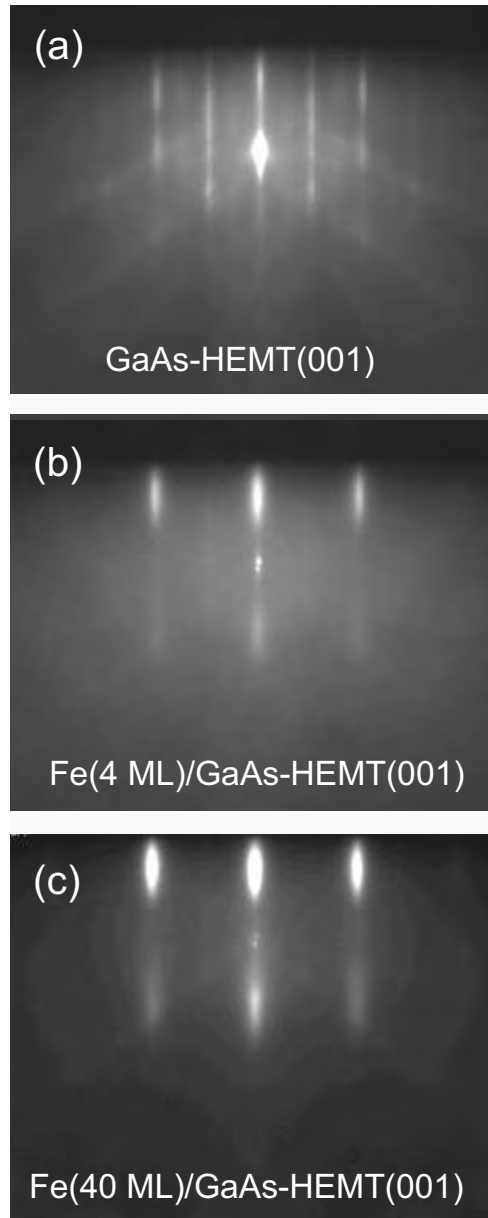


**Figure 5.7:** RHEED patterns measured along the [110] azimuthal direction of (a) clean GaAs(001)-HEMT substrate, covered by (b) 4 ML Fe and (c) 40 ML Fe. (Beam energy 9 keV,  $35\mu\text{A}$ ).

Analogous to the epitaxial growth of Fe on GaAs(001) (sample A), the epitaxial growth of Fe/GaAs(001)-HEMT (sample D) also exhibits 3D-type RHEED patterns after 5 ML (Fig. 5.7(b)) and 55 ML (Fig. 5.7(c)) Fe coverage. The only difference observed by RHEED between the growth of bcc-Fe on both types of substrates is a very weak 2-fold

surface reconstruction that appears after the deposition of 5 ML Fe on the GaAs-HEMT surface (hardly visible in Fig. 5.7(b)) and that disappears at thicker Fe thicknesses (Fig. 5.7(c)).

### 5.3.2 $^{57}\text{Fe}$ CEMS

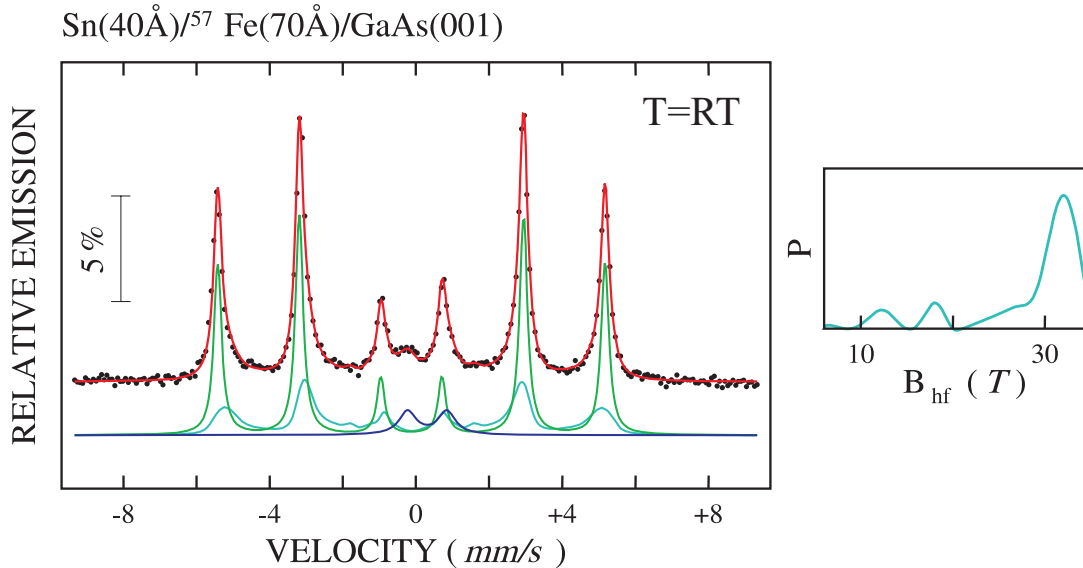
#### 5.3.2.1 Fe/GaAs(001)

Fig. 5.8 shows the  $^{57}\text{Fe}$  Mössbauer spectrum (CEMS) of sample A measured ex-situ at RT. This spectrum can be decomposed in terms of three subspectra: a sextet due to bulk-like bcc-Fe, a distribution of hyperfine magnetic fields assigned to the intermixed magnetic Fe/GaAs interface, and a central quadrupole-split doublet caused by a non-magnetic Fe-Sn alloy formed at the interface between Fe and the Sn coating layer.

From the intensity ratio of lines No.2 (5) and No.3 (4) in the sextet (see  $I_{2,5}/I_{3,4}$  in table 5.2) one can calculate the angle ( $\theta$ ) between the Fe magnetic moment and the incident  $\gamma$ -ray (perpendicular to the sample surface), averaged over the sample:

$$\sin^2\theta = \frac{2I_{2,5}/I_{3,4}}{4 + I_{2,5}/I_{3,4}} \quad (5.1)$$

In this case, we found  $\theta \approx 82^\circ$ , indicating that the Fe magnetic moments lie essentially parallel to the sample surface. The intensity ratio of lines 2 (5) and 3 (4) in the basic sextets of the hyperfine distribution was held constant at 4.0 ( $\theta=90^\circ$ ) during least-squares fitting assuming also in-plane Fe magnetic moments for the interface.



**Figure 5.8:** Mössbauer spectrum and hyperfine field distribution (right) obtained at 300 K for sample A: Sn(40 Å)/ $^{57}\text{Fe}$ (70 Å)/GaAs(001).

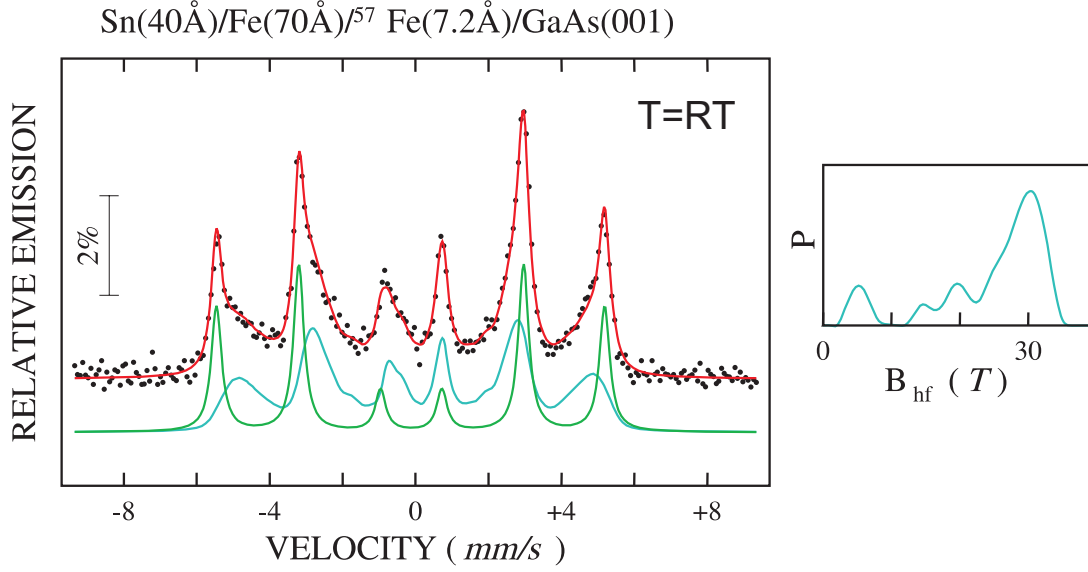


**Figure 5.9:** Mössbauer spectrum and hyperfine field distribution (right) obtained ex-situ at 300 K for sample B: Sn(40 Å)/Fe(70 Å)/ $^{57}\text{Fe}$ (7.2 Å)/GaAs(001).

In order to prove the absence of "magnetic dead layers" at the Fe/GaAs interface of these samples, an interface sensitive CEM spectrum (Fig. 5.9) of the  $^{57}\text{Fe}$ -probe-layer in sample B was measured. The spectrum was fitted with two components: a sextet due to bulk-like bcc-Fe, and a distribution of hyperfine magnetic fields for the intermixed Fe/GaAs interface. From the hyperfine field distribution (Fig. 5.9(right)) one concludes the absence of magnetic dead layers at the interface, since a peak at zero hyperfine-field is not observed. From the least-squares fit intensity ratio of lines 2 (5) and 3 (4) in the hyperfine field distribution it is calculated that the average angle between the Fe magnetic moments and the incident  $\gamma$ -ray is  $\approx 75^\circ$ , i.e. the sample is in-plane magnetized.

Fig. 5.10 shows an interface-sensitive CEM spectrum of the  $^{57}\text{Fe}$ -probe-layer (sample C) used to study the Fe/Sn interface. Similar to sample A, the Mössbauer spectrum was fitted with three components: a sextet due to bulk-like bcc Fe, a distribution of hyperfine magnetic fields assigned to an intermixed magnetic Fe/Sn interface component, and a central symmetric quadrupole-split doublet caused by a non-magnetic fraction of the Fe-Sn interface alloy. Note that the peak observed in the hyperfine field distribution at low field (8 T) is only a residual contribution of the non-magnetic Fe-Sn alloy that should be described by the central doublet. The least-squares fit used can not correctly separate both contributions in the central region of this spectrum. An interesting result is the large hyperfine field (second maximum of the  $B_{hf}$  distribution around 36 T in Fig. 5.10(right)) found for the Fe/Sn interfacial component; apparently it is 9 % enhanced with respect to bcc Fe at RT.

Similar to samples A and B, sample C also showed in-plane magnetization ( $\theta \approx 77^\circ$ ).

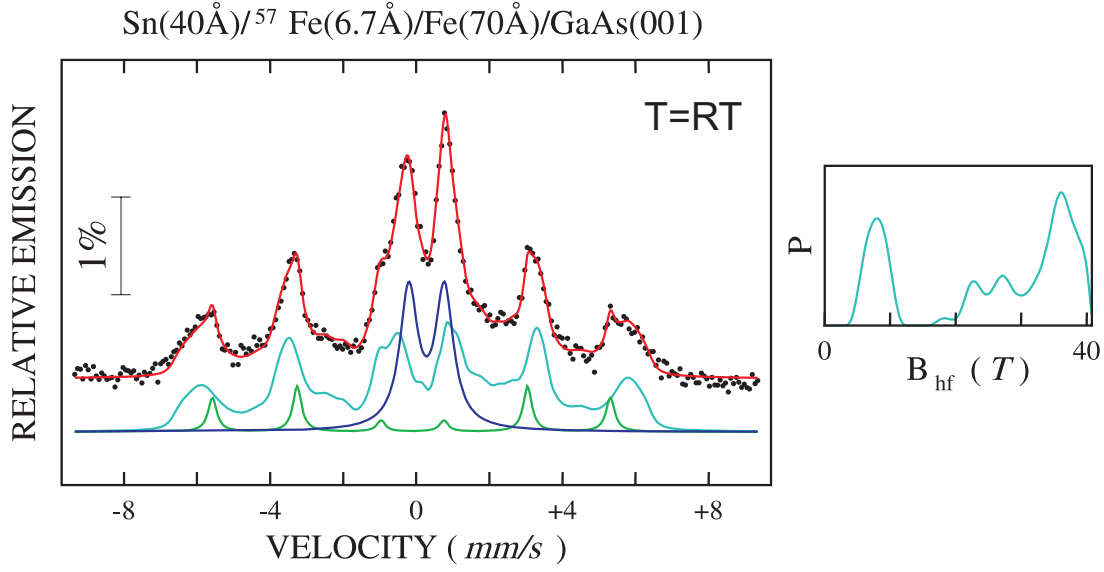


**Figure 5.10:** Mössbauer spectrum and hyperfine field distribution (right) obtained ex-situ at 300 K for sample C: Sn(40 Å)/<sup>57</sup>Fe(6.7 Å)/Fe(70 Å)/GaAs(001).

The Mössbauer parameters obtained by a least-squares fitting [120] the spectra of the different samples studied here are compiled in Table 5.2.

Sample		$\delta$ (mm/s)	$B_{hf}$ (T)	$I_{2,5}/I_{3,4}$	$2\epsilon$ (mm/s)	Rel. Area (%)
A	Sextet	$-0.017 \pm 0.001$	$32.843 \pm 0.007$	$3.84 \pm 0.04$	$-0.021 \pm 0.001$	65
	Distrib.(average) (peak)	0.012	$27.6 \pm 0.5$ 32.0	4.0*	0.0*	28
	Doublet	$0.42 \pm 0.02$			$1.07 \pm 0.03$	7
B	Sextet	$-0.022 \pm 0.006$	$33.00 \pm 0.03$	4.0*	$-0.018 \pm 0.007$	39
	Distrib.(average) (peak)	0.148	$24.7 \pm 0.3$ 31.0	$3.5 \pm 0.2$	0.0*	61
	Doublet	$0.368 \pm 0.007$			$0.97 \pm 0.03$	25.5
C	Sextet	$-0.014 \pm 0.01$	$33.76 \pm 0.07$	4.0*	$-0.03 \pm 0.01$	8
	Distrib.(average) (peak)	0.204	$25.5 \pm 0.4$ 36.0	$3.6 \pm 0.1$	$0.04 \pm 0.01$	66.5
	Doublet	$0.368 \pm 0.007$			$0.97 \pm 0.03$	25.5
D	Sextet	$-0.002 \pm 0.004$	$33.10 \pm 0.04$	4.0*	0.0*	25
	Distrib.(average) (peak)	0.191	$27.0 \pm 0.2$ 32.0	$3.86 \pm 0.08$	0.0*	75
	Doublet	$0.368 \pm 0.007$			$0.97 \pm 0.03$	25.5
E	Sextet	$-0.024 \pm 0.01$	$33.56 \pm 0.07$	4.0*	0.0*	26
	Distrib.(average) (peak)	0.171	$26.2 \pm 0.3$ 31.0	$3.9 \pm 0.2$	0.0*	74
	Doublet	$0.368 \pm 0.007$			$0.97 \pm 0.03$	25.5

**Table 5.2:** Mössbauer parameters (isomer shift  $\delta$ , hyperfine field  $B_{hf}$ , intensity ratio of lines 2,5 with respect to lines 3,4,  $I_{2,5}/I_{3,4}$ , quadrupole splitting  $2\epsilon$ , and relative spectral area) obtained from a least-squares fit of the spectra displayed in Figs.5.8,5.9,5.10,5.11. The isomer shift values are relative to bulk bcc-Fe at RT. (\*) indicates the parameters that have been held constant during the fit).

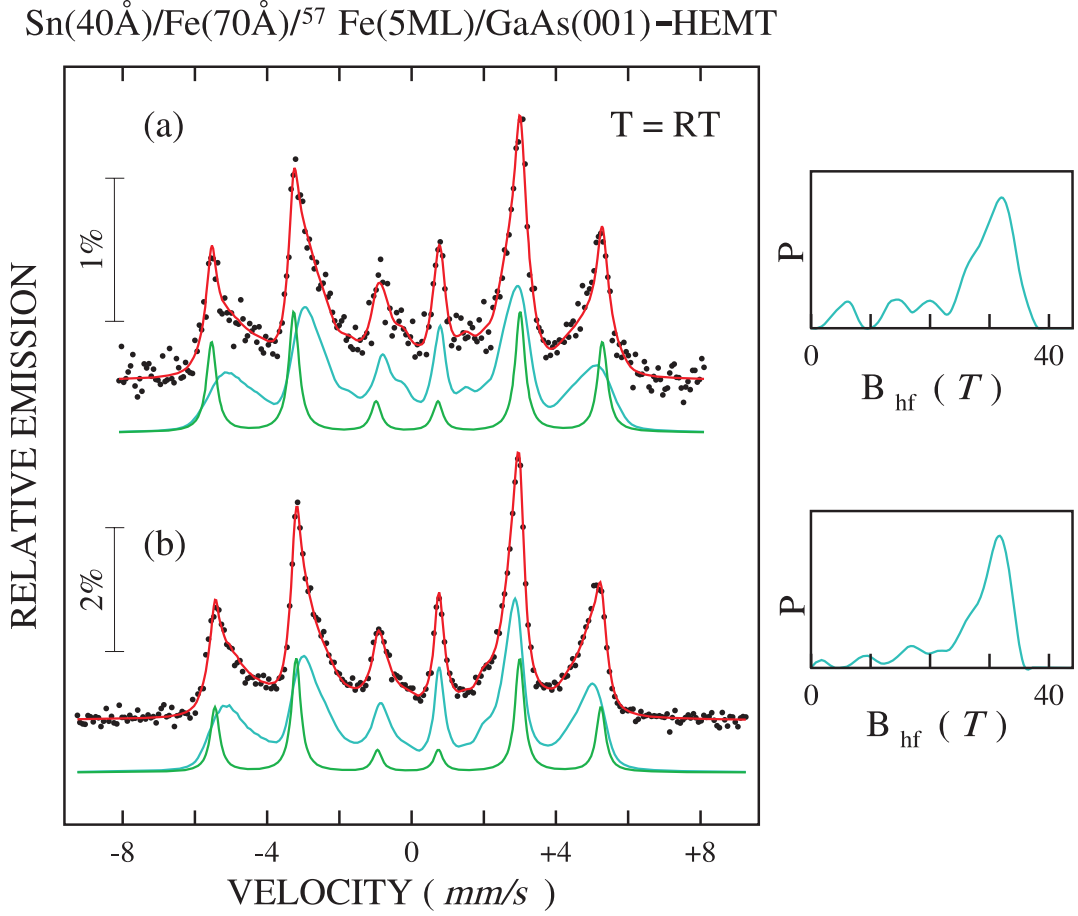


**Figure 5.11:** Mössbauer spectra and hyperfine field distributions (right) obtained ex-situ at 300 K for samples E and D: Sn(40 Å)/Fe(70 Å)/<sup>57</sup>Fe(7.2 Å)/GaAs(001)-HEMT, with substrates annealed previous to deposition up to 600° (sample E)(a) and 500°C (sample D)(b), respectively.

### 5.3.2.2 Fe/GaAs(001)-HEMT

Fig. 5.11 displays interface sensitive Mössbauer spectra of two <sup>57</sup>Fe-probe-layers (samples D and E) with the same composition, but with their GaAs(001)-HEMT substrates exposed to different cleaning treatments: for sample D (Fig. 5.11(b)) the substrate was annealed at 500°C prior to film deposition, while in case of sample E (Fig. 5.11(a)) the substrate was treated at a higher temperature (600°C), using the cleaning procedure of M. Doi. (The latter treatment resulted in sharper GaAs(001)-(4x6) LEED and RHEED reflections). Analogous to sample B, the Mössbauer spectra of samples D and E were fitted with two subspectra: a sextet corresponding to a crystalline magnetic phase (bcc-Fe), and a hyperfine field distribution that characterizes the magnetic Fe/GaAs(001)-HEMT interface. From the small spectral area that extends to the region near zero hyperfine field in the hyperfine field distributions (Fig. 5.11(a),(b)(right)) it is estimated that the non-magnetic contribution observed at the interface effectively amounts to only about 2

% of the 7.2 Å thick deposited  $^{57}\text{Fe}$  layer ( $\sim 0.1\text{-}0.2$  Å). This proves the absence of dead layers. Additionally, comparison of both spectra or of both hyperfine field distributions demonstrates that the sample annealed at lower temperature (Fig. 5.11(b)) presented a sharper magnetic interface, with a smaller contribution of hyperfine fields below 10 Tesla. Both samples showed preferred in-plane Fe magnetization, with  $\theta \approx 83^\circ$ .

### 5.3.2.3 $^{57}\text{Fe}(3 \text{ ML})/\text{GaAs}(001)$

A film of 3 ML thick epitaxial  $^{57}\text{Fe}(001)$  was grown on GaAs(001)-(4x6) (sample F) cleaned by M.Doï's procedure (600°C) prior to deposition. Mössbauer spectra (CEMS) of the uncoated film were measured in-situ in UHV as a function of temperature from room temperature down to 27 K (Fig. 5.12). All spectra were fitted with a single hyperfine field distribution. The intensity ratio of lines 2 and 3 was held constant at 4.0 ( $\theta=90^\circ$ ) assuming in-plane Fe magnetic moments.

At RT, the CEM spectrum consists of a broadened central line, and the hyperfine field distribution shows a dominant maximum near zero field (Fig. 5.12(f)). With decreasing temperature (Figs. 5.12(e)-(a)), the width of the spectra increases, and the hyperfine field distribution becomes broader, showing several maxima at non-zero fields. This behavior is typical for the transition from paramagnetism or superparamagnetism to ferromagnetism.

From Mössbauer measurements at zero applied field it is not possible to distinguish paramagnetism from superparamagnetism. Since the fluctuations of the magnetization in a superparamagnetic system are faster than the Mössbauer observation time ( $10^{-8}$  s), the time-averaged hyperfine field measured by the Mössbauer effect in the absence of an external field becomes zero, not being sensitive to the internal ferromagnetic order within the Fe clusters formed.

After the in-situ CEMS measurements in UHV, sample F was covered by 40 Å Pt (to avoid oxidation) and was studied ex-situ by CEMS at RT in an in-plane external field ( $B_{ext}$ ) of 1 Tesla. Similar to the zero field case (Fig. 5.12(f)), the Mössbauer spectrum observed at  $B_{ext}=1$  T consists of a central broad line (see Fig. 5.13). If the 3 ML Fe layer would be superparamagnetic, such a small external field would reveal superparamagnetism by the observation of a magnetic sextet with a large hyperfine splitting [103]. Since the application of a relatively large field did not significantly modify the Mössbauer spectrum as compared to that observed at zero field (except for a slight increase in the width of the line) one can conclude that the sample is paramagnetic at RT.

Our RHEED results (Fig. 5.6) demonstrate that 3 ML of Fe on GaAs(001) does not grow layer-by-layer, and that Fe clusters (islands) must be formed in the initial stage of growth and below a total coverage of 5 ML. The in-plane atomic distance determined by RHEED (Fig. 5.6(b)) also indicates strong expansion in this thickness region, most probably due to atomic intermixing at the Fe/GaAs interface. This alloy formation, together with a cluster size effect, could explain why the Curie temperature of the 3 ML Fe/GaAs sample lies below RT, in contrast to the results for Fe(3 ML)/Pd(110) (see chapter 3), where ferromagnetic order was observed at RT.



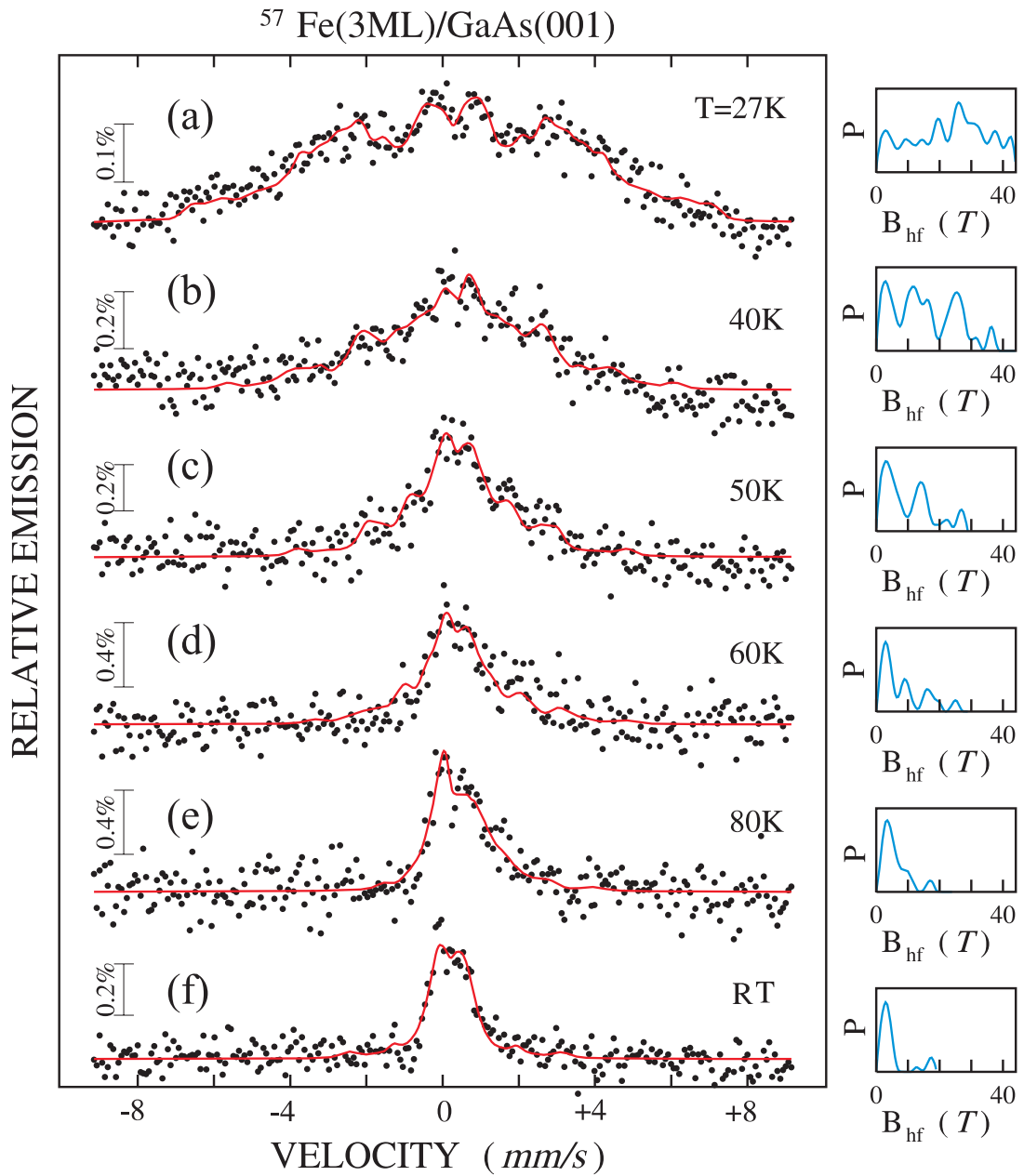


**Figure 5.12:** Mössbauer spectra (CEMS) and hyperfine field distributions (right) of sample F:  $^{57}\text{Fe}(3\text{ML})/\text{GaAs}(001)$ -(4x6), measured in-situ in UHV at a temperature of 27K (a), 40K (b), 50K (c), 60K (d), 80K (e), and room temperature (f).

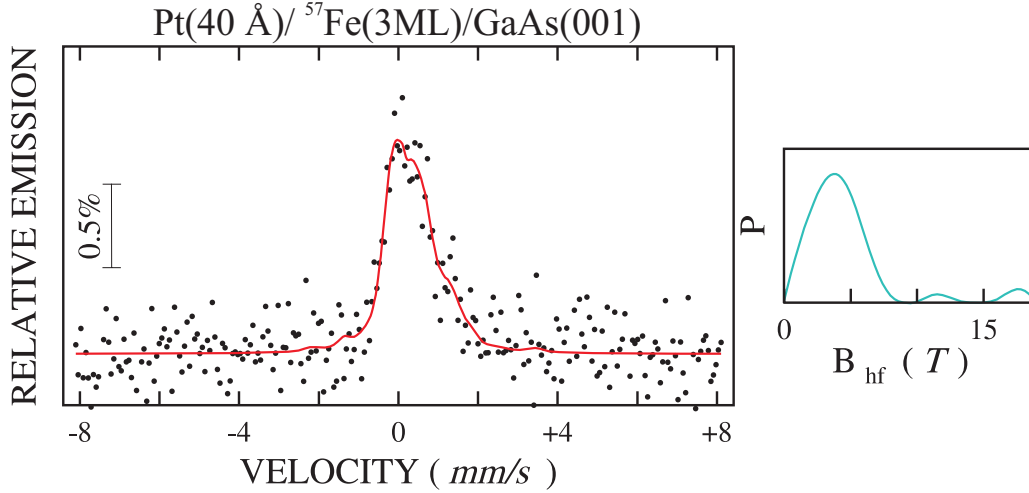


**Figure 5.13:** Mössbauer spectra (CEMS) and hyperfine field distributions (right) of sample F: Pt(40 Å)/ $^{57}\text{Fe}$ (3 ML)/GaAs(001)-(4x6), measured ex-situ at room temperature in an external magnetic field of 1 Tesla.

Xu et al. [97] observed superparamagnetism by MOKE during room-temperature growth of Fe/GaAs(001)-(4x6) within a narrow thickness range (3.5-4.8 ML) and the onset of long-range ferromagnetic ordering above these thicknesses. Below a coverage of 3.5 ML, they could not measure any magnetic signal by MOKE, and they attributed this lack of observed magnetization to a size effect, i.e. to a very small initial cluster size, which prevents the development of long-range magnetic ordering at and above room temperature (paramagnetism). The paramagnetic behavior measured by CEMS at room temperature for the 3-ML Fe sample confirms the result by Xu et al. [97]; we think however, that interfacial alloy formation also contributes to a low  $T_C$  value. As more Fe is deposited, the islands will grow and form larger clusters. The exchange interaction within these clusters becomes stronger and leads to internal ferromagnetic ordering [104], giving rise to superparamagnetism. With further increase in the coverage, the islands coalesce and long range ferromagnetic ordering is observed.

As mentioned before, the Curie temperature of the islands appears to lie below RT. During cooling, intrinsic ferromagnetic order within the islands should appear somewhere between 300 K and  $\approx 50$  K. (A  $T_C$  distribution is expected due to a large distribution of the island size). However, the magnetization within the islands will fluctuate thermally very fast above  $\approx 50$  K (Fig. 5.12(d-f)), as compared with the Mössbauer observation time, leading to superparamagnetism. Below a temperature of  $\approx 50$  K (Fig. 5.12(a-b)), the magnetization fluctuations (or relaxation) become blocked, and a magnetic hyperfine field is observed.

Under the assumption of superparamagnetism, the "blocking" temperature ( $T_B$ ) of the system can be extrapolated from the temperature dependence of the width of the hyperfine field distribution (Fig. 5.14), where the width of the distribution is defined as the root mean square (RMS) of  $B_{hf}$ . From Fig. 5.14  $T_B$  is found to be  $\sim 52$  K.

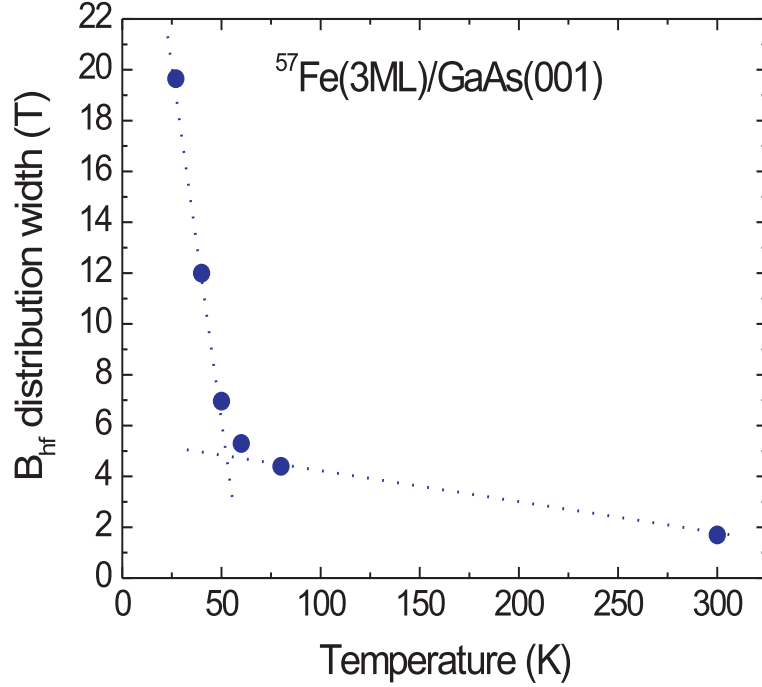


**Figure 5.14:** Temperature dependence of the width of the hyperfine field distributions displayed in Fig. 5.12

Superparamagnetic relaxation in zero applied field can be described by the Arrhenius law [105]:

$$\tau = \tau_0 e^{CV/k_B T} \quad (5.2)$$

,where  $k_B$  is the Boltzmann constant,  $\tau_0$  is a characteristic time (attempt time),  $C$  is the magnetic anisotropy constant,  $V$  is the cluster volume, and  $T$  is the temperature. From

$$T_B = \frac{CV}{k_B [\ln(\tau/\tau_0)]} \quad (5.3)$$

one can estimate the magnetic anisotropy energy ( $CV$ ) of the cluster using the characteristic Mössbauer observation time (nuclear Larmor precession time)  $\tau \approx 10^{-8}$  s and the blocking temperature obtained ( $T_B \approx 52$  K), and choosing  $\tau_0 \approx 10^{-10} - 10^{-12}$  s. Since only one observation time is employed here,  $\tau_0$  and  $CV$  cannot be determined independently. The situation would be improved if one employs another additional measurement technique with a widely different observation time, for example, low-field SQUID magnetometry ( $\tau \approx 10$  s) [31]. Also scanning tunneling microscopy (STM) would be useful here to measure the average cluster size in order to determine the magnetic anisotropy constant  $C$  from eq. ??eq5.2).

Under the assumption of superparamagnetism, one estimates from the Mössbauer measurements an anisotropy energy CV of  $\approx 3.3\text{-}6.6 \times 10^{-14}$  erg. This value, obtained for the Fe/GaAs clusters, is of the same order of magnitude as anisotropy energy values obtained by Chien et al. [31] on  $\text{Fe}_{50}(\text{SiO}_2)_{50}$  nano-particles of 25 Å average diameter, i.e.  $\text{CV} \approx 8.2 \times 10^{-14}$  erg.

## 5.4 Conclusions

Epitaxial 77 Å thick bcc-Fe(001) layers were grown on clean GaAs(001)-(4x6) and clean GaAs(001)-HEMT surfaces at 40-50°C. During growth of the first 5 ML Fe the in-plane atomic distance was found to be enlarged presumably due to interfacial alloy formation. Above this coverage, RHEED results demonstrate that the in-plane atomic distance is reduced to a value very close to that of bulk bcc-Fe. The formation of Fe islands was observed below 5 ML coverage. This result, together with the temperature dependence of Mössbauer spectra, suggests the existence of superparamagnetic Fe-alloy clusters in the thickness region below 5 ML, with a blocking temperature of  $\simeq 52$  K.

No magnetic dead layers have been found at the Fe/GaAs interface by Mössbauer spectroscopy for samples grown at temperatures below 50°C. This is in agreement with magnetization measurements by Zölfl et al. [100] who reported the absence of magnetic dead layers in similarly prepared samples. However, this result is in contrast to other previous studies, where a drastic reduction of the average magnetization has been found in Fe/GaAs(001) films thinner than 10 nm grown at 150°C [94], corresponding to a dead layer between 5-40 ML at the interfaces. This demonstrates that a low substrate temperature during deposition is required to avoid the formation of magnetic dead layers.

Sample	$\overline{B}_{hf}$ (T)	$B_{peak}$ (T)
B	24.7 T	31.0 T
D	27.0 T	32.0 T
E	26.2 T	31.0 T
Average	26.0 T	31.0 T

**Table 5.3:** Average ( $\overline{B}_{hf}$ ), and most probable ( $B_{peak}$ ) hyperfine fields obtained from the hyperfine field distributions after least-squares fitting of the Mössbauer spectra corresponding to samples B,D and E.

Assuming the well established approximate proportionality between hyperfine magnetic field and local Fe magnetic moment [106], it is concluded from the observed interfacial average and peak hyperfine field values (Table 5.3) of  $\sim 26$  T and  $\sim 31$  T, respectively, that interfacial Fe magnetic moments range from  $\sim 1.7 \mu_B$  to  $\sim 2\mu_B$  (where the usual conversion factor of  $\sim 15 \text{ T}/\mu_B$  for bcc-Fe was used). Since nearly the full magnetic moment of bcc Fe at the Fe/GaAs(001) interface was observed, the feasibility for injection of spin polarized electrons in devices based on Fe/GaAs remains promising.

## Part II

# Structure and vibrational dynamics



## 6 Epitaxial growth and interfacial structure of Sn on Si(111)(7x7)

### 6.1 Introduction

Bulk Sn is an element that can undergo a phase transformation at 13.2°C upon cooling from its metallic body centered tetragonal phase ( $\beta$ -Sn,  $a=5.83$  Å,  $c=3.18$  Å) to a semiconducting phase ( $\alpha$ -Sn,  $a=6.489$  Å) with diamond structure.  $\alpha$ -Sn is interesting for infrared applications because of its nearly-zero energy band gap (0.08 eV at room temperature, RT).

Since the discovery of the semiconducting properties of  $\alpha$ -Sn in 1950 [107], many groups have tried to grow macroscopic  $\alpha$ -Sn crystals ([108,109]). The first heteroepitaxial growth of metastable  $\alpha$ -Sn films stabilized at room temperature on closely lattice matched substrates such as InSb ( $a=6.4798$  Å at RT) or CdTe ( $a=6.4829$  Å at RT) was achieved by Farrow et al. [110]. Osaka and co-workers [111] showed that the symmetry of the substrate surface plays a very important role in the determination of the interfacial energy, and that the formation of the  $\beta$ -Sn phase (which is more stable in the bulk at RT than the bulk  $\alpha$ -phase) can be inhibited by heteroepitaxy of Sn thin films on appropriate substrates. Though the  $\alpha$ -Sn  $\rightarrow$   $\beta$ -Sn transformation was observed during heating of epitaxial  $\alpha$ -Sn on InSb(001) at 115°C [111], the stabilization of  $\alpha$ -Sn up to 170° on InSb(111) [111] was found to be possible, and melting occurred at such high temperature without a phase transformation to  $\beta$ -Sn. For large film thicknesses ( $> 10$  Å) [112,113], the formation of (bulk-like)  $\beta$ -Sn will be favored, because the free energy of the bulk Sn phase will be lower than the interfacial free energy that stabilizes epitaxial  $\alpha$ -Sn.

Sn/Si(111) is an example of an abrupt metal-semiconductor interface, uncomplicated by interdiffusion or chemical reaction (no silicide formation), that can be used to understand the details of the origin of the Schottky barrier [114]. For instance, it is known from the literature [115] that the difference in the Schottky barrier heights of two different surface phases of Pb/Si(111) is due to the correlation between the geometric and electronic structure in these systems. A detailed knowledge of the structural properties of the Sn/Si(111) system is then a requirement for the understanding of its electronic properties.

The growth of epitaxial  $\alpha$ -Sn on Si ( $a=5.43$  Å) [112,113,116–119] is difficult due to the large lattice mismatch ( $\sim 19.5$  %); since both,  $\alpha$ - and  $\beta$ -Sn are unfavorable on Si(111), it is not clear in which crystalline form Sn films will grow. Wang et al. [112] studied the growth of Sn on Si(111):Sn- $(\sqrt{3}\times\sqrt{3})R30^\circ$  and Sn- $(2\sqrt{3}\times 2\sqrt{3})R30^\circ$  reconstructions by means of low energy electron diffraction (LEED) and scanning tunneling microscopy (STM); they observed that up to 3.5 monolayers (ML)  $\alpha$ -like-Sn formed an ordered overlayer commensurate to the Si substrate, which, however, is unstable for larger thicknesses, where  $\beta$ -Sn islands were observed.

The structure of Sn at the *buried* Sn/Si interface is still an open question. It is not known whether interfacial  $\alpha$ -like-Sn remains stabilized after the deposition of thicker Sn

layers that undergo the transition to  $\beta$ -Sn. The purpose of the present work was to clarify this question. LEED and RHEED performed during the growth of Sn on the Si(111)-(7x7) surface will show that ultrathin  $\alpha$ -Sn layers are formed. It will be demonstrated by  $^{119}\text{Sn}$  conversion electron Mössbauer spectroscopy (CEMS) that these layers remain stabilized as buried  $\alpha$ -Sn at the interface up to  $\sim 3.5$  ML after further coverage by thick  $\beta$ -Sn layers. Moreover, the epitaxial relationship between thick  $\beta$ -Sn layers on Si(111) is reported.

## 6.2 Experimental

Thin epitaxial Sn layers of natural isotopic composition (of 99.995 at. % purity) and  $^{119}\text{Sn}$  enriched epitaxial Sn layers were grown in UHV on the (7x7) reconstructed clean Si(111) surface at room temperature (RT). The isotopic enrichment of  $^{119}\text{Sn}$  was 82.9 %.

Before being loaded into the UHV system (base pressure  $8 \times 10^{-11}$  mbar), the Si substrates were rinsed in acetone and ethanol. The (7x7) substrate surface was obtained after in-situ annealing in UHV at  $1100^\circ \text{C}$  for 15 minutes to eliminate the top  $\text{SiO}_2$  layers. Auger electron spectroscopy (AES) measurements after the in-situ cleaning showed a Si surface free of oxygen and carbon contaminants.

Sn layers with thicknesses ( $t_{\text{Sn}}$ ) between 2 and  $1000 \text{ \AA}$  were evaporated from Knudsen-cells ( $\text{Al}_2\text{O}_3$  crucible) with low deposition rates ( $0.02$ - $0.025 \text{ \AA/s}$ ). The deposition rates were controlled by a quartz-balance monitor. The pressure during the evaporation was always lower than  $5 \times 10^{-10}$  mbar. To avoid the oxidation of the Sn layers during the ex-situ measurements, all samples were covered with a  $50$ - $60 \text{ \AA}$  thick amorphous Si layer deposited from an e-gun.

For the structural characterization, RHEED measurements were carried out during deposition. The RHEED patterns were recorded by a CCD camera connected to a computerized data storage and processing system.

The thickness dependent  $\alpha$ - to  $\beta$ -Sn phase transition was also studied ex-situ by  $^{119}\text{Sn}$  conversion electron Mössbauer spectroscopy (CEMS) at room temperature. For the  $23.88 \text{ keV}$  Mössbauer  $\gamma$ -radiation,  $^{119}\text{Sn}^*$  in a  $\text{CaSnO}_3$  matrix was used as source. For electron detection a He-4%  $\text{CH}_4$  gas proportional counter was used, with the sample mounted inside of the counter. An electromechanical Mössbauer drive and conventional electronics were employed, the source being moved in constant acceleration mode. All isomer shift ( $\delta$ ) values are given relative to a  $\text{CaSnO}_3$  absorber at RT. The Mössbauer spectra were least-squares fitted with the program NORMOS [120] with a Lorentzian line shape.

## 6.3 Results

### 6.3.1 RHEED

Figure 6.1 displays RHEED patterns recorded during growth along the  $[112]$  azimuthal direction of the clean Si(111)(7x7) surface (a), and the Sn covered Si(111)(7x7) surface (b)-(d). All images are taken with a low electron beam voltage ( $6 \text{ keV}$ ) and a low beam



current (25  $\mu\text{A}$ ) to avoid heating of the sample surface by the electron beam. The sharpness of the superstructure streaks (six vertical streaks between the central (0,0) and the fundamental (1,1) or  $(\bar{1},\bar{1})$  reflection) observed in Fig. 6.1(a), and the presence of superstructure reflections along several Laue circles, together with the appearance of Kikuchi lines, indicate atomically smooth and well-ordered surfaces. In the same way, sharp fundamental (0,0), (1,1) and  $(\bar{1},\bar{1})$  reflections were found after the deposition of 6.8 ML Sn (Fig. 6.1(d)) demonstrating the flatness of the epitaxial layers.

The growth was observed to be pseudomorphic up to a thickness of 3 to 3.5 ML (Figs. 6.1(b-c)). The intensity of the fundamental RHEED reflections initially decreases with increasing film thickness (Fig. 6.1(c)), reaching a minimum at around 3.5 ML. Above this critical thickness, lattice relaxation starts, and the RHEED pattern becomes brighter again. Finally, after depositing 6.8 ML Sn (Fig. 6.1(d)), a clear increase in the separation of the (1,1) and  $(\bar{1},\bar{1})$  RHEED reflections as compared to the Si substrate was observed, implying a contraction of the in-plane atomic distance in real space (see Fig. 6.4(b) below). This fact can be understood if one considers that for thick Sn layers the more stable phase would be the bulk  $\beta$ -Sn phase, which has a smaller lattice parameter than  $\alpha$ -Sn. Therefore, the higher lattice mismatch between substrate and deposited material observed above 3.5 ML appears to be related to the  $\alpha \rightarrow \beta$ -Sn transition. A change in the structure of the film from diamond ( $\alpha$ -Sn) to body-centered tetragonal ( $\beta$ -Sn) can explain the end of the pseudomorphic growth of Sn on the silicon substrate with diamond structure above 3.5 ML.

After deposition of 30  $\text{\AA}$  Sn, a (1x1) RHEED pattern was observed (Fig. 6.2) characterized by sharp (1,1) and  $(\bar{1},\bar{1})$  fundamental streaks, together with weak (2,2) and  $(\bar{2},\bar{2})$  reflections indicating good epitaxial quality and surface flatness of the  $\beta$ -Sn islands grown on the interfacial  $\alpha$ -Sn layer. Thicker Sn films between 100  $\text{\AA}$  (Fig. 6.3(a)) and 200  $\text{\AA}$  (Fig. 6.3(b)) still showed relatively long and sharp RHEED streaks, and a weak 2-fold surface reconstruction appeared. The absence of a spotty pattern in RHEED (characteristic of 3D-islands growth) observed after the deposition of thick Sn layers indicates the growth of Sn islands with a very flat surface.

The evolution of the RHEED intensity during growth was measured on the (0,0) specular spot near the shadow-edge (in the region of diffuse scattering). Fig. 6.4(a) shows that immediately after opening the shutter, the intensity first increases to a maximum and then reaches a minimum at 1 ML thickness as expected under diffuse scattering conditions and layer-by-layer growth. Such intensity oscillations are observed up to 3 ML coverage. The observation of intensity oscillations by RHEED provides evidence for quasi layer-by-layer growth for the first 3 monolayers. Above this thickness, the intensity changes only weakly, and no more oscillations are found. The periodicity of the RHEED oscillations corresponds to the thickness of 1 ML  $\alpha$ -Sn that experienced a  $\sim 9\%$  expansion in the out of plane atomic distance along the [111]- $\alpha$ -Sn direction, as measured with a quartz microbalance during the evaporation. This effect is correlated with the contraction of the in-plane spacing that the interfacial  $\alpha$ -Sn experiences to match the in-plane atomic distance of the silicon substrate.

The intensity profiles obtained for different thicknesses from the horizontal scan (as

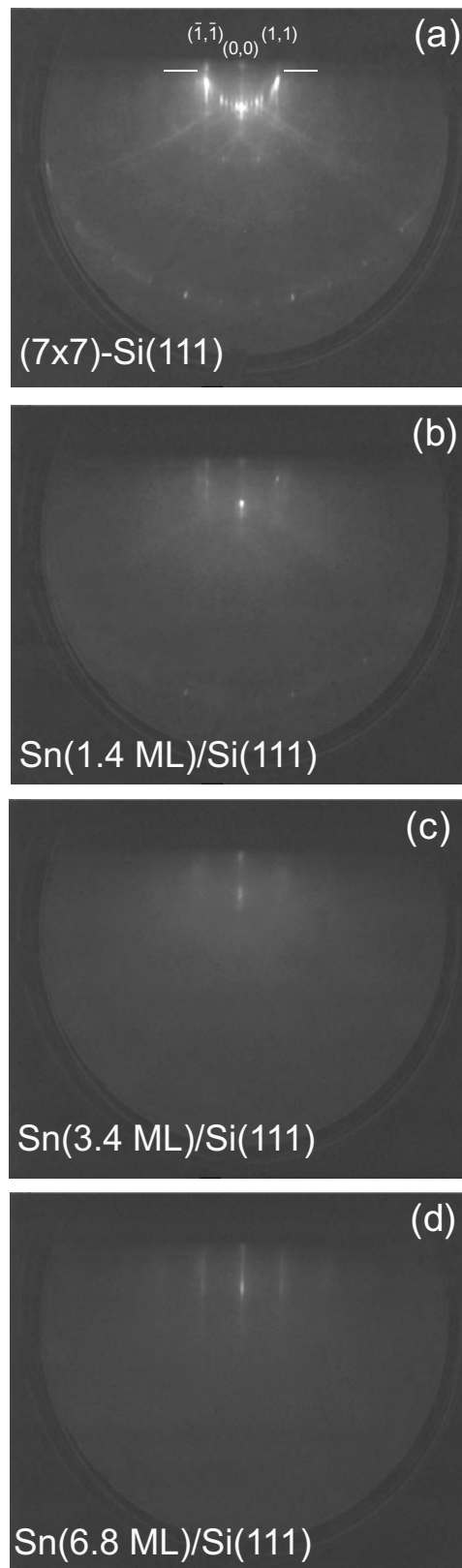


**Figure 6.1:** RHEED patterns recorded along the [112] azimuthal substrate direction with 6 keV electron energy and 25  $\mu\text{A}$  beam current: (a) (7x7) reconstruction of the clean Si(111) surface immediately prior to deposition; and after deposition of 1.4 ML Sn (b); 3.4 ML Sn (c), and 6.8 ML Sn (d).

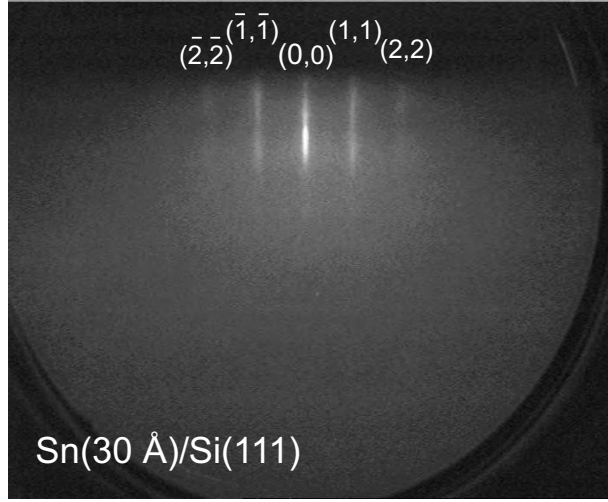


**Figure 6.2:** RHEED pattern recorded along the  $[112]$  azimuthal substrate direction with 10 keV electron energy and 25  $\mu\text{A}$  beam current after deposition of 30 Å Sn on Si(111).

indicated in Fig. 6.1(a) by the horizontal lines) were fitted with three Lorentzian lines (one for each intensity peak found at the positions where the fundamental reflections  $(\bar{1},\bar{1})$ ,  $(0,0)$  and  $(1,1)$  were observed) and a parabolic background. A typical example is shown in the insert of Fig.6.4(b). The distance ( $k_{Sn}$ ) between the  $(\bar{1},\bar{1})$  and  $(1,1)$  RHEED streaks in reciprocal space is a measure of the Sn in-plane atomic distance ( $d_{Sn//}$ ) in real space (perpendicular to the scattering plane) relative to that of the Si(111) substrate ( $d_{Si//}$ ):

$$\frac{d_{Sn//}}{d_{Si//}} = \frac{k_{Si}}{k_{Sn}} \quad (6.1)$$

The thickness dependence of the relative in-plane atomic distance (Fig.6.4(b)) also shows three oscillations, correlated with the formation of the first three atomic layers in a nearly layer-by-layer growth mode (Fig. 6.4(a)). The relative in-plane atomic distance decreases up to 3.5 ML coverage, and above this thickness it approaches a constant value of  $\sim 0.93$ - $0.94$  (at 12 ML). The critical thickness of 3.5 ML defines the boundary between the  $\alpha$ - and  $\beta$ -Sn phases. Experiments performed under similar conditions yield  $d_{\beta-Sn//}/d_{Si//} \sim 0.89$ - $0.90$  after the growth of 60 Å Sn.

Ex-situ X-ray diffraction measurements on a 1020 Å thick (bulk-like)  $\beta$ -Sn film epitaxially grown on Si(111)  $[121]$  indicated a preferential growth with  $(200)$  lattice planes parallel to the film surface, and with an out-of-plane lattice parameter of 5.825 Å (5.83 Å corresponds to bulk  $\beta$ -Sn). This provides information about the relative orientation of the  $\beta$ -Sn bct unit cell grown on the diamond structure of  $\alpha$ -Sn/Si(111): the  $c$  axis is lying within the film plane. The rectangular in-plane unit mesh of  $\beta$ -Sn then should have  $a=5.83$  Å and  $c=3.18$  Å as lattice parameters.

Figure 6.5 shows the proposed schematic of the epitaxial relationship of  $\beta$ -Sn/Si(111). It is assumed that the  $(7 \times 7)$  superstructure disappears upon covering by Sn  $[113]$ , and

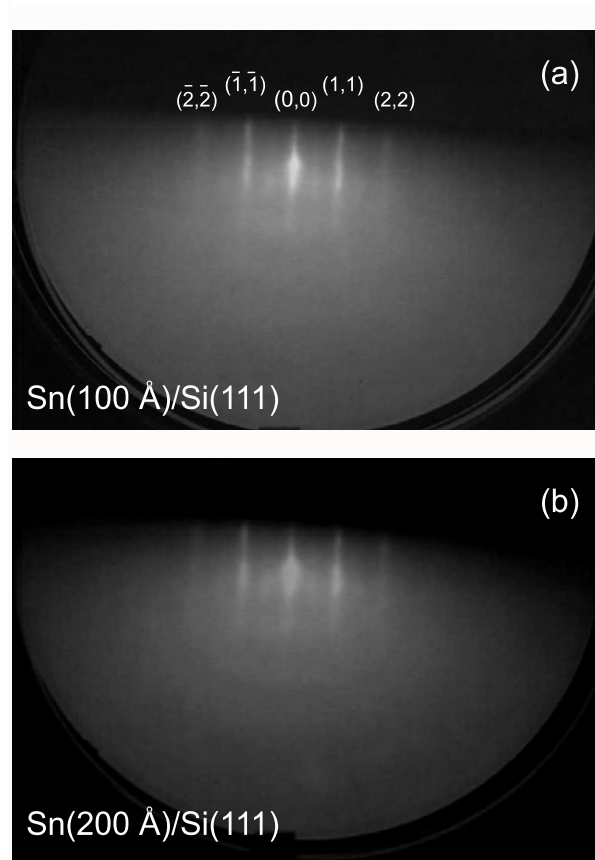


**Figure 6.3:** RHEED patterns recorded along the [112] azimuthal substrate direction with 10 keV electron energy and 30  $\mu$ A beam current after deposition of (a) 100 Å Sn and (b) 200 Å Sn on Si(111).

that the  $\beta$ -Sn overlayer is undistorted, with a bulk unit mesh of dimensions  $a=5.83$  Å and  $c=3.18$  Å in the film plane. Since the bct structure of  $\beta$ -Sn has no threefold rotational axis, the epitaxial commensurate growth of the  $\beta$ -Sn unit mesh and the Si(111) surface as observed by RHEED, as well as the hexagonal symmetry observed in the LEED patterns (as shown in the next section), can only be explained by a type of growth similar to Nishiyama-Wassermann growth, that explains the epitaxial commensurate growth of bcc-Fe(110) on fcc(111) or hcp(111) surfaces.

The suggested  $\beta$ -Sn(200)/Si(111) epitaxial relationship displayed in Fig. 6.5 is applicable to this case, where  $\beta$ -Sn was grown on an ultrathin interfacial  $\alpha$ -Sn film pseudomorphically grown on Si(111), because the interfacial  $\alpha$ -Sn experiences a strong in-plane contraction (Fig. 6.4) during the initial growth stage to match the smaller lattice parameter of Si. Following this epitaxial model, the in-plane atomic distance  $d_{Sn//}^{bulk}$  of undistorted bulk-like  $\beta$ -Sn observed perpendicular to the [112] azimuthal substrate direction should be smaller than that of Si(111),  $d_{Si//}^{bulk}$ . This is qualitatively in accordance with the RHEED result above 3.5 ML (Fig. 6.4(b)), where a 6-7 % contraction of the in-plane atomic spacing

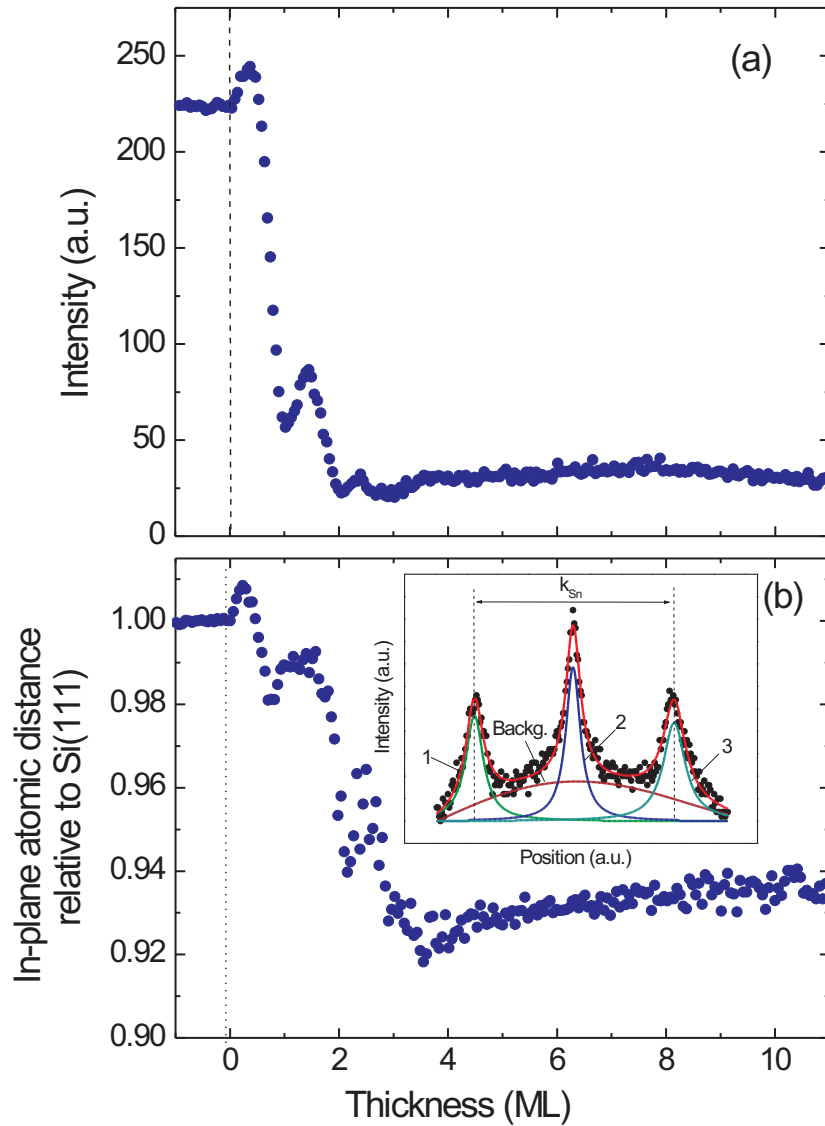


**Figure 6.4:** (a) RHEED intensity (diffuse scattering near the (0,0) spot) versus Sn thickness; (b) Thickness dependence of the Sn in-plane atomic distance relative to that of Si(111). Insert: intensity profile obtained for 6 ML Sn thickness from the horizontal scan indicated in Fig. 6.1(a) and fitted with three Lorentzian lines and a parabolic background. (The electron beam was along the [112] azimuthal substrate direction).

of Sn is measured. A larger in-plane contraction ( $\sim 11\%$ ) was measured by RHEED for thicker Sn films (60 Å) deposited under similar conditions (not shown). Quantitatively, following this growth model (Fig. 6.5), the relative in-plane atomic distance,  $d_{Sn//}^{bulk}/d_{Si//}^{bulk}$ ,

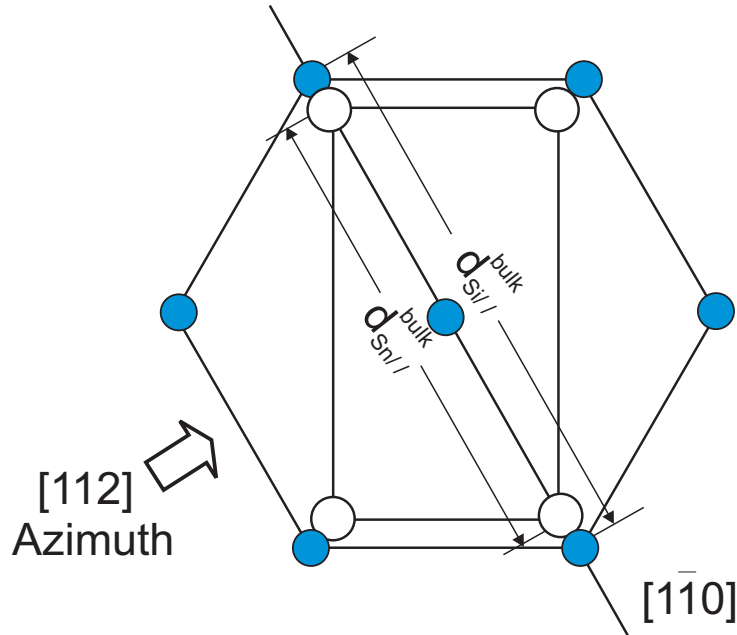


**Figure 6.5:** Schematic model of the epitaxial relationship of  $\beta$ -Sn on the Si(111) surface, where the full circles represent Si atoms, and the open circles  $\beta$ -Sn adatoms. The  $5.83 \text{ \AA} \times 3.18 \text{ \AA}$  rectangular unit mesh ((200) plane) of unrelaxed (bulk-like)  $\beta$ -Sn is plotted inside the unit mesh of Si(111) following a growth model similar to Nishiyama-Wassermann. The arrow indicates the incident direction of the electron-beam, i.e. the [112] direction of the substrate.  $d_{Sn//}$  and  $d_{Si//}$  are the in-plane atomic distances (perpendicular to the [112] substrate direction) of undistorted  $\beta$ -Sn and Si(111), respectively. Equivalent domains of  $\beta$ -Sn(200) grow with their unit cells rotated by  $\pm 60^\circ$  in the film plane.

of unstrained (bulk-like)  $\beta$ -Sn is expected to be 0.87, which should be compared with the value of  $d_{Sn//}/d_{Si//} \sim 0.90$ -0.94 measured by RHEED. The difference between these values demonstrates that in reality the epitaxial  $\beta$ -Sn(200) layers are in-plane expanded by 3-7 % along the  $[1\bar{1}0]$  direction.

### 6.3.2 LEED

Figure 6.6(a) shows a typical LEED pattern of the atomically clean Si(111)-(7x7) surface measured at room temperature with an incident electron energy of 76 eV. With the same energy and same azimuthal orientation, but after the deposition of 60  $\text{\AA}$  Sn, LEED images were recorded at RT (Fig. 6.6(b)) and  $-115^\circ\text{C}$  (Fig. 6.6(c)). The schematics of the arrangement of the LEED spots after the deposition of 60  $\text{\AA}$  Sn are plotted for Figs. 6.6(b) and (c) (right-hand side).

At RT (Fig. 6.6(b)), a (1x1) hexagonal pattern with the same dimensions and orientation as the Si(111) substrate can be observed. The sharpness of these spots and their circular shape also suggest that they originate from a well ordered surface, such as the substrate. This observation supports the idea of island growth, with substrate regions almost uncovered and other regions covered by flat Sn islands. No LEED spots of  $\alpha$ -Sn or

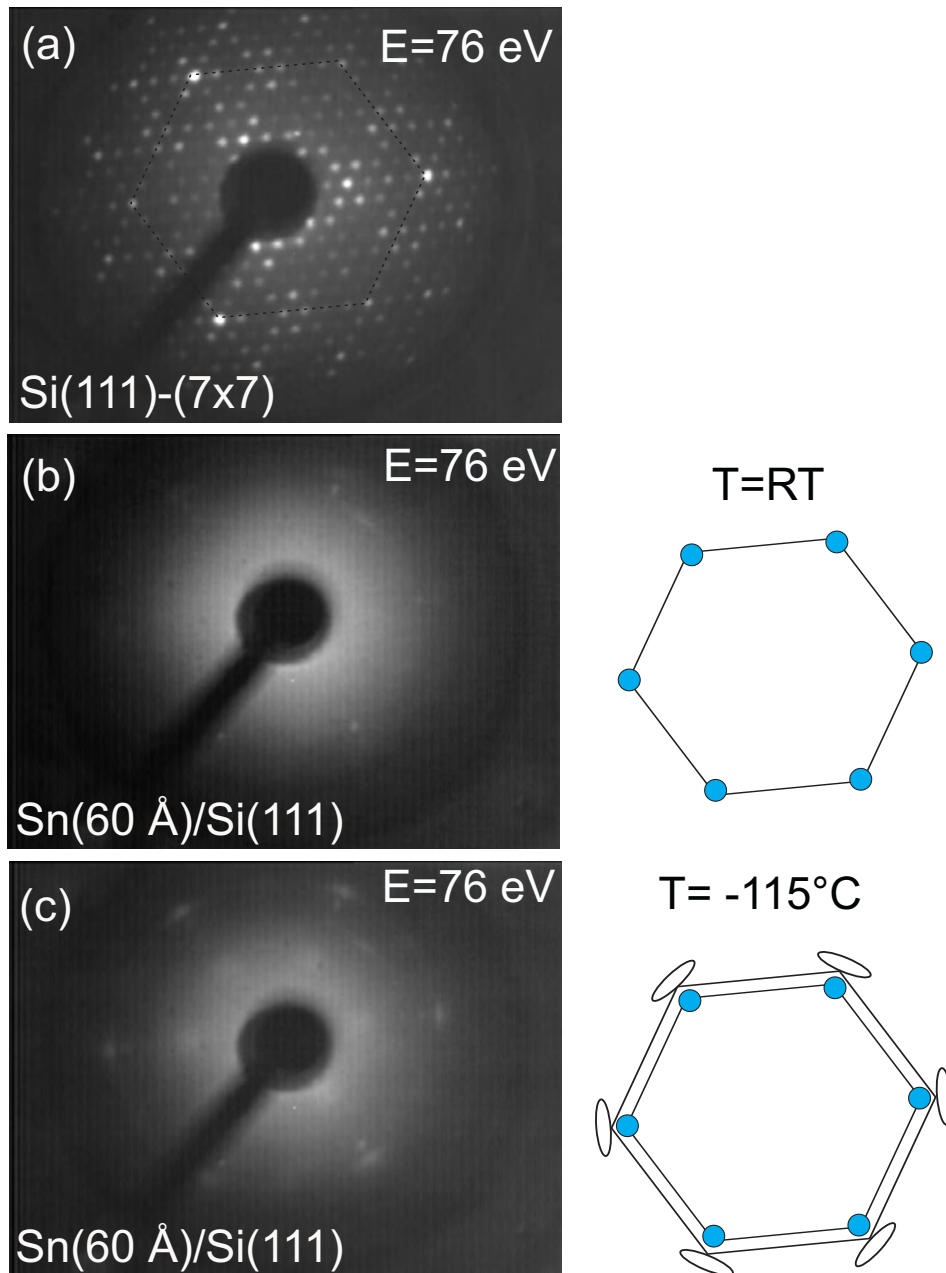


**Figure 6.6:** LEED patterns of the atomically clean Si(111)-(7x7) surface measured at RT (a) and of 60 Å Sn epitaxially grown on Si(111)-(7x7) measured at RT (b) and at -115°C (c), together with schematics of the arrangement of the spots observed (right). All images have been taken under the same angular geometry, and the relative distances of camera and sample to the LEED screen have been maintained constant. The incident electron energy was 76 eV. The circular sharp spots in (b) and (c) originate from the substrate, while the elongated spots in (c) originate from the epitaxial Sn overlayer.

$\beta$ -Sn can be observed at RT at 76 eV. The lack of  $\beta$ -Sn reflections in LEED at RT after the deposition of 60 Å Sn, in spite of the good epitaxial quality of up to 200 Å thick Sn

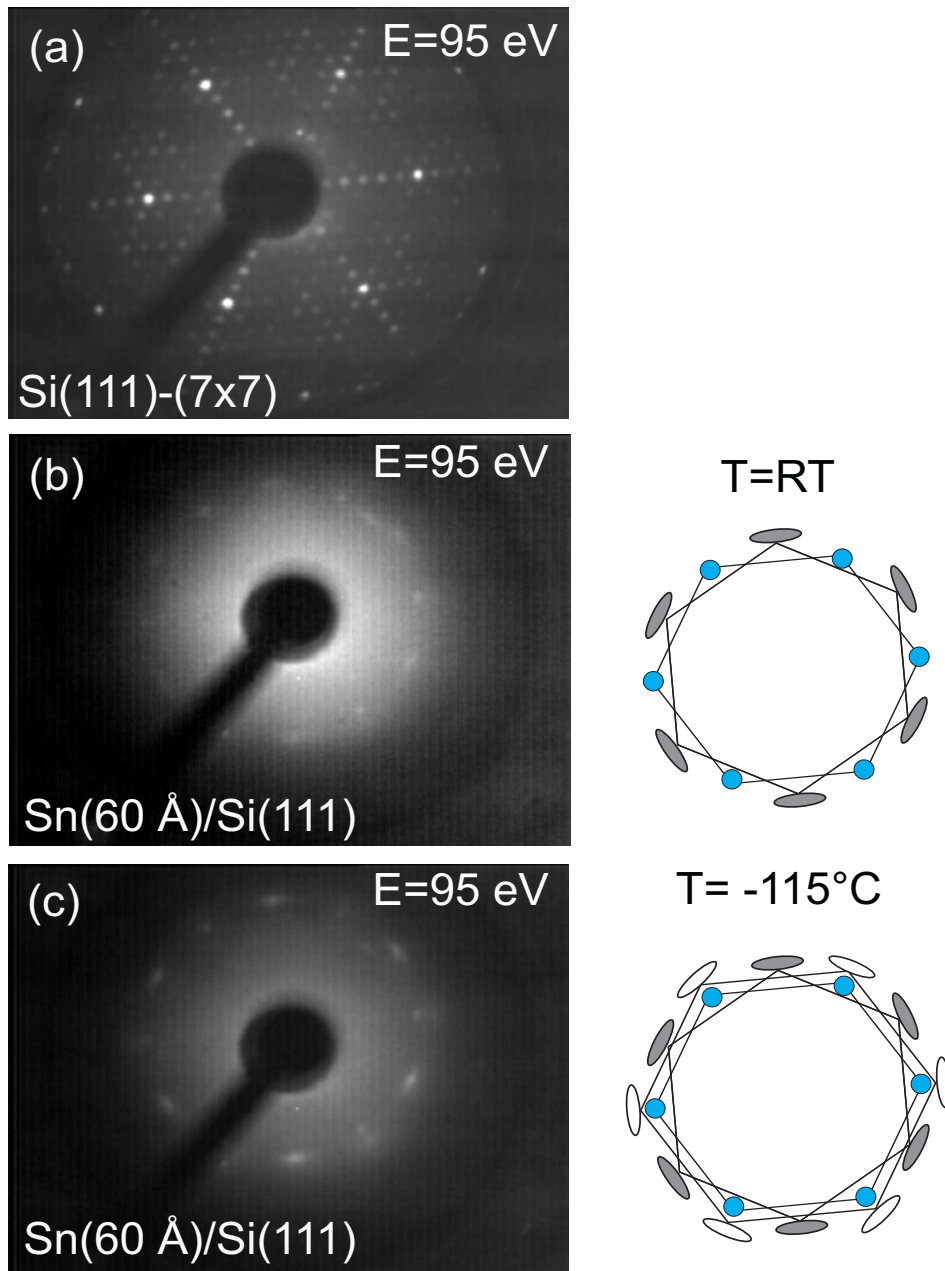


**Figure 6.7:** LEED patterns of the atomically clean Si(111)-(7x7) surface measured at RT (a) and of 60 Å Sn epitaxially grown on Si(111)-(7x7) measured at RT (b) and at -115°C (c), together with a schematics of the arrangement of the spots observed (right). All images have been taken under the same angular geometry, and the relative distances of camera and sample to the LEED screen have been maintained constant. The incident electron energy was 95 eV. Shaded circles: spots from Si substrate; open ellipses: spots from  $\beta$ -Sn. An additional hexagonal pattern rotated by 30° with respect to the hexagonal pattern (dark ellipses) of the Si(111) substrate appears in (b) and (c).



layers according to RHEED (see Fig. 6.3(b)), is explained by the very small Debye-Waller factor of  $\beta$ -Sn ( $f_\beta=0.042$  [122]). With decreasing measurement temperature, the Debye-Waller factor is known to increase strongly. In fact,  $f_\beta$  increases, and at a temperature of  $-115^\circ\text{C}$ , additional reflections with larger inverse spacing (smaller atomic distance) than the Si substrate, but with the same azimuthal orientation, appear in the LEED pattern (Fig. 6.6(c)). These reflections, clearly observed for energies between 70-80 eV, are attributed to  $\beta$ -Sn. This result is in accordance with the Nishiyama-Wassermann-like  $\beta$ -Sn(200)/Si(111) epitaxial model plotted in Fig. 6.5. The LEED spots related to  $\beta$ -Sn are circularly elongated. This shows that the  $\beta$ -Sn domains (according to Fig. 6.5) have a crystallographic texture in the film plane, with a small distribution of azimuthal twisting angles within  $10^\circ$ - $15^\circ$ .

Using the Si(111) substrate as reference, LEED measurements show that the ratio of atomic distances along the  $[1\bar{1}0]$  direction, i.e.  $d_{Si//}/d_{Sn//} \simeq 1.127$ , is compatible with the ratio for the bulk atomic distances  $d_{Si//}^{bulk}/d_{Sn//}^{bulk} \simeq 1.154$  (see Fig. 6.5), if a  $\approx 2.4\%$  in-plane expansion of  $\beta$ -Sn is taken into account. The in-plane atomic distance measured by RHEED along the same direction (see Fig. 6.4(b)) also points at an in-plane expansion of the  $\beta$ -Sn films, though the expansion is larger (3-7 %).

At higher electron energies (85-110 eV), an additional pattern with circularly elongated spots, hexagonal symmetry, and rotated by  $30^\circ$  with respect to the pattern of the Si substrate can be observed at room temperature for Sn thicknesses up to 100 Å. Fig. 6.7(a) displays a LEED pattern of the atomically clean Si(111)-(7x7) surface measured at RT with an energy of 95 eV. With the same angular geometry and energy as in Fig. 6.7(a), but after the deposition of 60 Å Sn, LEED images were recorded with the sample maintained at RT (Fig. 6.7(b)) and at  $-115^\circ\text{C}$  (Fig. 6.7(c)). The schematics of the spot arrangement observed in LEED are again plotted on the right. At RT (Fig. 6.7(b)), the pattern from the substrate appears, as well as a new hexagonal pattern with circularly elongated spots that is rotated by  $30^\circ$  with respect to the Si(111) pattern. The new rotated pattern observed presents a very similar in-plane atomic distance as the substrate, and since it can be observed at RT and low temperature, it cannot be attributed to  $\beta$ -Sn. Therefore, the rotated pattern must originate from substrate regions covered by only small amounts of Sn that remain stabilized as  $\alpha$ -like-Sn constrained by the Si substrate. These areas can be detected by LEED at RT because of the larger Debye-Waller factor ( $f_\alpha=0.16$ ) of  $\alpha$ -Sn relative to that of the  $\beta$ -Sn phase ( $f_\beta=0.042$ ). The  $30^\circ$  rotation observed is not unusual, as it is well known [113, 123] that submonolayer Sn films tend to form surface reconstructions that are rotated by  $30^\circ$  with respect to the diffraction pattern of the substrate. Similar LEED patterns with hexagonal symmetry and almost identical in-plane unit-mesh to the substrate, but rotated by  $30^\circ$ , have been recorded at RT also for total Sn thicknesses of 20 Å, 30 Å and 100 Å (not shown).

Fig. 6.7(c) shows a LEED pattern of 60 Å Sn deposited on Si(111) and measured at  $-115^\circ\text{C}$  ( $E=95$  eV). In this case, together with the two sets of reflections from the Si substrate and  $30^\circ$ -rotated  $\alpha$ -Sn, one can also recognize weak  $\beta$ -Sn spots, with an in-plane unit mesh larger than the Si substrate in reciprocal space. The  $\beta$ -Sn pattern is similar to that observed in Fig. 6.6(c) for a lower incident electron energy.

Above 115 eV and up to 200 eV, the LEED patterns observed show only reflections from the Si(111) substrate. The spots observed were not elongated or rotated, but rather sharp, showing a three-fold symmetry for certain energies which is characteristic of the Si(111) surface. Scanning electron microscopy images performed ex-situ on Sn(200 Å)/Si(111) (see section 6.3.4) will confirm the hypothesis of the formation of Sn islands that do not coalesce even after the deposition of a large amount of Sn, leaving regions on the substrate between  $\beta$ -Sn islands which are almost uncovered.

### 6.3.3 Auger Electron Spectroscopy (AES)

The Sn-thickness dependence of Auger electron spectra has been measured as an additional check of the origin of the substrate-like spots observed by LEED on Sn-covered Si(111). Fig. 6.8 displays AES spectra measured after the deposition of (a) 10 Å Sn, (b) 20 Å Sn, (c) 40 Å Sn, (d) 60 Å Sn, (e) 100 Å Sn, and (f) 200 Å Sn. In addition to the double peak of Sn at 430-437 eV, the weak peak of Si at 91 eV can be observed in all spectra. The intensity of the AES Si signal relative to the Sn signal decreases with increasing thickness from 10 to 200 Å Sn, but does not approach zero (Fig. 6.9). This demonstrates that there are substrate regions covered only by a small amount of Sn (very likely  $\alpha$ -Sn) even after the deposition of relatively thick Sn films, and these open regions provide a non-negligible substrate signal to the LEED patterns.

### 6.3.4 Scanning Electron Microscopy (SEM)

In collaboration with the group of Prof. E.F. Wassermann and Dr. G. Dumpich (Duisburg) scanning electron microscopy measurements were performed ex-situ on a 200 Å thick Sn film epitaxially grown on Si(111). Figures 6.10(a) and (b) show large Sn islands of diameters between 100-500 nm. The islands do not coalesce even after depositing 200 Å Sn, and regions of the Si substrate almost uncovered by Sn can be observed. This effect must be due to a large surface energy of the  $\beta$ -Sn clusters formed compared to the Sn/Si interfacial energy, resulting in agglomeration rather than wetting of the substrate. The rather sharp RHEED streaks (Fig. 6.3(b)) measured on such samples show that the top of the Sn islands must be relatively flat on an atomic scale.

### 6.3.5 $^{119}\text{Sn}$ CEMS

It is well known [124, 125], that measurements of the isomer shift in thin Sn layers and multilayers enable one to distinguish  $\alpha$ - from  $\beta$ -Sn [121, 126], taking into account the  $\simeq 0.5$  mm/s difference in the isomer shifts of bulk  $\alpha$ -Sn ( $\delta = + 2.03 \pm 0.02$  mm/s at RT) and bulk  $\beta$ -Sn ( $\delta = + 2.56 \pm 0.01$  mm/s at R.T.), both values relative to the BaSnO<sub>3</sub> (or CaSnO<sub>3</sub>) standard absorber [124–126].

Fig. 6.11 displays the thickness dependence of  $^{119}\text{Sn}$  CEM spectra of epitaxial Sn layers grown on Si(111)-(7x7) at RT. Below 4 ML coverage (Fig. 6.11(a)-(c)), pure  $\alpha$ -Sn was found.  $\beta$ -Sn appears above this critical thickness when the coverage is further increased (Fig. 6.11(d),(e)). Fig. 6.11(f) shows a typical  $\beta$ -Sn spectrum corresponding

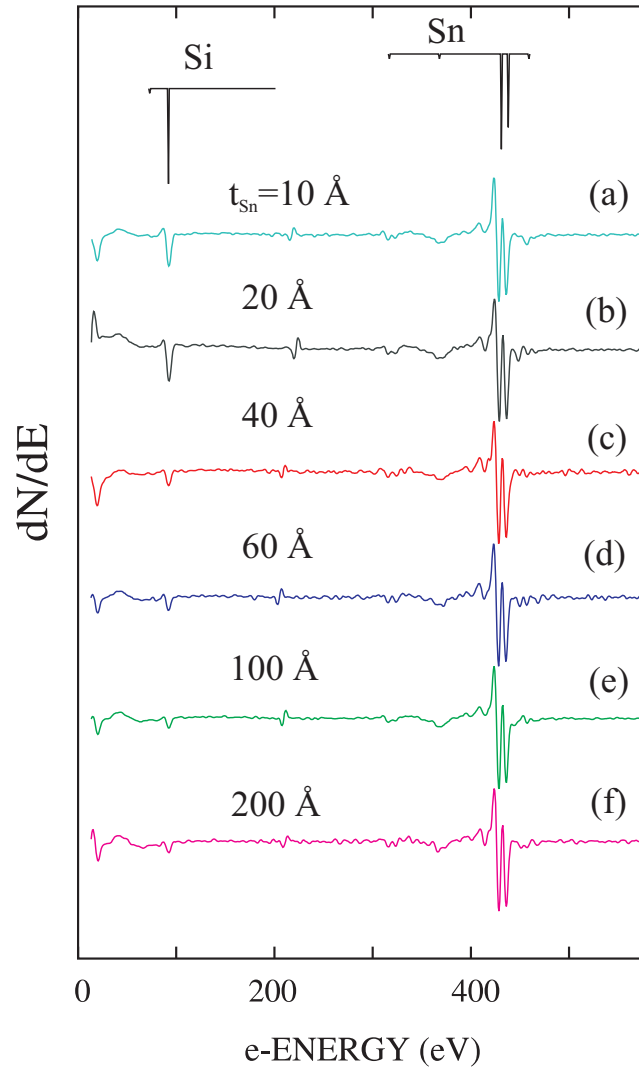


**Figure 6.8:** Auger electron spectra measured after the deposition of  $\text{Sn}(t_{\text{Sn}})/\text{Si}(111)$  with  $t_{\text{Sn}} = 10 \text{ \AA}$  (a),  $20 \text{ \AA}$  Sn (b),  $40 \text{ \AA}$  (c),  $60 \text{ \AA}$  (d),  $100 \text{ \AA}$  Sn (e), and  $200 \text{ \AA}$  Sn (f). The full solid lines on top of the spectra indicate the predicted position of the AES peaks of Si and Sn. For comparison, all spectra have been normalized to show the same peak-to-peak Sn intensity.

to approximately  $1020 \text{ \AA}$  natural Sn on Si(111). It is important to note that after the thickness dependent  $\alpha \rightarrow \beta$ -Sn transition at 3.5-4 ML,  $\alpha$ -Sn remains stabilized at the interface, and does not transform to  $\beta$ -Sn (Fig. 6.11(d),(e)).

Table 6.1 displays the Mössbauer parameters (isomer shift  $\delta$ , Lorentzian linewidth  $\Gamma$ , and the relative contribution of the  $\alpha$ - and  $\beta$ -Sn phases ( $A_\alpha$ ,  $A_\beta$ ) to the total spectral area of the Mössbauer spectra) obtained by least-squares fitting of the experimental spectra. All spectra were fitted either with one (Fig. 6.11(a),(b),(c), and (f)) or two (Figs. 6.11(d),(e)) Lorentzian lines. The isomer shifts obtained are in accordance with those of the  $\alpha$ -Sn and  $\beta$ -Sn phases, respectively.

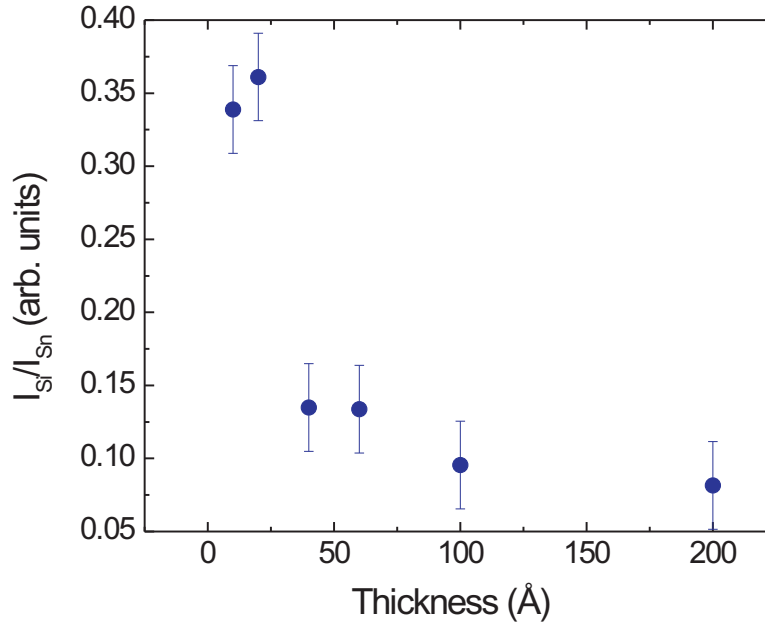


**Figure 6.9:** Sn-thickness dependence of the intensity ratio of the Auger signals (measured peak-to-peak) of Si (at 91 eV) and Sn (at 430 eV).

Sn( $t_{Sn}$ )/Si(111)	Isomer Shift		Lorentzian Linewidth (FWHM) $\Gamma$ (mm/s)		Area	
	$\delta$ (mm/s)		$\alpha$ -Sn	$\beta$ -Sn	%	
$t_{Sn}$	$\alpha$ -Sn	$\beta$ -Sn	$\alpha$ -Sn	$\beta$ -Sn	$A_\alpha$	$A_\beta$
6 Å	$2.023 \pm 0.008$		$1.40 \pm 0.03$		$100 \pm 2$	
10 Å	$2.07 \pm 0.02$		$1.41 \pm 0.07$		$100 \pm 4$	
13 Å	$2.06 \pm 0.02$		$1.61 \pm 0.07$		$100 \pm 4$	
18 Å	$1.89 \pm 0.04$	2.66	$1.3 \pm 0.1$	1.08	$70 \pm 8$	$30 \pm 5$
25 Å	$1.80 \pm 0.05$	2.66	$1.2 \pm 0.1$	1.08	$61 \pm 7$	$39 \pm 5$
1020 Å		$2.66 \pm 0.02$		$1.08 \pm 0.06$		$100 \pm 5$

**Table 6.1:**  $^{119}\text{Sn}$  Mössbauer parameters (isomer shift  $\delta$ , linewidth  $\Gamma$ ) measured at RT. For  $18 \text{ \AA} \leq t_{Sn} \leq 1020 \text{ \AA}$ , the isomer shift and linewidth of the  $\beta$ -Sn line was a fixed parameter at  $+2.66 \text{ mm/s}$  during the least-squares fitting, which is the value obtained for  $1020 \text{ \AA}$   $\beta$ -Sn epitaxially grown on Si(111).  $A_\alpha$  and  $A_\beta$  represent the relative contribution of the  $\alpha$ - and  $\beta$ -Sn phases, respectively, to the total spectral area of the Mössbauer spectra shown in Fig. 6.11

In Fig. 6.11(f), no  $\alpha$ -Sn contribution was detected, because this  $1020 \text{ \AA}$  thick Sn sample is made from natural Sn, and  $\sim 13 \text{ \AA}$  natural  $\alpha$ -Sn (maximum Sn thickness that

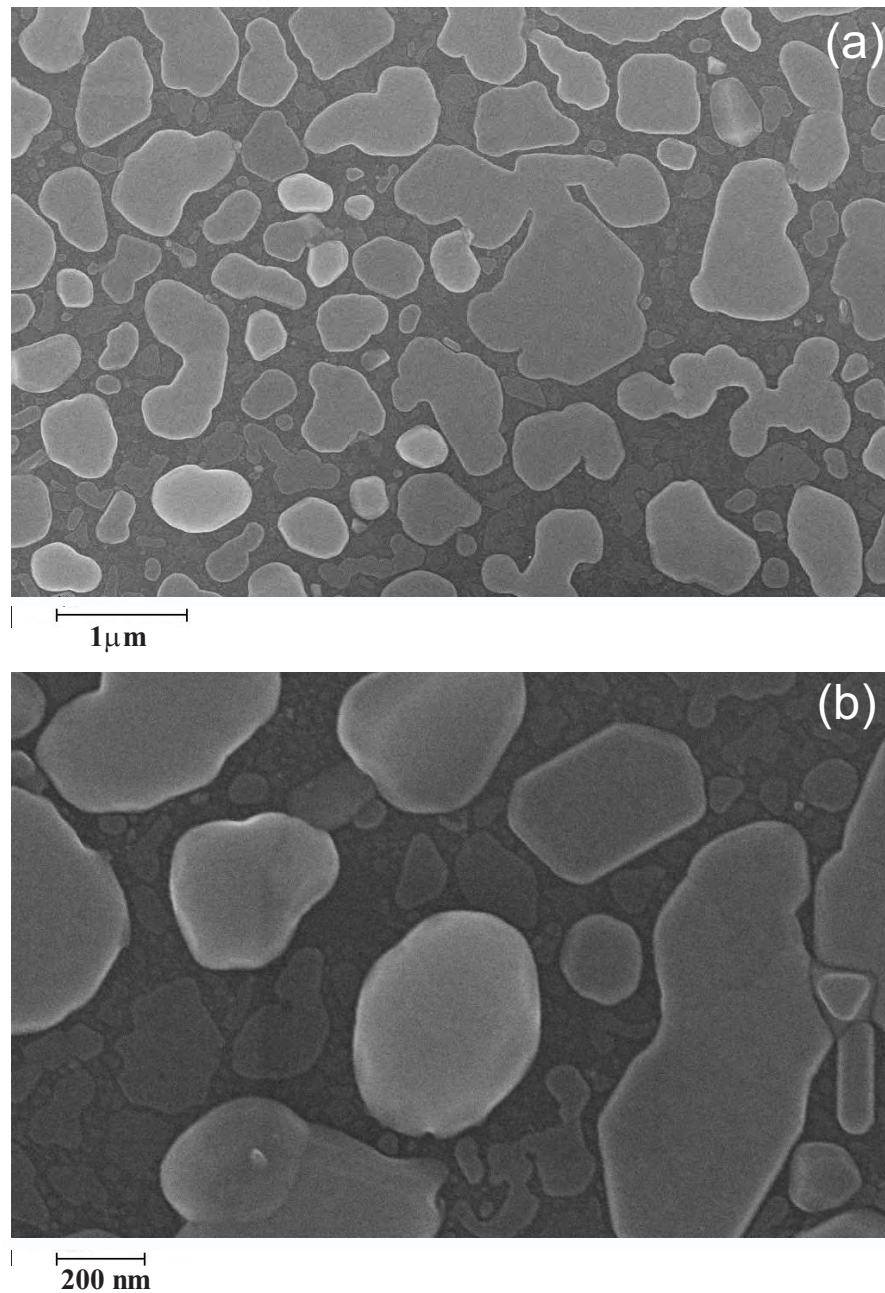


**Figure 6.10:** Ex-situ scanning electron microscopy images of Sn(200 Å)/Si(111) measured with scales of (a) 1  $\mu\text{m}$  and (b) 200 nm (High Voltage=20kV).

can be stabilized as  $\alpha$ -Sn at the Sn/Si interface) will give an effective contribution to the Mössbauer spectrum equivalent to one Angstrom of  $^{119}\text{Sn}$ , which provides a negligible signal as compared to that from the residual 1007 Å  $\beta$ -Sn layer.

For a more detailed study of the Sn/Si(111) interface, 0.7-1.5 ML thick isotopically

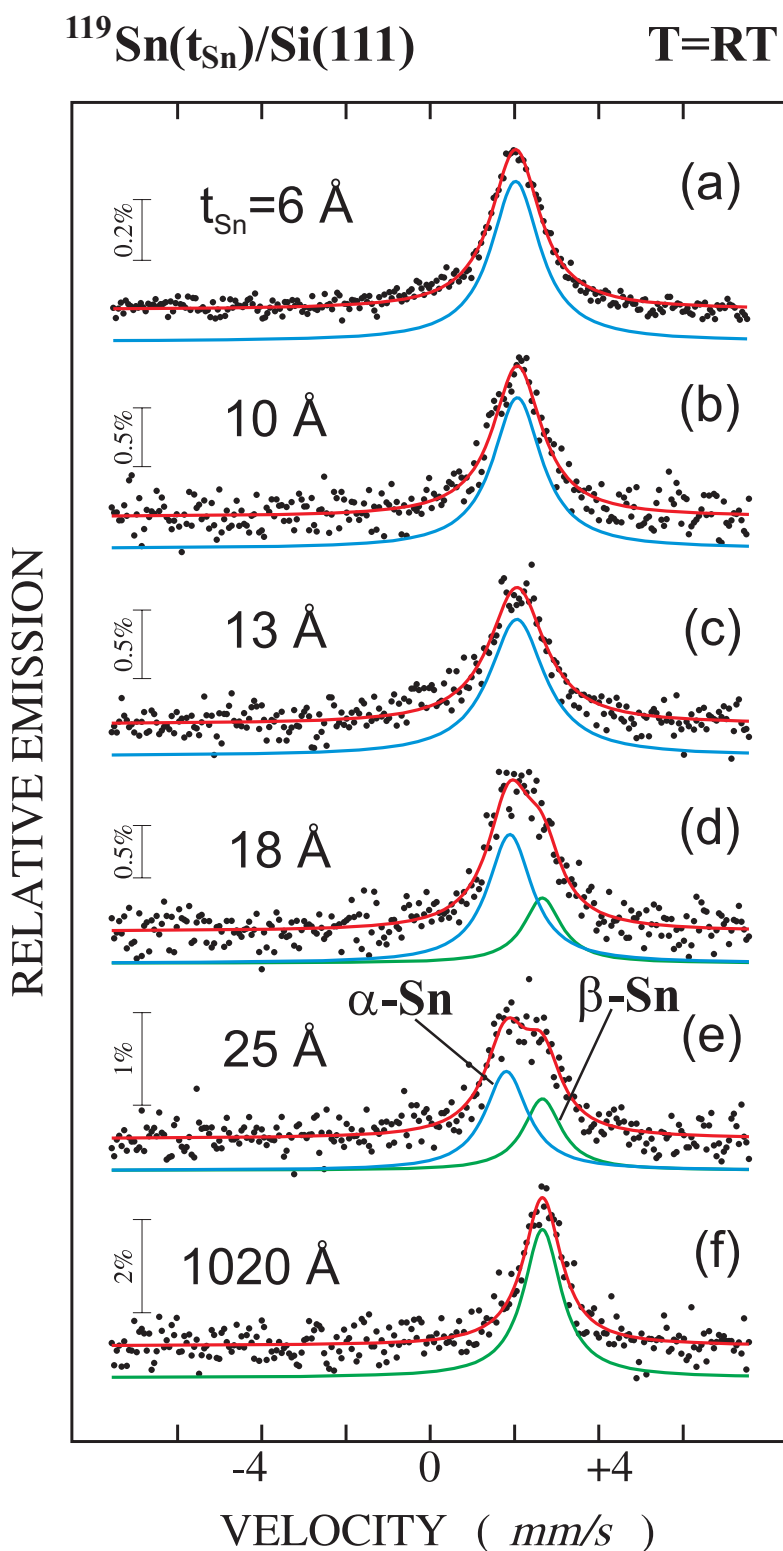


**Figure 6.11:**  $^{119}\text{Sn}$  CEM spectra of epitaxial  $^{119}\text{Sn}(t_{\text{Sn}})$  on  $\text{Si}(111)(7\times 7)$  deposited and measured (ex-situ) at RT : (a)  $t_{\text{Sn}} = 6 \text{ \AA}$ ; (b)  $t_{\text{Sn}} = 10 \text{ \AA}$ ; (c)  $t_{\text{Sn}} = 13 \text{ \AA}$ ; (d)  $t_{\text{Sn}} = 18 \text{ \AA}$ ; (e)  $t_{\text{Sn}} = 25 \text{ \AA}$ ; (f)  $t_{\text{Sn}} = 1020 \text{ \AA}$ ; all samples were coated by 50-60  $\text{\AA}$  amorphous Si for protection.

(82.9 %) enriched  $^{119}\text{Sn}$  probe layers were deposited in several positions directly at and near to the Sn/Si interface. Interface-selectivity is achieved by means of these strategically positioned  $^{119}\text{Sn}$  probe layers, which are surrounded by thin natural Sn layers. (Natural  $^{119}\text{Sn}$  abundance: 8.58 %).

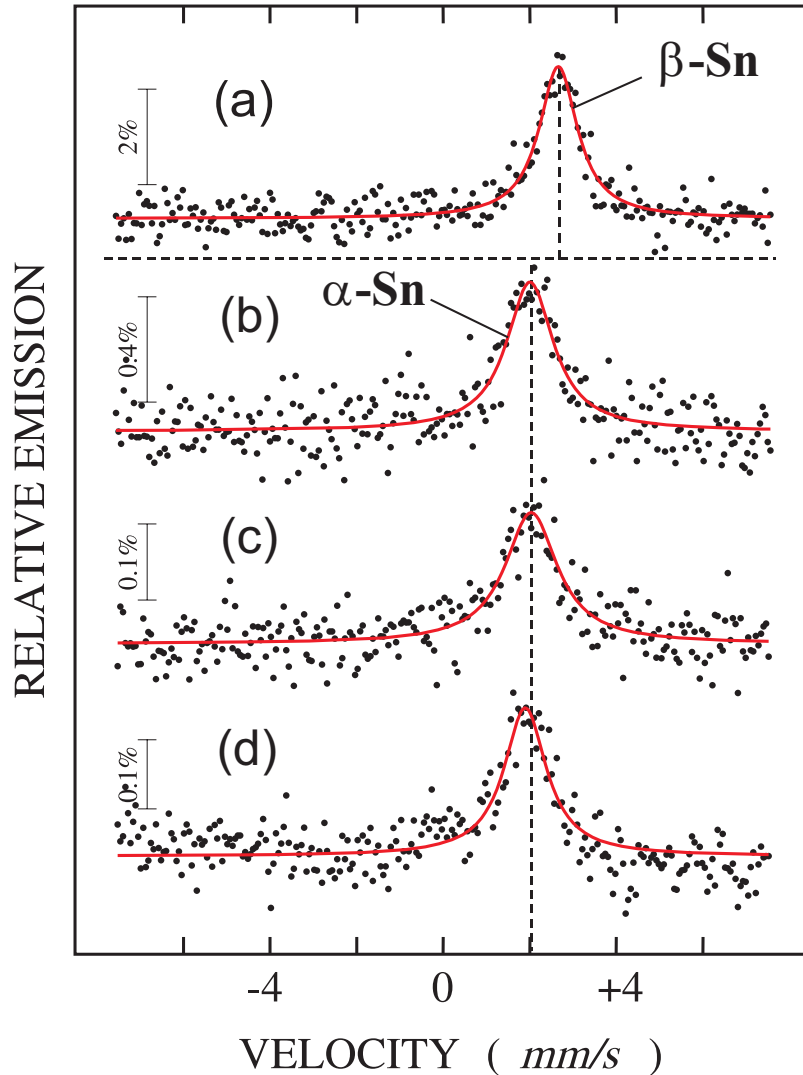


**Figure 6.12:**  $^{119}\text{Sn}$  probe-layer CEM spectra measured (ex-situ) at RT on epitaxial Sn films on Si(111) 7x7: (a)  $^{nat}\text{Sn}(1020 \text{ \AA})/\text{Si}(111)$ ; (b)  $^{nat}\text{Sn}(4.5 \text{ ML})/^{119}\text{Sn}(1.5 \text{ ML})/\text{Si}(111)$ , (c)  $^{nat}\text{Sn}(4.5 \text{ ML})/^{119}\text{Sn}(1.5 \text{ ML})/^{nat}\text{Sn}(1.5 \text{ ML})/\text{Si}(111)$  and (d)  $^{nat}\text{Sn}(3.7 \text{ ML})/^{119}\text{Sn}(0.7 \text{ ML})/\text{Si}(111)$ . All samples were coated by 50-60  $\text{\AA}$  amorphous Si for protection. ( $^{nat}\text{Sn}$  means Sn of natural isotopic abundance of 8.58 %).

Fig. 6.12 displays the CEMS spectra from the  $^{119}\text{Sn}$  probe layers. Since only 8.58 %  $^{119}\text{Sn}$  is found in natural Sn, the  $^{119}\text{Sn}$  CEMS originate almost exclusively from the  $^{119}\text{Sn}$  probe layers. The spectra in Fig. 6.12(b) to (d) exhibit the typical isomer shift of  $\alpha\text{-Sn}$  (Table 6.2), independent of the thin natural  $\beta\text{-Sn}$  layers. Fig. 6.12(b) demonstrates that

Sample	Isomer Shift $\delta$ (mm/s)		Lorentzian Linewidth (FWHM) $\Gamma$ (mm/s)
	$\alpha$ -Sn	$\beta$ -Sn	
$^{nat}\text{Sn}(1020 \text{ \AA})/\text{Si}(111)$		$2.66 \pm 0.02$	$1.08 \pm 0.06$
$^{nat}\text{Sn}(4.5 \text{ ML})/^{119}\text{Sn}(1.5 \text{ ML})/\text{Si}(111)$	$2.01 \pm 0.03$		$1.3 \pm 0.1$
$^{nat}\text{Sn}(4.5 \text{ ML})/^{119}\text{Sn}(1.5 \text{ ML})/^{nat}\text{Sn}(1.5 \text{ ML})/\text{Si}(111)$	$2.03 \pm 0.04$		$1.5 \pm 0.1$
$^{nat}\text{Sn}(3.7 \text{ ML})/^{119}\text{Sn}(0.7 \text{ ML})/\text{Si}(111)$	$1.90 \pm 0.03$		$1.19 \pm 0.09$

**Table 6.2:** Room-temperature  $^{119}\text{Sn}$  Mössbauer parameters (isomer shift  $\delta$ , linewidth  $\Gamma$ ) obtained from Fig. 6.12.

1.5 ML of  $\alpha$ -Sn remains stable at the Sn/Si(111) interface even after depositing another 4.5 ML of natural Sn on top.

Fig. 6.12(c) displays the Mössbauer spectrum of a 1.5 ML thick  $^{119}\text{Sn}$  probe layer that is coated by 4.5 ML of natural Sn and is separated from the Sn/Si(111) interface by 1.5 ML of natural Sn. Since this probe layer exhibits the isomer shift of  $\alpha$ -Sn (Table 6.2), this result proves that at least the first 3 ML of Sn grown on Si(111) are stabilized in the  $\alpha$ -Sn phase.

Finally, Fig. 6.12(d) and the isomer shift in Table 6.2 prove that a submonolayer (0.7 ML) of Sn at the Sn/Si(111) interface remains  $\alpha$ -like-Sn after the coating with 4 ML of natural Sn, since the isomer shift ( $\delta$ ) measured is close to that of bulk  $\alpha$ -Sn. Nevertheless, a slight difference in the isomer shift of this ultrathin layer with respect to that of bulk  $\alpha$ -Sn is found. In this case,  $\delta$  is equal to  $+1.90 \pm 0.03$  mm/s, which is slightly smaller than the value for bulk  $\alpha$ -Sn ( $+2.03$  mm/s at RT). This indicates a thickness dependent chemical shift for such submonolayer interfacial Sn layers.

## 6.4 Discussion

The  $\alpha$ -Sn/Si(111) interface has a lower misfit energy than the  $\beta$ -Sn/Si(111) interface, which would have to accommodate a considerable mismatch in symmetry and dimension via interfacial dislocations. The pseudomorphic growth observed in RHEED (Fig. 6.1) up to 3.5 ML shows that the  $\alpha$ -Sn/substrate misfit is accommodated largely by misfit elastic strain. This maximum interfacial  $\alpha$ -Sn thickness of  $\sim 3.5$  ML is in agreement with STM studies performed by Wang et al. [112], who observed the onset of  $\beta$ -Sn island-growth above 3.5 ML.

The in-plane atomic distances displayed in Fig. 6.4(b) show that the influence of the substrate on the condensing adatoms diminishes with increasing thickness during growth, and after reaching a critical thickness of 3.5 ML, the nucleation of  $\beta$ -Sn during growth at a temperature  $> 13.2^\circ\text{C}$  is energetically more favorable than the continuation of the  $\alpha$ -Sn growth.



During the experiments it was noticed the importance of a well ordered and clean Si(7x7) surface for the  $\alpha$ -Sn interfacial stabilization, because the deposition of Sn on C or O contaminated surfaces promoted the nucleation of  $\beta$ -Sn at earlier growth-stages ( $< 3.5$  ML). Even long time RHEED observations with a high electron beam voltage ( $> 10$  keV) during RT deposition were found to affect the Sn growth [113], because a slight increase in temperature promoted an earlier  $\alpha$  to  $\beta$ -Sn transformation. These facts explain the controversy in the literature, because from diffraction techniques it is difficult to determine, if  $\alpha$ -Sn is present at the Sn/Si(111) interface, and even more difficult to establish the maximum  $\alpha$ -Sn thickness that can be stabilized by the substrate.

Mössbauer measurements performed on 0.7 ML  $\alpha$ -Sn deposited directly at the Si(111) interface (Fig. 6.12 and Table 6.2) indicated a  $\sim 0.13$  mm/s decrease  $\Delta\delta$  in the isomer shift with respect to the value of bulk  $\alpha$ -Sn. Since the isomer shift is proportional to the total s-electron density at the nucleus,  $|\psi(0)|^2$ , the decrease in the isomer shift of interfacial  $\alpha$ -Sn obtained is equivalent to a reduction  $\Delta|\psi(0)|^2$  of the s-electron density at the Sn nucleus by  $\approx 1.5a_0^{-3}$  ( $a_0$ =Bohr radius), relative to bulk  $\alpha$ -Sn, as follows from eq. (6.2):

$$\Delta|\psi(0)|^2 = \Delta\delta/\alpha \quad (6.2)$$

,where  $\alpha=0.086 a_0^{-3}$  mm/s for  $^{119}\text{Sn}$  [127].

This effect indicates some kind of electronic interaction between Sn and Si atoms at the interface. Ichikawa et al. [113] proposed the formation of Sn germanides and Sn silicides in the surface regions as possible explanation for the appearance of new superstructures (e.g.  $\sqrt{91}\times\sqrt{3}$ ,  $\sqrt{133}\times 4\sqrt{3}$ ) during the growth of Sn on Ge(111) or Si(111) substrates at high temperatures. Ichikawa affirmed that the large superstructures observed were not the result from absorption of Sn atoms on special positions (e.g. on-top and hollow sites) of the substrate surface, but were Sn overlayers reconstructed by a deposit-substrate interaction. Such an interaction could also explain the slight reduction of s-electron density at the Sn nuclei that has been observed.

## 6.5 Conclusions

The epitaxial growth of Sn layers on Si(111)(7x7) surfaces at room temperature was investigated by RHEED, LEED and  $^{119}\text{Sn}$  CEMS. The formation of up to 3.5 ML of metastable  $\alpha$ -Sn at the Sn/Si(111) interface was observed. The interfacial  $\alpha$ -Sn layer remains stabilized even after further deposition of thick Sn layers that undergo the  $\alpha$ -Sn  $\rightarrow$   $\beta$ -Sn transformation. Layer-by-layer-like growth is observed up to 3 ML coverage, i.e. in the  $\alpha$ -Sn region. Only a small decrease (relative to bulk  $\alpha$ -Sn) by  $\sim 1.5 a_0^{-3}$  of the total s-electron density at the  $^{119}\text{Sn}$  nucleus was measured for submonolayers of  $^{119}\text{Sn}$  at the Sn/Si interface, indicating only weak electronic charge transfer at the interface.

The present RHEED and LEED results demonstrate that for Sn coverages larger than 3.5-4 ML flat epitaxial  $\beta$ -Sn islands grow, with the epitaxial relationship  $\beta$ -Sn(200)//Si(111) and  $\beta$ -Sn[011]//Si[1 $\bar{1}$ 0]. The observed six-fold LEED pattern is compatible with three crystallographic domains with this epitaxial relationship, but rotated

by  $60^\circ$  and  $120^\circ$ . These rotational angles show a small angular distribution in the film plane with a width of  $10^\circ$ - $15^\circ$ . The measured in-plane atomic distance of epitaxial  $\beta$ -Sn is expanded by 2-7 % relative to that of bulk- $\beta$ -Sn. AES signals and SEM images demonstrate that the flat  $\beta$ -Sn islands do not uniformly cover the substrate surface even after the deposition of up to 200 Å Sn. Thus, wetting of the Si substrate by Sn is inhibited, probably due to the high surface energy of Sn.

For several incident electron energies (85-110 eV) and rather thick Sn films, an additional six-fold (1x1) LEED pattern similar to that of the Si(111) substrate, but rotated by  $30^\circ$ , was observed. This pattern might originate from uncoated  $\alpha$ -Sn regions, located in the space between  $\beta$ -Sn islands.

## 7 Structure and vibrational dynamics of interfacial Sn layers in Sn/Si multilayers

### 7.1 Introduction

Elemental semiconductors with diamond structure, e.g. Si or Ge, are known to exist in amorphous form when prepared either as bulk glasses or as thin films [128, 129]. An exception is gray tin ( $\alpha$ -Sn) which in the crystalline state is a non-polar semiconductor with diamond structure and a band-gap nearly equal to zero (0.08 eV at 300 K) [130]. Only one literature report is known to exist on the observation of the *amorphous* phase of  $\alpha$ -Sn, in this case produced by ion implantation [131]. The amorphous structure of group IV semiconductors (Ge,Si) has been shown [132] to deviate from the ideal tetrahedral coordination of the diamond structure by bending of the four nearest neighbor covalent bonds, with a spread in bond angles of about 10 degrees around the ideal value of 109°. Deviations by bond lengthening are not observed to be more than 1% [132]. At ambient pressure  $\alpha$ -Sn is the stable low-temperature phase of bulk tin, which transforms into the metallic body-centered tetragonal  $\beta$ -Sn phase (with lattice parameters  $a=5.83 \text{ \AA}$ ,  $c=3.18 \text{ \AA}$ ) when the temperature is raised above  $T_c=13.2^\circ\text{C}$ . The  $\alpha \longleftrightarrow \beta$  phase transition of bulk Sn is an entropy driven structural transformation which is determined by the difference in vibrational entropy of the two phases [133]. It has been shown that crystalline  $\alpha$ -Sn ( $a=6.489 \text{ \AA}$ ) can be stabilized as a metastable phase above  $T_c$  (and in particular at room temperature, RT) in the form of a film of considerable thickness ( $\sim 1000 \text{ \AA}$ ) by heteroepitaxy on an appropriate substrate. For instance, epitaxial RT growth of  $\alpha$ -Sn films is feasible on InSb(001) substrates ( $a=6.4798 \text{ \AA}$ ) because of close lattice matching [110, 126, 130, 134–137]. On the other hand, RT growth of epitaxial  $\alpha$ -Sn type overlayers on Si(111) substrates has been shown in chapter 6 to be limited to only  $\sim 3$  atomic layers, because the larger lattice misfit (Si:  $a=5.4309 \text{ \AA}$ ) favors the transition to  $\beta$ -Sn above such low Sn coverages.

In the present work Sn( $t_{Sn}$ )/Si( $t_{Si}$ ) multilayers of different Sn and Si thicknesses ( $t_{Sn}$  and  $t_{Si}$ , respectively) are investigated. Contrary to the crystallographically well-ordered epitaxial systems described in chapter 6, the Sn layers in the present multilayers are embedded between amorphous Si (a-Si) layers. This poses the interesting question for the type of crystallographic structure of the Sn layers under this condition, in particular in the Sn/Si interfacial region. In general, knowledge of the interfacial structure is important for the detailed understanding of Schottky barriers in metal/semiconductor systems [138]. Sn/Si multilayers form an interesting system, where atomic interdiffusion at the Sn/Si interfaces may be excluded, because Sn and Si do not form any solid solutions or compounds, even after melting, according to the thermodynamic phase diagram [139]. The principle aim of this study was to gain insight on the structure and lattice dynamics of the Sn layers, in particular, the Sn/Si interfacial region. Phonons in superlattices are of general interest, because phenomena like Brillouin zone folding, interface modes and confined phonon modes that do not exist in bulk materials may be observed [140, 141].

Since the maximum phonon energy of bulk Sn ( $\alpha$ -Sn in this case) is near  $\sim 200 \text{ cm}^{-1}$  (or  $\sim 24.8 \text{ meV}$ ) and thus rather low [133], while the vibrational excitations of a-Si extend up to much higher energies ( $\sim 600 \text{ cm}^{-1}$  or  $\sim 74.4 \text{ meV}$ ) [128, 129, 132], confinement may be expected for a considerable part of high energy excitations in a-Si, but not in the Sn layers. However, phonons in the Sn layers might be influenced by evanescent modes of confined excitations in the a-Si layers [140, 141].

Several techniques have been employed, including X-ray diffraction (XRD), Raman scattering,  $^{119}\text{Sn}$  conversion-electron Mössbauer spectroscopy (CEMS), and  $^{119}\text{Sn}$  nuclear resonant inelastic X-ray scattering (NRIXS) of synchrotron radiation. NRIXS is an efficient and unique method for the direct measurement of the vibrational (or phonon) density of states (VDOS) of thin films and buried interfaces that contain Mössbauer isotopes, independent of whether the structure is crystalline or amorphous [12, 142–145]. CEMS and NRIXS are local methods providing information on an atomic scale.

## 7.2 Experimental

### 7.2.1 Sample preparation

$^{119}\text{Sn}/\text{Si}$  multilayers of composition  $[\text{Sn}(t_{\text{Sn}})/\text{Si}(t_{\text{Si}})]_n$  were grown on Si(111) wafers in an ultrahigh vacuum (UHV) system, with Sn thicknesses ( $t_{\text{Sn}}$ ) between  $0.4 \text{ \AA}$  and  $100 \text{ \AA}$ , and Si thicknesses ( $t_{\text{Si}}$ ) between  $20 \text{ \AA}$  and  $80 \text{ \AA}$ . The number of bilayers,  $n$ , varies between 1 and 50. The enrichment of  $^{119}\text{Sn}$  was 82.9 %. The Si substrates were rinsed in acetone and ethanol just before being loaded into the UHV chamber. The Si(111) substrates were cleaned in situ by annealing for 15 minutes at  $300^\circ\text{C}$ .

The multilayers were grown at two different deposition temperatures,  $T_s$ , i.e.  $-50^\circ\text{C}$  and RT, to investigate the effect of temperature on the  $\alpha \rightarrow \beta$  phase transition. High-purity (undoped) Si was evaporated by an electron gun with a deposition rate of  $0.1\text{-}0.2 \text{ \AA/s}$ , and a deposition pressure of  $3\text{-}5 \cdot 10^{-9} \text{ mbar}$ . At first, a Si layer was deposited on the Si(111) substrates, and all multilayers were coated with Si on the top to avoid oxidation. It is known that UHV deposition of Si films under such conditions results in amorphous (a-)Si layers. Metallic  $^{119}\text{Sn}$  was evaporated from a Knudsen cell ( $\text{Al}_2\text{O}_3$  crucible) at a deposition pressure of  $1\text{-}2 \cdot 10^{-9} \text{ mbar}$  and a deposition rate between  $0.02\text{-}0.025 \text{ \AA/s}$ . The real substrate temperature during deposition was somewhat higher than the previously indicated values, since up to  $40^\circ\text{C}$  was measured by a thermocouple at the sample holder for the RT case.

The evaporation rates and film thicknesses were monitored with a calibrated quartz-crystal microbalance and were determined from the bulk density of  $\beta$ -Sn. Additionally, X-ray ( $\theta$ - $2\theta$ ) reflectometry studies under grazing incidence geometry were performed to check the quality and thickness periodicity of the multilayers.

For comparison, also epitaxial  $200\text{-}500 \text{ \AA}$   $^{119}\text{Sn}(001)$  films (crystalline  $\alpha$ -Sn) on  $\text{InSb}(001)$  substrates were grown, as described in Ref. [126].

### 7.2.2 $^{119}\text{Sn}$ CEMS

$^{119}\text{Sn}$  conversion electron Mössbauer spectroscopy (CEMS) provides information on the structural phase of tin in the multilayers from the  $\simeq 0.5$  mm/s difference in the isomer shifts of bulk  $\alpha$ -Sn ( $\delta = 2.03 \pm 0.02$  mm/s at RT) and bulk  $\beta$ -Sn ( $\delta = 2.56 \pm 0.01$  mm/s at RT). Both isomer shift values are relative to  $\text{BaSnO}_3$  or  $\text{CaSnO}_3$  standard absorbers as shown in Ref [124,125]. Electric quadrupole interactions in non-cubic covalent and/or metallic Sn systems (e.g. in tetragonal  $\beta$ -Sn) are very weak due to the small electric quadrupole moment of only -0.064 barn for the excited state of the  $^{119}\text{Sn}$  Mössbauer nucleus [125]. For the 23.88-keV Mössbauer  $\gamma$ -radiation,  $^{119}\text{Sn}^*$  in a  $\text{CaSnO}_3$  matrix was used as source. For electron detection a He-4%  $\text{CH}_4$  gas proportional counter was used, with the sample mounted inside of the counter. An electromechanical Mössbauer drive and conventional electronics (Wissel GmbH., Starnberg, Germany) were employed, the source being moved in constant acceleration mode. The Mössbauer spectra were least-squares fitted with the program NORMOS [120], either with a Lorentzian line shape or occasionally with a Voigt profile (convolution of a Lorentzian single line with a Gaussian), depending on the type of sample.

### 7.2.3 $^{119}\text{Sn}$ Inelastic Nuclear Resonant Scattering (NRIXS)

The NRIXS experiments displayed in this work were performed at the Advanced Photon Source (Sector 3-ID undulator beamline), Argonne National Laboratory, USA.

The re-emission of X-rays from the 23.88 keV nuclear resonance of  $^{119}\text{Sn}$  is observed. The deexcitation of the nucleus by emission of a conversion electron followed by fluorescence radiation takes place on a time scale of the lifetime of the nuclear resonance. If the nucleus is excited by pulsed synchrotron radiation, the discrimination of nuclear resonant absorption from the electronic contribution is efficiently done by counting only delayed fluorescence photons. Tuning the energy of the incident synchrotron radiation with respect to the nuclear resonance while monitoring the total yield of the fluorescence photons gives a direct measure of the phonon or vibrational density of states (VDOS) [12].

The NRIXS measurements were done at RT in an experimental setup very similar to the one described in Fig.6 in Ref. [146] (see also figure 2.10 and section 2.3.5). A high resolution monochromator for the 23.88 keV X-rays (nuclear resonance energy of  $^{119}\text{Sn}$ ) was tested during these experiments [147]. The energy resolution achieved was  $\simeq 0.8$  meV. The energy scan ranges were about  $\pm 80$  meV. The scan step size was chosen to be about one third the energy band width of the monochromatized X-ray beam, 0.2 meV in this case. The electronic absorption length is  $133 \mu\text{m}$  in  $\alpha$ -Sn for 23.88 keV X-rays, and the elastic nuclear resonant absorption length is only  $0.24 \mu\text{m}$  for enriched  $^{119}\text{Sn}$ . Since all films studied by this technique were only  $\simeq 0.05 \mu\text{m}$  thick, all  $^{119}\text{Sn}$  layers in the multilayers provide a NRIXS signal.

From the measured spectra the vibrational density of states (VDOS) of the Sn films in the multilayers is determined, and subsequently the recoilless factor ( $f$ ), mean kinetic energy per atom ( $\overline{T}$ ), mean force constant ( $\overline{K}$ ), and the vibrational entropy of the Sn layers is deduced.

### 7.2.4 Raman spectroscopy

Raman spectra were obtained with a Jobin-Yvon triple spectrometer (T64000) equipped with a liquid N<sub>2</sub>-cooled CCD detector, using 50 mW of 476 nm radiation from a Kr<sup>+</sup> laser (spectra Physics-Model 171). All spectra were obtained in a quasi-backscattering geometry with the sample in a He atmosphere to avoid Raman lines from O<sub>2</sub> and N<sub>2</sub>.

## 7.3 Results

### 7.3.1 X-ray reflectometry and diffractometry

Small-angle X-ray reflectometry measurements were performed for independent thickness control. Fig.7.1 shows the reflectometry curves obtained from the multilayers with nominal Sn thicknesses ( $t_{Sn}$ ) of 1.6, 15 and 30 Å.

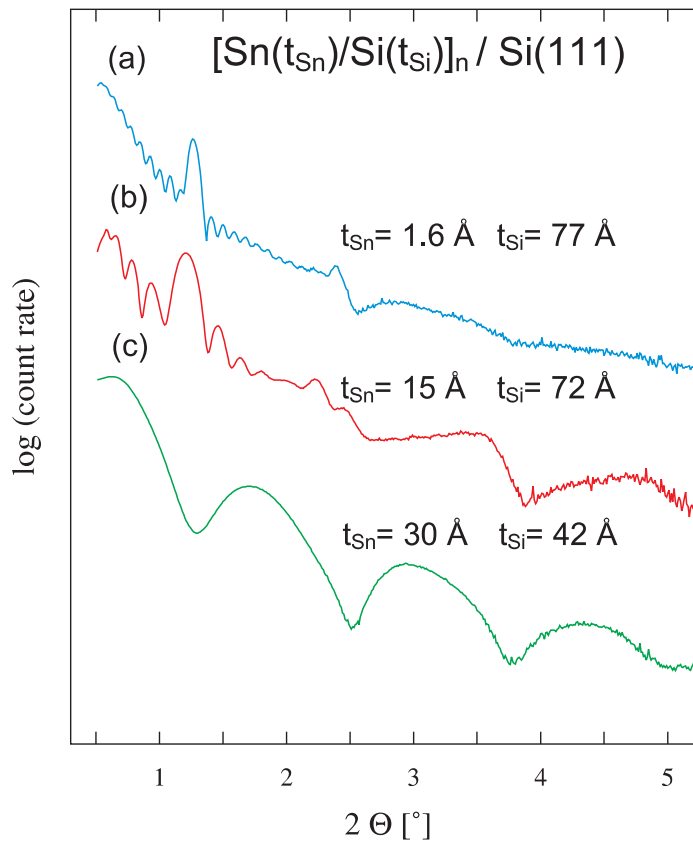


**Figure 7.1:** Small-angle X-ray reflectometry scans ( $\theta$ - $2\theta$ ) measured in grazing incidence for (a) [<sup>119</sup>Sn(1.6 Å)/Si(77 Å)]<sub>12</sub>, (b) [<sup>119</sup>Sn(15 Å)/Si(72 Å)]<sub>6</sub>, and (c) [<sup>119</sup>Sn(30 Å)/Si(42 Å)]<sub>1</sub>. ( $\lambda_{K\alpha} = 1.54178$  Å)

In Fig.7.1(a) and (b) one can recognize a double periodicity. The oscillations with a small period (Kiessig fringes) correspond to the total thickness interference of the multilayer, that is to  $(t_{Sn} + t_{Si}) \cdot n$ . The larger periodicity (superstructure Bragg peaks)

observed in Fig.7.1(a),(b) reflects the bilayer thickness ( $t_{Sn}+t_{Si}$ ) in the multilayer. One can see only one period (Kiessig fringes) in Fig.7.1(c), because this sample consists of only one bilayer ( $n=1$ ).

Since the calibration of the Sn-layer thicknesses with the quartz-microbalance for the low deposition rates used is quite accurate (stable evaporation cells) contrary to the more unstable electron gun for Si evaporation, the values of the total thicknesses of the multilayers obtained by X-Ray reflectometry will be used as in Ref. [148, 149], to calculate the individual thickness of the Si layers. By using the data in Fig.7.1(a),(b) and (c), thicknesses  $t_{Si} \simeq 77, 72$  and  $42$  Å, respectively, were obtained.

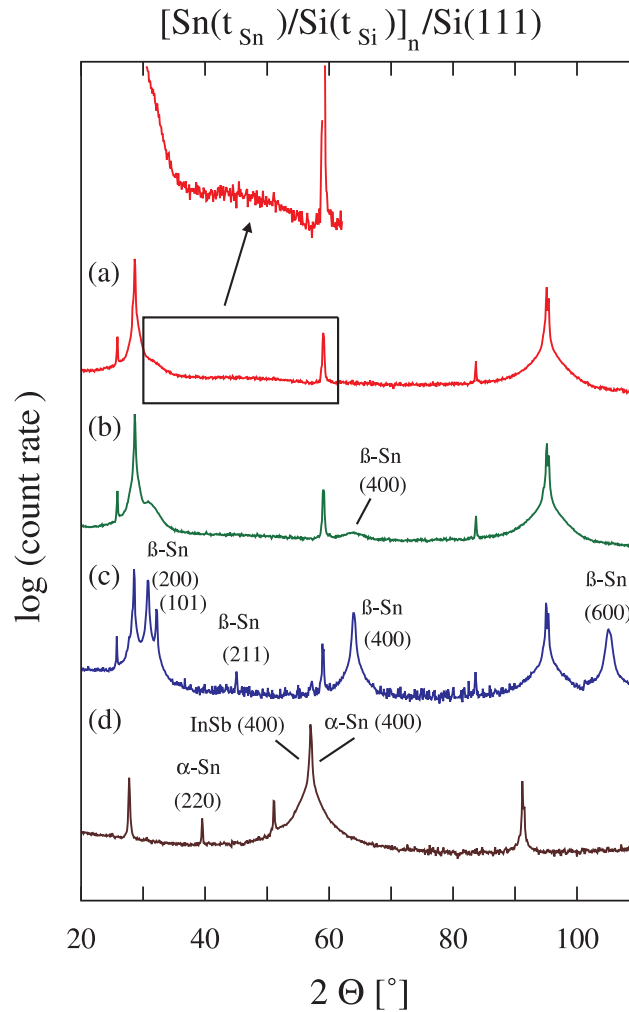


**Figure 7.2:** Wide-angle X-ray diffractometry scans ( $\theta$ - $2\theta$ ) of: (a)  $[\text{Sn}(10 \text{ \AA})/\text{Si}(50 \text{ \AA})]_{50}/\text{Si}(111)$ , (b)  $[\text{Sn}(20 \text{ \AA})/\text{Si}(50 \text{ \AA})]_{25}/\text{Si}(111)$ ; (c) epitaxially grown crystalline  $\beta$ -Sn with (200) and (101) texture in  $\text{Si}(70 \text{ \AA})/\text{Sn}(1000 \text{ \AA})/\text{Si}(111)$ , and (d) epitaxial  $\alpha$ -Sn with predominant (400) orientation and some (220) orientation in  $\text{Si}(100 \text{ \AA})/\text{Sn}(200 \text{ \AA})/\text{InSb}(001)$ . The observed Bragg peaks of  $\alpha$ -Sn in (d) and  $\beta$ -Sn in (b), (c) are indicated. All other peaks observed in the figure belong to the corresponding substrates. ( $\lambda_{K\alpha} = 1.54178 \text{ \AA}$ )

The observation of Kiessig fringes demonstrates that the surfaces of the multilayers are nearly atomically flat. Since at least two superstructure Bragg peaks are detected, the samples are of good multilayer quality.

Fig.7.2 displays wide-angle X-ray diffractometry results on Sn/Si multilayers grown on Si(111) for  $[\text{Sn}(10 \text{ \AA})/\text{Si}(50 \text{ \AA})]_{50}$  (a) and  $[\text{Sn}(20 \text{ \AA})/\text{Si}(50 \text{ \AA})]_{25}$  (b), together with two scans showing crystalline  $\beta$ -Sn in Sn(1000  $\text{\AA}$ )/Si(111) (c), and crystalline  $\alpha$ -Sn in Sn(200  $\text{\AA}$ )/InSb(001) (d), the latter being used as references. In Fig.7.2(a) only the Bragg peaks of the Si(111) substrate clearly appear, but one can also notice a weak upward curvature of the background around  $2\theta=40^\circ$ - $50^\circ$  which includes the position of the (220)  $\alpha$ -Sn peak (Fig.7.2 (d)). This is more clearly demonstrated in the insert of Fig.7.1(top), where the region near  $40^\circ$ - $50^\circ$  is magnified. The curved background near  $40^\circ$ - $50^\circ$  might be evidence for the presence of amorphous  $\alpha$ -like Sn. In addition to the Si(111) substrate diffraction peaks, a small peak corresponding to the (400)  $\beta$ -Sn peak (Fig.7.2(c)) was observed in Fig.7.2(b), that is, 20  $\text{\AA}$  Sn in the Sn/Si multilayers contain a contribution of crystalline  $\beta$ -Sn. As in the case of  $[\text{Sn}(10 \text{ \AA})/\text{Si}(50 \text{ \AA})]_{50}$ , no crystalline  $\alpha$ -Sn peaks were observed in Fig.7.2(b).

### 7.3.2 $^{119}\text{Sn}$ CEMS

The Sn thickness dependence of CEM spectra at RT in  $[\text{Sn}(t_{\text{Sn}})/\text{Si}(50 \text{ \AA})]_n$  multilayers was measured to obtain information about the critical thickness at which the  $\alpha$ -type Sn to  $\beta$ -Sn phase transition occurs. All of these samples were deposited at RT. Fig.7.3 shows typical  $^{119}\text{Sn}$  Mössbauer spectra. From the Lorentzian or Gaussian (Voigt profile) least-squares fit performed with NORMOS [120], the isomer shift is obtained, which is a useful parameter to distinguish the two possible tin phases ( $\alpha$  or  $\beta$ ), as mentioned before. All isomer shift ( $\delta$ ) values are given relative to a  $\text{CaSnO}_3$  absorber at RT. (At RT,  $\text{CaSnO}_3$ ,  $\text{BaSnO}_3$  and  $\text{SnO}_2$  absorbers have the same isomer shifts [125]).

The Mössbauer spectra of Fig.7.3(a),(b), (c) and (d) could be fitted with only one single line, resulting in an isomer shift very close to the bulk value of  $\alpha$ -Sn [124, 125]. Therefore, pure  $\alpha$ -like Sn exists up to  $t_{\text{Sn}}$  of 10  $\text{\AA}$ . Above 10  $\text{\AA}$  of Sn, two single lines were needed to fit the spectra, corresponding to the isomer shift of the  $\alpha$ -like Sn and  $\beta$ -Sn phases. The presence of  $\beta$ -Sn above 10  $\text{\AA}$  contributes to a characteristic asymmetry in the peak shape, (Fig.7.3(e),(f),(g),(h)). With increasing Sn layer thickness, the relative intensity of the  $\beta$ -Sn peak becomes larger, and at a thickness of 100  $\text{\AA}$  (Fig.7.3(i)), the  $\beta$ -Sn contribution dominates. These results demonstrate that  $\alpha$ -like Sn in these multilayers is only stable for very small thicknesses, less than or equal to 10  $\text{\AA}$ .

Table 7.1(a) displays the Mössbauer parameters (isomer shift  $\delta$  and linewidth  $\Gamma$ ) of the  $\text{Sn}(t_{\text{Sn}})/\text{Si}(50 \text{ \AA})$  multilayers deposited and measured at RT. For one of the samples, with  $t_{\text{Sn}}=10$ , a least-squares fitting with a Voigt profile for the  $\alpha$ -like Sn line resulted in a slightly better fitting of the corresponding spectra.

Table 7.1(b) shows the Mössbauer parameters (isomer shift and linewidth) of epitaxial  $\alpha$ -Sn(500  $\text{\AA}$ ) on InSb(001) and of a  $\beta$ -Sn foil, both measured at RT, in comparison with the  $\alpha$ - and  $\beta$ -Sn bulk values taken from the literature [124, 125].



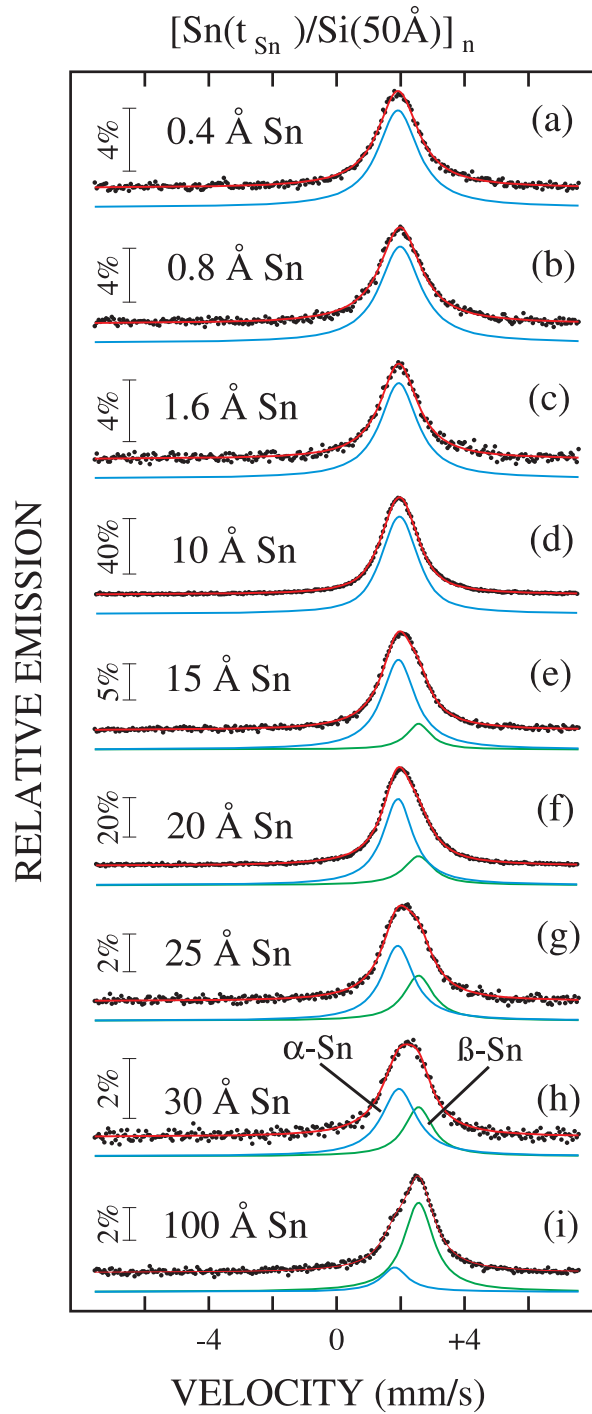


**Figure 7.3:** Mössbauer (CEM) spectra at RT of  $[\text{Sn}(t_{\text{Sn}})/\text{Si}(50\text{\AA})]_n$  multilayers with  $t_{\text{Sn}} = 0.4\text{\AA}$  (a),  $0.8\text{\AA}$  (b),  $1.6\text{\AA}$  (c),  $10\text{\AA}$  (d),  $15\text{\AA}$  (e),  $20\text{\AA}$  (f),  $25\text{\AA}$  (g),  $30\text{\AA}$  (h), and (i)  $100\text{\AA}$ . The deposition temperatures were approximately RT. Least-squares fitting was performed with a single line for  $\alpha$ -like Sn ( $t_{\text{Sn}} \leq 10\text{\AA}$ ) or with two single lines for the  $\alpha$ -like Sn and  $\beta$ -Sn, respectively ( $t_{\text{Sn}} > 10\text{\AA}$ ).

(a) Sn/Si Multilayers [Sn( $t_{Sn}$ )/Si(50Å)] <sub>n</sub> T <sub>S</sub> =300 K		Isomer Shift δ(mm/s)		Lorentzian Linewidth Γ(mm/s)	
n	$t_{Sn}$	α-Sn-like	β-Sn	α-Sn-like	β-Sn
40	0.4 Å	1.916 ± 0.005		1.52 ± 0.02	
24	0.8 Å	1.986 ± 0.006		1.55 ± 0.02	
12	1.6 Å	1.945 ± 0.008		1.42 ± 0.02	
46	10 Å	1.965 ± 0.001		1.01 ± 0.01 σ=0.284 ± 0.006 mm/s	
6	15 Å	1.935 ± 0.008	2.56	1.27 ± 0.02	0.90 ± 0.04
25	20 Å	1.917 ± 0.004	2.56	1.145 ± 0.009	1.09 ± 0.02
2	25 Å	1.91 ± 0.01	2.56	1.21 ± 0.03	1.12 ± 0.03
1	30 Å	1.95 ± 0.03	2.56	1.32 ± 0.06	1.07 ± 0.05
1	100 Å	1.88 ± 0.04	2.58 ± 0.01	1.11 ± 0.03	1.12 ± 0.08
(b) Sample		α-Sn	β-Sn	α-Sn	β-Sn
α-Sn(500Å)/InSb(001)		1.99 ± 0.01		0.924 ± 0.004	
α-Sn (bulk) [124, 125]		2.03 ± 0.02			
β-Sn (foil)			2.520 ± 0.002		0.854 ± 0.004
β-Sn (bulk) [124, 125]			2.56 ± 0.01		

**Table 7.1:** (a) <sup>119</sup>Sn Mössbauer parameters (isomer shift δ, linewidth Γ (for the Lorentzian line), and Gaussian width σ (for the Voigt profile)) of the [Sn( $t_{Sn}$ )/Si(50 Å)]<sub>n</sub> multilayers measured at RT. All samples were deposited at RT. For 15 Å ≤  $t_{Sn}$  ≤ 30 Å the isomer shift of the β-Sn line was a fixed parameter at +2.56 mm/s, which is the literature value for bulk β-Sn [125]. (b) Mössbauer parameters (isomer shift δ and linewidth Γ) of epitaxial α-Sn(500 Å) on InSb(001) and of a β-Sn foil, both measured at RT, and comparison with the crystalline bulk values taken from the literature [124, 125].

One can notice that the isomer shift values of the α-like Sn phase in the multilayers of Table 7.1(a) are very close to those of bulk α-Sn and epitaxial α-Sn (Table 7.1(b)).

[Sn( $t_{Sn}$ )/Si(50Å)] <sub>n</sub>		Area (%)	
n	$t_{Sn}$	α-Sn-like (A <sub>α</sub> )	β-Sn (A <sub>β</sub> )
40	0.4 Å Sn	100.0 ± 0.9	
24	0.8 Å Sn	100.0 ± 1	
12	1.6 Å Sn	100 ± 1	
46	10 Å Sn	100.0 ± 0.4	
6	15 Å Sn	83 ± 2	17 ± 1
25	20 Å Sn	76 ± 1	24 ± 1
2	25 Å Sn	64 ± 3	36 ± 2
1	30 Å Sn	63 ± 5	37 ± 4
1	100 Å Sn	19 ± 2	81 ± 2

**Table 7.2:** Relative contribution of the α-Sn-like and β-Sn phases to the total spectral area of the Mössbauer spectra shown in Fig.7.3

The relative contributions of the α-like Sn and β-Sn phases to the total spectral area

of the Mössbauer spectra (as shown in Fig.7.3) are displayed in Table 7.2. The measured relative spectral area,  $A_\alpha$ , of the  $\alpha$ -like phase as a function of the individual Sn thickness,  $t_{Sn}$ , in the multilayers is plotted in Fig.7.4(full squares).

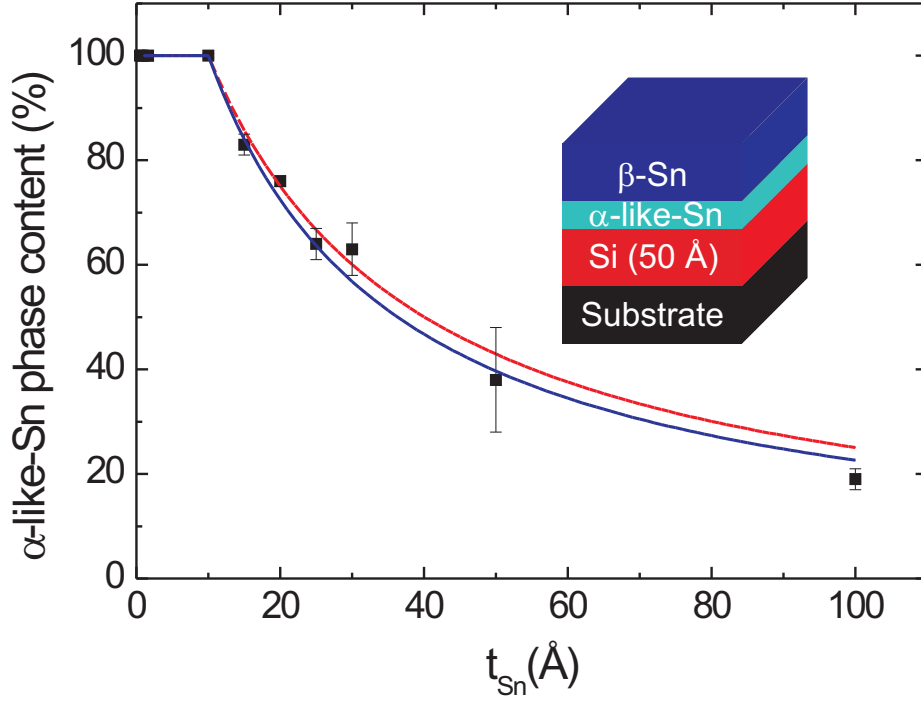


**Figure 7.4:** Relative  $\alpha$ -like-Sn content in the Sn layers as a function of Sn layer thickness,  $t_{Sn}$ . The samples are  $[\text{Sn}(t_{Sn})/\text{Si}(50 \text{ \AA})]_n$  multilayers for  $t_{Sn} \leq 30 \text{ \AA}$ , and  $[\text{Sn}(50 \text{ \AA})/\text{Si}(50 \text{ \AA})]_1$  and  $[\text{Sn}(100 \text{ \AA})/\text{Si}(50 \text{ \AA})]_1$  bilayers for  $t_{Sn} > 30 \text{ \AA}$ . The bilayer with  $t_{Sn} = 50 \text{ \AA}$  was grown at  $T_s = -50 \text{ }^\circ\text{C}$ , and all other samples were grown at room temperature. The experimental data points correspond to the relative Mössbauer spectral areas,  $A_\alpha$ , of  $\alpha$ -like Sn (full squares). They are compared to calculations using eq.(7.1) and the bulk values of the Lamb-Mössbauer factors, i.e.  $f_\alpha=0.16$ , and  $f_\beta=0.042$  for  $\alpha$ - and  $\beta$ -Sn, respectively (red line), or using the values  $f_\alpha=0.14$ ,  $f_\beta=0.042$  (blue line), with  $f_\alpha$  obtained from NRIXS measurements on  $500 \text{ \AA}$  epitaxial  $\alpha$ -Sn on InSb(001).

Up to  $t_{Sn}=10 \text{ \AA}$  only  $\alpha$ -like Sn exists, while with increasing  $t_{Sn}$  the  $A_\alpha$  values drop monotonically. This latter behavior can be explained by the assumption that the  $\alpha$ -like Sn phase of  $10 \text{ \AA}$  maximum thickness exists exclusively at the Sn/Si interface, and that the part of the Sn film in excess of  $10 \text{ \AA}$  thickness consists only of  $\beta$ -Sn. For this purpose, recall that in the thin absorber approximation [150], the absolute experimental Mössbauer spectral area  $A_\alpha^{abs} \propto f_\alpha n_\alpha t_\alpha$  for  $\alpha$ -like Sn, and  $A_\beta^{abs} \propto f_\beta n_\beta t_\beta$  for  $\beta$ -Sn. Here  $f_\alpha$  is the Lamb-Mössbauer factor (f-factor),  $n_\alpha$  is the number density of  $^{119}\text{Sn}$  nuclei ( $^{119}\text{Sn}$  nuclei/cm<sup>3</sup>), and  $t_\alpha$  is the physical thickness (cm) of the  $\alpha$ - $^{119}\text{Sn}$  layer. (For the

$\beta$ -Sn layer the corresponding quantities carry the index  $\beta$ ). The relative spectral area  $A_\alpha$  normalized to the total spectral area,  $(A_\alpha^{abs} + A_\beta^{abs})$  is given by:

$$A_\alpha = \frac{f_\alpha n_\alpha t_\alpha}{(f_\alpha n_\alpha t_\alpha + f_\beta n_\beta t_\beta)} \quad (7.1)$$

In Fig.7.4, values of  $A_\alpha$ , calculated according to eq.(7.1), are shown, where the values  $t_\alpha=10 \text{ \AA}$ ,  $t_\beta = t_{Sn} - t_\alpha$ , and  $f_\alpha=0.16$ ,  $f_\beta=0.042$  [122] (red line), or alternatively  $f_\alpha=0.14$ ,  $f_\beta=0.042$  (blue line) have been used (see section 7.3.4). Comparison of experimental and calculated  $A_\alpha$  values indicates good agreement. The small deviation observed in Fig.7.4 for  $t_{Sn} = 100 \text{ \AA}$  is due to the fact that this data point was obtained from a Sn(100  $\text{\AA}$ )/Si(50  $\text{\AA}$ ) bilayer, where the rather thick  $\beta$ -Sn layer is closer to the surface than the  $\alpha$ -like Sn layer. Since the probability of escape of conversion electrons decays as a function of depth, the Mössbauer signal  $A_\beta^{abs}$  will be enhanced relative to  $A_\alpha^{abs}$  in this bilayer. Then, this leads to the observed slight drop of the experimental data point relative to the calculated value. Fig.7.4 provides strong evidence for the assumption of a layered  $\beta$ -Sn/ $\alpha$ -like Sn structure (see inset Fig.7.4).

Changing the Si thickness from  $t_{Si}=50 \text{ \AA}$  to  $20 \text{ \AA}$  has no influence on the Sn phase formation. This has been checked by comparing spectra of RT grown [Sn(10  $\text{\AA}$ )/Si(50  $\text{\AA}$ )]<sub>46</sub> and [Sn(10  $\text{\AA}$ )/Si(20  $\text{\AA}$ )]<sub>50</sub> multilayers with identical Sn thicknesses. For  $t_{Si}=20 \text{ \AA}$ , the single line spectrum (Fig. 7.5(b)) was found to be very similar to that of Fig.7.5(a) containing  $t_{Si}=50 \text{ \AA}$ . Only a slight linewidth broadening is observed, and pure  $\alpha$ -like-Sn is identified by the isomer shift value of  $+ 2.011 \pm 0.004 \text{ mm/s}$  (compare with Table 7.1(a)).

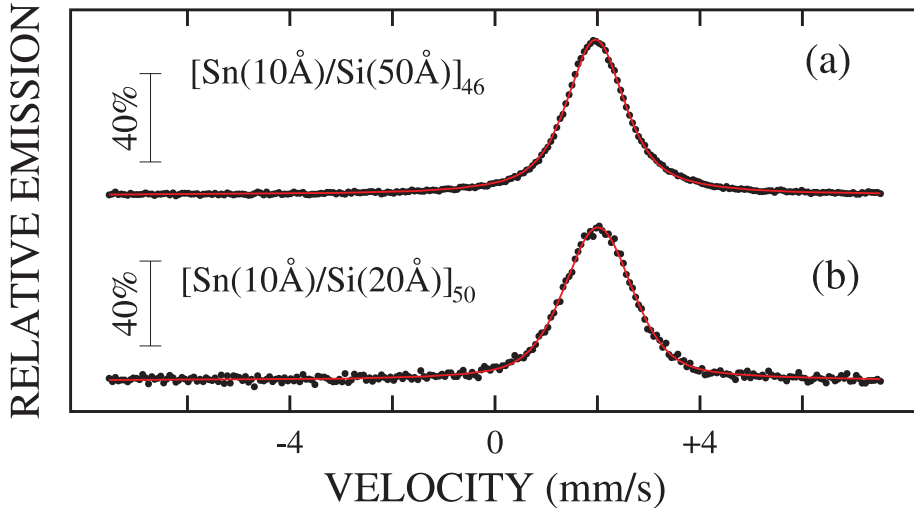


**Figure 7.5:** CEM spectra of [Sn(10  $\text{\AA}$ )/Si( $t_{Si}$ )]<sub>n</sub> multilayers with  $t_{Si} = 50 \text{ \AA}$  and  $n=46$  (a), and  $t_{Si}=20 \text{ \AA}$  and  $n=50$  (b), measured and grown at RT.

The interesting aspect of the  $\alpha$ -like Sn phase grown in these multilayers is that it can be stabilized on a-Si by RT deposition up to 10 Å. Therefore, also low temperature depositions (LT,  $T_s = -50^\circ\text{C}$ ) for Sn thicknesses of 1.6 Å and 50 Å in  $[\text{Sn}(t_{Sn})/\text{Si}(50 \text{ Å})]_n$  multilayers, with  $n=20$  and 1, respectively, were carried out. The results are very similar to the case of RT growth. 1.6 Å Sn grows as  $\alpha$ -like Sn (Fig.7.6(a)). Fig.7.6(b) shows that LT deposition does not allow Sn to remain in its  $\alpha$ -like phase for thicker layers. Table 7.3 displays the Mössbauer parameters of these LT deposited multilayers. The relative spectral area of  $\beta$ -Sn in the 50 Å Sn sample ( $62 \pm 10 \%$ ) is much larger than that of  $\alpha$ -like Sn ( $38 \pm 10 \%$ ). The experimental point corresponding to the LT growth of the 50 Å Sn/Si bilayer fits well into the behavior of RT grown samples, as shown in Fig.7.4. Thus LT growth does not favor the formation of  $\alpha$ -like Sn interface layers thicker than 10 Å.

[Sn( $t_{Sn}$ )/Si(50Å)] <sub>n</sub>		Isomer Shift $\delta(\text{mm/s})$		Lorentzian Linewidth $\Gamma(\text{mm/s})$		Area %	
n	$t_{Sn}$	$\alpha$ -Sn-like	$\beta$ -Sn	$\alpha$ -Sn-like	$\beta$ -Sn	$\alpha$ -Sn-like ( $A_\alpha$ )	$\beta$ -Sn ( $A_\beta$ )
20	1.6 Å	$1.946 \pm 0.002$		$1.27 \pm 0.02$		$100.0 \pm 0.5$	
1	50 Å	$1.87 \pm 0.08$	$2.58 \pm 0.04$	$1.3 \pm 0.1$	$1.15 \pm 0.07$	$38 \pm 10$	$62 \pm 10$

**Table 7.3:** Mössbauer parameters of  $[\text{Sn}(t_{Sn})/\text{Si}(50 \text{ Å})]_n$  multilayers deposited at  $-50^\circ\text{C}$  and measured at RT.

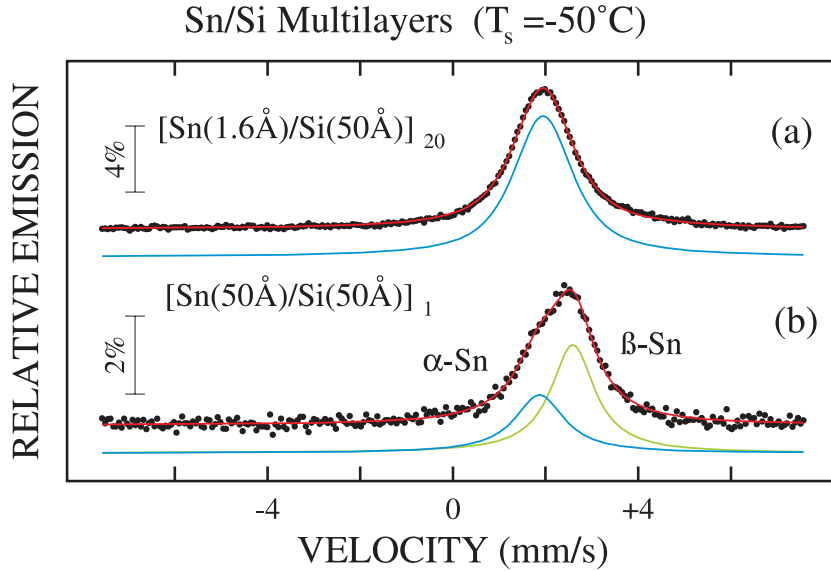


**Figure 7.6:** CEM spectra of  $[\text{Sn}(t_{Sn})/\text{Si}(50 \text{ Å})]_n$  multilayers with  $t_{Sn} = 1.6 \text{ Å}$  and  $n=20$  (a), and  $t_{Sn} = 50 \text{ Å}$  and  $n=1$  (b), measured at RT. The samples were grown at  $-50^\circ\text{C}$ .

Finally, the possibility to observe the  $\alpha$ - to  $\beta$ -Sn transition in the multilayers after annealing was tested. The RT grown sample of composition  $[\text{Sn}(10 \text{ Å})/\text{Si}(77 \text{ Å})]_4$ ,

was annealed in UHV for 30 minutes at 350°C. Before annealing (Fig.7.7(a)), the 10 Å Sn layers of these multilayers were in the  $\alpha$ -like Sn phase (see Table 7.4). Mössbauer measurements at RT after the annealing process (Fig.7.7(b)) were repeated, and no  $\beta$ -Sn, but only  $\alpha$ -like Sn was observed. So if there was a  $\alpha$ -like Sn  $\rightarrow$   $\beta$ -Sn transformation above RT, the  $\beta$ -Sn formed should be unstable upon cooling to RT, and this transformation must be reversible.

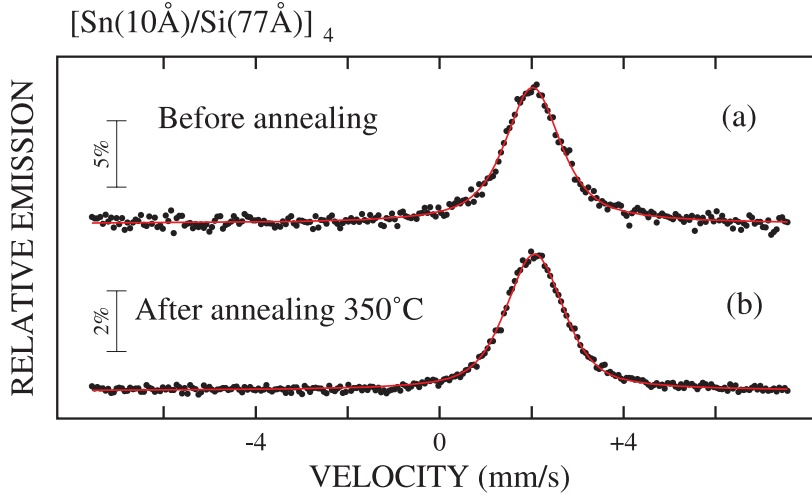


**Figure 7.7:** CEM spectra of room-temperature grown  $[\text{Sn}(10 \text{ \AA})/\text{Si}(77 \text{ \AA})]_4$  multilayer measured at RT before (a) and after (b) annealing up to 350°C.

$[\text{Sn}(10 \text{ \AA})/\text{Si}(50 \text{ \AA})]_4$ $\alpha$ -Sn-like phase	Isomer Shift $\delta(\text{mm/s})$	Lorentzian Linewidth $\Gamma(\text{mm/s})$	Gaussian Linewidth $\sigma(\text{mm/s})$ in Voigt profile
Before annealing	$2.021 \pm 0.008$	$1.12 \pm 0.07$	$0.28 \pm 0.04$
After annealing (350°C)	$2.064 \pm 0.004$	$0.94 \pm 0.04$	$0.38 \pm 0.02$

**Table 7.4:** Mössbauer parameters of  $[\text{Sn}(10 \text{ \AA})/\text{Si}(77 \text{ \AA})]_4$  multilayer deposited and measured at RT before and after annealing at 350°C.

### 7.3.3 Raman spectroscopy

The first-order Raman scattering by phonons (or vibrational excitations) was measured in Sn/Si multilayers at RT.

Fig. 7.8 displays intensity versus Raman shifts of four different samples: (a)  $\text{Si}(70 \text{ \AA})/\text{Sn}(1000 \text{ \AA})/\text{Si}(111)$ , (b)  $[\text{Sn}(15 \text{ \AA})/\text{Si}(50 \text{ \AA})]_6/\text{Si}(111)$ , (c)  $[\text{Sn}(10 \text{ \AA})/\text{Si}(50 \text{ \AA})]_{50}/\text{Si}(111)$ , and (d)  $\text{Pt}(20 \text{ \AA})/\alpha\text{-Sn}(60 \text{ \AA})/\text{InSb}(001)$ , all grown at RT.

The spectrum in Fig. 7.8(a) shows a sharp peak at  $523 \text{ cm}^{-1}$  that originates from transverse optical (TO) phonons of the crystalline Si substrate [151, 152]. The 1000 Å

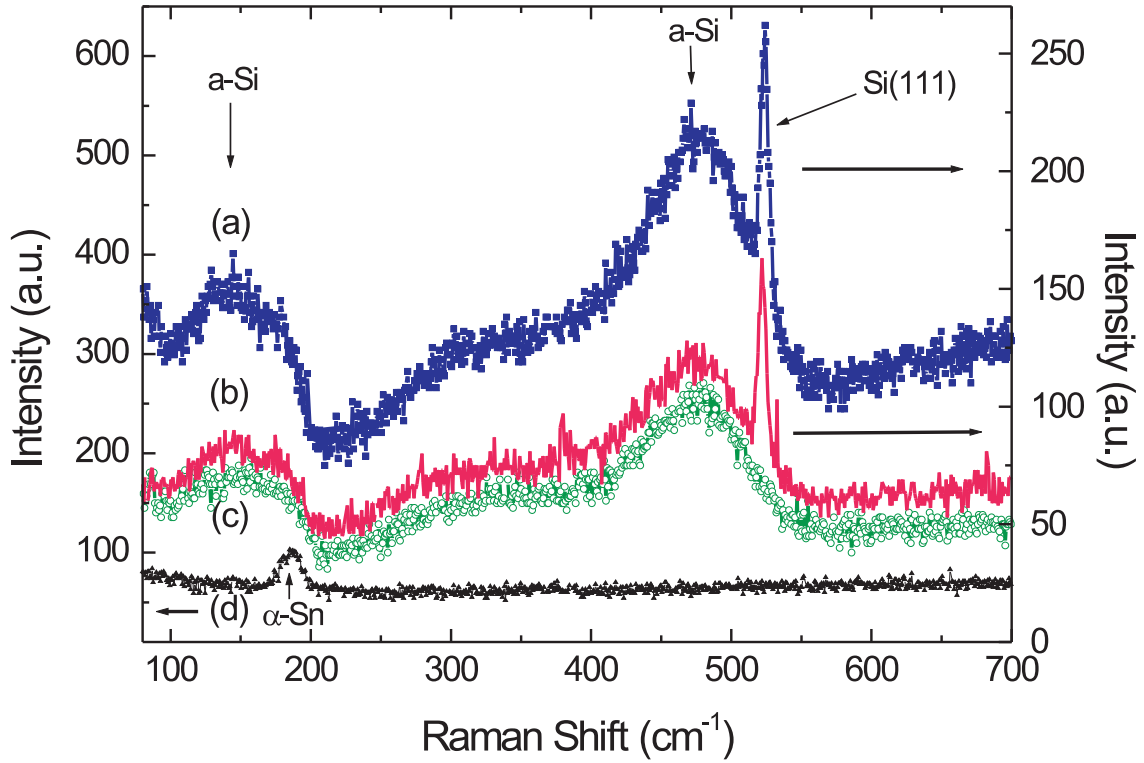


**Figure 7.8:** Raman spectra measured at RT in He atmosphere of (a) Si(70 Å)/Sn(1000 Å)/Si(111); (b) [Sn(15 Å)/Si(50 Å)]<sub>6</sub>/Si(111); (c) [Sn(10 Å)/Si(50 Å)]<sub>50</sub>/Si(111); and (d) Pt(20 Å)/Sn(60 Å)/InSb(001).

Sn layer in this sample exists in the crystalline (metallic)  $\beta$ -Sn phase (see section 7.3.1) with bct structure which cannot be detected by means of Raman spectroscopy. The broad peaks observed in Fig. 7.8(a)-(c) at around 476 and 144  $\text{cm}^{-1}$  are those of the TO-like and transverse acoustical (TA) like excitations, respectively, of amorphous (a-)Si, indicating the amorphous structure of the deposited Si layers [152]. Since the total amount of Si in samples (b) and (c) is much larger than that of Sn, it is very difficult to detect any contribution of  $\alpha$ -Sn (if present at all) in these spectra. Furthermore the Raman peak of the TO phonons in  $\alpha$ -Sn grown on InSb is found at 180  $\text{cm}^{-1}$  (Fig. 7.8(d)), in agreement with Ref. [153]. Since the broad 144- $\text{cm}^{-1}$  peak of a-Si is in the same Raman shift region, it is not possible to distinguish  $\alpha$ -Sn from a-Si because of considerable overlap of the spectra. One should note that if the  $\alpha$ -Sn layers were in a highly disordered or amorphous  $\alpha$ -Sn-like structure, they are expected to show a broadened TO-like peak with reduced intensity, making its detection even more difficult.

### 7.3.4 Nuclear resonant inelastic X-ray scattering (NRIXS)

NRIXS spectra were measured at RT on the following samples:  $^{119}\text{Sn}(500 \text{ \AA})/\text{InSb}(001)$ ,  $^{119}\text{Sn}(10 \text{ \AA})/\text{Si}(20 \text{ \AA})$ ,  $^{119}\text{Sn}(10 \text{ \AA})/\text{Si}(50 \text{ \AA})$  and  $^{119}\text{Sn}(20 \text{ \AA})/\text{Si}(50 \text{ \AA})$ . The

spectra (raw data) are shown in Fig. 7.9(a), 7.10(a) and 7.11(a), respectively. Since the spectra of the  $[^{119}\text{Sn}(10 \text{ \AA})/\text{Si}(20 \text{ \AA})]_{50}$  and  $[^{119}\text{Sn}(10 \text{ \AA})/\text{Si}(50 \text{ \AA})]_{46}$  multilayers were found to be identical within statistical error bars, they were added in order to improve the statistical quality; this result is displayed in Fig.7.10(a).

The main features of these NRIXS spectra are an elastic central peak at  $E-E_0=0$  meV, and side bands at lower and higher energy. Here,  $E$  is the incident photon energy and  $E_0=23.88$  keV is the nuclear resonance energy. The elastic peak dominates the spectrum as expected for solids with reasonable probability for recoilless absorption (reasonably high Lamb-Mössbauer factor or  $f$ -factor). Photons with less energy than  $E_0$  can excite the nuclear resonance by annihilation of a phonon (low energy side band). The high energy side band corresponds to phonon creation. Phonon annihilation is proportional to the temperature dependent phonon occupation number, whereas the creation of phonons can also occur spontaneously, which explains the observed asymmetry in the spectra.

Fig.7.9(a) displays the NRIXS spectrum of a thick (500 Å)  $\alpha$ -Sn film. The result obtained looks similar to that measured in Ref. [13] on Sn(2000 Å)/CdTe(001), where the crystalline  $\alpha$ -Sn phase was observed, too. The instrumental resolution function of 0.8 meV width is plotted around  $E-E_0=0$  meV. Especially sharp phonon excitation peaks are observed at 6, 11 and 22 meV (phonon creation part of the spectrum), indicating the crystallographic long-range order present in this sample.

Figure 7.9(b) displays the phonon excitation probability function, obtained directly from the experimental data after normalization and subtraction of the elastic peak contribution as described in Ref. [12, 14, 154, 155]. This spectrum can be decomposed into single and multi-phonon contributions. At ambient temperature one may recognize various contributions to this spectrum, corresponding to inelastic nuclear absorption accompanied by excitation or annihilation of different number of phonons. The normalized probability of the inelastic nuclear absorption,  $W(E)$ , can be decomposed in terms of a multiphonon expansion [12, 14]:

$$W(E) = [\delta(E) + \sum_{n=1}^{\infty} S_n(E)] \cdot f \quad (7.2)$$

Here the  $\delta$ -function describes the elastic part of the nuclear absorption (zero-phonon term), and the  $n$ -th term of the series  $S_n(E)$  represents the inelastic nuclear absorption accompanied by creation (annihilation) of  $n$  phonons.  $f$  is the Lamb-Mössbauer factor. The one-phonon term is given by:

$$S_1(E) = \frac{E_R \cdot g(E)}{E \cdot (1 - e^{-\beta E})} \quad (7.3)$$

and the subsequent terms in the harmonic approximation may be found through the recursive relation:



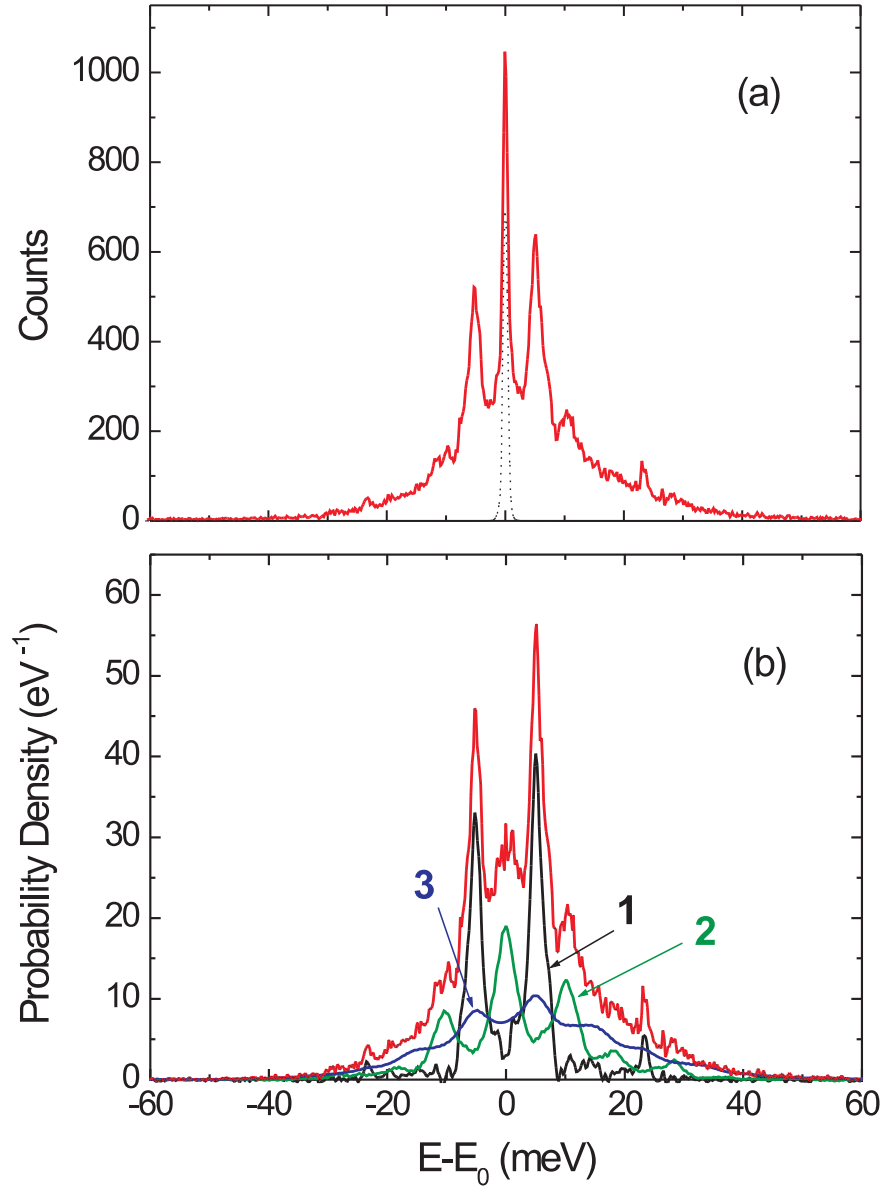


**Figure 7.9:** (a) NRIXS spectrum (raw data) of 500 Å thick epitaxial  $\alpha$ - $^{119}\text{Sn}$  on InSb(001) measured at RT. The dotted line shows the instrumental resolution function; (b) decomposition of the NRIXS spectrum (after normalization and removal of the elastic peak) in a one-phonon (1), two-phonon (2) and a higher-order phonon (3) contribution.

$$S_n(E) = \frac{1}{n} \int_{-\infty}^{\infty} S_1(E') S_{n-1}(E - E') dE' \quad (7.4)$$

Here  $\beta = (k_B T)^{-1}$  with  $k_B$  the Boltzmann constant,  $T$  is the temperature,  $E_R = \hbar^2 k^2 / 2M$  the recoil energy of the free nucleus,  $k$  the wave vector of the photon, and  $M$  the mass of

the atom. The function  $g(E)$  is the normalized phonon (or vibrational) density of states (VDOS). The relative contribution  $\int S_n(E)dE$  of the n-phonon term is given by  $(-\ln f)^n/n!$ .

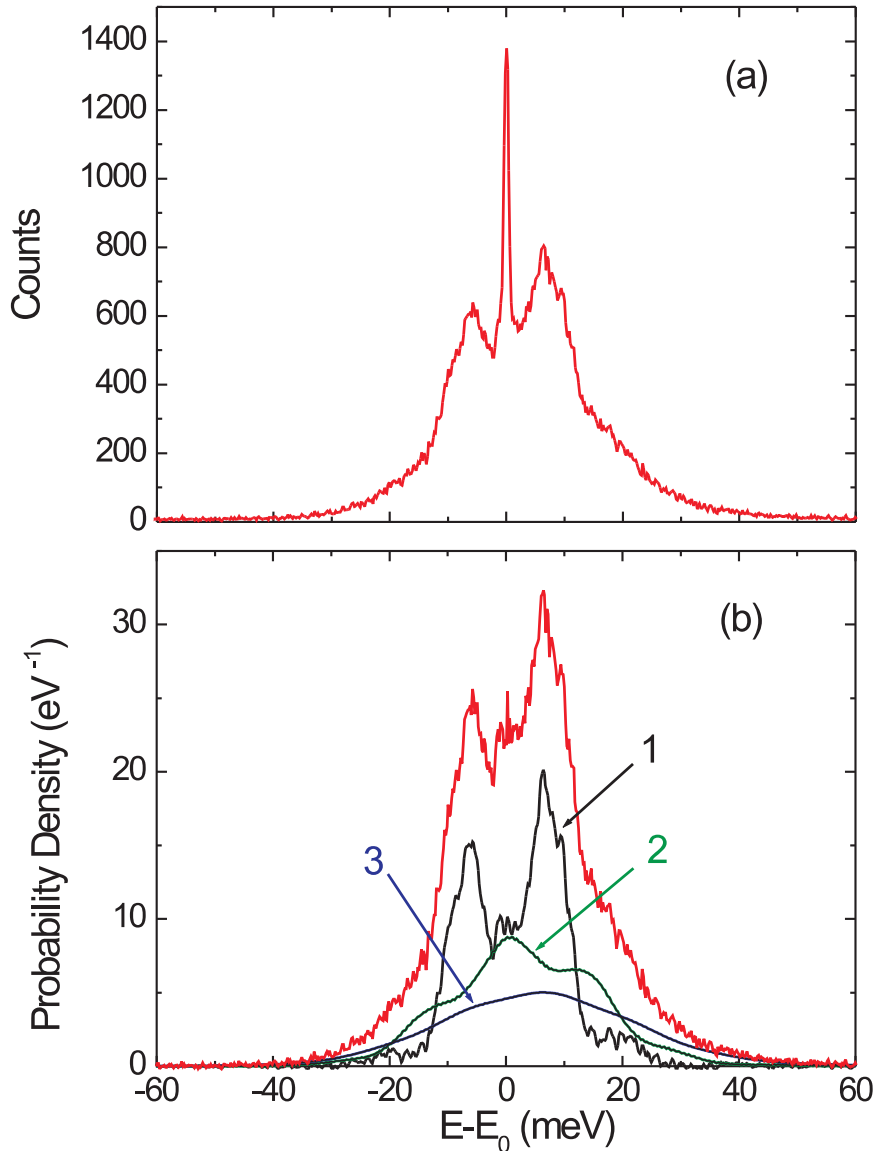


**Figure 7.10:** (a) The sum of NRIXS spectra (raw data) of  $[^{119}\text{Sn}(10 \text{ \AA})/\text{Si}(50 \text{ \AA})]_{50}$  and  $[^{119}\text{Sn}(10 \text{ \AA})/\text{Si}(20 \text{ \AA})]_{46}$  measured at RT; (b) decomposition of the NRIXS spectrum (after normalization and removal of the elastic peak) in a one-phonon (1), a two-phonon (2), and a higher-order-phonon (3) contribution.

In order to extract the phonon excitation probabilities, the program PHOENIX [154] was used. The contributions of the one-, two- and higher order phonon excitation probabilities are displayed in Fig.7.9(b), 7.10(b) and 7.11(b), respectively. The clear distinction of the multi-phonon contributions is no longer possible, if the Lamb-Mössbauer factor is

small, like in  $\beta$ -Sn [13,122]. In this case, the expansion in eq.(7.2) converges slowly, and a large number of terms has to be taken into account. With an  $f$  factor of 0.16 [13],  $\alpha$ -Sn has significant multiphonon contributions, but not to the degree of preventing the separation of  $S_1(E)$ ,  $S_2(E)$ ,  $S_3(E)$ .

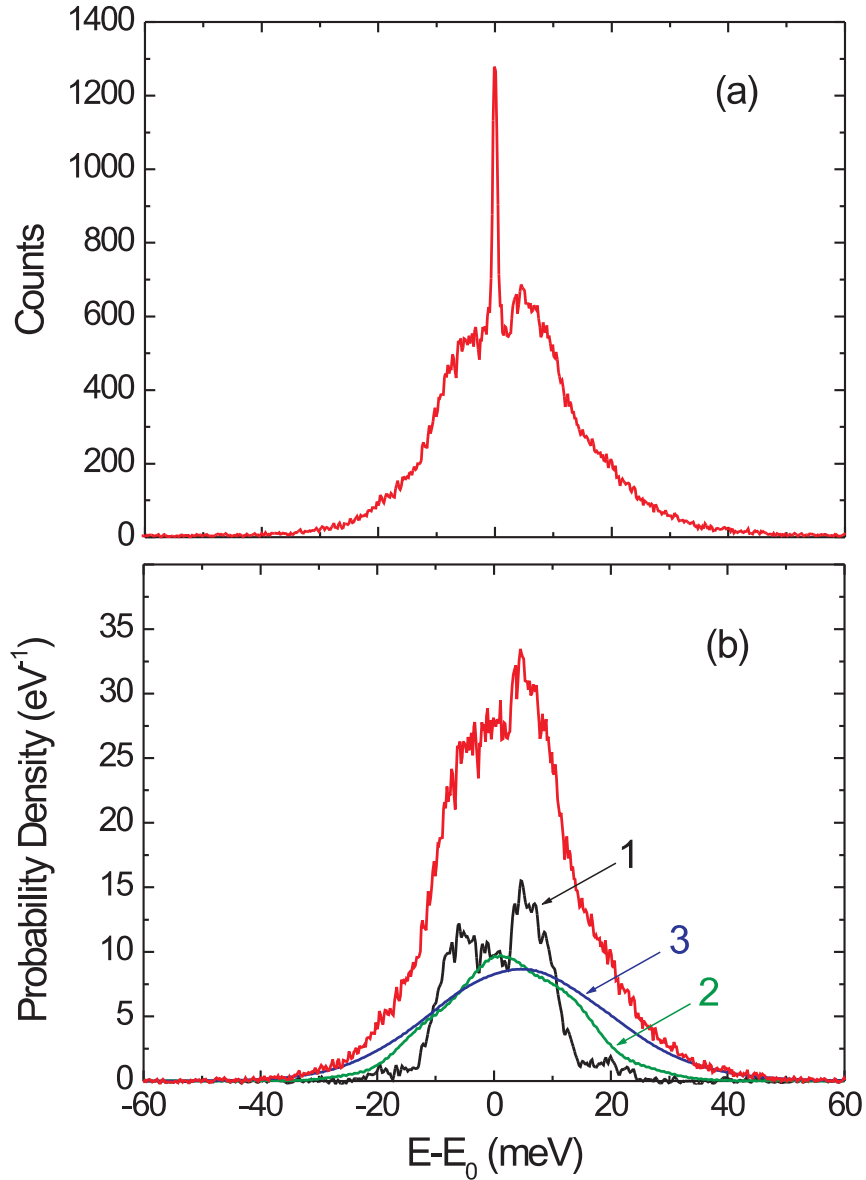


**Figure 7.11:** (a) INRS spectrum (raw data) of  $[^{119}\text{Sn}(20 \text{ \AA})/\text{Si}(50 \text{ \AA})]_{25}$  measured at RT; (b) decomposition of the INRS spectrum (after normalization and removal of the elastic peak) in a one-phonon (1), a two-phonon (2), and a higher-order phonon (3) contribution.

The phonon (or vibrational) density of states  $g(E)$  in eq.(7.3) is proportional to the one-phonon term in the expansion of eq.(7.2). The measured spectra of Figs.7.9(b), 7.10(b) and 7.11(b) were deconvoluted with the resolution function and eq.(7.3) was ap-

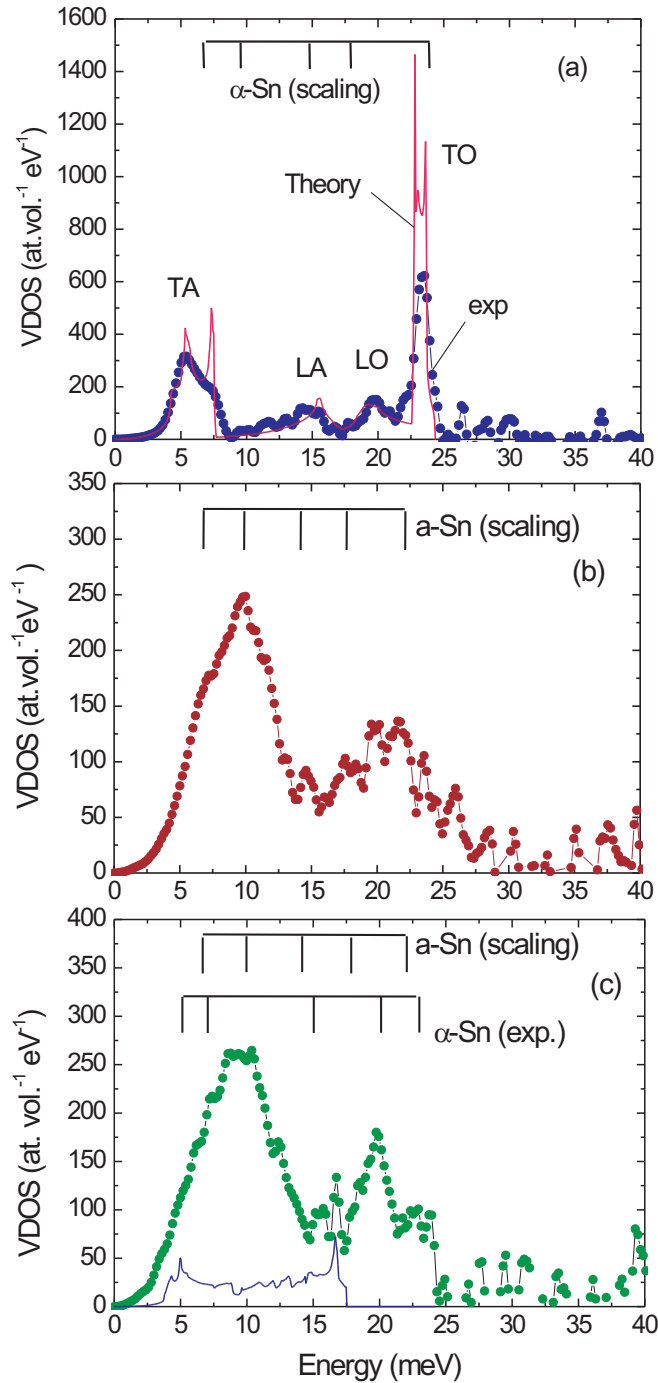
plied to obtain the VDOS. Again the program PHOENIX [154] was used for that purpose. The results are shown in Figs. 7.12(a),(b) and (c), respectively.

In the case of the 500 Å thick epitaxial  $\alpha$ -Sn film (Fig. 7.12(a)),  $g(E)$  shows several distinct peaks at positions in good agreement with those theoretically predicted in Ref. [133] for bulk  $\alpha$ -Sn, although experimental features are not as sharp as in the calculation (bold solid line in Fig. 7.12(a)). Observation was made of the transverse-acoustical (TA) peak at 5 meV, the longitudinal acoustical (LA) peak at 15 meV, the longitudinal optical (LO) peak at 20 meV, and the strong transverse-optical (TO) peak at 23 meV. There is also a pronounced shoulder near 7 meV in the TA band.

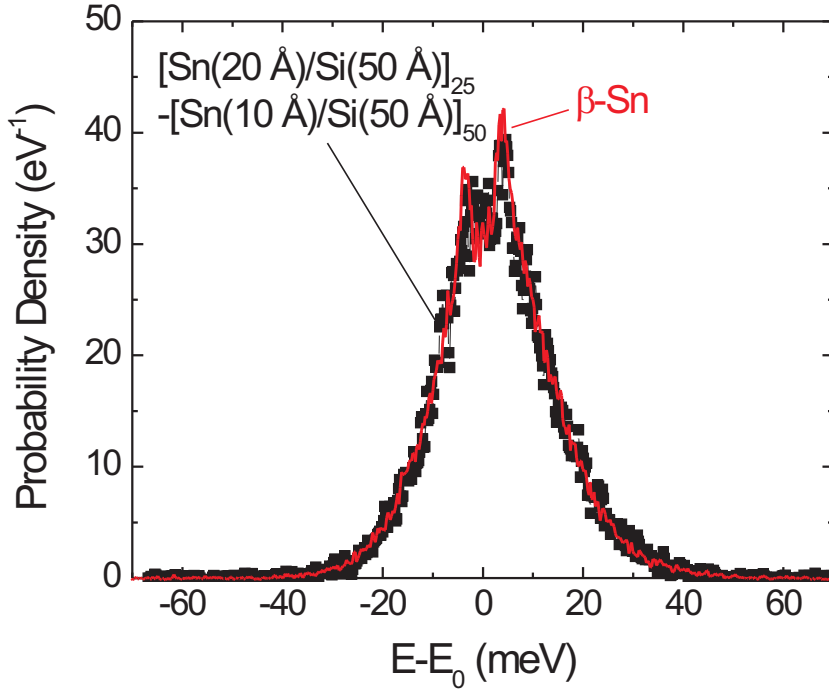
The NRIXS spectrum of the  $^{119}\text{Sn}(10 \text{ \AA})/\text{Si}$  multilayer, as displayed in Fig. 7.10(a), looks quite different from the one plotted in Fig. 7.9(a) for the crystalline  $\alpha$ -Sn film. As compared to  $\alpha$ -Sn, the  $^{119}\text{Sn}(10 \text{ \AA})/\text{Si}$  multilayer exhibits broader phonon creation and annihilation features and disappearance of the sharp peak at 11 and 22 meV. This indicates the existence of considerable atomic disorder in the 10 Å interfacial Sn layer. For example, a similar disappearance of sharp peaks has been observed in NRIXS spectra of thin films of amorphous  $\text{TbFe}_2$  films, as compared to films of the crystalline Laves phase  $\text{TbFe}_2$  [143]. Comparing Fig. 7.9(a) and Fig. 7.10(a), and taking into account that for both cases almost the same isomer shift (of  $\alpha$ -like Sn) was measured with CEMS, it is presumed that the 10 Å thick Sn layers in Sn/a-Si multilayers exist in a long-range disordered, amorphous  $\alpha$ -like structure. Fig. 7.10(b) shows the decomposition of the NRIXS spectrum of Fig.7(a), after normalization and removal of the elastic peak in one-, two- and higher order-phonon contributions. The VDOS of the 10-Å Sn/a-Si multilayer (Fig. 7.12(b)) looks strikingly different from the DOS of the crystalline  $\alpha$ -Sn film (Fig. 7.12(a)). The vibrational spectrum of the Sn(10 Å)/a-Si multilayer is characterized by two extremely broad peaks positioned at 10 meV and about 20-22 meV. The dominant 10 meV peak also shows a shoulder near 7 meV. On the high energy side the broad band with a maximum near  $\sim 22$  meV extends up to a cut-off energy of about 28 meV, which is much larger than the position (23 meV) of the TO peak of crystalline  $\alpha$ -Sn (Fig. 7.12(a)). It is obvious that the four rather sharp phonon peaks of crystalline  $\alpha$ -Sn (in particular its dominant TO peak and the TA band) have been drastically modified with respect to energy and intensity in the 10 Å thick amorphous  $\alpha$ -like Sn interface layers.

Fig. 7.11(a) shows the NRIXS spectrum of the  $[^{119}\text{Sn}(20 \text{ \AA})/\text{Si}(50 \text{ \AA})]_{25}$  multilayer. CEMS shows that 20 Å Sn in these multilayers consists of 10 Å thick interfacial  $\alpha$ -like Sn and  $\sim 10$  Å  $\beta$ -Sn. Concluding from Fig. 7.10(a) and (b) that 10 Å Sn at the Sn/Si interface is in an amorphous state, the spectrum displayed in Fig. 7.11(a) must be a superposition of two contributions: one originating from amorphous interfacial  $\alpha$ -like Sn, and one from crystalline  $\beta$ -Sn. Since in Fig. 7.11(a) the elastic peak does not completely disappear (as would occur for pure  $\beta$ -Sn at 300 K [13, 122]), therefore the Sn(20 Å)/a-Si multilayer contains amorphous  $\alpha$ -like-Sn and additionally a contribution of  $\beta$ -Sn, in agreement with the CEMS results.

This sample also presents a dominant multiphonon contribution (Fig. 7.11(b)), similar to the  $\beta$ -Sn case [13, 122]. As observed for 10 Å amorphous  $\alpha$ -like-Sn in Fig. 7.12(b), the VDOS shown in Fig. 7.12(c) also exhibits broad features. In particular, the width of



**Figure 7.12:** Vibrational density of states (VDOS): (a) for  $\alpha\text{-}^{119}\text{Sn}(500 \text{ \AA})/\text{InSb}(001)$ , derived from Fig.7.9(b) (full circles); the theoretical phonon DOS convoluted with the the experimental resolution function of 0.8 meV is shown for comparison (pink solid line) [133]. (b) for  $[^{119}\text{Sn}(10 \text{ \AA})/\text{a-Si}(50 \text{ \AA})]_{46}$  and  $[^{119}\text{Sn}(10 \text{ \AA})/\text{a-Si}(20 \text{ \AA})]_{50}$  multilayers, derived from Fig.7.10(b) (full circles). (c) for  $[^{119}\text{Sn}(20 \text{ \AA})/\text{a-Si}(50 \text{ \AA})]_{25}$  multilayer, derived from Fig.7.11(b) (full circles); the bar diagram ( $\alpha\text{-Sn (exp.)}$ ) indicates the measured peak and shoulder positions for  $\alpha\text{-}^{119}\text{Sn}(500 \text{ \AA})$  in (a); the theoretical VDOS for bulk  $\beta\text{-Sn}$  (in arbitrary units) is also shown for comparison (blue solid line) [133]. The other bar diagrams indicate the energies of the prominent peak or shoulder of the various phonon-like bands predicted for amorphous  $\alpha$ -like Sn (a-Sn) by scaling (use of eq.(7.5), see also Fig.7.14(b)).



**Figure 7.13:** Phonon excitation probability density (after normalization and removal of the elastic peak) of a  $\beta$ -Sn foil [13] (full line) plotted together with the difference of the spectra shown in Figs. 7.11(b) and 7.10(b)(full squares).

the lower-energy peak in Fig. 7.12(c) near  $\sim 10$  meV appears to be larger than that of the corresponding peak in Fig. 7.12(b). One reason for this broadening is the additional contribution of  $\beta$ -Sn in the VDOS of Fig. 7.12(c), which is known to extend only up to  $\sim 17$  meV ( $\sim 140$   $\text{cm}^{-1}$ ) [122, 133] (see solid blue curve in Fig. 7.12(c)), and thus essentially overlaps with the 10 meV VDOS peak of amorphous  $\alpha$ -like-Sn. Similar to the case of Fig. 7.12(b), the strong TO peak of crystalline  $\alpha$ -Sn near 23 meV appears to be largely suppressed, also in the VDOS of  $\beta$ -Sn covered interfacial amorphous  $\alpha$ -like-Sn (Fig. 7.12(c)). The peak near 20 meV (which coincides with the position of the LO peak of crystalline  $\alpha$ -Sn) is more pronounced in Fig. 7.12(c) than in Fig. 7.12(b).

Definitive evidence of the presence of  $\beta$ -Sn in the multilayer with 20 Å Sn is shown in Fig. 7.13. Here, the phonon excitation probability density of a  $\beta$ -Sn foil [13] (full line) is plotted together with the phonon probability density obtained after the subtraction of the spectra shown in Fig. 7.10(b) and Fig. 7.11(b)(full squares). These spectra correspond to multilayers with 10 Å and 20 Å Sn, respectively. The difference spectrum obtained (Fig. 7.13, data points) is in excellent agreement with the phonon excitation probability

density of the  $\beta$ -Sn foil measured by Hu et al. [13], demonstrating that 20 Å Sn in the Sn/Si multilayers are composed by amorphous  $\alpha$ -like Sn and crystalline  $\beta$ -Sn.

From the normalized probability of inelastic nuclear absorption,  $W(E)$ , the Lamb-Mössbauer recoilless factor ( $f$ ), the mean kinetic energy per atom ( $\bar{T}$ ), and the mean atomic force constant ( $\bar{K}$ ) have been obtained after removal of the elastic contribution, by using model-independent sum rules [156]. Moreover, the vibrational density of states  $g(E)$ , provides information on the vibrational entropy per atom ( $S$ ) [14]. Table 7.5 displays values of  $f$ ,  $\bar{T}$ , and  $\bar{K}$  thus obtained. The value of the  $f$  factor obtained for 500 Å  $\alpha$ -Sn on InSb(001),  $f=0.14 \pm 0.02$ , is very close to the bulk value of  $\alpha$ -Sn given in Ref. [13] ( $f=0.16 \pm 0.02$ ) for 2000 Å epitaxial  $\alpha$ -Sn grown on CdTe(001). For the case of the amorphous  $\alpha$ -like-Sn sample ( $[\text{Sn}(10 \text{ \AA})/\text{Si}(20,50 \text{ \AA})]_{50}$ ), the  $f$ -factor of  $0.21 \pm 0.01$  is found to be significantly larger than these values. The sample that contained amorphous  $\alpha$ -like-Sn and  $\beta$ -Sn ( $[\text{Sn}(20 \text{ \AA})/\text{Si}(50 \text{ \AA})]_{25}$ ) shows a much smaller  $f$  factor,  $f=0.13 \pm 0.02$ , suggesting that this value is about the average value between  $f=0.21$  for interfacial amorphous  $\alpha$ -like-Sn and  $f=0.042$  for crystalline  $\beta$ -Sn. The latter sample has also the smallest average kinetic energy  $\bar{T}$  of all samples (Table 7.5).

Sample	$f$	$\bar{T}$ (meV)	$\bar{K}$ (N/m)
$\alpha$ -Sn(500Å)/InSb(001)	$0.14 \pm 0.02$	$13.9 \pm 0.3$	$117 \pm 33$
$\alpha$ -Sn(2000Å)/CdTe(001) [13]	$0.16 \pm 0.02$	$13.4 \pm 0.2$	$155 \pm 16$
amorphous $\alpha$ -like-Sn in $[\text{Sn}(10\text{\AA})/\text{Si}(20\text{\AA})]_{50} +$ $[\text{Sn}(10\text{\AA})/\text{Si}(50\text{\AA})]_{46}$	$0.21 \pm 0.01$	$13.5 \pm 0.2$	$168 \pm 18$
amorphous $\alpha$ -like-Sn+ $\beta$ -Sn $[\text{Sn}(20\text{\AA})/\text{Si}(50\text{\AA})]_{25}$	$0.13 \pm 0.02$	$13.0 \pm 0.2$	$97 \pm 20$
$^{119}\text{Sn}$ ion-implanted in (bulk) $\alpha$ -Sn [131]	$0.133 \pm 0.006$		

**Table 7.5:** Recoilless fraction (Lamb-Mössbauer factor  $f$ ), mean kinetic energy per atom ( $\bar{T}$ ), and mean atomic force constant ( $\bar{K}$ ) for the Sn layers, derived from NRIXS measurements.

## 7.4 Discussion

### 7.4.1 Structure

The Raman spectra (Fig. 7.8(a)-(c)) demonstrate conclusively that the evaporated Si layers in the Sn/Si multilayers are amorphous. This result agrees with the wide-angle XRD scans (Fig. 7.2(a)-(c)), where no sharp Bragg peaks of crystalline Si, except that of the Si(111) substrate, are observed. (This conclusion is based on the hypothesis that the RT deposited Si layers are polycrystalline.)

Concerning the Sn phases in the multilayers, Bragg reflections of crystalline  $\alpha$ -Sn have not been detected on any of the Sn/a-Si multilayers, for instance in Fig. 7.2(a) for  $t_{\text{Sn}}=10 \text{ \AA}$  and Fig. 7.2(b) for  $t_{\text{Sn}}=20 \text{ \AA}$ . On the other hand, the crystalline  $\beta$ -Sn

(400) Bragg reflection is observed in Fig. 7.2(b) for the multilayer with  $t_{Sn}=20 \text{ \AA}$ , which (according to the CEMS result, Fig. 7.4) contains much more  $\alpha$ -like Sn (70%) than  $\beta$ -Sn (30 %). This demonstrates that the XRD sensitivity is high enough to detect the crystalline  $\alpha$ -Sn phase (if any was present) in multilayers with  $t_{Sn}=10 \text{ \AA}$  or  $t_{Sn}=20 \text{ \AA}$ . For this reason, and since Bragg reflections of crystalline  $\alpha$ -Sn have not been observed for  $t_{Sn}=10\text{-}20 \text{ \AA}$  (or any other Sn thicknesses), one may conclude that the  $\alpha$ -Sn-like phase (which is unambiguously identified by CEMS (Fig. 7.3) in such multilayers) has a disordered (amorphous) structure that does not yield Bragg peaks.

The CEMS result displayed in Fig. 7.4 demonstrates that the amorphous  $\alpha$ -like-Sn layer of  $\sim 10 \text{ \AA}$  thickness is located at the interface with amorphous Si. Moreover it must be emphasized that the isomer-shift (i.e. chemical-shift) values,  $\delta$ , of interfacial amorphous  $\alpha$ -like-Sn (Table 7.1) are in very good agreement with  $\delta$  values of pure crystalline epitaxial  $\alpha$ -Sn films and of bulk  $\alpha$ -Sn (Table 7.1). This observation proves that interfacial Sn-Si alloy formation does *not* occur in these multilayers, as expected from the thermodynamic phase diagram [139]. This is corroborated by the fact that the  $^{119}\text{Sn}$  isomer shift of  $\alpha$ -Sn was found to be remarkably larger (by 0.26 mm/s) than that of epitaxial metastable  $\text{Si}_{1-x}\text{Sn}_x$  dilute-alloy films [157], i.e. the isomer shift (relative to pure  $\alpha$ -Sn) is reduced by Sn-Si alloying, which is not observed in these samples (Table 7.1). Further, the similar isomer shifts suggest that the average local electronic structure (which is related to the average local environment or short range order) in the amorphous  $\alpha$ -like-Sn interface is similar to that of crystalline  $\alpha$ -Sn, since the isomer shift is proportional to the s-electron density at the Mössbauer nucleus [158]. Also of note, is an enhancement of the Mössbauer linewidth of the amorphous  $\alpha$ -like-Sn interfacial layer as compared to the linewidth of the  $\beta$ -Sn phase in the multilayers (Table 7.1). This excess broadening may originate from a small distribution of isomer shifts and/or weak quadrupole interactions in the disordered (amorphous)  $\alpha$ -like-Sn phase. When comparing with literature reports [131], the isomer shift of amorphous  $\alpha$ -like-Sn produced by  $^{119}\text{Sn}$  ion implantation in (bulk)  $\alpha$ -Sn ( $2.14 \pm 0.04 \text{ mm/s}$ ) is slightly larger than that of bulk  $\alpha$ -Sn and the amorphous Sn films (Table 7.1). Differences in the deviations from the ideal local tetrahedral structure in both types of samples may account for this small difference in isomer shifts.

## 7.4.2 Vibrational dynamics

### (a) Vibrational density of states

One of the most important results is the observation of remarkable differences in the VDOS of the crystalline (epitaxial)  $\alpha$ -Sn film (Fig. 7.12(a)) and of 10  $\text{ \AA}$  thick  $\alpha$ -like Sn in the Sn/a-Si multilayers (Fig. 7.12(b)). The arguments for the amorphous structure of this interfacial  $\alpha$ -like-Sn (called amorphous (a-)Sn in the following) have been presented in section 7.4.1. Moreover, the energies of the prominent features (peaks and shoulders) in the VDOS bands (Fig. 7.12(b)) are typical for the amorphous phase of  $\alpha$ -Sn and are predicted by scaling of the respective energies of a-Ge and a-Si. This is demonstrated in Fig. 7.14(a), plotted are the known energies of the prominent VDOS features (peaks and



shoulders) of various phonon-like bands (TO-, LO-, LA-, and TA- type) of amorphous (a-)Ge [152] and a-Si [152, 159] as a function of  $M^{-1/2} a_0^{-3/2}$  are shown. ( $M$  is the atomic mass number and  $a_0$  the lattice parameter). It is known that the prominent energies,  $E_i$ , of a certain vibrational band,  $i$ , of a-Ge and a-Si (and also of crystalline (cr-)Ge and (cr-)Si, as shown in Fig. 7.14(b)) are proportional to  $M^{-1/2} a_0^{-3/2}$  [152, 160, 161]. This proportionality is well described by the straight lines in Fig. 7.14. The corresponding vibrational energies of a-Sn may be predicted by the scaling relation [152]:

$$\omega_i(Sn) = \omega_i(Ge, Si) \left( \frac{M_{Sn}}{M_{Ge, Si}} \right)^{-1/2} \left( \frac{a_0(\alpha - Sn)}{a_0(Ge, Si)} \right)^{-3/2} \quad (7.5)$$

The results thus obtained are shown as a bar diagram for  $\alpha$ -Sn in Fig. 7.12(a) and for a-Sn in Fig. 7.12(b),(c). For  $\alpha$ -Sn Fig. 7.12(a), the differences between the energies predicted from scaling and the experimentally observed peak/shoulder are small and at most 2 meV; best agreement is found for the TO mode. For interfacial a-Sn (Fig. 7.12(b)), the experimentally observed energies of prominent features and those predicted from scaling also are in good agreement; in particular the observed dominant peak near 10 meV of the TA-like band (called TA(2) in Fig. 7.14) and the shoulder near 7 meV of the TA-like band (called TA(1) in Fig. 7.14) are well reproduced by scaling. In the region of the TO-like band the maximum at  $\sim 20.6$  meV of the observed broad hump coincides within only  $\sim 1.5$  meV with the position of the predicted TO-like peak (Fig. 7.12(b)). Other, less intense, peaks at 14 and 17.5 meV in the experimental data coincide with the LA-like and LO-like peak positions obtained from scaling. (The larger scatter of the data points at and above  $\sim 24$  meV (Fig. 7.12(b)) make identification of peaks in that region uncertain). The good agreement between experimental and predicted (from scaling) vibrational energies can also be noticed in Fig. 7.14, where the experimental values for interfacial a-Sn all fall on the respective straight line (given by eq.(7.5)). This good agreement provides further strong evidence for the amorphous nature of the 10 Å thick  $\alpha$ -like Sn layers embedded between a-Si layers.

It is worthwhile mentioning that the strong TA-like band (Fig. 7.12(b)) of interfacial a-Sn is shifted towards higher energy by 2-3 meV relative to its crystalline bulk-like counterpart (Fig. 7.12(a)). Further, the intensity ratio TA(2)/TA(1) (10 meV peak to 7 meV peak) of interfacial a-Sn is  $> 1$ , while its crystalline counterpart (7-meV shoulder to 5-meV peak) is  $< 1$ . This difference is possibly the consequence of the quasi two-dimensional nature of the 10-Å thick a-Sn films. One can speculate that interface coupling (hybridization) of TA-like modes of interfacial a-Sn with the TA-like modes of a-Si that are higher in energy (near 18.6 and 26.7 meV [152]) might cause these VDOS differences between (bulk-like)  $\alpha$ -Sn and interfacial a-Sn.

Figs. 7.12(a) and 7.12(b) reveal that the VDOS of interfacial a-Sn extends to about 11 % higher energies than the VDOS of  $\alpha$ -Sn, and surprisingly the strong TO band of  $\alpha$ -Sn is largely suppressed in interfacial a-Sn. Both effects may be caused by the very high degree of local atomic disorder in a-Sn as compared to  $\alpha$ -Sn. As has been pointed out in Ref. [129] on Raman spectroscopy, the strength of the TA Raman band

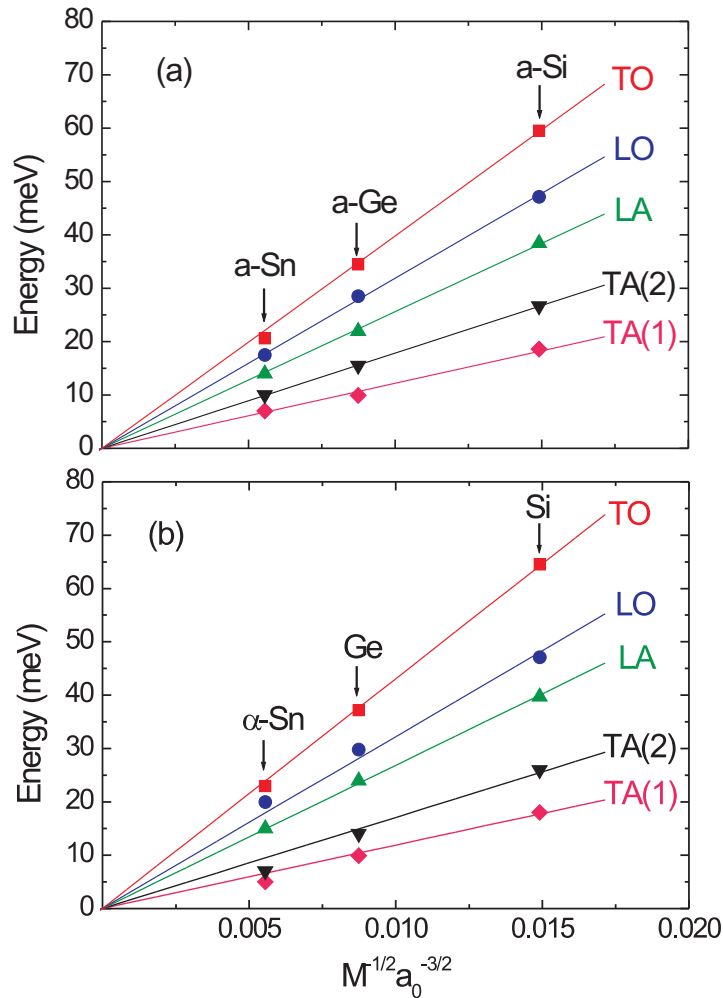


**Figure 7.14:** Measured energies of the prominent peak or shoulder of various phonon-like bands related to the VDOS of (bulk-like) a-Ge [152] and (bulk-like) a-Si [152, 159] (a), and of (bulk) crystalline (cr-)Ge [152] and cr-Si [152, 159] (b), plotted versus  $M^{-1/2}a_0^{-3/2}$  ( $M$ : atomic mass number;  $a_0$ : lattice parameter). The straight lines are least-squares fits to the data points for a-(cr-)Ge and a-(cr-)Si and we forced to pass through the origin. The data for amorphous  $\alpha$ -like Sn (a-Sn) obtained from Fig. 7.12(b) scale very well with the data of a-Ge and a-Si. (The values  $a_0(\text{Si})=5.43 \text{ \AA}$ ,  $a_0(\text{Ge})=5.65 \text{ \AA}$  and  $a_0(\alpha\text{-Sn})=6.489 \text{ \AA}$  were used).

of a-Si is enhanced (and the strength of the TO Raman band is reduced) by increasing disorder. Disorder in a-Si may be enhanced, for instance, by increasing average bond angle fluctuations, resulting in larger Raman linewidths of the TO band [162] combined with an enhanced ratio of the strengths of the TA to the TO Raman bands [163]. As the Raman bands reflect the VDOS, similar behavior may be expected of the VDOS bands upon disorder, i.e., a reduction of the relative strength of the TO peak (combined with

enhanced broadening) upon increasing disorder. This is what is observed in going from Fig. 7.12(a) to Fig. 7.12(b); here, the TO band is largely suppressed by the high degree of disorder (Fig. 7.12(b)). A dependence upon atomic disorder of the optical phonon peak in the Fe-projected VDOS of crystalline Pt<sub>3</sub>Fe has been also reported by Fultz et al. [164]. With increasing disorder in Pt<sub>3</sub>Fe, the optical-phonon VDOS peak at 25 meV underwent a reduction in intensity combined with asymmetric broadening towards higher and lower energies. This observation is qualitatively similar to the changes seen in the TO region of the VDOS in going from Fig. 7.12(a) to Fig. 7.12(b), except that the TO peak is nearly entirely suppressed in Fig. 7.12(b), presumably by a very high degree of atomic disorder in the 10 Å thick Si-embedded Sn layers.

In this context it is interesting to note that in the VDOS of 20 Å Sn embedded between a-Si (Fig. 7.12(c)), sharper features than in Fig. 7.12(b) (for 10 Å Sn) appear in the region of the optical phonons of  $\alpha$ -Sn. For 20 Å Sn (Fig. 7.12(c)), the cut-off at 25 meV is as sharp as that of  $\alpha$ -Sn (Fig. 7.12(a)), and the weaker TO peak near 23 meV and the stronger LO peak near 20 meV, both of  $\alpha$ -Sn, can be clearly detected in Fig. 7.12(c). This means that the interfacial amorphous  $\alpha$ -Sn-like layers in the Sn(20 Å)/Si(50 Å) multilayer are less disordered than the amorphous Sn layers in the Sn(10 Å)/a-Si multilayer. Possibly the crystallization process to  $\beta$ -Sn that occurs above the critical Sn thickness of 10 Å, lowers the degree of disorder in the residual 10 Å thick amorphous  $\alpha$ -Sn-like layer at the a-Si interface.

#### (b) f-factor and vibrational entropy

The f-factor of the amorphous interfacial  $\alpha$ -Sn-like layer is found to be enhanced relative to the f-factor of crystalline  $\alpha$ -Sn (Ref. [131] and Table 7.5). The calculation of the f-factor strongly weights the low energy part of the VDOS; and the observed enhancement originates from the shift towards higher energy of the low-energy TA band of crystalline  $\alpha$ -Sn (Fig. 7.12(a)) to the strong 10-meV peak of amorphous  $\alpha$ -like Sn (Fig. 7.12(b)).

In Fig. 7.15 the temperature dependence of the vibrational entropy per atom of the crystalline  $\alpha$ -Sn(500 Å)/InSb(001) system and of the amorphous  $\alpha$ -like-Sn interface layer, as calculated from the corresponding measured VDOS (i.e.  $g(E)$ ) and eq.(8.5) in Ref. [14] are shown. Also displayed in Fig. 7.15 is the theoretical vibrational entropy of crystalline (bulk)  $\alpha$ - and  $\beta$ -Sn by Pavone et al. [133]. The agreement between theory and experiment in the case of  $\alpha$ -Sn is very good, suggesting that a 500 Å thick  $\alpha$ -Sn film behaves like bulk  $\alpha$ -Sn with respect to the vibrational dynamics. The vibrational entropy of the [Sn(20 Å)/Si(50 Å)]<sub>25</sub> multilayer, that contains  $\beta$ -Sn and interfacial amorphous  $\alpha$ -like Sn, is also shown in Fig. 7.15; its entropy is located about midway between the entropy of interfacial amorphous  $\alpha$ -like Sn and  $\beta$ -Sn, as expected from the composition of this sample.

Fig. 7.15 also demonstrates that the vibrational entropy per atom of the 10-Å thick amorphous  $\alpha$ -Sn-like interface layer is fairly close to that of crystalline  $\alpha$ -Sn. This gives an answer to the question of why a thin metastable amorphous  $\alpha$ -Sn-like layer is more favorable at the a-Si interface at RT than the stable high-temperature  $\beta$ -phase. The

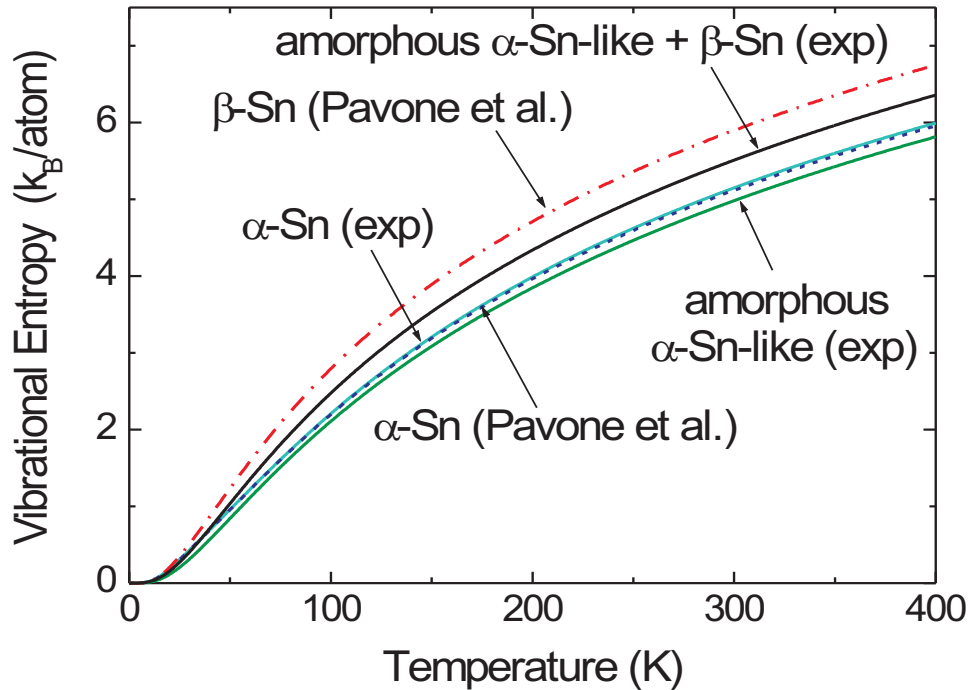


**Figure 7.15:** Temperature dependence of the vibrational entropy of epitaxial  $\alpha$ -Sn(500 Å)/InSb(001) (light blue solid line), of amorphous  $\alpha$ -Sn(10 Å)/a-Si multilayer (green solid line), and of Sn(20 Å)/a-Si multilayer (black solid line) deduced from the VDOS in Fig. 7.12(a),(b), and (c), respectively. The theoretical VDOS of bulk  $\alpha$ -Sn and  $\beta$ -Sn are shown for comparison (dotted dark blue line, and dashed-dotted red line, respectively) [133].

theoretical study by Pavone et al. [133] for bulk Sn demonstrates that the  $\beta$ -Sn phase is stabilized at high T (e.g. at 300 K) by its larger vibrational entropy, and consequently by its lower free energy ( $F=U-TS$ ), relative to  $\alpha$ -Sn. Because of the nearly identical vibrational entropies per atom of  $\alpha$ -Sn and the interfacial amorphous  $\alpha$ -like Sn layer (Fig. 7.15), one could expect the  $\beta$ -phase to be more stable at high T than the amorphous  $\alpha$ -Sn-like structure. However, the observed stability of the interfacial amorphous Sn layer contradicts this hypothesis. Preliminary high-temperature Mössbauer measurements on these samples demonstrate that this interfacial amorphous Sn layer is stable at least up to 200°C. Therefore, it must be the *interface free energy* between amorphous  $\alpha$ -Sn and the underlying amorphous Si film that provides the basis for the observed stabilization of the metastable amorphous  $\alpha$ -Sn-like layer, and is *not* the vibrational entropy. One must assume that the interfacial free energy of the amorphous  $\alpha$ -like Sn/a-Si system is lower than that of the  $\beta$ -Sn/a-Si system in order to understand the metastability

of the amorphous Sn/a-Si system. At 300 K, there has been observed a critical film thicknesses of 10 Å below which thickness the amorphous Sn structure is stable with respect to the crystalline  $\beta$ -phase (Fig. 7.4). This phenomenon is reminiscent of the pseudomorphic growth of metastable phases of epitaxial thin films on a single-crystalline substrate [165, 166]. However, the growing amorphous  $\alpha$ -Sn-like structure is probably able to accommodate the "lattice" misfit with the a-Si film more easily than a crystalline system.

## 7.5 Concluding remarks

The structure and vibrational dynamics of nanoscale Sn/a-Si multilayers grown at room temperature (RT) in ultrahigh vacuum on Si(111) wafers have been studied by means of X-ray diffraction (XRD), Raman scattering,  $^{119}\text{Sn}$  Mössbauer spectroscopy (CEMS), and  $^{119}\text{Sn}$  inelastic nuclear resonant scattering (NRIXS) of synchrotron radiation. The Raman line shifts observed are typical for amorphous (a-Si). Mössbauer isomer shifts demonstrate that the Sn layers in these multilayers exist in a pure  $\alpha$ -Sn-like phase up to a Sn thickness ( $t_{\text{Sn}}$ ) of 10 Å. The formation of crystalline  $\beta$ -Sn was observed with increasing Sn thickness, with 10 Å thick  $\alpha$ -Sn-like layers remaining stabilized at the Sn/Si interfaces at RT. Since no high-angle XRD Bragg peaks typical for crystalline  $\alpha$ -Sn could be detected, it is likely that the 10 Å  $\alpha$ -Sn-like interfacial layers are amorphous, similar to the underlying Si layers. By means of NRIXS, the Sn-projected vibrational density of states (VDOS) was measured in Sn/a-Si multilayers with thicknesses  $t_{\text{Sn}}=10,20$  Å and  $t_{\text{Si}}=20,50$  Å, and in 500 Å thick epitaxial  $\alpha$ -Sn on InSb(001) as a reference. The VDOS of the multilayers were found to be distinct from those of the crystalline (bulk)  $\alpha$ -Sn and  $\beta$ -Sn phases. Scaling arguments for the VDOS provide further evidence for the amorphous nature of 10 Å thick  $\alpha$ -Sn-like/Si interfaces.

Further, the Lamb-Mössbauer factor, the mean kinetic energy per atom, the mean atomic force constant, and the vibrational entropy per atom were obtained. The vibrational entropy deduced from the VDOS of a 500 Å thick epitaxial  $\alpha$ -Sn film on InSb(001) is found to be in good agreement with a recent theory [133]. At 300K, the observed small difference in vibrational entropy,  $\Delta S/k_B$ , of  $+ 0.17 \pm 0.05$  per atom between  $\alpha$ -Sn and interfacial amorphous  $\alpha$ -like Sn does not account for the stability of the interfacial amorphous Sn layer. Consequently, it is the amorphous-Sn/a-Si interface free energy that stabilizes the metastable amorphous Sn phase. Finally, the present results demonstrate that NRIXS is a unique method for investigating the vibrational dynamics of buried interfaces.



---

## References

- [1] K. Wilmers, *Aufbau einer Ultrahochvakuumanlage für Molekularstrahlepitaxie und Untersuchungen zu Struktur und Magnetismus von kubisch-flächenzentrierten Eisenfilmen mittels Mössbauerspektroskopie*, Diplomarbeit, Gerhard-Mercator-Universität Duisburg, Duisburg, (1995)
- [2] Ch. Sauer and W. Zinn, in: L.H. Bennet and R.E. Watson (Eds.) *Magnetic multilayers* (World Scientific, Singapore, 1993)
- [3] G. Schatz and A. Weidinger, *Nukleare Festkörperphysik*, (B.G. Teubner, Stuttgart, 1995)
- [4] H. Wegener, *Der Mössbauer Effect und seine Anwendung in Physik und Chemie*, (Bibliograph. Institut Mannheim, Mannheim, 1966)
- [5] B. Scholz, R.A. Brand, W. Keune, *Phys. Rev. B* **50** (1994) 2537
- [6] Z.Q. Qiu, S.D. Bader, *Rev. Scientific Instr.* **71** (2000) 1243
- [7] G. Cubiotti, G. Mondio, K. Wandelt (Eds.), *Auger Spectroscopy and Electronic Structure*, Springer Series in Surface Science **18** (Berlin, Heidelberg, New York, London, Paris, Tokyo, Hong Kong, 1988)
- [8] H. Lüth, *Surfaces and Interfaces of Solid Materials*, (Springer-Verlag, Berlin, Heidelberg, New York, 1995)
- [9] H.E. Bishop, in *Methods of surface analysis*, J.M. Walls (Ed.) (Cambridge University Press, 1992) p.87
- [10] M.A. Van Hove, W.H. Weinberg, C.M. Chan, *Low Energy Electron Diffraction*, Springer Series in Surface Science **6** (Springer, Heidelberg, New York, London, 1986) p.105
- [11] J.B. Pendry, *Low Energy Electron Diffraction*, (Academic Press, New York, London, 1974)
- [12] W. Sturhahn, T.S. Toellner, E.E. Alp, X.W. Zhang, M. Ando, Y. Yoda, S. Kikuta, M. Seto, C.W. Kimball, and B. Dabrowski, *Phys. Rev. Lett.* **74** (1995) 3832
- [13] M. Hu, *Inelastic Nuclear Resonant Scattering and Its Application to Tin Materials*, Dissertation, Northwestern University, Evanston, Illinois, USA (1999)
- [14] A.I. Chumakov and W. Sturhahn, *Hyperfine Int.* **123-124** (1999) 781
- [15] See, for example, the articles in *J. Magn. Magn. Mater.* **200**, (1999)

- 
- [16] F. J. Himpsel, T. Jung, A. Kirakosian, J.-L. Lin, D.Y. Petrovykh, H. Rauscher, and J. Viernow, *Nanowires by Step Decoration*, *MRS Bulletin* **24** (8) (1999) 20; F.J. Himpsel, T. Jung, and J.E. Ortega, *Surf. Rev. Lett.* **4** (1997) 371
- [17] P.Gambardella, M. Blanc, H. Brune, K. Kuhnke, and K. Kern, *Phys. Rev. B* **61** (2000) 2254
- [18] P. Gambardella, M. Blanc, L. Bürgi, K. Kuhnke, and K. Kern, *Surf. Sci.* **449** (2000) 93
- [19] H. J. Elmers, J. Hauschild, H. Höche, U. Gradmann, H. Bethge, D. Heuer, and U. Köhler, *Phys. Rev. Lett.* **73** (1994) 898;
- [20] J. Hauschild, H.J. Elmers, and U. Gradmann, *Phys. Rev. B* **57** (1998) 677
- [21] J. Shen, M. Klaua, P. Ohresser, H. Jenniches, J. Barthel, C.V. Mohan, and J. Kirschner, *Phys. Rev. B* **56**, (1997) 11134; J. Shen, R. Skomski, M. Klaua, H. Jenniches, S. Sundar Manoharan, and J. Kirschner, *Phys. Rev. B* **56** (1997) 2340
- [22] D. Wingert and D. Stauffer, *Physica A* **219**, (1995) 135; P. Sen, D. Stauffer, and U. Gradmann, *Physica A* **245** (1997) 361
- [23] J.-P. Bucher, E. Hahn, P. Fernandez, C. Massobrio, and K. Kern, *Europhysics Lett.* **27** (1994) 473
- [24] H. J. Choi, R. K. Kawakami, E. J. Escorcia-Aparicio, Z. Q. Qiu, J. Pearson, J.S. Jiang, Dongqi Li, and S.D. Bader, *Phys. Rev. Lett.* **82** (1999) 1947, and references therein.
- [25] X.F. Jin, J. Barthel, J. Shen, S. S. Manoharan, and J. Kirschner, *Phys. Rev. B* **60** (1999) 11809
- [26] C. Liu and S.D. Bader, *J. Appl. Phys.* **67** (1990) 5758
- [27] J. Quinn, Y.S. Li, H. Li, D. Tian, F. Jona, and P. M. Marcus, *Phys. Rev. B* **43** (1991) 3959
- [28] J. Dorantes-Dávila and G.M. Pastor, *Phys. Rev. Lett.* **81** (1998) 208
- [29] Dongqi Li, M.Freitag, J. Pearson, Z.Q. Qiu, and S.D.Bader, *Phys. Rev. Lett.* **72** (1994) 3112; S.D. Bader, Dongqi Li, and Z. Q. Qiu *J. Appl. Phys.* **76** (1994) 6419
- [30] H. Kronmüller, K.D. Durst, and M. Sagawa, *J. Magn. Magn. Mat.* **74** (1988) 291
- [31] C.L. Chien, *J. Appl. Phys.* **69** (1991) 5267, and references therein.
- [32] M.E. Fisher and A.E. Ferdinand, *Phys. Rev. Lett.* **19** (1967) 169; M.E. Fischer and M.N. Barber, *Phys. Rev. Lett.* **28** (1972) 1516



- 
- [33] H.J. Elmers, J. Hauschild, and U. Gradmann, *Phys. Rev. B* **54** (1996) 15224
- [34] B. Roldan Cuenya, M. Doi, T. Ruckert, W. Keune, and T. Steffl, *J. Phys. Soc. Japan* **69**, Suppl. A (2000) 125
- [35] H. Mühlbauer, Ch. Müller, and G. Dumpich, *J. Magn. Magn. Mat.* **192** (1999) 423
- [36] V.I. Moruzzi, P.M. Marcus, and J. Kübler, *Phys. Rev. B* **39** (1989) 6957, and references cited therein.
- [37] G.L. Krasko and G.B. Olson, *Phys. Rev. B* **40** 11536 (1989)
- [38] C.H. Herper, E. Hoffmann, and P. Entel, *Phys. Rev. B* **60** (1999) 3839, and references cited therein.
- [39] T. Shinjo and W. Keune, *J. Magn. Magn. Mater.* **200** (1999) 598, and references therein.
- [40] W. Keune, A. Schatz, R.D. Ellerbrock, A. Fuest, Katrin Wilmers, and R.A. Brand, *J. Appl. Phys.* **79** (1996) 4265, and references cited therein.
- [41] Y. Yamada, B. Sadeh, C.Lee, M. Doi, and M. Matsui, *J. Magn. Soc. Japan* **23** (1999) 575
- [42] A. Clarke, P.J. Rous, M. Arnott, G. Jennings, and R.F. Willis, *Surf. Sci.* **192** (1987) L843
- [43] P. Ehrhard, B. Schönfeld, H.H. Ettwig, and W. Pepperhoff, *J. Magn. Magn. Mater.* **22** (1980) 79
- [44] D. Schmitz, C. Charton, A. Scholl, C. Carbone, and W. Eberhardt, *Phys. Rev. B* **59** (1999) 4327
- [45] S. Müller, P. Bayer, C. Reischl, K. Heinz, B. Feldmann, H. Zillgen, and M. Wuttig, *Phys. Rev. Lett.* **74** (1995) 765
- [46] J. Thomassen, F. May, B. Feldmann, M. Wuttig, and H. Ibach, *Phys. Rev. Lett.* **69** (1992) 3831
- [47] Dongqi Li, M. Freitag, J. Pearson, T.Q. Qiu, and S.D. Bader, *Phys. Rev. Lett.* **72** (1994) 3112
- [48] S. Müller, A. Kinne, M. Kottcke, R. Metzler, P. Bayer, L. Hammer, and K. Heinz, *Phys. Rev. Lett.* **75** (1995) 2859
- [49] A. Schatz and W. Keune, *Surf. Sci.* **440** (1999) L841
- [50] M.-T. Lin, J. Shen, W. Kuch, H. Jenniches, M. Klaua, C.M. Schneider, and J. Kirschner, *Surf. Sci.* **410** (1998) 290

- 
- [51] S.H. Lu, J. Quinn, D. Tian, F. Jona, and P.M. Marcus, *Surf. Sci.* **209** (1989) 364
- [52] W.A.A. Macedo, W. Keune, and R.D. Ellerbrock, *J. Magn. Magn. Mater.* **93** (1991) 552
- [53] R. Rochow, C. Carbone, Th. Dodt, F.P. Johnen, and E. Kisker, *Phys. Rev. B* **41** (1990) 3426
- [54] D. Tillmann and E. Kisker, *Solid State Commun.* **100** (1996) 415
- [55] F. Baudelet, M.-T. Lin, W. Kuch, K. Meinel, B. Choi, C.M. Schneider, and J. Kirschner, *Phys. Rev. B* **51** (1995) 12563
- [56] M.-T. Lin, J. Shen, W. Kuch, H. Jenniches, M. Klaua, C.M. Schneider, and J. Kirschner, *Phys. Rev. B* **55** (1997) 5886
- [57] B. Feldmann, B. Schirmer, A. Sokoll, and M. Wuttig, *Phys. Rev. B* **57** (1998) 1014
- [58] B. Schirmer, B. Feldmann, and M. Wuttig, *Phys. Rev. B* **58** (1998) 4984
- [59]  $r_{ws}$  is given by  $4\pi r_{ws}^3/3 = ca^2/2$ =atomic volume, a= in-plane lattice spacing, c=out-of-plane lattice parameter. The atomic unit (a.u.) is the first Bohr radius,  $a_o = 5.292 \times 10^{-11}$  m.
- [60] P. Bayer, S. Müller, P. Schmailzl, and K. Heinz, *Phys. Rev. B* **48** (1993) 17611
- [61] T. Ezawa, W.A.A. Macedo, U. Glos, W. Keune, K.P. Schletz, and U. Kirschbaum, *Physica B* **161** (1989) 281
- [62] W. Keune, T. Ezawa, W.A.A. Macedo, U. Glos, K.P. Schletz, and U. Kirschbaum, *Physica B* **161** (1989) 269
- [63] D.J. Keavney, D.F. Storm, J.W. Freeland, I.L. Grigorov, and J.C. Walker, *Phys. Rev. Lett.* **74** (1995) 4531
- [64] Z. Nishiyama, in *Martensitic Transformations* (Academic Press, New York 1978)
- [65] H.C. Herper, E. Hoffmann, and P. Entel, *J. Physique IV France* **7** (1997) C5-71
- [66] E.F. Wassermann, M. Acet, P. Entel, W. Pepperhoff, *J. Magn. Soc. Japan* **23** (1999) 385
- [67] K. Kalki, D.D. Chambliss, K.E. Johnson, R.J. Wilson, S. Chiang, *Phys. Rev. B* **48** (1993) 18344
- [68] M. Wuttig, B. Feldmann, J. Thomassen, F. May, H. Zillger, A. Brodde, H. Hanne-  
mann, and H. Neddermeyer, *Surf. Sci.* **291** (1993) 14

- 
- [69] J. Giergiel, J. Kirschner, J. Landgraf, J. Shen, J. Woltersdorf, Surf. Sci. **310** (1994) 1
- [70] A. Kirilyuk, J. Giergiel, J. Shen, M. Straub, and J. Kirschner, Phys. Rev. B **54** (1996) 1050
- [71] N. Memmel and Th. Detzel, Surf. Sci. **307** (1994) 490
- [72] P. Schmailzl, K. Schmidt, P. Bayer, R. Doell, and K. Heinz, Surf. Sci. **312** (1994) 73
- [73] K. Kadau, R. Meyer, and P. Entel, Surf. Rev. and Lett. **6** (1990) 35
- [74] E.C. Bain, Trans. AIME **70** (1924) 25
- [75] P. Alippi, P.M. Marcus, and M. Scheffler, Phys. Rev. Lett. **78** (1997) 3892
- [76] M.G. Donato, P. Ballone, and P.V. Giaquinta, Phys. Rev. B **61** (2000) 24
- [77] E. Hahn, E. Kampshoff, N. Wälchli, and K.Kern, Phys. Rev. Lett. **74** (1995) 1803
- [78] B.Roldan Cuenya, M. Doi, S. Löbus, R. Courths and W. Keune, Surface Science (in press)
- [79] P.M. Marcus and F. Jona, Surf. Rev. Lett. **1** (1994) 15
- [80] W.Kiauka, C. van Cuyck, and W. Keune, Mater. Sci. and Engin. B **12** (1992) 273
- [81] J. Fassbender, U. May, B. Schirmer, R.M. Jungblut, B. Hillebrands, and G. Güntherodt, Phys. Rev. Lett. **75** (1995) 4476
- [82] R.W. Balluffi, Y. Komem, T. Schober, Surf. Sci. **31** (1972) 68
- [83] G.K. Wertheim, *Mössbauer Effect: Principles and Applications* (Academic Press, New York, 1964)
- [84] R.D. Ellerbrock, A. Fuest, A. Schatz, W. Keune and R.A. Brand, Phys. Rev. Lett. **74** (1995) 3053
- [85] B. Scholz, R.A. Brand, and W. Keune, Phys. Rev. B **50** (1994) 2537
- [86] M. Friák, M. Šob, and V. Vitek, Phys. Rev. B **63** (2001) 052405
- [87] G.A. Prinz, *Ultrathin Magnetic Structures*, edited by B. Heinrich and J.A.C. Bland, vol. II, (Springer, Berlin, 1994) p.1-44
- [88] J.R. Waldrop and R.W. Grant, Appl. Phys. Lett. **34** (1979) 630
- [89] G.A. Prinz and J.J. Krebs, Appl. Phys. Lett. **39** (1981) 397

- 
- [90] J.J. Krebs, B.T. Jonker, G.A. Prinz, J. Appl. Phys. **61** (1987) 2596
- [91] A. Filipe, A. Schuhl, P. Galtier, Appl. Phys. Lett. **70** (1997) 129
- [92] J.M. Florczak and E.D. Dahlberg, Phys. Rev. B **44** (1991) 9338
- [93] C. Daboo, R.J. Hicken, E. Gu, M. Gester, S.J. Gray, D.E.P. Eley, E. Ahmad, and J.A.C. Bland, Phys. Rev. B **51** (1995) 15964
- [94] M. Gester, C. Daboo, R.J. Hicken, S.J. Gray, A. Ercole, and J.A.C. Bland, J. Appl. Phys. **80** (1996) 347
- [95] P.M. Thibado, E. Kneedler, B.T. Jonker, B.R. Bennett, B.V. Shanabrook, and L.J. Whitman, Phys. Rev. B **53** (1996) R10481
- [96] E. Kneedler, B.T. Jonker, P.M. Thibado, R.J. Wagner, B.V. Shanabrook, and L.J. Whitman, Phys. Rev. B **56** (1997) 8163
- [97] Y.B. Xu, E.T.M. Kernohan, D.J. Freeland, A. Ercole, M. Tselepi, and J.A.C. Bland, Phys. Rev. B **58** (1998) 890
- [98] Y.B. Xu, E.T.M. Kernohan, D.J. Freeland, M. Tselepi, A. Ercole, and J.A.C. Bland, J. Magn. Magn. Mat. **198-199** (1999) 703
- [99] H.P. Schönherr, R. Nötzel, W. Ma, K.H. Ploog, J. Appl. Phys. **89** (2001) 169
- [100] M. Zölfl, M. Brockmann, M. Köhler, S. Kreuzer, T. Schweinböck, S. Miethaner, F. Bensch, and G. Bayreuther, J. Magn. Magn. Mat. **175** (1997) 16
- [101] M. Brockmann, M. Zölfl, S. Miethaner, G. Bayreuther, J. Magn. Magn. Mat. **198-199** (1999) 384
- [102] Q. Xue, T. Hashizume, J.M. Zhou, T. Sakata, T. Ohno, T. Sakurai, Phys. Rev. Lett. **74** (1995) 3177
- [103] H. Spies, *Mössbauerspektroskopische Untersuchung eisenhaltiger Nanopartikel und Gläser und Konstruktion eines Elektronendetektors fuer Mössbauerspektroskopie*, Diplomarbeit, Gerhard-Mercator-Universität Duisburg, Duisburg, (2000)
- [104] I.M.L. Billas, A. Chatelain, W.A. de Heer, Science **265** (1994) 1682
- [105] E.M. Logothetis, W.J. Kaiser, H.K. Plummer, and S.S. Shinozaki, J. Appl. Phys. **60** (1986) 2548
- [106] V. Uzdin, W. Keune, H. Schör, and M. Walterfang, Phys. Rev. B **63** (2001) 104407
- [107] G.A. Busch and R. Kern, Solid State Phys. **11** (1961) 1
- [108] A.W. Ewald and O.N. Tufle, J. Appl. Phys. **29** (1958) 1007

- 
- [109] J.H. Becker, J. Appl. Phys. **29** (1958) 1110
- [110] R.F.C. Farrow, D.S. Robertson, G.M. Williams. A. G. Cullis, G. R. Jones, I.M. Young, and P.N.J. Dennis, J. Crystal Growth **54** (1981) 507
- [111] T. Osaka, H. Omi, K. Yamamoto, and A. Ohtake, Phys. Rev. B **50** (1994) 7567
- [112] D.T. Wang, N. Esser, M. Cardona, and J. Zegenhagen, Surf. Sci. **343** (1995) 31
- [113] T. Ichikawa, Surf. Sci. **140** (1984) 37
- [114] R.F. Schmitsdorf, T.U. Kampen, and W. Mönch, J. Vac. Sci. Tech. B **15** (1997) 1221
- [115] D.R. Heslinga, H.H. Weitering, D.P. van der Werf, and T.M. Klapwijk, Phys. Rev. Lett. **64** (1990) 1589
- [116] P.J. Estrup and J. Morrison, Surf. Sci. **2**, 465 (1964)
- [117] C. Törnevik, M. Hammar, N.G. Nilsson, and S.A. Flodström, Phys. Rev. B **44** (1991) 13144
- [118] M.S. Worthington, J.L. Stevens, C.S. Chang, and I.S.T. Tsong, Nuclear Instr. and Methods in Phys. Research B **64** (1992) 566
- [119] A.H. Levermann, P.B. Howes, K.A. Edwards, H.T. Anyele, C.C. Matthai, J.E. Macdonald, R. Feidenhans'l, L. Lottermoser, L. Seehofer, G. Falkenberg, and R.L. Johnson, Applied Surface Science **104-105** (1996) 124
- [120] R.A. Brand, Nucl. Instr. Meth. B **28** (1987) 417
- [121] B. Roldan Cuenya, W. Keune, W. Sturhahn, M.Y. Hu, and T.S. Toellner, Phys. Rev. B (submitted)
- [122] A. Barla, R. Rüffer, A.I. Chumakov, J. Metge, J. Plessel, M. M. Abd-Elmeguid, Phys. Rev. B **61** (2000) R14881
- [123] T. Ichikawa, and S. Ino, Surface Science **105** (1981) 395
- [124] A. Svane, N.E. Christensen, C.O. Rodriguez, and M. Methfessel, Phys. Rev. B **55** (1997) 12572
- [125] *Mössbauer Effect Data Index covering the 1974 literature*, J.G. Stevens and V.E. Stevens (Eds.), (IFI/Plenum, New York, 1975), p.153
- [126] B. Roldan Cuenya, M. Doi, O. Marks, W. Keune, and K. Mibu, in *Structure and Dynamics of Heterogeneous Systems*, P. Entel and D.E. Wolf (Eds.), (World Scientific, Singapore, 2000), p.251.

- 
- [127] M. Grodzicki, V. Männing, A.X. Trautwein, and J.M. Friedt, *J. Phys. B: At. Mol. Phys.* **20** (1987) 5595
- [128] D.L. Weaire, in *Amorphous Solids-Low Temperature Properties*, Topics in Current Physics vol. **24**, W.A. Phillips (Ed.), (Springer, Berlin, Heidelberg, New York 1981), p.13, and references cited therein.
- [129] M. Cardona, in : *Phonon Physics*, J. Kollár, N. Kroó, N. Menyhárd and T. Siklós (Eds.), (World Scientific, Singapore, 1985) p.2, and references cited therein.
- [130] H. Omi, H. Saito, and T. Osaka, *Phys. Rev. Lett.* **72** (1994) 2596
- [131] L.K. Nanver, G. Weyer, and B.I. Deutch, *Z. Phys. B-Condensed Matter* **47** (1982) 103
- [132] R. Alben, D. Weaire, J.E. Smith, Jr., and M.H. Brodsky, *Phys. Rev. B* **11**, 2271 (1975); *Phys. Rev. Lett.* **29** (1972) 1505
- [133] P. Pavone, S. Baroni, and S. Gironcoli, *Phys. Rev. B* **57** (1998) 10421
- [134] W.T. Yuen, W.K.Liu, S.N. Holmes, and R.A. Stradling, *Semicond. Sci. Technol.* **4** (1989) 819
- [135] W.T. Yuen, W.K.Liu, B.A. Joyce, and R.A. Stradling, *Semicond. Sci. Technol.* **5** (1990) 373
- [136] W.T. Yuen, W.K.Liu, R.A. Stradling, and B.A. Joyce, *J. Crystal Growth* **111** (1991) 943
- [137] B.F. Mason, and B.R. Williams, *Surf. Sci.* **262** (1992) 169
- [138] see, for instance, W. Mönch, *Semiconductor surfaces and interfaces*, Springer Series in Surface Science vol. **XV**, (Springer, Berlin, New York 1995)
- [139] M. Hansen and K. Anderko, *Constitution of binary alloys*, (McGraw-Hill, New York 1958), p.1193
- [140] J.M. Worlock, in: *Phonon Physics*, J. Kollár, N. Kroó, N. Menyhárd, and T. Siklós (Eds.), (World Scientific, Singapore, 1985), p.506
- [141] T. Ruf, *Phonon Raman Scattering in Semiconductors, Quantum Wells and Superlattices-Basic Results and Applications*, Springer Tracts in Modern Physics vol. **142** (Springer, Berlin, Heidelberg, 1998), p.9
- [142] M. Seto, Y. Yoda, S. Kikuta, X.W. Zhang, and A. Ando, *Phys. Rev. Lett.* **74** (1995) 3828
- [143] W. Keune and W. Sturhahn, *Hyperfine Int.* **123/124** (1999) 847

- 
- [144] W. Sturhahn, R. Röhlsberger, E.E. Alp, T. Ruckert, H. Schrör, and W. Keune, J. Magn. Magn. Mat. **198-199** (1999) 590
- [145] Röhlsberger, E.E. Alp, E. Gerdau, O. Leupold, K.W. Quast, R. Ruffer, W. Sturhahn, T.S. Toellner, and E. Burkel, Physica B **263-264** (1999) 574
- [146] R. Ruffer, and A.I. Chumakov, Hyperfine Int. **97/98** (1996) 589
- [147] T.S. Toellner, to be published.
- [148] H. Kiessig, Annalen d. Physik **10** (1931) 769
- [149] L.G. Parratt, Phys. Rev. B **5** (1954) 359
- [150] D.A. Shirley, M. Kaplan, and P. Axel, Phys. Rev. B **123** (1961) 816
- [151] X. Zhang, J.D. Comins, A.G. Every, P.R. Stoddart, W. Pang, and T.E. Derry, Phys. Rev. B **58** (1998) 13677
- [152] D. Bermejo and M. Cardona, J. Non-Cryst. Solids **32** (1979) 405
- [153] J. Menendez and M. Cardona, Phys. Rev. B **29** (1984) 2051
- [154] W. Sturhahn, Hyperfine Int. **125** (2000) 149
- [155] M. Hu, W. Sturhahn, T.S. Toellner, P.M. Hession, J.P. Sutter, and E.E. Alp, Nucl. Instrum. Meth. in Phys. Res. A **428** (1999) 5511
- [156] W. Sturhahn and A.I. Chumakov, Hyperfine Int. **123-124** (1999) 809
- [157] M. Fanciulli, H.C. Vestergaard, G. Weyer, M. Fyhn, S. Yu Shiryaev, and A. Nylandsted Larsen, in: *Proceedings of 23rd International Conference on the Physics of Semiconductors*, M. Scheffler and R. Zimmermann (Eds.), (World Scientific, Singapore, 1996), vol.2, p.1059
- [158] U. Gonser, in: *Mössbauer Spectroscopy*, U. Gonser (Ed.), (Springer, Berlin, Heidelberg, New York 1975) p.1
- [159] W.A. Kamitakahara, H.R. Shanks, J.F. McClelland, U. Buchenau, F. Gompf, and L. Pintschovius, Phys. Rev. Lett. **52** (1984) 644
- [160] R.M. Martin, Phys. Rev. B **1** (1970) 4005
- [161] C.J. Buchenauer, M. Cardona, and F.H. Pollak, Phys. Rev. B **3** (1971) 1243
- [162] R. Tsu, J. González-Hernández, and F.H. Pollak, Solid State Commun. **54** (1985) 447
- [163] J.E. Yehoda and J.S. Lannín, J. Vac. Sci. Technol. **A1** (1983) 392

- [164] B. Fultz, T.A. Stephens, E.E. Alp, M.Y. Hu, J.P. Sutter, T.S. Toellner, and W. Sturhahn, *Phys. Rev. B* **61** (2000) 14517
- [165] G. Prinz, *J. Magn. Magn. Mat.* **100** (1991) 469
- [166] E.S. Machlin, in: *An Introduction to Aspects of Thermodynamics and Kinetics relevant to Materials Science*, (Giro Press, Croton-on-Hudson, New York, 1991), p.131



# Summary

This thesis describes research on magnetism, structure, and vibrational dynamics in a number of magnetic and non-magnetic nanoscaled heterostructures. Much attention is paid to a thorough structural characterization of the materials, because this is essential for understanding the stabilization of metastable phases (here: fcc-like Fe and  $\alpha$ -Sn), magnetic properties such as anisotropy and magneto-volume instabilities, or lattice vibrational behavior. A number of experimental techniques were used, such as  $^{57}\text{Fe}$  and  $^{119}\text{Sn}$  Conversion Electron Mössbauer Spectroscopy (CEMS), Magneto-Optic Kerr Effect (MOKE),  $^{119}\text{Sn}$  Nuclear Resonant Inelastic X-ray Scattering (NRIXS), X-Ray Diffraction (XRD), Reflection High Energy Electron Diffraction (RHEED), Low Energy Electron Diffraction (LEED), and Auger Electron Spectroscopy (AES).

The most important results are listed below:

- In chapter 3 the magnetization behavior of nanoscaled selfassembled Fe stripes grown on Pd(110) by step-decoration is discussed. The stripes are ferromagnetic starting at  $\sim 0.3$  ML coverage, and have a magnetic easy axis along the surface normal up to  $\sim 0.7$  ML, where the easy axis starts to reorient. An exponential decay of remanent and saturation magnetizations with increasing temperature is observed up to 0.7 ML coverage, attributed to the finite size rounding of the Curie temperature of quasi-1D stripes. The effective Curie temperature as function of coverage exhibits finite size scaling with a shift exponent  $\lambda=1.2 \pm 0.3$ , consistent with the 2D Ising model. The observed decrease of the in-plane atomic distance with increasing Fe film thickness is explained by initial pseudomorphic growth followed by relaxed epitaxial growth of fcc-like Fe(110) on Pd(110). The observed 15 % enhancement of the hyperfine magnetic field (relative to bulk bcc-Fe) indicates the presence of the ferromagnetic fcc-like Fe phase with an enhanced Fe atomic moment.
- Chapter 4 deals with the relation between crystal structure, film thickness and spin-reorientation in the Fe/Cu<sub>3</sub>Au(001) system. A continuous fcc-bcc Bain transformation takes place with increasing coverage. The atomic volume of the tetragonal states versus in-plane atomic spacing is found to be close to fct or bct epitaxial lines. A crossover from ferromagnetic high-moment high-volume fct Fe to bct Fe is found to occur between  $\sim 3.5$ -6.5 ML, where the in-plane atomic spacing is nearly constant. Correlated with the Bain transformation is a spin reorientation from preferentially perpendicular (for fct structure) to in-plane (for bct) spin direction at 25 K. The observed hyperfine field enhancement of 6 % is smaller than for the case of Fe/Pd(110) (chapter 3).

- In chapter 5 results upon the growth and magnetic behavior of Fe/GaAs(001)-(4x6) and Fe/GaAs(001)-(4x6)-HEMT layers are described. The in-plane atomic distance was found to be enlarged due to interfacial alloy formation during the first 5 ML of Fe. For thicker Fe layers the in-plane atomic distance is reduced to a value close to bulk bcc-Fe. No magnetic dead layers exist at the Fe/GaAs interface for samples grown at low temperatures (below 50°C). The observed large hyperfine fields correspond to a nearly full magnetic moment of bcc-Fe at the Fe/GaAs(001) interface (estimated mean value  $\sim 1.7 \mu_B$ , most probable value  $\sim 2 \mu_B$ ), leaving open the possibility of injection of spin-polarized electrons in devices based on Fe/GaAs.
- Chapter 6 reports on the room temperature stabilization of up to 3.5 ML epitaxial metastable  $\alpha$ -Sn at the Si(111)-(7x7) surface. The  $\alpha$ -Sn layers remain stabilized at the interface even after the deposition of thick Sn layers that undergo the  $\alpha$ -Sn  $\rightarrow$   $\beta$ -Sn transformation. Additionally, a small decrease in the s-electron density at the  $^{119}\text{Sn}$  nucleus is found for submonolayer of Sn at the Sn/Si(111)-(7x7) interface.
- The structure and vibrational dynamics of Sn/Si multilayers is reported in chapter 7. Raman measurements indicate that the Si layers grown are amorphous. Mössbauer isomer shifts demonstrate that the Sn layers in these multilayers exist in a pure metastable  $\alpha$ -like Sn phase up to a Sn thickness of 10 Å. The formation of crystalline  $\beta$ -Sn was observed with increasing Sn thickness, with 10 Å thick  $\alpha$ -like-Sn layers remaining stabilized at the Sn/Si interface at room temperature. NRIXS measurements of the Sn-projected vibrational density of states provide evidence that 10 Å Sn in the Sn/a-Si multilayers are amorphous. It was also found that the a-Sn/a-Si interface free energy stabilizes the metastable amorphous  $\alpha$ -like Sn phase, and not the vibrational entropy.

# Acknowledgments

I wish to thank my thesis advisor, Prof. Werner Keune, for providing me with the guidance I needed to progress through the graduate program at the university of Duisburg. His particular way of leading the group, treating his co-workers as his own family, provide a very pleasant work atmosphere, optimal for doing research. Also, the other members of the group have been enormously helpful to this work, in particular Ulrich von Hörsten, who gave a base of knowledge on UHV techniques, epitaxial growth and Mössbauer spectroscopy, without which this research would have taken considerably longer.

The diversity of topics I have studied during the last three years allowed me to cooperate with many scientist all over the world, so that my acknowledgments should be longer than my thesis. I am grateful to all of them.

I have especially benefited from Prof. Masaaki Doi's experience in surface science during his stay in Duisburg at the beginning of my work, and from all his patience with the many questions he got from this unexperienced student.

I am also indebted to Dr. Sam Bader for the good acceptance I found in his group during my stay at the Argonne National Laboratory, USA, and to Dr. Dongqi Li for teaching me magneto-optics and nanoscale magnetism during the many hours we spent working together in Argonne. I also would like to thank John Pearson for his technical support at the Argonne National Laboratory, and especially for making of my stay in the USA a wonderful experience.

I would like to thank Dr. Marcos Grimsditch for making available some of his laboratory (Raman) equipment. Also, I acknowledge Dr. Wolfgang Sturhahn's assistance and guidance with the nuclear resonant inelastic X-ray scattering measurements at the Advanced Photon Source, Argonne, and Dr. Hermann Nienhaus' helpful discussions concerning Sn/Si.

Dr. Francisco Salas deserves special mention for encouraging me to go to Germany to work with Prof. Werner Keune. His advice has completely changed the way of my life.

Furthermore, I would like to thank my parents for all their love and for educating me in the thought that hard work will take you wherever you want.

I am grateful for financial support by the Deutsche Forschungsgemeinschaft (Graduiertenkolleg 277).



# Curriculum Vitae

## Personal Data

**Name:** Beatriz Roldán Cuenya  
**Date of birth:** May 6., 1976  
**Place of birth:** Oviedo, Spain  
**Nationality:** Spanish (European citizen)  
**Marital status:** single



## Academic degrees

- Licenciada en Física (Master of Sciences: Physics), 1998 University of Oviedo, Spain  
Speciality: Física de Materiales (Solid state physics).
- Since October 1998: PhD work in experimental solid state physics at the Gerhard-Mercator University of Duisburg, Germany (Supervisor: Prof. Dr. W. Keune).

## Experience

- 06/01/1998-09/30/1998: Instituto Nacional del Carbón in Oviedo, Spain.  
X-ray Reflectometry.
- Since 10/01/1998: Laboratorium für Angewandte Physik, University of Duisburg, Germany.  
UHV, AES, RHEED, LEED, X-ray diffraction and Mössbauer spectroscopy on magnetic thin films and multilayers: Fe/Cu(001), Fe/Cu<sub>3</sub>Au(001), Fe/GaAs(001), Sn/Cu<sub>3</sub>Au(001), Sn/InSb(006), Sn/Si(111)(7x7), Sn/Si multilayers.
- 03/01/2000-08/01/2000: Materials Science Division, Argonne National Laboratory, (Illinois) USA.  
Growth and magnetic properties of Fe nanowires on stepped Pd(110). Surface Magneto-optic Kerr Effect. Raman Spectroscopy on Sn/Si multilayers.
- 11/03/2000-11/15/2000: Advanced Photon Source, Argonne National Laboratory, (Illinois) USA.  
Nuclear resonant inelastic X-ray scattering studies on amorphous Sn/Si multilayers.

## Languages

Fluent in Spanish, German and English, and good knowledge of French.

## **Contributions to conferences and international meetings.**

- International Symposium on Structure and Dynamics of Heterogeneous Systems (SDHS 99), 02/24-26/1999, Duisburg, Germany.
- Spring meeting of the DPG (Deutsche Physikalische Gesellschaft), 03/22-26/1999, Münster, Germany.
- International Conference of Applications of the Mössbauer Effect (ICAME), 08/29/1999-09/03/1999, Garmisch-Partenkirchen, Germany.
- 57th International Symposium of the American Vacuum Society, 10/02-06/2000, Boston, MA, USA.
- Workshop: Correlation of Structure and Magnetism in Novel Nanoscale Magnetic Particles, 10/29-30/2000, Slomenice Castle, Slovakia.
- Spring meeting of the DPG (Deutsche Physikalische Gesellschaft), 03/25-28/2001, Hamburg, Germany.
- 4th International Symposium on Metallic Multilayers, 06/24-29/2001, Aachen, Germany.
- Workshop: Mesomagnetism, Spin Dynamics and Spin Electronics, 06/30/-07/05/2001, Santorini, Greece.

# List of publications

- B. Roldan Cuenya, M. Doi, O. Marks, W. Keune, K. Mibu, Reflection High-Energy Electron Diffraction and  $^{119}\text{Sn}$  Mössbauer investigations of Epitaxial  $\alpha$ -Sn Films, in *Strukture and Dynamics of Heterogeneous Systems*, eds. P. Entel and D.E. Wolf, World Scientific, Singapore, p. 251 (2000).
- B. Roldan Cuenya, M. Doi, T. Ruckert, W. Keune, T. Steffel, Magnetism and Structure of Epitaxial Face-Centered Tetragonal Fe Thin Films, in *Frontiers in Magnetism*, J. Phys. Soc. Japan **79**, Suppl. A, p. 125 (2000)
- B. Roldan Cuenya, M. Doi, S. Löbus, R. Courths and W. Keune, Observation of the fcc-to-bcc Bain transformation in epitaxial Fe ultrathin films on  $\text{Cu}_3\text{Au}(001)$ , Surface Science (in press)
- B. Roldan Cuenya, J. Pearson, Chengtao Yu, Dongqi Li, S.D. Bader, Growth and Magnetic Properties of Ultrathin Fe on Pd(110), Journal of Vacuum Science and Technology A (in press)
- Dongqi Li, B. Roldan Cuenya, J. Pearson, S.D. Bader, W. Keune, Magnetism of Step-Decorated Fe/Pd(110), Phys. Rev. B **64**, (in press)
- B. Roldan Cuenya, W. Keune, W. Sturhahn, T.S. Toellner, M.Y. Hu, Structural and Dynamical Properties of Sn/Si Multilayers, Phys. Rev. B, (in press)
- M. Doi, B. Roldan Cuenya, W. Keune, T. Schmitte, A. Nefedov, H. Zabel, D.Spoddig, R. Meckenstock, and J. Pelzl, Magnetic and structural properties of epitaxial Fe thin films on GaAs(001) and interfaces, (submitted to J. Magn. Magn. Mat.)
- B. Roldan Cuenya, M. Doi, and W. Keune, Epitaxial growth and interfacial structure of Sn on Si(111)-(7x7), (submitted to Surface Science)